Lecture Notes in Electrical Engineering 974

Jitendra Kumar
Manoj Tripathy
Premalata Jena *Editors*

Control Applications in Modern Power Systems

Select Proceedings of EPREC 2022

Springer

Lecture Notes in Electrical Engineering

Volume 974

The book series *Lecture Notes in Electrical Engineering* (LNEE) publishes the latest developments in Electrical Engineering—quickly, informally and in high quality. While original research reported in proceedings and monographs has traditionally formed the core of LNEE, we also encourage authors to submit books devoted to supporting student education and professional training in the various fields and applications areas of electrical engineering. The series cover classical and emerging topics concerning:

- Communication Engineering, Information Theory and Networks
- Electronics Engineering and Microelectronics
- Signal, Image and Speech Processing
- Wireless and Mobile Communication
- Circuits and Systems
- Energy Systems, Power Electronics and Electrical Machines
- Electro-optical Engineering
- Instrumentation Engineering
- Avionics Engineering
- Control Systems
- Internet-of-Things and Cybersecurity
- Biomedical Devices, MEMS and NEMS

For general information about this book series, comments or suggestions, please contact leontina.dicecco@springer.com.

To submit a proposal or request further information, please contact the Publishing Editor in your country:

China

Jasmine Dou, Editor (jasmine.dou@springer.com)

India, Japan, Rest of Asia

Swati Meherishi, Editorial Director (Swati.Meherishi@springer.com)

Southeast Asia, Australia, New Zealand

Ramesh Nath Premnath, Editor (ramesh.premnath@springernature.com)

USA, Canada

Michael Luby, Senior Editor (michael.luby@springer.com)

All other Countries

Leontina Di Cecco, Senior Editor (leontina.dicecco@springer.com)

**** This series is indexed by EI Compendex and Scopus databases. ****

Jitendra Kumar · Manoj Tripathy · Premalata Jena
Editors

Control Applications in Modern Power Systems

Select Proceedings of EPREC 2022

Springer

Editors
Jitendra Kumar
Department of Electrical Engineering
National Institute of Technology
Jamshedpur
Jamshedpur, India

Manoj Tripathy
Department of Electrical Engineering
Indian Institute of Technology Roorkee
Roorkee, India

Premalata Jena
Department of Electrical Engineering
Indian Institute of Technology Roorkee
Roorkee, India

ISSN 1876-1100 ISSN 1876-1119 (electronic)
Lecture Notes in Electrical Engineering
ISBN 978-981-19-7787-9 ISBN 978-981-19-7788-6 (eBook)
https://doi.org/10.1007/978-981-19-7788-6

Contents

About the Editors

Jitendra Kumar is currently Assistant Professor at the Department of Electrical Engineering, National Institute of Technology Jamshedpur, India. He received his B.Tech. from IMS Engineering College, Ghaziabad, India, in 2009, M.Tech. from the National Institute of Technology Kurukshetra, Kurukshetra, in 2011, and the Ph.D. degree in electrical engineering from the Indian Institute of Technology Roorkee, India, in 2017. He has over 4 years of teaching experience and taught subjects like power system, advanced power system, control system, control and instrumentation, power system operation, and control, signal and system, power system protection, circuit and network theory. He has many papers in reputed journals. His research areas are power system protection and restructuring, protection algorithms design in smart grid and microgrid environment, design of protection algorithms in FACTS environment.

Manoj Tripathy received his B.E. degree in electrical engineering from Nagpur University, Nagpur, India, in 1999, the M.Tech. degree in instrumentation and control from Aligarh Muslim University, in 2002, and a Ph.D. degree from the Indian Institute of Technology Roorkee (IIT Roorkee) in 2008. He is currently working as Associate Professor in the Department of Electrical Engineering, IIT Roorkee. His fields of interest are wavelets, neural networks, optimization techniques, content-based image retrieval, digital instrumentation, digital protective relays, and digital speech processing. He is a reviewer for various international journals in the area of power systems and speech.

Premalata Jena is currently Associate Professor at the Department of Electrical Engineering, IIT Roorkee. She received her B.Tech. degree in electrical engineering from the Utkal University, Bhubaneswar, India, in 2001, the M.Tech. degree in Electrical Engineering from IIT Kharagpur, India, in 2006, and a Ph.D. degree from IIT Kharagpur, India, in 2011. She has seven years of teaching experience. She is IEEE Member and INAE, Young Associate. She received many awards such as the Women Excellence Award and Early Carrier Research Award, SERB, DST, Gov. of India, New Delhi, INAE Young Engineer Award, POSOCO Power System Award, in 2013.

She has published many papers in different reputed journals and conferences. Her fields of interest are smart grid, smart grid technology, and protection, microgrid, microgrid protection, signal processing application to power system relaying, power system protection, protection issues with FACTS devices, protection scheme development for a line with FACTS devices, disturbance localization, signal processing application for disturbance localization.

Lyapunov Stability Analysis of Time-Delayed Load Frequency Control System with Electric Vehicles and Demand Response

A. Jawahar and K. Ramakrishnan

Abstract This manuscript explores the influence of time-delays on the single-area load frequency control (LFC) system stability with electric vehicles (EVs) integration in addition to the demand response (DR) control. The signal transmission through communication links in the LFC systems results in inevitable non-identical time-delays in the system feedback paths causing delay-dependent stability issues. The existence of time-delays hinders the transmission of signals among the different entities involved in the control task. This, in turn, invariably degrades the overall performance and affects the system stability. If the network induced time-delays go beyond a critical value called stable delay margin, the overall system loses stability. In this manuscript, using Lyapunov–Krasovskii functional approach, a new stability analysis is presented for ascertaining delay-dependent stability of networked load frequency control systems. The stable delay margins are obtained for different scenarios by varying the controller values of LFC controller and DR control along with participation ratios of conventional generation, electric vehicles and demand response control. The extensive simulation results are also provided to demonstrate the obtained analytical delay margin results.

Keywords Load frequency control systems · Electric vehicle aggregator · Demand response · Linear matrix inequality · Delay-dependent stability · Time-delays

1 Introduction

LFC is a mechanism employed in power systems to maintain harmony between power generation and load demand. Nowadays, open communication networks are widely used for transmission of load frequency control signals from central controller to the various sub-systems. Time-delays are the offspring of the usage of open communication networks in the LFC systems [1–3]. The time-delays, if neglected and not dealt properly can drive the system to instability. Unstable system operation is the most

A. Jawahar (✉) · K. Ramakrishnan
Department of Electrical and Electronics Engineering, Pondicherry Engineering College, Puducherry, India
e-mail: jawahar.a@pec.edu

J. Kumar et al. (eds.), *Control Applications in Modern Power Systems*, Lecture Notes in Electrical Engineering 974, https://doi.org/10.1007/978-981-19-7788-6_1

undesirable power system characteristic feature. The time-delays can show strong adverse impact on the closed loop system performance. Therefore, the maximum permissible limit of these delays (also termed as delay margin) needs to be determined for the system [4–6, 10].

EV based energy storage devices are employed for counteracting the fluctuations in the power due to intermittent nature of renewable energy resources. Generally, numerous EVs are integrated to the power system and this fleet of EVs is termed as Electric vehicle aggregator (EVA). Thus, EVA consists of thousands of EVs and act as a co-ordination center between the central control center and individual EV. The function of EVA is to obtain the control signals from the main control center and transmit the individual EV status to the main control center for necessary control action and attention. EVA can also aid in the frequency regulation apart from meeting the power requirements in the power system [7–9, 19–22].

DR is the heart and soul of the evolving modern power systems which can also assist in the process of frequency regulation. The main objective of DR deployment in the power systems happens to be optimising the electricity consumption during the peak usage time and promote off-peak energy utilisation by providing monetary benefit to the consumers as well as utilities [11–15]. The EV and DR control also require communication infrastructure for signal transmission in the LFC system thereby paving a way for delays in the LFC-EV-DR system.

This manuscript presents the determination of the delay margins of the LFC-EV-DR systems with non-identical communication network time-delays in the EVA loop and DR control. In the literature, the time-delays in EVA loop and DR control are assumed to be identical and similar for assessing the delay-dependent stability of LFC systems. In practical viewpoint, the delays in the closed loop system are unique and dissimilar in nature. Using a novel Lyapunov–Krasovskii functional based approach, delay-dependent stability is established for LFC-EV-DR systems.

2 LFC-EV-DR System with Time-Delays

The schematic diagram of the LFC-EV-DR system is shown in Fig. 1. In the event of generation-power demand mismatch, the central controller on the basis of feedback signal from the incremental frequency variable Δf_i and the incremental tie-line power $\Delta P_{tie,i}$, initiates the control action to re-establish the balance between the generation-power demand.

The load frequency control signal is routed through communication channels along with the appropriate load sharing factors that choose the sharing of surplus/shortage load demand by the traditional generation, EVA and DR control methodologies correspondingly. In the practical situations, the delays in the EVA loop and DR control loop of a particular control area are dissimilar. However, in the existing literature, the delays in the feedback loops are considered as similar or same while analysing the system delay-dependent stability. The notations used in Fig. 1 are given in Table 1.

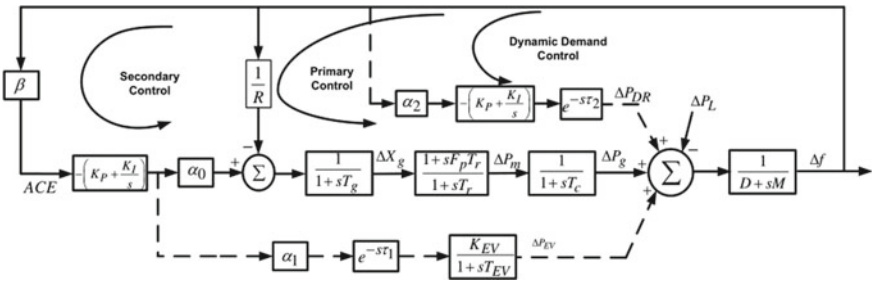

Fig. 1 LFC-EV-DR system

Table 1 Notations

Notation	Nomenclature
ΔP_g	Generator power output
ΔP_m	Mechanical power output
ΔP_{EV}	Power output of electric vehicle aggregator
D	Damping coefficient
R	Speed regulation coefficient
β	Frequency bias factor
F_p	Fraction of the turbine power
T_c	Turbine time constant
T_r	Reheat turbine time constant
T_g	Governor time constant
M	Inertia constant of generator
T_{EV}	Time constant of electric vehicle aggregator
K_{EV}	Gain of electric vehicle aggregator
K_P	Proportional gain of PI controller
K_I	Integral gain of PI controller
α_0	Participation factor of conventional generation
α_1	Participation factor of electric vehicle aggregator
α_2	Participation factor of DR control
τ_1	Time-delay in electric vehicle aggregator
τ_2	Time-delay in DR control loop
τ_d	Time-delay margin

The LFC system with dissimilar time-delays in the EVA and DR control loops as shown in Fig. 1 is modeled in the following autonomous state-space analysis as follows:

$$\dot{x}(t) = Ax(t) + A_1x(t - \tau_1) + A_2x(t - \tau_2) \tag{1}$$

$$x(t) = \Phi(t), \forall t \in [-\max(\tau_1, \tau_2), 0] \tag{2}$$

where $x(t) \in R^{6\times1}$ is the state vector, and $A \in R^{6\times6}$, $A_1 \in R^{6\times6}$ and $A_2 \in R^{6\times6}$ are the system matrices associated with current state vector and delayed state vectors. The initial condition $\Phi(t)$ is defined in $t \in [-\max(\tau_1, \tau_2), 0]$.

$$A = \begin{bmatrix} -\frac{D}{M} & \frac{1}{M} & 0 & 0 & 0 & \frac{1}{M} \\ 0 & -\frac{1}{T_c} & \frac{1}{T_c} & 0 & 0 & 0 \\ \frac{F_p\alpha_0K_p\beta}{T_g} & -\frac{F_p}{RT_g} & 0 & -\frac{1}{T_r} & -\frac{F_p}{T_g}+\frac{1}{T_r} & \frac{F_p\alpha_0K_i}{T_g} & 0 \\ -\frac{\alpha_0K_p\beta}{T_g} & -\frac{1}{RT_g} & 0 & 0 & -\frac{1}{T_g} & -\frac{\alpha_0K_i}{T_g} & 0 \\ \beta & 0 & 0 & 0 & 0 & 0 \\ 0 & 0 & 0 & 0 & 0 & -\frac{1}{T_{EV}} \end{bmatrix}$$

$$A_1 = \begin{bmatrix} 0 & 0\,0\,0 & 0 & 0 \\ 0 & 0\,0\,0 & 0 & 0 \\ 0 & 0\,0\,0 & 0 & 0 \\ 0 & 0\,0\,0 & 0 & 0 \\ 0 & 0\,0\,0 & 0 & 0 \\ -\frac{K_{EV}\alpha_1K_p\beta}{T_{EV}} & 0\,0\,0 & -\frac{K_{EV}\alpha_1K_i}{T_{EV}} & 0 \end{bmatrix}$$

$$A_2 = \begin{bmatrix} -\frac{K_p\alpha_2}{M} & 0\,0\,0\,0 & -\frac{K_i\alpha_2}{M} \\ 0 & 0\,0\,0\,0 & 0 \\ 0 & 0\,0\,0\,0 & 0 \\ 0 & 0\,0\,0\,0 & 0 \\ 0 & 0\,0\,0\,0 & 0 \\ 0 & 0\,0\,0\,0 & 0 \end{bmatrix}$$

3 Stability Criterion

For deriving the stability criterion for assessing the delay-dependent-stability of system (1) subjected to (2), following lemmas are required.

Lemma 1: Jenson Integral Inequality [16]: For any positive symmetric constant matrix $M \in R^{n\times n}$, scalars $r_1 < r_2$, a vector valued function $\omega : [r_1, r_2] \to R^n$ such that the integrations concerned are well defined, then the inequality (3) holds.

$$\left(\int_{r1}^{r2} \omega(s)ds\right)^T M \left(\int_{r1}^{r2} \omega(s)ds\right) \leq (r_2 - r_1) \int_{r1}^{r2} \omega^T(s) M\, \omega(s)ds \tag{3}$$

Lemma 2: Wirtinger Inequality [17]: For given symmetric positive definite matrix R, and for any differentiable signal ω in $[a, b] \rightarrow R^n$, then the equality (4) holds.

$$\int_b^a \dot{\omega}^T(u)\mathrm{R}\dot{\omega}(u)\mathrm{du} \geq \frac{1}{b-a}\begin{bmatrix} \omega(b) \\ \omega(a) \\ \frac{1}{b-a}\int_a^b \omega(u)du \end{bmatrix}^T \begin{bmatrix} 4R & 2R & -6R \\ * & 4R & -6R \\ * & * & 12R \end{bmatrix} \begin{bmatrix} \omega(b) \\ \omega(a) \\ \frac{1}{b-a}\int_a^b \omega(u)du \end{bmatrix} \tag{4}$$

The proposed stability criterion for the system in (1) is given in the form of the following theorem:

Theorem 1 The system (1) with time-delays τ_1 and τ_2 is asymptotically stable in the sense of Lyapunov, if there exists real symmetric positive definite matrices $P_{11}, S_1, S_2, R_1, R_2$ *and* R_3; symmetric matrices P_{22} *and* P_{33}; free matrices P_{12}, P_{13} *and* P_{23} of appropriate dimensions such that the following linear matrix inequalities (LMIs) hold:

$$\Pi_0 > 0 \tag{5}$$

$$\begin{bmatrix} \sum_{k=1}^{5}\Pi_k & \overline{A}^T U_1 & \overline{A}^T U_2 \\ * & -U_1 & 0 \\ * & * & -U_2 \end{bmatrix} < 0 \tag{6}$$

where

$\Pi_0 = P + diag\left(\left[0, \tau_1^{-1}S_1, \tau_2^{-1}S_2\right]\right)$,

$\Pi_1 = \Phi_1^T P \Phi_2 + \left(\Phi_1^T P \Phi_2\right)^T$,

$\Pi_2 = diag([S_1 + S_2, -S_1, -S_2, 0, 0])$,

$$\Pi_3 = \begin{bmatrix} -\frac{4}{\tau_1}R_1 & -\frac{2}{\tau_1}R_1 & 0 & \frac{6}{\tau_1}R_1 & 0 \\ * & -\frac{4}{\tau_1}R_1 & 0 & \frac{6}{\tau_1}R_1 & 0 \\ * & * & 0 & 0 & 0 \\ * & * & * & -\frac{12}{\tau_1}R_1 & 0 \\ * & * & * & * & 0 \end{bmatrix},$$

$$\Pi_4 = \begin{bmatrix} -\frac{4}{\tau_2}R_2 & 0 & -\frac{2}{\tau_2}R_2 & 0 & \frac{6}{\tau_2}R_2 \\ * & 0 & 0 & 0 & 0 \\ * & * & -\frac{4}{\tau_2}R_2 & 0 & \frac{6}{\tau_2}R_2 \\ * & * & * & 0 & 0 \\ * & * & * & * & -\frac{12}{\tau_2}R_2 \end{bmatrix},$$

$\Pi_5 = \begin{bmatrix} 0 & I & -I & 0 & 0 \end{bmatrix}^T (-R_{12}) \begin{bmatrix} 0 & I & -I & 0 & 0 \end{bmatrix}$.

with

$$P = \begin{bmatrix} P_{11} & P_{12} & P_{13} \\ * & P_{21} & P_{22} \\ * & * & P_{33} \end{bmatrix},$$
$$\Phi_1 = \begin{bmatrix} I & 0 & 0 & 0 & 0 \\ 0 & 0 & 0 & \tau_1 & 0 \\ 0 & 0 & 0 & 0 & \tau_2 \end{bmatrix}^T,$$
$$\Phi_2 = \begin{bmatrix} A & A_1 & A_2 & 0 & 0 \\ I & -I & 0 & 0 & 0 \\ I & 0 & -I & 0 & 0 \end{bmatrix},$$
$$\overline{A} = \begin{bmatrix} A & A_1 & A_2 & 0 & 0 \end{bmatrix},$$
$$U_1 = \tau_1 R_1 + \tau_2 R_2,$$
$$U_2 = (\tau_2 - \tau_1)^2 R_{12}.$$

Proof The LK functional $V(x(t)) = \sum_{i=1}^{4} V_i(x(t))$ with

$$V_1(x(t)) = \Xi^T(t) P \Xi(t) \tag{7}$$

$$V_2(x(t)) = \sum_{i=1}^{2} \int_{t-\tau_i}^{t} x^T(s) S_i x(s) ds \tag{8}$$

$$V_3(x(t)) = \sum_{i=1}^{2} \int_{-\tau_i}^{0} \int_{t+\theta}^{t} \dot{x}^T(s) R_i \dot{x}(s) ds d\theta \tag{9}$$

$$V_4(x(t)) = (\tau_2 - \tau_1) \int_{-\tau_2}^{-\tau_1} \int_{t+\theta}^{t} \dot{x}^T(s) R_3 \dot{x}(s) ds d\theta \tag{10}$$

with $\Xi(t) = \left[x^T(t) \ \int_{t-\tau_1}^{t} x^T(s) ds \ \int_{t-\tau_2}^{t} x^T(s) ds \right]^T$.
The following conditions hold, by (3):

$$\int_{t-\tau_1}^{t} x^T(s) S_1 x(s) ds \geq \left[\int_{t-\tau_1}^{t} x(s) ds \right]^T \left(\frac{S_1}{\tau_1} \right) \left[\int_{t-\tau_1}^{t} x(s) ds \right] \tag{11}$$

$$\int_{t-\tau_2}^{t} x^T(s) S_2 x(s) ds \geq \left[\int_{t-\tau_2}^{t} x(s) ds \right]^T \left(\frac{S_2}{\tau_2} \right) \left[\int_{t-\tau_2}^{t} x(s) ds \right] \tag{12}$$

By using the above Eqs. (11) and (12), one can readily obtain a lower bound for $V(x(t))$ as follows:

$$V(x(t)) \geq \Xi(t)^T \Pi_0 \Xi(t) + V_3(x(t)) + V_4(x(t) \tag{13}$$

The positive definiteness of S_i, R_j; and $\Pi_0 > 0$ implies positive definiteness of V (x(t)).

The time-derivative of $V_1(x(t))$ is given by

$$\dot{V}_1(x(t)) = 2\Xi^{\mathrm{T}}(t) P \dot{\Xi}(t) \tag{14}$$

which can be rewritten as

$$\dot{V}_1(x(t)) = \delta^T(t)\, \Pi_1 \delta(t) \tag{15}$$

where $\delta(t) = \left[x^T(t)\ x^T(t-\tau_1)\ x^T(t-\tau_2)\ \frac{1}{\tau_1}\int_{t-\tau_1}^{t} x^T(s)ds\ \frac{1}{\tau_2}\int_{t-\tau_2}^{t} x^T(s)ds \right]^T$ is an augmented state vector.

The time-derivative of $V_2(x(t))$ is given by

$$\dot{V}_2(x(t)) = x^T(t)(S_1 + S_2)x(t) - \sum_{i=1}^{2} x^T(t-\tau_i) S_i x(t-\tau_i) \tag{16}$$

The Eq. (16), in terms of $\delta(t)$, is expressed as follows:

$$\dot{V}_2(x(t)) = \delta^T(t)\Pi_2\delta(t) \tag{17}$$

The time-derivative of the $V_3(x(t))$ is given by

$$\dot{V}_3(x(t)) = \dot{x}^T(t)U_1\dot{x}(t) - \int_{t-\tau_1}^{t} \dot{x}^T(s)R_1\dot{x}(s)ds - \int_{t-\tau_2}^{t} \dot{x}^T(s)R_2\dot{x}(s)ds \tag{18}$$

Now, by using Wirtinger inequality, the Eq. (18) is expressed as follows:

$$\dot{V}_3(x(t)) \leq \delta^T(t)\left(\overline{A}^T U_1 \overline{A}\right)\delta(t) + \delta^T(t)\Pi_3\delta(t) + \delta^T(t)\Pi_4\delta(t) \tag{19}$$

The time-derivative of $V_4(x(t))$ is given by

$$\dot{V}_4(x(t)) = \dot{x}^T(t)U_2\dot{x}(t) - (\tau_2 - \tau_1)\int_{t-\tau_2}^{t-\tau_1} \dot{x}^T(s)R_{12}\dot{x}(s)ds \tag{20}$$

Now, (20) is expressed as an inequality using (3) as:

$$\dot{V}_4(x(t)) \leq \delta^T(t)\left(\overline{A}^T U_2 \overline{A}\right)\delta(t) + \delta^T(t)\Pi_5\delta(t) \tag{21}$$

By combining the $\dot{V}(x(t)), i = 1\,to\,4$, the following condition was obtained:

$$\dot{V}(x(t)) = \sum_{i=1}^{4} \dot{V}_i(x(t)) \leq \delta^T(t)\left[\sum_{k=1}^{5} \Pi_k + \overline{A}^T(U_1 + U_2)\overline{A}\right]\delta(t). \tag{22}$$

Now, by Schur Complement, if the inequality conditions (3) and (4) hold simultaneously, then there exists a sufficiently small scalar $\alpha > 0$ such that $\dot{V}(x(t)) \leq -\alpha||x(t)||^2$, which, in turn, implies that the LFC systems described by (1) are asymptotically stable in the sense of Lyapunov [18]. By solving the stability criterion, the delay margin values for the LFC-EV-DR systems are obtained.

4 Results

The system parameters are given in Table 2. The controllers in secondary frequency loop and DR loop are of PI type with same controller gains (K_P and K_I). The stable delay margin values obtained using the Lyapunov stability criterion are listed in Tables 3, 4, 5, 6 and 7 for different K_P, K_I values. The time-delays are given as $\tau_d = \sqrt{\tau_1^2 + \tau_2^2}\, and\, \theta = tan^{-1}\left(\frac{\tau_2}{\tau_1}\right)$.

For the stable delay margin computation, the K_P is varied from 0.4 to 1.0 in steps of 0.2, and the K_I is set as 0.6 and 0.8. The Tables 3 and 4 present the delay margin values provided by the proposed stability criterion for various values of K_p and K_I of LFC controller with participation factor $\alpha_0 = 0.8$, $\alpha_1 = 0.1$ and $\alpha_2 = 0.1$. The Tables 5 and 6 show the delay margin values for different controller gains with participation factor $\alpha_0 = 0.7$, $\alpha_1 = 0.2$ and $\alpha_2 = 0.1$. The Tables 7 and 8 present

Table 2 Parameters under study

Notation	Value
M	8.8
D	1
F_p	1/6
R	1/11
β	21
T_g	0.2
T_c	0.3
T_r	12
T_{EV}	0.1
K_{EV}	1

Table 3 Delay margin results for $K_I = 0.6$, $\alpha_0 = 0.8$, $\alpha_1 = 0.1$ and $\alpha_2 = 0.1$

θ	$K_p = 0.4$	$K_p = 0.6$	$K_p = 0.8$	$K_p = 1$
5	1.520	2.154	2.708	3.293
10	1.546	2.187	2.742	3.310
20	1.633	2.295	2.843	3.344
30	1.781	2.470	3.007	3.438
40	2.015	2.747	3.278	3.659
45	2.185	2.953	3.490	3.847
50	2.366	3.183	3.737	4.093
60	2.937	3.880	4.526	5.021
70	4.051	5.388	6.538	7.340
80	7.562	10.612	12.877	14.458
85	15.068	21.144	25.657	28.806

the delay margin values for different controller gains with participation factor $\alpha_0 = 0.7$,$\alpha_1 = 0.1$ and $\alpha_2 = 0.2$. The results illustrate that the LFC-EV-DR system stability is enhanced when a DR control loop is added while the delay margin is decreased with the higher EV participation.

For the purpose of validation of the analytical results, simulation studies are conducted, where the system is subjected to a unit step load perturbation of $\Delta P_D = 0.1 pu$ at $t = 0$, and the incremental frequency variable $\Delta f(t)$ response is observed for $t > 0$. For $K_P = 0.6$ and $K_I = 0.8$, with $\alpha_0 = 0.7$, $\alpha_1 = 0.2$ and $\alpha_2 = 0.1$, from Table 5, the stable delay margin obtained is $\tau_d = 2.339$ for $\theta = 50^0$. The LFC-EV-DR system is stable upto $\tau_d = 2.339$ as per the presented stability criterion. The incremental frequency variable exhibits an asymptotically stable response for $\tau_d =$

Table 4 Delay margin results for $K_I = 0.8$, $\alpha_0 = 0.8$, $\alpha_1 = 0.1$ and $\alpha_2 = 0.1$

θ	$K_p = 0.4$	$K_p = 0.6$	$K_p = 0.8$	$K_p = 1$
5	0.864	1.353	1.756	2.081
10	0.881	1.378	1.786	2.112
20	0.938	1.460	1.879	2.202
30	1.034	1.595	2.026	2.341
40	1.188	1.805	2.255	2.564
45	1.298	1.957	2.426	2.736
50	1.415	2.109	2.607	2.927
60	1.799	2.592	3.152	3.515
70	2.507	3.529	4.278	4.948
80	4.256	6.504	8.397	9.746
85	8.052	12.959	16.732	19.418

Table 5 Delay margin results for $K_I = 0.6$, $\alpha_0 = 0.7$, $\alpha_1 = 0.2$ and $\alpha_2 = 0.1$

θ	$K_p = 0.4$	$K_p = 0.6$	$K_p = 0.8$	$K_p = 1$
5	1.128	1.437	1.609	1.665
10	1.147	1.460	1.633	1.688
20	1.213	1.540	1.716	1.767
30	1.327	1.674	1.853	1.897
40	1.510	1.888	2.071	2.104
45	1.642	2.042	2.231	2.257
50	1.781	2.212	2.412	2.435
60	2.241	2.735	2.960	2.975
70	3.118	3.774	4.111	4.212
80	5.663	7.267	8.098	8.297
85	11.284	14.48	16.136	16.532

Table 6 Delay margin results for $K_I = 0.8$, $\alpha_0 = 0.7$, $\alpha_1 = 0.2$ and $\alpha_2 = 0.1$

θ	K_p=0.4	K_p=0.6	K_p=0.8	K_p=1
5	0.743	1.020	1.209	1.313
10	0.758	1.039	1.230	1.335
20	0.806	1.102	1.301	1.407
30	0.889	1.209	1.417	1.522
40	1.021	1.376	1.598	1.701
45	1.116	1.497	1.729	1.832
50	1.218	1.616	1.865	1.973
60	1.552	2.013	2.285	2.398
70	2.168	2.762	3.114	3.265
80	3.695	4.955	5.909	6.391
85	6.976	9.873	11.773	12.735

2.3, marginally stable response for $\tau_d = 2.339$ and unstable response for $\tau_d = 2.4$ as illustrated in Fig. 2. Therefore, the effectiveness of the analytical delay bounds is validated through the simulation results.

5 Conclusions

This study presents the comprehensive delay-dependent stability analysis of a class of networked single-area LFC systems with communication delays. The electric vehicles and demand response are integrated to the LFC systems. This network architecture introduces two non-identical time-delays in the system feedback paths.

Table 7 Delay margin results for $K_I = 0.6$, $\alpha_0 = 0.7$, $\alpha_1 = 0.1$ and $\alpha_2 = 0.2$

θ	K_p=0.4	K_p=0.6	K_p=0.8	K_p=1
5	1.721	2.393	3.019	3.830
10	1.760	2.438	3.054	3.772
20	1.872	2.551	3.109	3.598
30	2.041	2.704	3.190	3.527
40	2.294	2.944	3.367	3.612
45	2.479	3.136	3.536	3.739
50	2.639	3.322	3.718	3.906
60	3.156	3.889	4.324	4.571
70	4.156	5.122	6.055	6.624
80	7.356	10.051	11.926	13.047
85	14.656	20.026	23.761	25.996

Table 8 Delay margin results for $K_I = 0.8$, $\alpha_0 = 0.7$, $\alpha_1 = 0.1$ and $\alpha_2 = 0.2$

θ	K_p=0.4	K_p=0.6	K_p=0.8	K_p=1
5	1.018	1.531	1.971	2.349
10	1.047	1.572	2.016	2.388
20	1.133	1.681	2.119	2.456
30	1.268	1.834	2.249	2.536
40	1.470	2.055	2.446	2.688
45	1.612	2.217	2.604	2.828
50	1.715	**2.339**	2.743	2.967
60	2.115	2.752	3.171	3.411
70	2.791	3.558	4.077	4.540
80	4.300	6.072	7.776	8.942
85	7.603	12.099	15.494	17.817

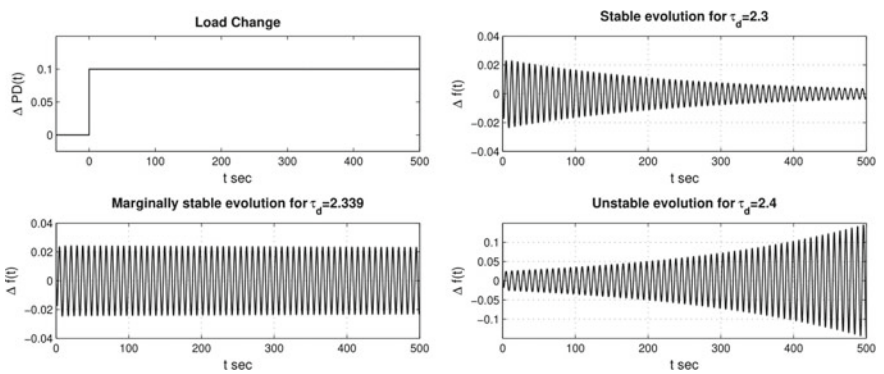

Fig. 2 Evolution of $\Delta f(t)$ for various values of delay

Such time-delays in the feedback loop affect the system dynamic performance. Stable delay margins are computed for different subsets of control parameters and load sharing factors. The proposed stability criterion will be used for assessing the LFC-EV-DR system delay-dependent stability with time-varying delays will be explored in future.

References

1. H. Bevrani, A. Ghosh, G. Ledwich, Renewable energy sources and frequency regulation: survey and new perspectives. IET Renew. Power Gener. **4**(5), 438–457 (2010)
2. J. Chen, G. Gu, C.N. Nett, A new method for computing delay margins for stability of linear delay systems. System and Control Letters **26**(2), 107–117 (1995)
3. A.O. David, I. Al-Anbagi, EVs for frequency regulation: cost benefit analysis in a smart grid environment. IET Electrical Systems in Transportation **7**(4), 310–317 (2017)
4. S.A. Hosseini, M. Toulabi, A.S. Dobakhshari, A. Ashouri-Zadeh, A.M. Ranjbar, Delay compensation of demand response and adaptive disturbance rejection applied to power system frequency control. IEEE Trans. Power Syst. **35**, 2037–2046 (2020)
5. H. Hui, Y. Ding, Y. Song, S. Rahman, Modeling and control of flexible loads for frequency regulation services considering compensation of communication latency and detection error. Appl. Energy **250**, 161–174 (2019)
6. L. Jin, C.K. Zhang, Y. He, L. Jiang, M. Wu, Delay-dependent stability analysis of multi-area load frequency control with enhanced accuracy and computation efficiency. IEEE Trans. Power Syst. **34**(5), 3687–3696 (2019)
7. A. Khalil, A.S. Peng, Delay margin computation for load frequency control system with plug-in electric vehicles. Int. J. Power Energy Syst **38**(3), 1–17 (2018)
8. K.S. Ko, D.K. Sung, The effect of EV aggregators with time-varying delays on the stability of a load frequency control system. IEEE Trans. Power Syst. **33**(1), 669–680 (2018)
9. K. Ko, D.K. Sung, The Effect of cellular network-based communication delays in an EV aggregator's domain on frequency regulation service. IEEE Transactions on Smart Grid **10**(1), 65–73 (2019)
10. P. Kundur, *Power System Stability and Control* (McGraw-Hill, New York, NY, USA, 1994)
11. T. Masuta, A. Yokoyama, Supplementary load frequency control by use of a number of both electric vehicles and heat pump water heaters. IEEE Transactions on Smart Grid **3**(3), 1253–1262 (2012)
12. N.G. Paterakisa, O. Erdinç, J.P.S. Catalao, An overview of demand response: Key-elements and international experience. Renew. Sustain. Energy Rev. **69**, 871–891 (2017)
13. Q. Shi, F. Li, Q. Hu, Z. Wang, Dynamic demand control for system frequency regulation: Concept, review, algorithm comparison, and future vision. Electric Power Systems Research **154**, 75–87 (2018)
14. A. Pourmousavi, M.H. Nehrir, Introducing dynamic demand response in the LFC model. IEEE Trans. Power Syst. **29**(4), 1562–1572 (2014)
15. V.P. Singh, P. Samuel, N. Kishor, Impact of demand response for frequency regulation in-two-area thermal power system. International Transactions on Electrical Energy Systems **27**(2), 1–23 (2017)
16. X.L. Zhu, G.H. Yang, Jensen integral inequality approach to stability analysis of continuous-time systems with time-varying delay. IET Control Theory Appl. **2**(6), 524–534 (2008)
17. A. Sauret, F. Gouaisbaut, On the use of Wirtinger inequalities for time-delay systems. Proceedings of the 10-th IFAC Workshop on Time Delay Systems, Northeastern University, Boston, USA, June 22–24 (2012)
18. K. Gu, V.L. Kharitonov, J. Chen, *Stability of Time Delay Systems* (Birkhauser, New York, 2003)

19. H. Gunduz, S. Sonmez, S. Ayasun, Identification of gain and phase margins based robust stability regions for a time-delayed micro-grid system including fractional-order controller in presence of renewable power generation. Turk. J. Electr. Eng. Comput. Sci. **30**(3), 1097–1114 (2022)
20. S.B. Pandu, T. Santhanakrishnan, C.K. Sundarabalan, V. Venkatachalam, Stability analysis and region in control parameter space of thermal system with constant delays. J. Control Eng. Appl. Inform. **23**(3), 24–31 (2021)
21. A. Naveed, S. Sonmez, S. Ayasun, Impact of electric vehicles aggregators with communication delays on stability delay margins of two-area load frequency control system. Trans. Inst. Meas. Control. **43**(12), 2860–2871 (2021)
22. Q. Hai, Mean-square delay-distribution-dependent exponential synchronization of discrete-time Markov jump chaotic neural networks with random delay. J. Control. Eng. Appl. Inform. **23**(3), 42–52 (2021)

Coordinated Control of PHEVs and DEGs for Frequency Control of Two Area Hybrid Microgrid: An Effective Utilization of PID Controller for Renewable Applications

Anil Annamraju, Sheba Rani, SreenivasaRatnam, and Dileep Mathi

Abstract Present Microgrid (MG) faces uncertainty from Renewable Energy Sources (RES) and loads which cause hefty frequency deviations. Apart from the control strategies for Diesel Engine Generators (DEGs) and Energy Storage Systems (ESSs), MG requires an effective and intelligent coordinate strategy between DEG and ESSs for MG frequency control. In response to this, present paper addresses a coordinated control strategy between Plug-in Hybrid Electric Vehicles (PHEVs) and DEGs for MG frequency control under different operating scenarios. The proposed strategy is based on Cascade PD-PI controller whose gains are tuned using Sparrow Search Optimization (SSO) algorithm. Proposed controller is tested on Two-Area MG Simulink model. MG dynamic responses are obtained by considering load and RES changes. A comparative assessment of the proposed approach with SSO and BES optimized PID controller was performed. Simulation results confirm that the proposed controller enhances frequency dynamics of MG significantly. Moreover, the proposed Cascade PD-PI approach is robust to MG and PHEV parametric uncertainties as compared to PID controller.

Keywords Frequency control · PHEVs · Primary and secondary loops · Cascade PD-PI controller · Coordinated control · Sparrow search algorithm

A. Annamraju (✉) · S. Rani
Department of Electrical Engineering, School of Engineering, Malla Reddy University, Hyderabad, India
e-mail: ani223kumar@gmail.com

SreenivasaRatnam
Department of Electrical Engineering, Vasavi College of Engineering, Hyderabad, India

D. Mathi
Department of Electrical Engineering, Vidya Jyothi Institute of Technology, Hyderabad, India

J. Kumar et al. (eds.), *Control Applications in Modern Power Systems*, Lecture Notes in Electrical Engineering 974, https://doi.org/10.1007/978-981-19-7788-6_2

1 Introduction

Production of electricity by using fossil fuels caused a serious threat to environment due to emission of toxic gases that led to global warming. Fossil fuels reserve has reached the edge of depletion and could not meet the continuously increasing energy demand. Despite today's technological advancements electrical energy is still inaccessible for low populated areas rural regions and islands due to geographical and monetary constraints. A need to address all these issues arose which necessitated lot of research and development. Microgrid (MG) is associated with an integrated operation of multiple renewable energy resources and energy storage systems (ESSs). MG provides an efficient solution for aforementioned problems of rural electrification and extinction of fossil fuels [1].

A method for Load frequency control (LFC) involves employing a traditional controller to introduce a restorative signal at the governor summing point [2, 3]. Factors such as low system inertia and non-linear behavior of source and load affect the performance of controller thus resulting in frequency deviations beyond admissible limits. The conventional controller fails to exhibit adequate performance in all possible operating scenarios [4]. To overcome this problem several authors proposed Artificial Intelligent (AI) technique based PID controllers for LFC problem of hybrid MG [5–9]. PI/PID controllers whose gains were determined using GA were employed for compensating load frequency deviations in an MG [5]. Social Spider Optimization (SSO) was adopted for tuning of PID controller to achieve coordinated control in the event of sudden disturbances occurring in MG [6]. A novel algorithm by name quasi-oppositional harmony search algorithm (QOHSA) was introduced for optimization of controller gains when frequency deviations occur at generation side and load side [7]. Another method for LFC was presented using Grass Hopper Optimizer (GOA) based PID controller operating in coordination with Redox Flow Batteries [8]. A load frequency controller tuned by Grey Wolf Optimizer (GWO) was introduced for a standalone Two-Area hybrid MG system [9].

Though AI based PID controllers are providing an acceptable performance in wide range of operating conditions, the main drawback with these controllers is improper arbitrates between derivative and integral parts which leads to under performance than its capability. To overcome this problem, in literature, authors recommended various multi-stage PID controllers [10–12]. In [10] authors proposed hybrid optimization based multi-stage PID controller. In [11] authors suggested Slap Swarm Algorithm (SSA) based Cascade PI-PD controller, in [12] authors proposed a Chaotic Crow Search algorithm based PD-tilt PI controller. From the detailed study of these papers, the aforementioned controllers provided a guaranteed improved performance than PID controllers. In continuation to this, in present paper PD controller in primary control and PI controller in secondary control were proposed. Gains of Cascade PD-PI controller are optimized using Sparrow Search Optimization (SSO) algorithm. According to No Free Lunch theorem, no single meta-heuristic technique is suitable to optimize all engineering problems and improvement always persists. For this test system and operating conditions, SSO gave optimal performance than several recent algorithms. The key contributions of this paper are listed as follows.

2 Two-Area MG Modeling

Figure 1 illustrates the mathematical model of Two-Area MG. It depicts the linearized model of autonomous Two-Area hybrid MG which consists of Diesel Engine Generator (DEG), Wind Turbine Generator (WTG), Photo Voltaic (PV) array and Plug-in Hybrid Electric Vehicles (PHEVs) [4, 13]. Modeling of these components is presented in subsequent sections. Parameters required for simulation are available in [8, 13].

2.1 Modeling of DEG

Simulink model of DEG is shown in Fig. 2. Taking RES output into consideration DEG will supply the power that is deficit to the load. Depending on the command signal (Uc) obtained from the controller; speed governor will adjust the position of the valve. Change in the valve position is denoted as ΔX.

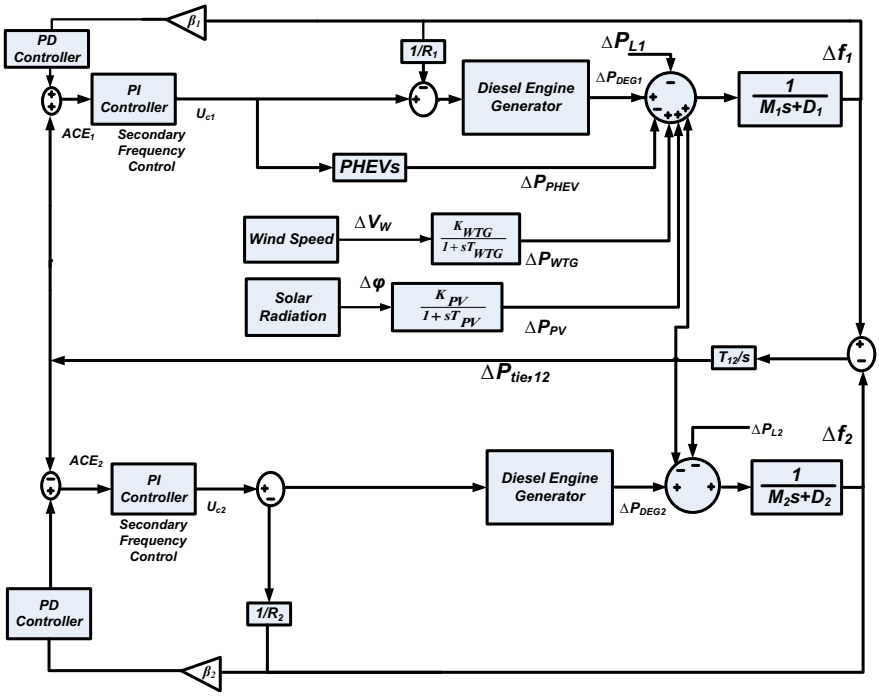

Fig. 1 Mathematical model of Two-Area Microgrid

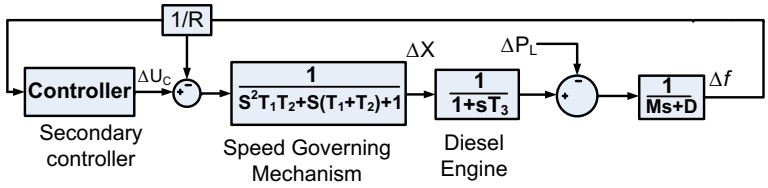

Fig. 2 Mathematical model of DEG

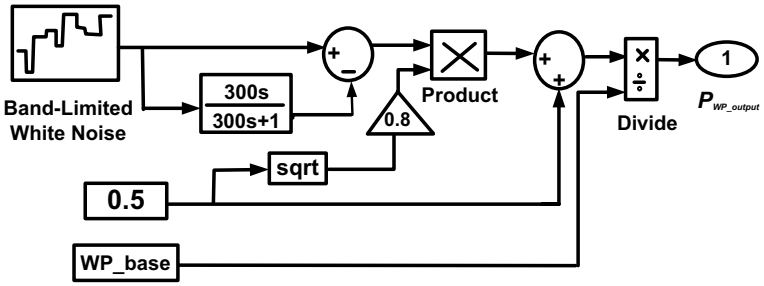

Fig. 3 Mathematical model for wind velocity pattern generation

2.2 Modeling of WTG

Output power of WTG is a function of speed of the wind. Due to the inconsistent nature of the wind, its speed keeps varying randomly. Mechanical power output of the windmill (P_{wp}) is expressed as [4]:

$$P_{wp} = 0.5\rho A V_w^3 C_p(\beta, \lambda) \tag{1}$$

Linear model of WTG can be expressed as [4]:

$$TF_{WTG} = \frac{\Delta P_{WTG}}{P_{WP\_output}} = \frac{K_{WTG}}{1 + ST_{WTG}} \tag{2}$$

Mathematical modeling for generating wind output power fluctuations is given in Fig. 3.

2.3 Modeling of PV Array

A PV array is a collection of many PV modules connected together in both series and parallel combinations. Voltage and current ratings of the PV array is determined by the number of PV modules arranged in series–parallel combinational circuits.

Changes in load current and solar radiation are the factors that regulate the output power of PV array. In this research work in order to study frequency regulation it is assumed that PV output power varies only with solar radiation.

First-order model of the PV system can be expressed as [4]:

$$TF_{PV} = \frac{\Delta P_{PV}}{\Delta \varphi} = \frac{K_{PV}}{1 + sT_{PV}} \tag{3}$$

WTG data and PV power data used in this work are available in [4].

2.4 Mathematical Model of PHEVs

DEG usually delivers the electrical energy that is deficit to the demand side thus causing a balance between generation and the load. However DEG exhibits a very slow response in the event of frequency oscillations due to its large time constants. This makes it less effective when sudden frequency variations occur in RES output power and load [14]. To withstand these deviations in frequency regulation of MG with DEG and suitable distributed storage systems have been proposed. Recent studies revealed the significance and suitability of PHEVs in RES integrated systems. As compared to other existing technologies PHEVs have simple modular structure, slow discharge rate, fast-acting capability and distributed availability. Figure 4 illustrates the mathematical model of PHEV aggregator for LFC studies [14]. Instantaneous change in PHEV power can be expressed as follows [14]: (Fig. 5)

$$\Delta P_{PHEV,i} = \begin{cases} K_{EV,i}\Delta f; \left|K_{EV,i}\Delta f\right| \leq P_{max} \\ P_{max}; K_{EV,i}\Delta f > P_{max} \\ -P_{max}; K_{EV,i}\Delta f < -P_{max} \end{cases} \tag{4}$$

$$\Delta P_{PHEV,AG} = \text{NEV}^{*}\Delta P_{PHEV,i} \tag{5}$$

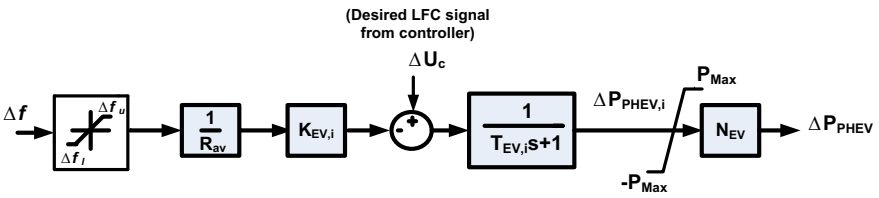

Fig. 4 PHEV aggregator model for frequency control studies

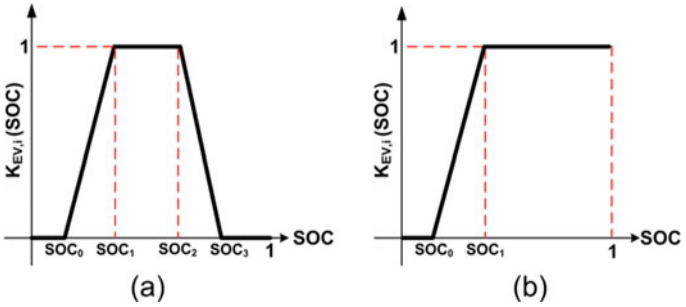

Fig. 5 $K_{EV,i}$ versus SOC **a** discharge mode, **b** idle mode

where $K_{EV,i}$ denotes the participation gain of each EV. The value of $K_{EV,i}$ depends on the state of charge (SOC) of battery and Fig. 5 depicts the variation of $K_{EV,i}$ versus SOC of PHEV [14].

3 Sparrow Search Optimization Algorithm Based Cascade PD-PI Controller

Superior LFC response in modern power systems can be achieved by precise tuning of control parameters. In this regard, several intelligent techniques such as cat swarm optimization (CSO), Harmony Search Algorithm (HSO), Grasshopper Optimization Algorithm (GOA), Genetic Algorithm (GA), and Particle Swarm Optimization (PSO) were introduced in the literature for fine tuning of PI/ PID controllers. Ability to operate independently to plant model and exclusion of derivative term are the attributes that made these algorithms to stand out as compared to other techniques. As articulated in no free lunch (NFL) algorithm all engineering optimization problems cannot be resolved by a single swarm of intelligent algorithms which drives the need for advanced algorithms. Sparrow Search Optimization algorithm was proposed for tuning of Cascade controller more accurately. SSO algorithm is developed based on the foraging behavior of sparrows. SSO algorithm has few control parameters hence it is simple to implement as compared to other intelligent techniques. SSO exhibits faster convergence and its structural simplicity makes it possible to provide efficient solutions for complicated engineering problems. SSO algorithm has outperformed other optimization techniques and hence is used as a benchmark for standard test problems [15].

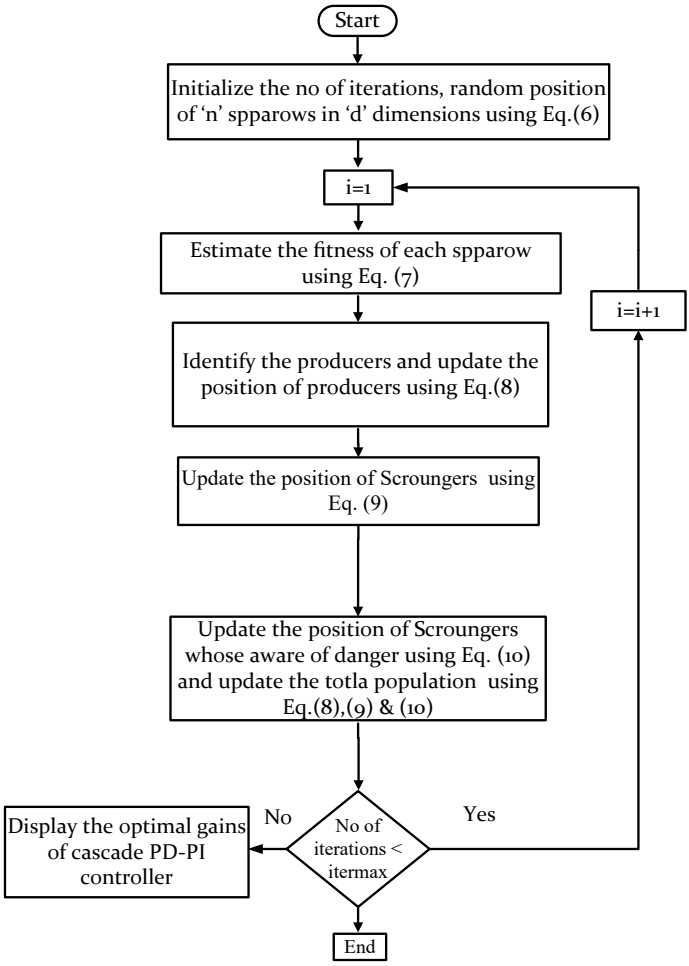

Fig. 6 SSO flowchart for optimization of cascade PD-PI controller

3.1 Procedure to Tune Proposed Cascade PD-PI Controller with SSO Algorithm

Step 1: **Initialization:** In this stage, generate a random population by using Eq. (6). As there are 10 controller parameters (K_{PP}, K_D, N, $K_{P,}K_{I,}$) related to the proposed controller in two-areas, the population size is considered as 50 × 10. In this 50 represents number of sparrows and 10 represents dimension of search space.

$$X(i,:) = 1b + (ub - 1b)^{*}_{.} rand(1,d) \tag{6}$$

where lb = lower bound and ub = upper bound.

Step 2: **Fitness Evaluation**: Evaluate the fitness value of each sparrow using the following equation.

$$ITAE = \int_0^{t_{sim}} t * |\Delta f| dt \tag{7}$$

Subjected to the optimization of $0.1 \leq K_{P,} K_{PP}$, K_I, $K_D \leq 5$ and $10 \leq N \leq 400$ where 't_{sim}' denotes the total simulation time.

Step 3: **Identification of Producers**: Based on fitness function identify the best and worst sparrows. Best sparrows in the population are considered as producers and these producers are responsible for searching food and guiding other sparrows.

$$X_{i,j}^{k+1} = \begin{cases} X_{i,j}^{k}.exp\left(\frac{-i}{\alpha iter_{max}}\right) if\, R_2 < ST \\ X_{i,j}^{k} + Q.L if\, R_2 \geq ST \end{cases} \tag{8}$$

where k denotes the current iteration and i denotes current population. $X_{i,j}$ denotes population of ith sparrow in jth dimension. R_2 represents a random number between [0–1]. ST represents the safe threshold which acts like an alarm for sparrows against predators. R_2 value less than 0.5 represents absence of predators around the producers, hence they can start search process. R_2 value greater than or equal to 0.5 denotes that predators are present around producers, hence they can migrate to a safe place.

Step 4: **Updating Scroungers**: Scroungers are intended to often monitor the producers. If producers identify any food, then scroungers update their position to compete with food. If the scroungers win, they get food from producers immediately or else go with Eq. (10)

$$X_{i,j}^{k+1} = \begin{cases} exp\left(\frac{X_{worst}^{k} - X_{i,j}^{k}}{i^2}\right) * Q\, if\, i > n/2 \\ X_p^{k+1} + \left|X_{i,j}^{k} - X_p^{k+1}\right| * A^+ * L\, or\, Else \end{cases} \tag{9}$$

where Xp denotes the optimal position occupied by the producers, and A^+ can be expressed as:

$$A^+ = A^T (AA^T)^{-1}$$

Step 5: **Update the Population:** Update the population of sparrows by using the following equation:

$$X_{i,j}^{k+1} = \begin{cases} X_{best}^{k} + \beta * \left(|X_{i,j}^{k} - X_{p}^{k+1}| if \ f_i > f_g \right) \\ X_{i,j}^{k} + K * \left(\frac{\left| X_{i,j}^{k} - X_{worst}^{k} \right|}{\varepsilon + (f_i - f_w)} \right) \end{cases} \tag{10}$$

Detailed explanation of Eq. (10) is available in [15]. Update the total population based on Eqs. (8–10).

Step 6: **Termination criteria:** If number of iterations reaches the maximum value (iter ≥ itermax), then display optimal gains of proposed Cascade PD-PI controller. Flow chart for SSO algorithm for tuning the proposed controller is illustrated in Fig. 6.

4 Results and Discussion

This section deals with the time-domain simulation analysis on the frequency dynamics of Two-Area MG under different operating scenarios. Two-Area MG with various RES and PHEVs are modeled in Simulink. Necessary data for simulation has been taken from following papers [8–13]. Simulation for all models have been carried out on a personal computer system having, 8 GB RAM, Intel core i3 processor in the MATLAB 2019a environment. Frequency dynamics of MG are analysed under the presence of load (ΔP_L), solar (ΔP_φ), wind power (ΔP_{WTG}) disturbances and PHEV, MG parameter uncertainties. Performance of proposed coordinated strategy and proposed Cascade PD-PI controller are tested under following disturbances.

Scenario 1: Only Load Disturbances in MG

In this scenario, various levels of load disturbances (both raise and fall in step loads) are considered at different time intervals. Figure 7a, b, c and d represent load disturbances and corresponding frequency deviations in MG respectively. Optimized gains of various controllers are given in Table1. From Fig. 7, it is evident that proposed Cascade PD-PI controller provides better dynamic response in terms of fast settling time, less overshoots and low ITAE value. Proposed controller structure attained at least 30% minimized overshoot compared to PID controller. This type of controller structure is more suitable for renewable applications where overshoot is more concerned.

Scenario 2: Only wind Disturbances in MG

In this scenario, wind power disturbances alone are considered in MG. Figure 8a, b, c and d represent the wind disturbances and corresponding frequency deviations in MG respectively. From Fig. 8, it is evident that proposed Cascade PD-PI controller

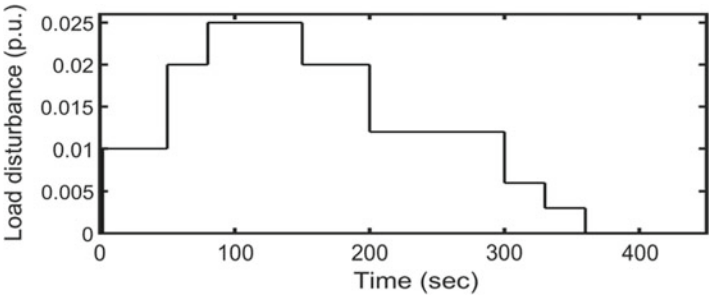

(a)

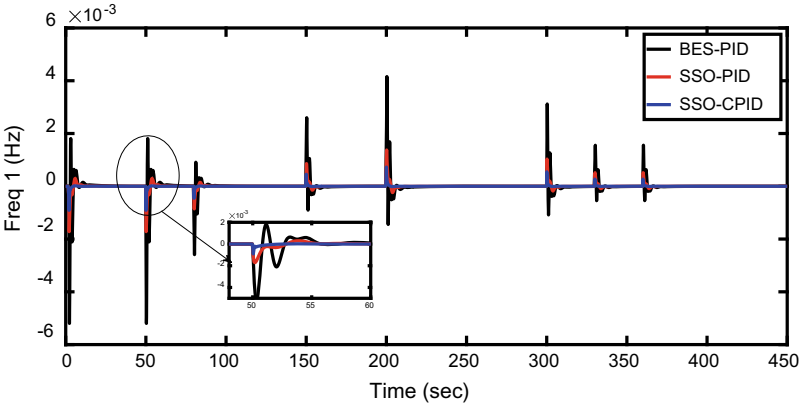

(b)

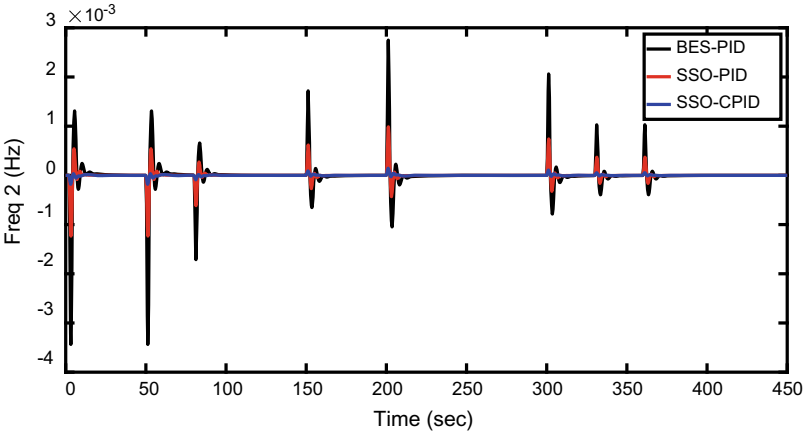

(c)

Fig. 7 **a** Load disturbances in MG, **b** Corresponding MG frequency deviations in area1, **c** Corresponding MG frequency deviations in area2 **d** Tie-line power deviations in between area1 and area2

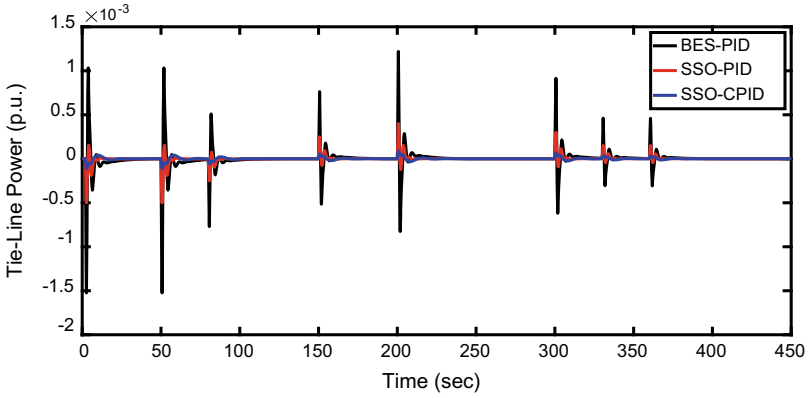

(d)

Fig. 7 (continued)

Table 1 Optimized gains of various controllers

Controller parameters	BES-PID	SSO-PID	SSO cascade PD-PI
K_{PPI}	–	–	5
K_{D1}	0.1	0.5545	0.1
N_1	83.604	82.6428	146.685
K_{P1}	1.3179	4.5212	4.9021
K_{I1}	3.0327	5	5
K_{PP2}	–	–	0.5636
K_{D2}	1	4.0210	1.9259
N_2	42.1145	133.1926	80.5638
K_{P2}	0.1402	3.6366	5

provides better dynamic response in less overshoots and low ITAE value. Proposed controller structure attained at least 50% minimized overshoot compared to PID controller. This type of controller structure is more suitable for renewable applications where overshoot is more concerned.

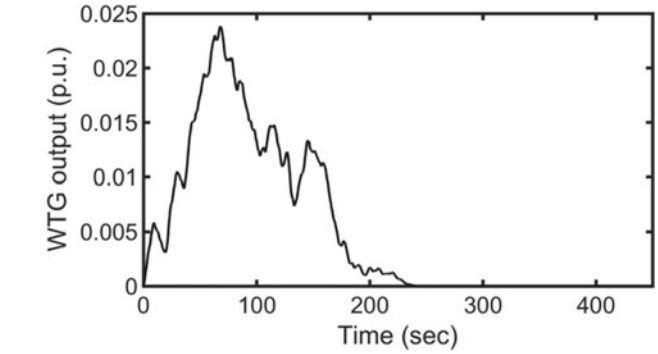

(a)

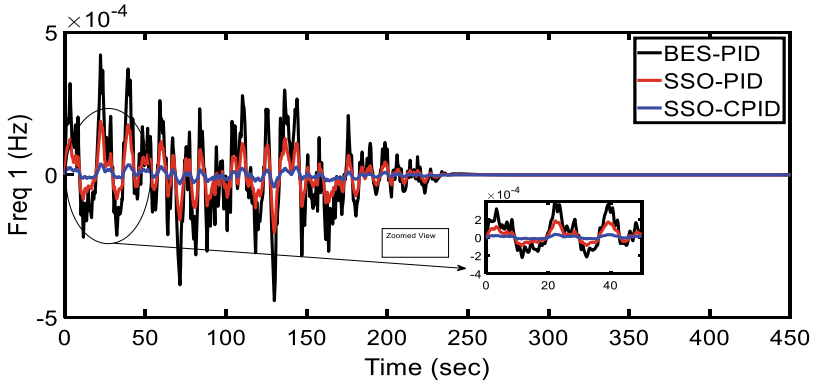

(b)

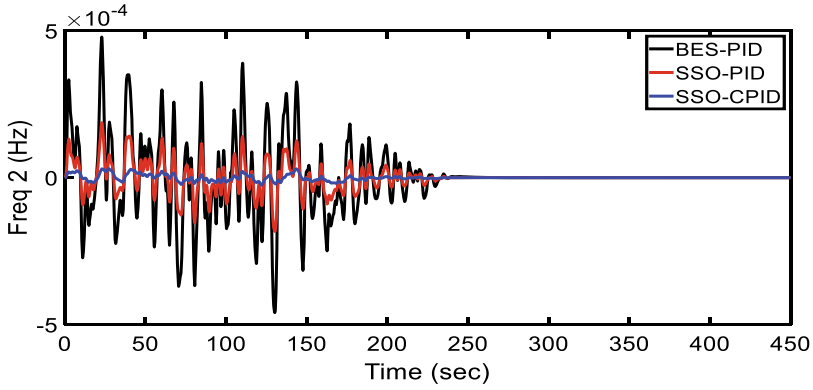

(c)

Fig. 8 **a** Wind power disturbances in MG, **b** Corresponding MG frequency deviations in area1, **c** Corresponding MG frequency deviations in area2 **d** Tie-line power deviations in between area1 and area2

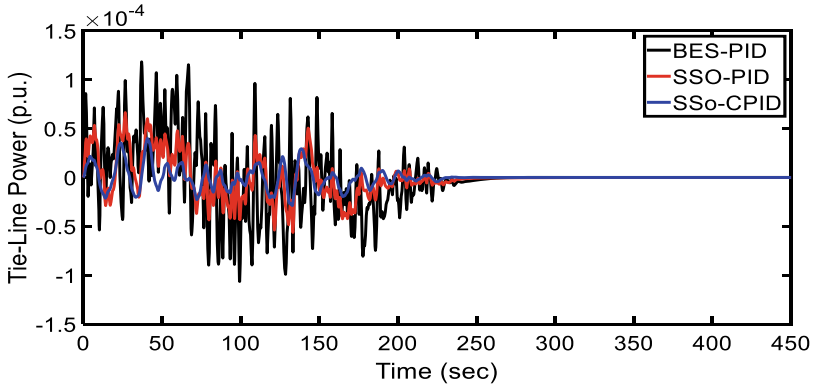

(d)

Fig. 8 (continued)

Scenario 3: Multiple Disturbances in MG simultaneously

In this scenario, concurrent disturbances (load, wind and solar power disturbances) are considered in MG. Figure 9a, b, c and d represent the concurrent disturbances and corresponding frequency deviations in MG respectively. From this scenario, it is evident that proposed controller is more robust to uncertainties caused by RES and load and experiences less swings compared to PID controller.

Scenario 4: Comparison of Proposed Coordinated versus Non-coordinated Approach with multiple Disturbances as mentioned in scenario 4 with parametric uncertainties (50% uncertainty in M&D)

In this scenario, the PHEVs are placed in primary frequency loop (non-coordinated approach) and PHEVs are placed in secondary frequency loop (coordinated approach) and frequency deviations in MG were observed. Figure 10a, b and c depict the frequency deviations in MG. From scenario 6 operating conditions, the participation of PHEV aggregator in SFC loop (coordination between DEGs and PHEVs with CPID controller) improves the frequency response of MG over PHEV aggregator in PFC loop.

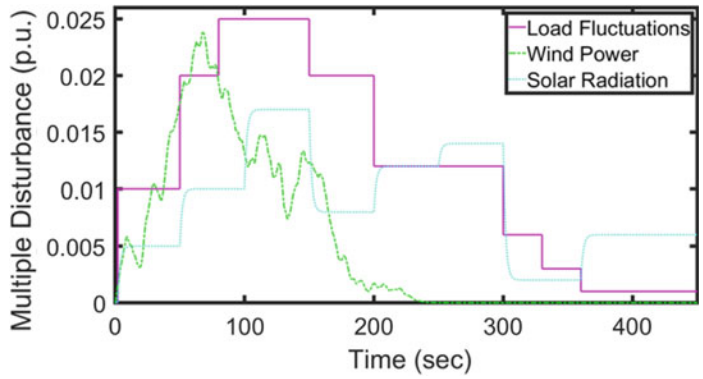

(a)

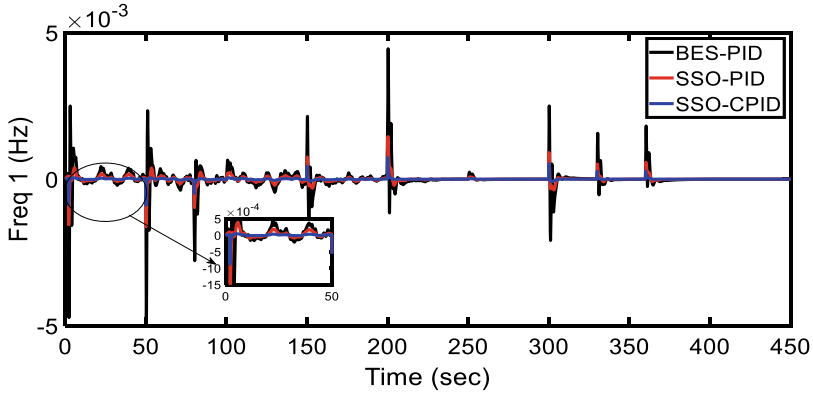

(b)

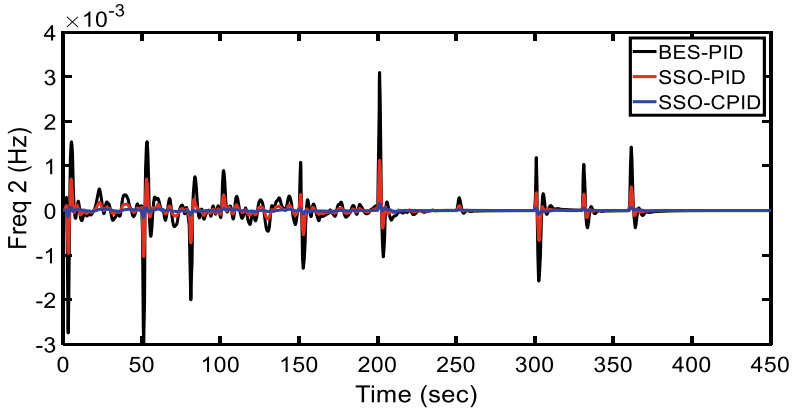

(c)

Fig. 9 **a** Multiple disturbances in MG, **b** Corresponding MG frequency deviations in area1, **c** Corresponding MG frequency deviations in area2 **d** Tie-line power deviations in between area1 and area2

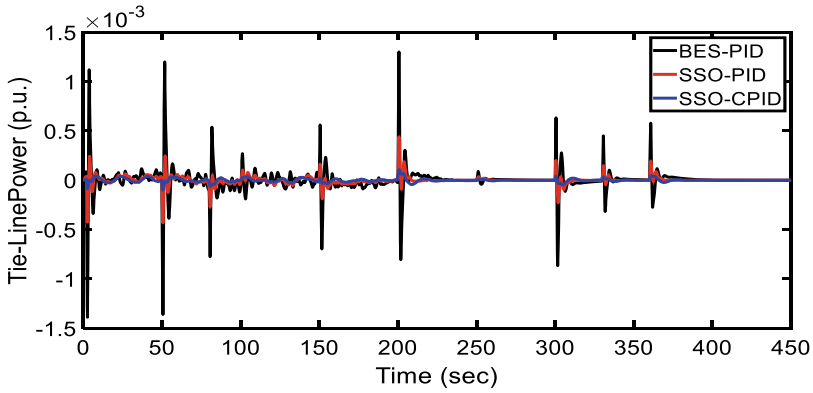

(d)

Fig. 9 (continued)

5 Conclusion

This paper proposed a coordinated control between DEGs and PHEVs for frequency control of hybrid MG under renewable environment. Proposed coordinated strategy minimized the frequency deviations significantly than non-coordinated strategy under all possible operating scenarios. Besides that, an effective utilization of PID controller in different loops is proposed which established an optimal tradeoff between Integral and Derivative controllers. With proposed controller, the dynamic response of MG (in particular overshoot) is significantly reduced compared to optimized PID controller. Particularly in critical operating scenario, the overall error and overshoots are reduced by nearly 50% as compared to PID controller. Moreover, the proposed controller is more stringent to parametric uncertainties as compared to several existing controllers in literature. From the results and analysis it can be concluded that proposed coordinated strategy and proposed controller are more suitable to present microgrid operating scenarios.

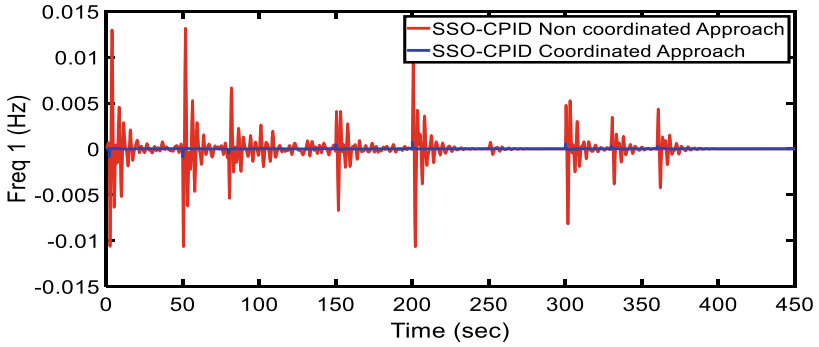

(a)

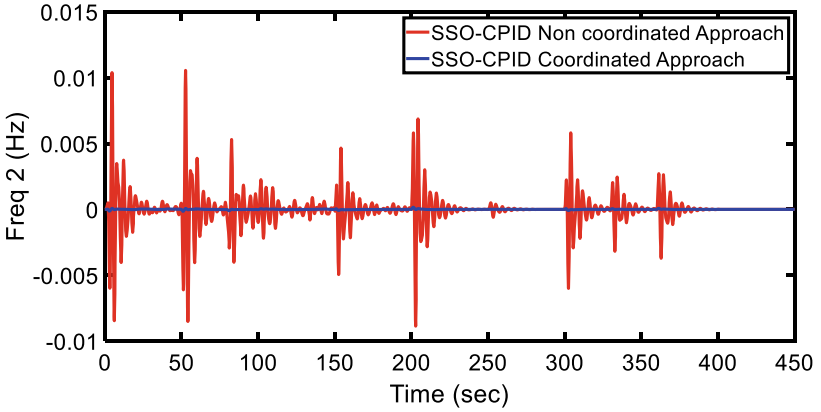

(b)

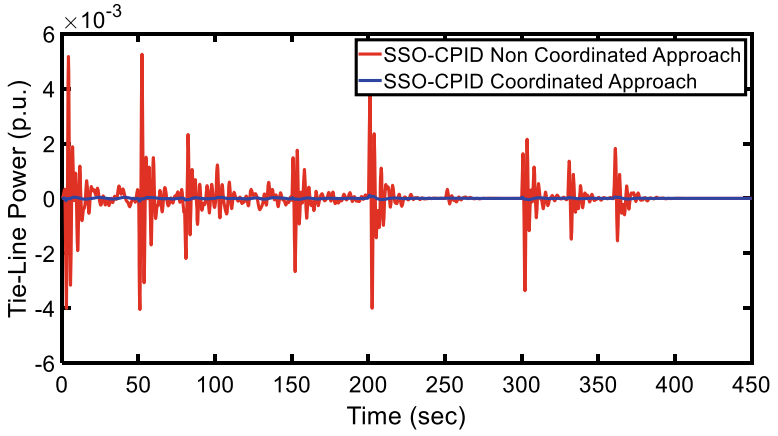

(c)

Fig. 10 **a** Corresponding MG frequency deviations in area1, **b** Corresponding MG frequency deviations in area2 **c** Tie-line power deviations in between area1 and area2 for scenario 4 conditions

References

1. IEEE Standards Coordinating, C. 21: IEEE guide for design, operation, and integration of distributed resource Island systems with electric power systems (2011)
2. A. Annamraju, L. Bhukya, S. Nandiraju, Robust frequency control in a standalone microgrid: an adaptive fuzzy based fractional order cascade PD-PI approach. Adv. Control. Appl. **3**(3), e72 (2021)
3. Rajesh K. S. and Dash, S. S. and R. R., Load frequency control of microgrid: a technical review. In J. and P. V. and S. V. M. DrückHarald and Mathur (Ed.), *Green Buildings and Sustainable Engineering* (Springer, Singapore, 2020), pp. 115–138
4. A. Annamraju, S. Nandiraju, Robust frequency control in an autonomous microgrid: a two-stage adaptive fuzzy approach. Electr. Power Compon. Syst. **46**(1), 83–94 (2018)
5. DCh., Das, A.K. Roy, N. Sinha, GA based frequency controller for solar thermal–diesel–wind hybrid energy generation/energy storage system. Int. J. Electr. Power Energy Syst. **43**(1), 262–279 (2012)
6. A.A. El-Fergany, M.A. El-Hameed, Efficient frequency controllers for autonomous two-area hybrid microgrid system using social-spider optimiser. IET Gener. Transm. Distrib. **11**(3), 637–648 (2017)
7. G. Shankar, V. Mukherjee, Load frequency control of an autonomous hybrid power system by quasi-oppositional harmony search algorithm. Int. J. Electr. Power Energy Syst. **78**, 715–734 (2016)
8. Annamraju, A., &Nandiraju, S. (2018). Frequency control in an autonomous two-area hybrid microgrid using grasshopper optimization based robust PID controller. *2018 8th IEEE India International Conference on Power Electronics (IICPE)*, 1–6
9. C, S., Yammani, C., & Maheswarapu, S., Load frequency control of multi-microgrid system considering renewable energy sources using grey wolf optimization. Smart Sci. **7**(3), 198–217 (2019)
10. R.K. Khadanga, S. Padhy, S. Panda, A. Kumar, Design and analysis of multi-stage PID controller for frequency control in an islanded micro-grid using a novel hybrid whale optimization-pattern search algorithm. Int. J. Numer. Model. Electron. Networks Devices Fields **31**(5), e2349 (2018)
11. B. Khokhar, S. Dahiya, K.P.S. Parmar, A robust cascade controller for load frequency control of a standalone microgrid incorporating electric vehicles. Electr. Power. Componen. Syst. **48**(6–7), 711–726 (2020)
12. B. Khokhar, S. Dahiya, K.P.S. Parmar, A novel hybrid fuzzy PD-TID controller for load frequency control of a standalone microgrid. Arab. J. Sci. Eng. **46**(2), 1053–1065 (2021). https://doi.org/10.1007/s13369-020-04761-7
13. A. Annamraju, S. Nandiraju, Robust frequency control in a renewable penetrated power system: an adaptive fractional order-fuzzy approach. Prot Control. Mod. Power. Syst. **4**(1), 16 (2019). https://doi.org/10.1186/s41601-019-0130-8
14. S. Izadkhast, P. Garcia-Gonzalez, P. Frías, An aggregate model of plug-in electric vehicles for primary frequency control. IEEE Trans. Power Syst. **30**(3), 1475–1482 (2015)
15. J. Xue, B. Shen, A novel swarm intelligence optimization approach: sparrow search algorithm. Syst. Sci. Control. Eng. **8**(1), 22–34 (2020)
16. B. Khokhar, S. Dahiya, K.P.S. Parmar, A novel fractional order proportional integral derivative plus second-order derivative controller for load frequency control. Int. J. Sustain. Energ. **40**(3), 235–252 (2021)

Frequency Regulation in a Small Microgrid Using Robust Controller

Samrat Vishnu Hari, Anshul Yadav, Sheetla Prasad, and Yogesh Kumar

Abstract The microgrid is located at distribution network side and generates power according to power demand in a specific region using several distributed generations such as wind, solar, fuel cell etc. Due to uncertainty in distributed generations, the frequency regulation is a formidable problem in islanded microgrid. Thus, a centralised linear quadratic regulator-based controller is designed for islanded microgrid in order to get good performance and zero deviation in terms of frequency deviation. The closed loop control law convergence is obtained using the Lyapunov stability theorem. In presence of distributed generation uncertainties, proposed controller performance is compared and it enhances closed loop system stability with reduction in over/under shoots, settling time and oscillations. In addition, also through well said controller regulates power generation from power from flywheel storage plant, fuel cell plant and battery storage plant to sustain minimum frequency deviations effectively. The performance, stability and ability to keep in synchronism with the proposed control scheme are validated on several distributed generations through MATLAB© simulations.

Keywords Linear quadratic regulator-based controller · Frequency deviation · Linear matrix equality and islanded microgrid

1 Introduction

The continuous localised increased power demand can be managed by a community Microgrid. In India, there are many villages those haven't proper energy due to higher demand of power in the remote society [1, 2]. Microgrid is a reliable option to create a link between villages or any remote location to the society. In order to get maximum use of sustainable power or energy, a very new methodology is developed named microgrid. It is a localised grid and interconnected several loads as well as other distributed generations (DGs). Hence, microgrid system should be smart in terms of

S. V. Hari · A. Yadav · S. Prasad (✉) · Y. Kumar
Department of Electrical, Electronics and Communication Engineering, Galgotias University, Delhi-NCR, India
e-mail: sheetla.prasad@galgotiasuniversity.edu.in

J. Kumar et al. (eds.), *Control Applications in Modern Power Systems*, Lecture Notes in Electrical Engineering 974, https://doi.org/10.1007/978-981-19-7788-6_3

control, efficiency, reliability and power backup. Thus, in a microgrid, a robust load frequency controller is highly recommended to maintain constant frequency [3].

In a distribution type system, if high renewable penetration is considered then it faces too many technical and operational problems just like quality of power, stability and voltage of network as well as frequency deviation. In order to solve this issue using the concept of microgrid was developed by researchers [4, 5]. In [6], several functional and technical problems such as ownership, coordinated equipment control, frequency control etc. are highlighted effectively. With the help of two methodologies of microgrid named as grid connected mode, which is connected to utility grid by a static stitch, while another one named as islanding mode, which is not giving any power to microgrid [7]. Very basic parameters of distinct type microgrid described as a single controllable entity from grid and generate frequency and reference voltage in an islanded operation mode [8–10]. The microgrid possesses AC and DC distribution network. The grid connected mode DC microgrid, the power is converted by an inverter and supplied it in DC network. With the help of long and short term, parameters of a supervisory controller are designed to get power demand information as constant power load as reported in [9]. In [10], model predictive controller is developed to achieve desirable frequency regulation. Therefore, it could be said that if designers do a proper design of the system for filters and controllers then power quality is to be done in better manner that is influenced by harmonics [11, 12]. However, to improve power quality issues, inner loop current control and outer voltage control loop were designed as reported in [13, 14].

In the islanded mode of microgrid, distributed generation is responsible to ensure the reference voltage and frequency deviation [15]. The deviations in voltage and frequency are regulated via proper balance of power between generation and demand [16]. The islanded microgrid is prevented frequent power or load outages because the utility grid is not available to provide power backup [17, 18]. Due to randomness and intermittency in distributed energy resources, the distributed energy resources penetration level in islanded microgrid is enhanced by several uncertainties and disturbances as given in [18]. As a result, microgrid is affected from the frequency deviation or even leads to system instability. The frequency deviation is minimized due to intermittent nature of distributed energy resources and stochastic behaviour of loads in an isolated microgrid via intelligent bee colony-based terminal sliding mode control [19]. However, the frequency deviation in an isolated mode of operation of microgrid is still a formidable task due to intermittent nature of distributed energy resources.

The greenhouse initiative taken by several countries is the main cause to develop various community based isolated microgrids. The small signal model of an isolated microgrid is sufficient to the analysis of frequency deviation against load deviations and intermittent nature of distributed energy resources. Sliding mode controller is utilized to extract maximum power from wind even in presence of wind speed uncertainties [19]. The microgrid frequency is regulated even in presence of stochastic uncertainties and disturbances using several optimizations such as two dimensional Sine Logistic map based chaotic sine cosine algorithm (2D-SLCSCA) based PID controller [20], grasshopper algorithmic technique based PI controller [21], fast

frequency response optimized power point tracking method [22], h-infinity optimization based PID controller [23], genetic algorithms based PI controller [24], genetic algorithm based grid-forming droop control [25] etc. Thus, islanded microgrid frequency deviations against uncertainties, outage of power or load and load disturbances in distributed generations are still required further developments.

Hence, due to uncertainty in distributed generations, the frequency regulation is a formidable problem in islanded microgrid. Thus, a centralised linear quadratic regulator-based controller is designed for islanded microgrid in order to get good performance and zero deviation in terms of frequency deviation. The closed loop control law convergence is obtained using the Lyapunov stability theorem. In presence of distributed generation uncertainties, proposed controller enhances closed loop system performance with reduction in over/under shoots, settling time and oscillations. In addition, also through well said controller regulates power generation from power from flywheel storage plant, fuel cell plant and battery storage plant to sustain minimum frequency deviations effectively. Thus, a centralised linear quadratic regulator-based controller is developed for a linearized islanded microgrid in order to get good responses and minimum deviation in terms of frequency deviation.

The organization of rest section are represented as follows: small signal based islanded microgrid model dynamic is depicted in Sect. 2. In Sect. 3, design steps of control law and its convergence is described. The demonstration of the simulated results is investigated in Sect. 4. Finally, based on the simulation demonstration conclusion is drawn in Sect. 5.

2 Microgrid System Description

By proper operation and control of islanded microgrid, provides effective operation and sustainability of electric grid with economic and high efficiency as shown in Fig. 1a. The islanded microgrid is also used to provide isolation from larger grid that results in microgrid to have the ability to conduct as well as parallel conduction to make grid more competitive in future. Basically, microgrids are three types: remote microgrid, grid-connected and network grid. The remote grids are free intelligence and insight from industry experts and leading companies on the global energy transformation. In grid connected mode, current controller is utilized to inject power to the main grid depending on the power generation. In the network microgrid, the operation of multiple microgrids in coordination with distribution system is allowed to enable high penetration of locally available distributed energy resources. This happens because of the involuntary stress on distributed generators and harmonic produced due to such frequency deviations as discussed in [23–25]. It is important to minimize the frequency deviation before microgrid gets connected with grid. The synchronization conditions may fail after synchronization of the microgrid with grid due to large frequency deviations. A simplified dynamics model of islanded microgrid integrated with wind plant, solar plant, flywheel energy plant, fuel cell plant,

battery energy storage plant, small turbine plant, and diesel generation plant models are taken and described by first order transfer function for small signal analysis as shown in Fig. 1.

The dynamics of the given microgrid in Fig. 1b are represented as:

$$\Delta \dot{P}_{WTG} = \frac{1}{T_{WTG}}(P_{WTG} - \Delta P_{WTG}) \tag{1}$$

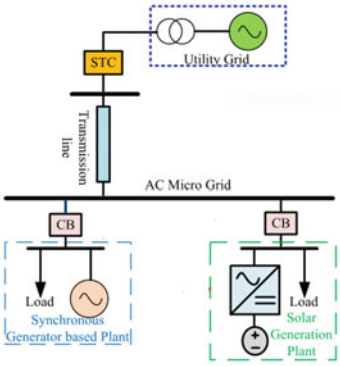

a) Microgrid structure

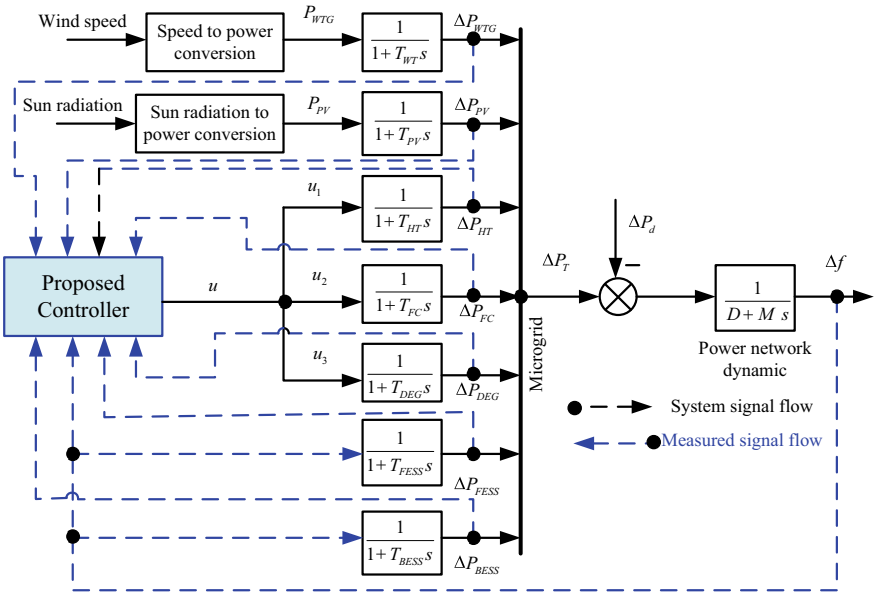

b) Simplified dynamics based microgrid structure

Fig. 1 Representation of a microgrid and its dynamics

$$\Delta \dot{P}_{PV} = \frac{1}{T_{PV}}(P_{PV} - \Delta P_{PV}) \tag{2}$$

$$\Delta \dot{P}_{HT} = \frac{1}{T_{HT}}(u_1 - \Delta P_{HT}) \tag{3}$$

$$\Delta \dot{P}_{FC} = \frac{1}{T_{FC}}(u_2 - \Delta P_{FC}) \tag{4}$$

$$\Delta \dot{P}_{DEG} = \frac{1}{T_{DEG}}(u_3 - P_{DEG}) \tag{5}$$

$$\Delta \dot{P}_{FESS} = \frac{1}{T_{FESS}}(\Delta f - \Delta P_{FESS}) \tag{6}$$

$$\Delta \dot{P}_{BESS} = \frac{1}{T_{BESS}}(\Delta f - \Delta P_{BESS}) \tag{7}$$

$$\Delta \dot{f} = \frac{1}{M}(\Delta P_T - \Delta P_{dis} - D\Delta f) \tag{8}$$

where, $\Delta P_T = \Delta P_{WTG} + \Delta P_{PV} + \Delta P_{HT} + \Delta P_{FC} + \Delta P_{DEG} + \Delta P_{FESS} + \Delta P_{BESS}$. All system equation dynamic terms are illustrated in Table 1.

The Eqs. (1–8) are used to represent it in state space dynamics as:

Table 1 Microgrid system terms

Terms	Description	Terms	Descriptions
ΔP_{WTG}	Wind power generation (puMW)	T_{WTG}	Wind plant model time constant (Sec)
ΔP_{PV}	Solar power generation (puMW)	T_{PV}	Solar plant model time constant (Sec)
ΔP_{HT}	Small turbine plant power generation (puMW)	T_{HT}	Small turbine model time constant (Sec)
ΔP_{FC}	Fuel cell plant power generation (puMW)	T_{FC}	Fuel cell model time constant (Sec)
ΔP_{DEG}	Diesel generator plant power generation (puMW)	T_{DEG}	Diesel generator time constant (Sec)
ΔP_{FESS}	Flywheel plant power generation (puMW)	T_{FESS}	Flywheel model time constant (Sec)
ΔP_{BESS}	Battery plant power generation (puMW)	T_{BESS}	Battery model time constant (Sec)
Δf	Microgrid frequency deviations (Hz)	P_{WTG}, P_{PV}	Disturbances in wind and solar (puMW)
D, M	Microgrid damping and inertia constant (per sec)	ΔP_{dis}	Microgrid load disturbance (puMW)

$$\begin{aligned} \dot{x}(t) &= Ax(t) + Bu(t) + F\Delta P_d(t) \\ y(t) &= Cx(t) \end{aligned} \tag{9}$$

where, $x(t), u(t), y(t)$ and $\Delta P_d(t)$ are the microgrid state variables, input, output and load disturbances respectively. The system matrices $A \in \Re^n$, $B \in \Re^{n\times k}$, $D \in \Re^{n\times r}$ and $C \in \Re^{m\times n}$ are system matrix, input matrix and output matrix respectively. The microgrid system matrices are given as:

$$A = \begin{bmatrix} -\frac{1}{T_{WTG}} & 0 & 0 & 0 & 0 & 0 & 0 & 0 \\ 0 & -\frac{1}{T_{PV}} & 0 & 0 & 0 & 0 & 0 & 0 \\ 0 & 0 & -\frac{1}{T_{HT}} & 0 & 0 & 0 & 0 & 0 \\ 0 & 0 & 0 & -\frac{1}{T_{FC}} & 0 & 0 & 0 & 0 \\ 0 & 0 & 0 & 0 & -\frac{1}{T_{DEG}} & 0 & 0 & 0 \\ 0 & 0 & 0 & 0 & 0 & -\frac{1}{T_{FESS}} & 0 & 0 \\ 0 & 0 & 0 & 0 & 0 & 0 & -\frac{1}{T_{BESS}} & 0 \\ \frac{1}{M} & \frac{1}{M} & \frac{1}{M} & \frac{1}{M} & \frac{1}{M} & \frac{1}{M} & \frac{1}{M} & -\frac{D}{M} \end{bmatrix},$$

$$B = \begin{bmatrix} 0 & 0 & 0 \\ 0 & 0 & 0 \\ \frac{1}{T_{HT}} & 0 & 0 \\ 0 & \frac{1}{T_{FC}} & 0 \\ 0 & 0 & \frac{1}{T_{DEG}} \\ 0 & 0 & 0 \\ 0 & 0 & 0 \\ 0 & 0 & 0 \end{bmatrix},$$

$$F = \begin{bmatrix} 0 & \frac{1}{T_{WTG}} & 0 \\ 0 & 0 & \frac{1}{T_{PV}} \\ 0 & 0 & 0 \\ 0 & 0 & 0 \\ 0 & 0 & 0 \\ 0 & 0 & 0 \\ 0 & 0 & 0 \\ -\frac{1}{M} & 0 & 0 \end{bmatrix}$$

$C =$ Indentity matrix (I_8), $x(t) = [\Delta P_{WTG}\ \Delta P_{PV}\ \Delta P_{HT}\ \Delta P_{FC}\ \Delta P_{DEG}\ \Delta P_{FESS}\ \Delta P_{BESS}\ \Delta f]^T$, $u = [\,u_1\ u_2\ u_3\,]^T$ and $\Delta P_d = [\,P_{WTG}\ P_{PV}\ \Delta P_{dis}\,]^T$.

3 Proposed Control Methodology

In controller design and performance domain, the linear quadratic regulator (LQR) is a well-known control strategy that changes the trajectories of a nonlinear or linear network by use of an external control signal. The LQR is an optimal control law with cost function and does not depend on the system state controllability. The LOR follow linear input-state output system conditions for all stabilizable states in finite time. Thus, LQR can control effectively a weakly controllable linear or nonlinear state space system. All things being said, it can change starting with one continuous system and then going to the next depending on the current situation in the state space. Subsequently, it can be optimized easily through linear matrix inequalities (LMIs) optimization platform [20]. The weights of linear quadratic regulator controllers are linearly optimized via a pre-defined objective quadratic criterion function with states dynamic and control. To achieve both fast state trajectory speed and effective control efforts simultaneously, pre-defined objective quadratic criterion function is considered as:

$$\Upsilon_{\min} = \int_0^{\infty} \left(x^T Q\, x + u^T R\, u\right) dt \tag{10}$$

where, positive definite matrices are defined as $Q = Q^T > 0$, $R = R^T > 0$, and obtained using proper optimization. The weights matrices Q and R are optimized to improve fast responses and reduce penalty factors in control efforts. Most of the research work in the literature, weight matrices Q and R are considered as unity values to give a moderate response and equal penalty on each control effort respectively. In this study, control law is selected as:

$$u(t) = -K\, x(t) \tag{11}$$

The state feedback gain K is optimized using LMI optimization. To obtain microgrid asymptotic stability in the sense of Lyapunov, system trajectories always should exactly converge to equilibrium point against initial states.

Proof Let the LQR objective Lyapunov function is considered as:

$$\kappa = x^T(t) P\, x(t) \tag{12}$$

After time derivative with respect time of Eqs. (10) and (12), the optimal solution can be written below using Eq. (11).

$$x^T(t)\left\{Q + K^T R K\right\} x(t) = -\frac{d}{dt}\left(x^T(t) P\, x(t)\right) \tag{13}$$

From microgrid state space Eq. (9) substitution in Eq. (13), it is written as:

$$x^T(t)\{Q + K^T RK\}x(t) = -x^T(t)\{(A - BK)^T P + P(A - BK)\}x(t) - x^T(t)2PF\Delta P_d(t) \tag{14}$$

$$x^T(t)\{A^T P + PA + Q - K^T RK - K^T B^T P - PBK\}x(t) - x^T(t)2PF\Delta P_d < 0 \tag{15}$$

Using lemma given in [21], term in above Eq. (15) can be written as $-\{K^T RK + K^T B^T P + PBK\} \cong -B^T PR^{-1}PB$ and substitute in above Eq. (15).

$$x^T(t)\{A^T P + PA + Q - B^T R^{-1}PB\}x(t) - x^T(t)2PF\Delta P_d(t) < 0 \tag{16}$$

To achieve accurate convergence $\dot{\kappa} < 0$, the above Eq. (16) may be converted in LMI using lemma in [21].

$$\{A^T P + PA + Q - B^T R^{-1}PB\} < 0 \tag{17}$$

Thus, closed loop system state trajectories converge asymptotically.

The Eq. (17) is transferred into LMI using Schur complements [14] to obtain optimized value of as:

Select positive definite matrix P and R in such way that following LMIs holds simultaneously with a minimum of $\gamma_{\min}$

$$P > 0$$

$$Q > 0$$

$$R > 0$$

$$A^T P + PA + Q - B^T R^{-1}PB < 0 \tag{18}$$

After calculation of optimized parameters from Eq. (18), now control law Eq. (11) is obtained.

$$u = \begin{bmatrix} u_1 & u_2 & u_3 \end{bmatrix}^T = -R^{-1}PB\,x(t) \tag{19}$$

Proposed controller design steps are given below:

- Select all LMI variables in order as per microgrid system using '*lmivar*' and write LMI Eq. (18) using '*lmiterm*' in MATLAB LMI optimization platform.
- Set objective function threshold value using '*decnbr*' in LMI toolbox.

- Find feasibility of the LMI Eq. (18) using '*feasp*' in MATLAB LMI optimization platform.
- For feasible LMI, obtain P and R variables using optimization '*mincx*' command in MATLAB.
- Finally, calculate state feedback gain K using Eq. (11).

Thus, this completes proof and optimization.

4 Simulations and Demonstrations

In order to facilitate the development of the microgrid control structure, an ideal DC voltage source is considered as shown in Fig. 1b. The linearized dynamics of the islanded microgrid is demonstrated with proposed control scheme effectiveness using MATLAB© platform. The LMIs is optimized using '*mincx*' function in MATLAB LMI toolbox. The parameters of the wind plant, solar plant, flywheel energy plant, fuel cell plant, battery energy storage plant, small turbine plant, and diesel generation plant models are described in Table 2.

The linearized microgrid system state space system poles, undamped natural frequency and damping ratio with and without controller are given in Table 3. From the said table, it is seen that open loop state space system state dynamics are unstable. The desired overall system in regular form state space time dynamics is also mentioned in Table 3. It is evident that overall system dynamics behaves comparably more stable.

Now, proposed control strategy is simulated in presence of random change in input power in the wind plant (WTG), solar plant (PV) and load disturbances in microgrid. The WTG and PV maximum power extraction from wind and solar are

Table 2 Microgrid parameters [23]

D	M	T_{BESS}	T_{FESS}	T_{DEG}	T_{FC}	T_{HT}	T_{PV}	T_{WTG}
0.012	0.300	0.100	0.100	2.00	4.00	1.00	0.3643	1.50

Table 3 Time characteristics and poles

Open-loop system poles locations	Open-loop system	Overall microgrid system pole's locations	Overall system
Stable pole: −0.25, −0.50, −0.6667, −1.00, −2.7452, −10.00, −10.00 Unstable pole: 5.000	Open-loop system is unstable with high oscillations	Stable pole: −4.7097, −0.3850, −2.0171 −1.1827, −9.9914, −10.0000 −0.6667, −2.7452	Closed loop system is stable

not considered in this study. Hence, random change with uncertainty in input power is directly applied to simplified wind and solar plant models for small signal analysis as shown in Fig. 2a, b respectively. The random change in microgrid load is also given in the third subfigure of Fig. 2c. The simulated responses of the microgrid with proposed control scheme are given in Figs. 2d, 3 and 4. The required control effort for small turbine (HT) plant to sustain frequency deviation within feasible range is shown in Fig. 2d. It is evident that the required control effort is found satisfactory. The deviations in generated power responses from wind plant (WTG), solar plant (PV), flywheel storage plant (FESS) and battery storage plant (BESS) are shown in Fig. 3a, b, c and d respectively.

From said Fig. 3, the generation power from wind plant, solar plant, flywheel storage plant and battery storage plant are regulated indirectly via proposed controller according to microgrid frequency deviation even in presence of uncertainties in wind plant, solar plant and random load disturbances respectively. However, the deviation in microgrid frequency response, generated power from flywheel storage plant, fuel cell plant and battery storage plant are controlled using proposed controller against uncertainties in wind plant, solar plant and random load disturbances as shown in Fig. 4a, b, c and d respectively. It is evident that the proposed controller is used to regulate power generation from power from flywheel storage plant, fuel cell plant and battery storage plant to sustain minimum frequency deviations effectively. Thus, proposed controller enhances the closed loop system stability even in presence of plant uncertainties.

Further, the proposed control scheme and state PID controller [26] responses are compared in presence of the above uncertainties as given in Fig. 2a, b and c in islanded microgrid system. The deviations in microgrid frequency and generated power from flywheel storage plant, fuel cell plant and battery storage plant's comparative responses are depicted in Fig. 5a, b, c and d respectively. Due to presence of parameter uncertainties, state PID controller performance deteriorates in terms of larger over/undershoots characteristics while proposed control scheme is completely less sensitive against above parameters uncertainties. The proposed control scheme has negligible oscillations in generated power from flywheel storage plant, fuel cell plant and battery storage plants compared to state PID controller. It is observed that proposed control scheme is capable to sustain the islanded microgrid system stability and kept less sensitive even in presence of parameter uncertainties. Thus, proposed control scheme is able to minimize islanded microgrid frequency issues effectively.

5 Conclusion

A centralised linear quadratic regulator-based controller was developed for a linearized islanded microgrid in order to achieve closed loop stability with better performance in terms of frequency deviation. The closed loop control law convergence was obtained using the Lyapunov stability theorem. In presence of distributed

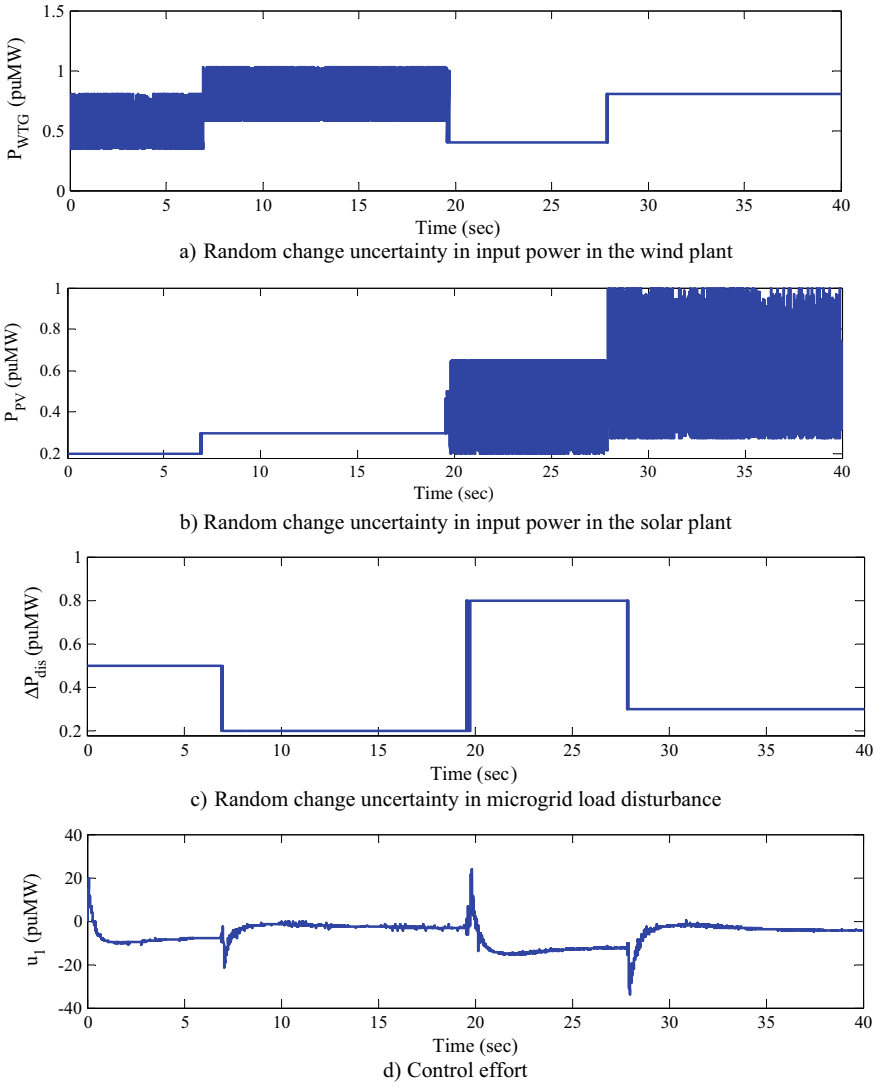

Fig. 2 Wind plant and solar plant input power deviations, load disturbance and control effort for small turbine (HT)

generation uncertainties, proposed controller performance was compared and found to enhance closed loop system stability with reduction in over/under shoots, settling time and oscillations. In addition, also through well said controller regulated power generation with minimum power mismatch from the power from flywheel storage plant, fuel cell plant and battery storage plant to sustain minimum frequency deviations effectively. The performance, stability and ability to keep in synchronism

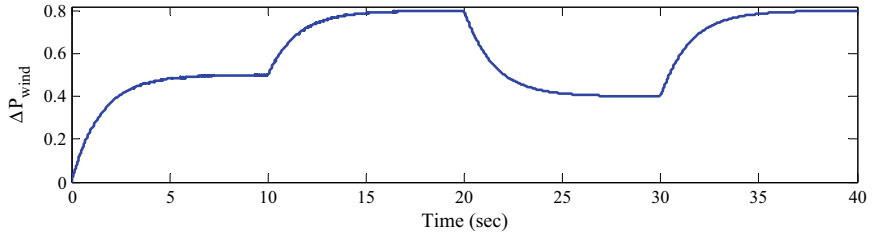

a) Deviation in generation of wind power plant with proposed controller

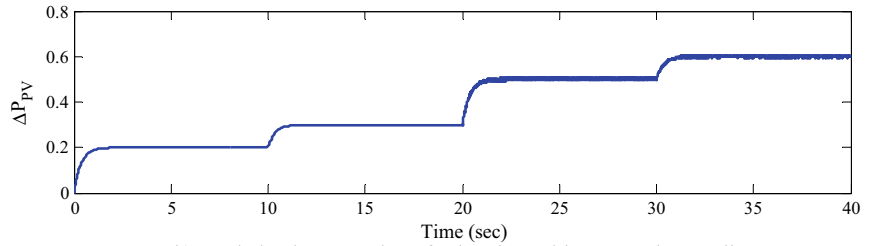

b) Deviation in generation of solar plant with proposed controller

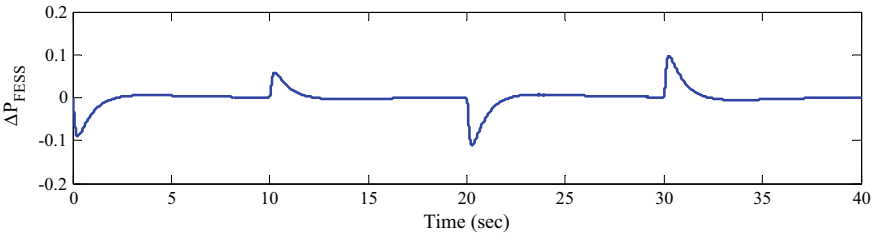

c) Deviation in generation of flywheel energy storage plant with proposed controller

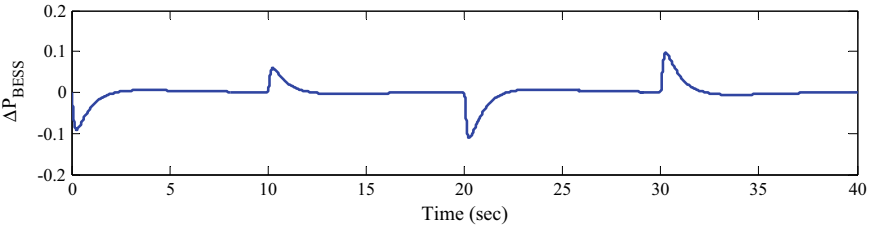

d) Deviation in generation of battery storage plant with proposed controller

Fig. 3 Deviation in generation of wind (WTG) plant, solar (PV) plant, flywheel energy storage (FESS) plant and battery storage (BESS) plant

with the proposed control scheme are found satisfactory. In future, wind plant and solar plant dynamics will be considered in place of the simplified model.

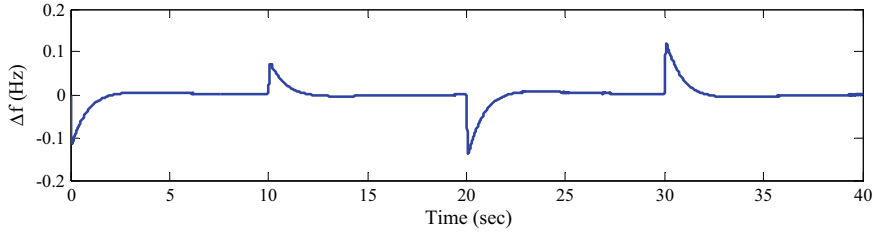

a) Frequency deviation response with proposed controller

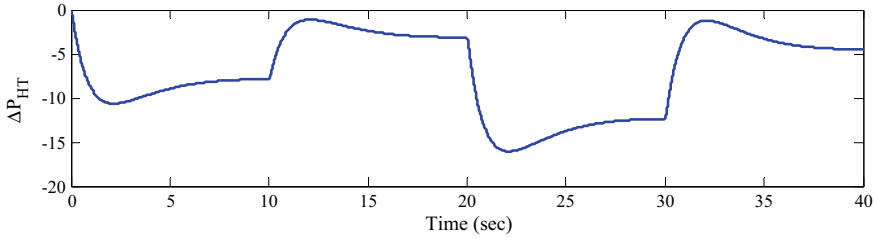

b) Deviation in generation of small turbine plant with proposed controller

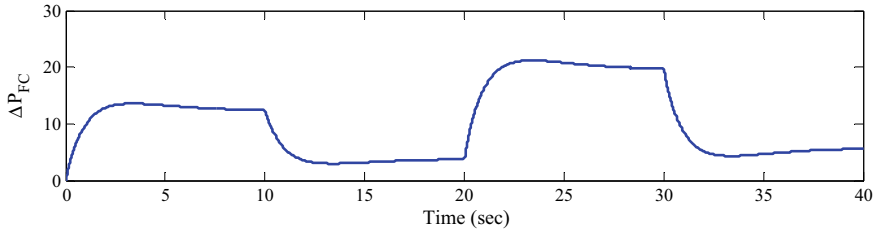

c) Deviation in generation of fuel cell plant with proposed controller

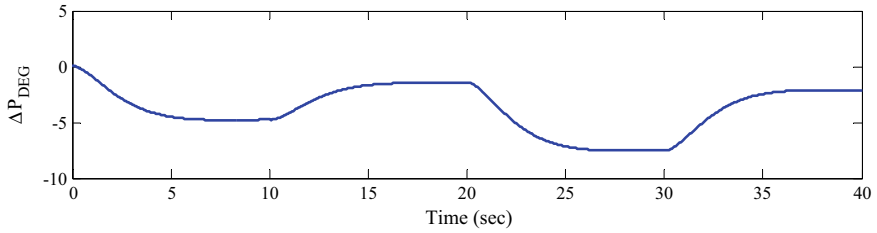

d) Deviation in generation of diesel generation plant with proposed controller

Fig. 4 Deviations in microgrid frequency, deviations in generation of small turbine (HT) plant, fuel cell (FC) plant and diesel generation (DEG) plant

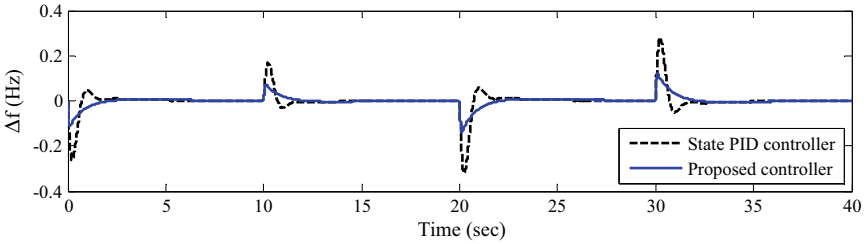

a) Comparative response in terms of microgrid frequency deviation

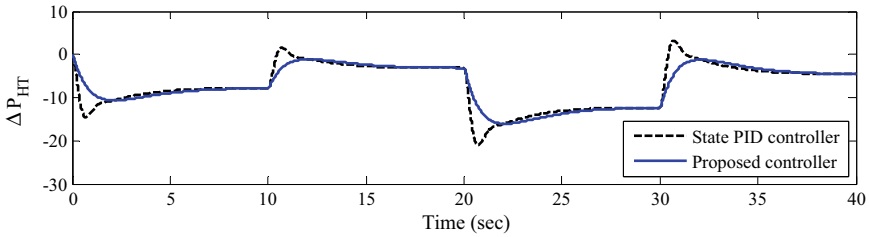

b) Comparative response in terms of deviations in generation of small turbine plant

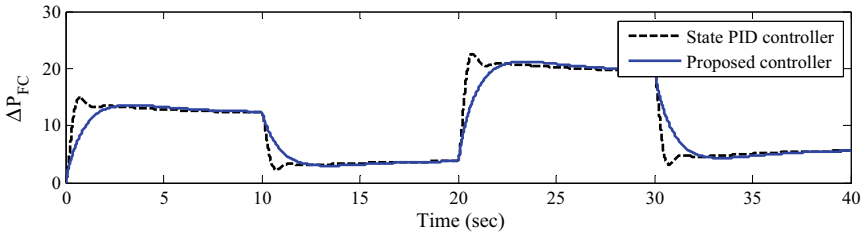

c) Comparative response in terms of deviations in generation of fuel cell plant

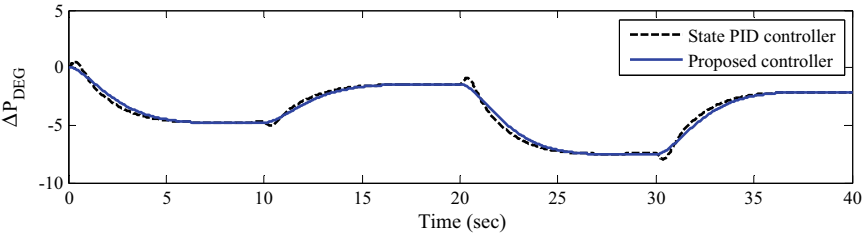

d) Comparative response in terms of deviations in generation of diesel generation plant

Fig. 5 Comparative analysis

References

1. P. Kundur, *Power System Stability and Control* (McGraw hill, New York, 1994), pp. 780–808
2. M.E. Khodayar, Rural electrification and expansion planning of off-grid microgrids. Electr. J. **30**(4), 68–74 (2017)
3. S. Prasad, M.R. Ansari, Frequency regulation using neural network observer-based controller in power system. Control Engineering Practice. 102, September (2020). https://doi.org/10.1016/

j.conengprac.2020.104571
4. W. Li, X. Tang, Z. Shen, Adaptive coordinated control of microgrid under communication interruption scenario. 2021 3rd Asia Energy and Electrical Engineering Symposium (AEEES), pp. 1–6 (2021). https://doi.org/10.1109/AEEES51875.2021.9403130
5. M.A. Hossain, H.R. Pota, A.M.O. Haruni, M.J. Hossain, DC-link voltage regulation of inverters to enhance microgrid stability during network contingencies. Electric Power Systems Research **147**, 233–244 (2017)
6. S. Sandelic, S. Peyghami, A. Sangwongwanich, F. Blaabjerg, Reliability aspects in microgrid design and planning: status and power electronics-induced challenges. Renew. Sustain. Energy Rev. **159**, 112127 (2022)
7. R. Trivedi, S. Khadem, Implementation of artificial intelligence techniques in microgrid control environment: current progress and future scopes. Energy and AI. **8**, 100147 (2022)
8. A.K. Barik, S. Jaiswal, D.C. Das, Recent trends and development in hybrid microgrid: a review on energy resource planning and control. Int. J. Sustain. Energ. **41**(4), 308–322 (2022)
9. S. Choudhury, Review of energy storage system technologies integration to microgrid: types, control strategies, issues, and future prospects. J. Ener. Stor. **48**, 103966 (2022)
10. F. Kamal, B. Chowdhury, Model predictive control and optimization of networked microgrids. Int. J. Electr. Power Energy Syst. **138**, 107804 (2022)
11. D. Kanakadhurga, N. Prabaharan, Demand side management in microgrid: a critical review of key issues and recent trends. Renew. Sustain. Energy Rev. **156**, 111915 (2022)
12. Y. Yang, P. Yang, A novel strategy for improving power quality of islanded hybrid AC/DC microgrid using parallel-operated interlinking converters. Int. J. Electr. Power Energy Syst. **138**, 107961 (2022)
13. D.L. Gerber, O.A. Ghatpande, M. Nazir, W.G.B. Heredia, W. Feng, R.E. Brown, Energy and power quality measurement for electrical distribution in AC and DC microgrid buildings. Appl. Energy **138**, 118308 (2022)
14. Han, Y. (2022). Small-signal modeling and controller synthesis of BPF-based droop control for single-phase Islanded microgrid. In: Modeling and Control of Power Electronic Converters for Microgrid Applications. Springer, Cham. https://doi.org/10.1007/978-3-030-74513-4_5
15. Braitor, AC. (2022). Control design and stability analysis of DC microgrids consisting of unidirectional DC/DC boost converters. In: Advanced Hierarchical Control and Stability Analysis of DC Microgrids. Springer Theses. Springer, Cham. https://doi.org/10.1007/978-3-030-95415-4_5
16. Braitor, AC. (2022). Stability analysis of DC microgrids under decentralised primary and distributed secondary control. In: Advanced Hierarchical Control and Stability Analysis of DC Microgrids. Springer Theses. Springer, Cham. https://doi.org/10.1007/978-3-030-95415-4_7
17. D.P. Silva, J.L.F. Salles, J.F. Fardin, M.M.R. Pereirac, Management of an island and grid-connected microgrid using hybrid economic model predictive control with weather data. Appl. Energy **278**, 115581 (2020)
18. Sun, Y., Hou, X., Lu, J., Liu, Z., Su, M., and M. Guerrero, J. (2022). A local-distributed and global-decentralized control scheme. In: Series-Parallel Converter-Based Microgrids. Power Systems. Springer, Cham. https://doi.org/10.1007/978-3-030-91511-7_15
19. B. Yang, Y. Tao, H. Shu, J. Dong, L. Chen, Y. Sang, L. Jiang, Robust sliding-mode control of wind energy conversion systems for optimal power extraction via nonlinear perturbation observers. Appl. Energy **210**, 711–723 (2018)
20. B. Khokhar, S. Dahiya, K.P.S. Parmar, Load frequency control of a microgrid employing a 2D sine logistic map based chaotic sine cosine algorithm. Appl. Soft Comput. **109**, 107564 (2021)
21. A. Latif, S.M. Suhail Hussain, D.C. Das, T.S. Ustun, Double stage controller optimization for load frequency stabilization in hybrid wind-ocean wave energy based maritime microgrid system". Appl. Energy **282**, 117161 (2021)
22. X. Zhao, Z. Lin, B.F.S. Gong, Research on frequency control method for micro-grid with a hybrid approach of FFR-OPPT and pitch angle of wind turbine". Int. J. Electr. Power Energy Syst. **127**, 106670 (2021)

23. D. Kumar, H.D. Mathur, S. Bhanot, R.C. Bansal, Modeling and frequency control of community micro-grids under stochastic solar and wind sources". Engineering Science and Technology, an International Journal. **23**(5), 1084–1099 (2020). https://doi.org/10.1016/j.jestch.2020.02.005
24. Yadav, M., and Singh, N. (2021). Small-signal modeling based hybrid optimized current and voltage controller for unbalanced DC microgrid. International Transactions on Electrical Energy Systems, 31(3). https://doi.org/10.1002/2050-7038.12797
25. S. Eberlein, K. Rudion, Small-signal stability modelling, sensitivity analysis and optimization of droop-controlled inverters in LV microgrids. Int. J. Electr. Power Energy Syst. **125**, 106404 (2021)
26. Robert, J.B. (2015). Experiments with PID controllers using state feedback design techniques. Proceedings of the IEEE Southeast Conference, pp. 1–2

Enhanced Predictive Torque Control of Open Winding Permanent Magnet Synchronous Motor Drive with Common Mode Voltage Elimination

Ravi Eswar Kodumur Meesala, Sivaprasad Athikkal, U. Ramanjaneya Reddy, and Narender Reddy Kedika

Abstract Nowadays, Predictive Torque Control (PTC) strategy is recognized as a strong tool for controlling the motor drive. Intuitive and multi-objective controlling are significant benefits of PTC. Owing to these benefits, its application is introduced for Open Winding Permanent Magnet Synchronous Motor (OW-PMSM) drive. The basic PTC operated OW-PMSM drive consequences high Common Mode Voltage (CMV) and leads to early failure of motor bearings. In this paper, CMV elimination is proposed for OW-PMSM drive using voltage vector selection in PTC operation. In proposed PTC, the possible voltage vectors (VVs) are identified to gain zero CMV and preselected as prediction VVs for cost-function evaluation. From cost-function evaluation, optimal VV is considered for controlling OW-PMSM drive. In addition, decrease in switching frequency is achieved through proper utilization of optimal VV's redundant switching states. Therefore, the overall modifications in proposed PTC of OW-PMSM drive ensure simple operational control, CMV elimination, and switching frequency and loss reduction. The claims of proposed PTC are verified through Matlab/Simulink platform and its proficiency is highlighted against basic PTC operation. Thus, the enhanced operation of proposed PTC for OW-PMSM drive with zero CMV is justified.

Keywords Common Mode Voltage (CMV) · Open Winding Permanent Magnet Synchronous Motor (OW-PMSM) drive · Predictive Torque Control (PTC)

R. E. K. Meesala (✉) · S. Athikkal
SRM Institute of Science and Technology, Chennai, Tamil Nadu, India
e-mail: ravieswm@srmist.edu.in

S. Athikkal
e-mail: sivanuday@gmail.com

U. Ramanjaneya Reddy
SRM University, Andhra Pradesh, India
e-mail: ramanjaneya.r@srmap.edu.in

N. R. Kedika
Institute of Aeronautical Engineering, Dhundigal, Hyderabad, Telangana, India
e-mail: kdk.reddy@gmail.com

J. Kumar et al. (eds.), *Control Applications in Modern Power Systems*, Lecture Notes in Electrical Engineering 974, https://doi.org/10.1007/978-981-19-7788-6_4

1 Introduction

Permanent Magnet Synchronous Motor (PMSM) is now widely applicable in most of the electric drive applications. High power density and torque/weight ratio, superior efficiency, and simple construction are some of its primary characteristics. As a result, its use in electric vehicles (EVs) is becoming more popular [1–3]. When compared to two-level voltage source inverter (VSI), the introduction of Multi Level Inverters (MLIs) to supply for motor drive [4] operation provides better harmonic spectrum with less Total Harmonic Distortion (THD) of voltage and current through increased voltage levels in supply. Besides this, reduced CMV, lower dv/dt across the power electronic switches, and reduced switching losses are additional benefits [5]. For MLI fed PMSM drives, dual two-level VSI configuration is the optimum option, owing to its special benefits [6–8]: (1). Using two distinct DC link voltages, multilevel voltage supply across the motor drive is simply established, (2). The ability to withstand faults, (3). No clamping diodes and no difficulty with capacitor voltage un-balance (which exist in basic neutral-point clamp and flying capacitor MLI), (4) a simple construction, and (5) integration of hybrid supplies such as fuel cells, batteries, or ultra-capacitors. The dual two-level VSI is supplied to open three phase windings of PMSM drive.

To attain superior dynamic performance of OW-PMSM drive, Field-Oriented Control (FOC) or Direct Torque Control (DTC) or Predictive Torque Control (PTC) technique is applied, which are part of vector control [9]. Even though FOC operated motor drive achieves good steady state behavior, it demands precise tuning of Proportional and Integral (PI) controllers in the inner current loop, as well as rotational coordinate frame transformations. DTC works in a stationary reference frame and achieves a rapid dynamic response with a minimal setup (i.e., simple structure). However, due to the hysteresis-based controlling [10], DTC has two key flaws: large torque ripples and switching frequency increment with reverse voltage vectors (VVs) selection. To address the shortcomings of DTC in motor drives, several researches have been done including the application of Finite control Set-Model Predictive Control (FS-MPC). FS-MPC has become a more efficient and competent technique in motor drive applications nowadays. FS-MPC is termed as Predictive Torque Control (PTC) when cost-function is built with torque and flux control objectives. Thus, PTC is widely employed in high-performance motor drive applications, owing to rapid dynamic as well as good steady state nature [11–13].

In the motor drive operation, there exist some parasitic capacitances (in the range of picofarads). The CMV on stator windings generates shaft voltage by capacitive coupling through the motor air gap. As a result, electro-static discharge occurs in the bearing lubricating film. The bearings' lifespan is reduced [14] due to parasitic currents. In addition, the presence of CMV affects protection system by creating failures in fault detection [15]. The stated problems are also experienced in PTC operated OW-PMSM drive. To deal with the CMV problem, a variety of techniques have been proposed, such as including the additional active and/or passive devices in motor drive system. The extra hardware generates a large increase in the system's

volume and demands sophisticated control methods [15]. Therefore, CMV minimization or elimination through control modifications is preferable. Modified PTC of open winding induction motor drive is presented in [16, 17] to minimize CMV. However, these techniques need a weighting factor and demand its optimal tuning which is a cumbersome process. In [18–20], CMV mitigation is achieved through modified space vector pulse width modulation scheme for VSI operation.

In this paper, CMV elimination is introduced for dual two-level VSI fed OW-PMSM drive. The proposed PTC uses optimal VVs which produce zero CMV as prediction VVs for cost-function evaluation process. From this, the final optimal VV is applied with a suitable switching combination to gain reduced switching frequency. Therefore, the overall modifications in proposed PTC introduce CMV elimination and switching frequency reduction for OW-PMSM drive.

2 Mathematical Model of OW-PMSM Drive

Figure 1 depicts arrangement of dual two-level VSI fed OW-PMSM drive. It has dual two-level VSIs with identical DC-link voltages. (v_{ao}, v_{bo}, v_{co}) and ($v_{a'o'}$, $v_{b'o'}$, $v_{c'o'}$) are the pole voltages of VSI-1 (1) and VSI-2 (2), respectively. The resultant pole voltages are given by (3). The OW phase voltages are represented by (4). When the resultant pole voltages from (4) are added together, a nonzero term called CMV is generated as (5).

$$\begin{pmatrix} v_{a0} \\ v_{b0} \\ v_{c0} \end{pmatrix} = V_{dc1} \begin{pmatrix} S_{a1}^{+} \\ S_{b1}^{+} \\ S_{c1}^{+} \end{pmatrix} \tag{1}$$

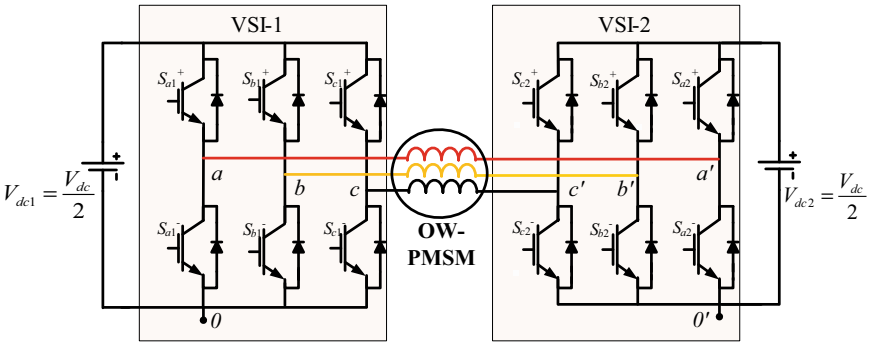

Fig. 1 OW-PMSM with dual two-level VSI circuit

$$\begin{pmatrix} v_{a'0'} \\ v_{b'0'} \\ v_{c'0'} \end{pmatrix} = V_{dc2} \begin{pmatrix} S_{a2}^{+} \\ S_{b2}^{+} \\ S_{c2}^{+} \end{pmatrix} \tag{2}$$

$$\begin{pmatrix} \Delta v_{aa'} \\ \Delta v_{bb'} \\ \Delta v_{cc'} \end{pmatrix} = \begin{pmatrix} v_{a0} - v_{a'0'} \\ v_{b0} - v_{b'0'} \\ v_{c0} - v_{c'0'} \end{pmatrix} \tag{3}$$

$$\begin{pmatrix} v_{aa'} \\ v_{bb'} \\ v_{cc'} \end{pmatrix} = \begin{pmatrix} \Delta v_{aa'} \\ \Delta v_{bb'} \\ \Delta v_{cc'} \end{pmatrix} - \begin{pmatrix} v_o \\ v_o \\ v_o \end{pmatrix} \tag{4}$$

$$v_o = \frac{\Delta v_{aa'} + \Delta v_{bb'} + \Delta v_{cc'}}{3} \tag{5}$$

Equations (6) and (7) are voltage space vector generations of VSI-1 and 2 respectively. From these, the net voltage space vector is realized as (8). Equations (6)–(8) are evaluated with possible 64 switching states of dual two-level VSI to identify effective VVs. From this analysis, Table 1 present unique 19 three-level VVs of dual two-level VSI operation. Using (5), calculated CMV values of 19 VVs are also listed in Table 1.

$$v_{s1} = \frac{2V_{dc1}}{3}\left(S_{a1}^{+} + S_{b1}^{+} e^{\frac{j2\pi}{3}} + S_{c1}^{+} e^{\frac{j4\pi}{3}}\right) \tag{6}$$

$$v_{s2} = \frac{2V_{dc2}}{3}\left(S_{a2}^{+} + S_{b2}^{+} e^{\frac{j2\pi}{3}} + S_{c2}^{+} e^{\frac{j4\pi}{3}}\right) \tag{7}$$

$$v_s = v_{s1} - v_{s2} \tag{8}$$

The current and flux state space representations of OW-PMSM are given by (9) and (10). Motor torque is calculated by (11). Using (12), motor-load torque relation is framed. All these mathematical analyses are required to build PTC operation for OW-PMSM drive.

$$\frac{\mathrm{d}i_s}{\mathrm{dt}} = \frac{v_s - R_s i_s - \phi_r \omega_r e^{j\theta}}{L_s} \tag{9}$$

$$\frac{\mathrm{d}\varnothing_s}{\mathrm{dt}} = v_s - R_s i_s \tag{10}$$

$$T_m = (0.75P) \times \mathrm{imag}(\overline{\phi}_s \times i_s) \tag{11}$$

$$T_m = T_l + J\frac{\mathrm{d}\omega}{\mathrm{dt}} \tag{12}$$

Table 1 Switching states and VV representation of three-level dual two-level VSI

Switching states (S_{a1}^+, S_{b1}^+, S_{c1}^+, S_{a2}^+, S_{b2}^+, S_{c2}^+)	VVs notation	VV representation in αβ frame ($v_{s\alpha} + \mathrm{j}\, v_{s\beta}$) × V_{dc}	CMV × V_{dc}/2
(0,0,0,0,0,0); (1,1,1,1,1,1); (1,0,0,1,0,0); (1,1,0,1,1,0); (0,1,0,0,1,0); (0,1,1,0,1,1); (0,0,1,0,0,1); (1,0,1,1,0,1)	$\mathbf{V_0}$	0	**0**
(1,1,0,0,1,0)	V_1	1/3	0.333
(0,1,0,0,1,1)	V_2	1/6 + j sqrt (3)/6	−0.333
(0,1,1,0,0,1)	V_3	−1/6 + j sqrt (3)/6	0.333
(0,0,1,1,0,1)	V_4	−1/3	−0.333
(1,0,1,1,0,0)	V_5	−1/6 − j sqrt (3)/6	0.333
(1,0,0,1,1,0)	V_6	1/6 − j sqrt (3)/6	−0.333
(1,0,0,0,1,1)	V_7	2/3	−0.333
(1,0,0,0,0,1); (1,1,0,0,1,1)	$\mathbf{V_8}$	1/2 + j sqrt (3)/6	**0**
(1,1,0,0,0,1)	V_9	1/3 + j sqrt (3)/3	0.333
(1,1,0,1,0,1); (0,1,0,0,0,1)	$\mathbf{V_{10}}$	j sqrt (3)/3	**0**
(0,1,0,1,0,1)	V_{11}	−1/3 + j sqrt (3)/3	−0.333
(0,1,0,1,0,0); (0,1,1,1,0,1)	$\mathbf{V_{12}}$	−1/2 + j sqrt (3)/6	**0**
(0,1,1,1,0,0)	V_{13}	−2/3	0.333
(0,1,1,1,1,0); (0,0,1,1,0,0)	$\mathbf{V_{14}}$	−1/2 − j sqrt (3)/6	**0**
(0,0,1,1,1,0)	V_{15}	−1/3 − j sqrt (3)/3	−0.333
(0,0,1,0,1,0); (1,0,1,1,1,0)	$\mathbf{V_{16}}$	−j sqrt (3)/3	**0**
(1,0,1,0,1,0)	V_{17}	1/3 − j sqrt (3)/3	0.333
(1,0,0,0,1,0); (1,0,1,0,1,1)	$\mathbf{V_{18}}$	1/2 − j sqrt (3)/6	**0**

In (9)–(12), i_s and v_s are stator current and voltage space vectors, R_s is stator resistance, ϕ_r is rotor magnetic flux and ϕ_s is stator flux vector, T_m and T_l are motor and load torque respectively. P and θ are pole number and rotor angle, ω_r and ω are rotor electrical and mechanical speeds. J is moment of inertia.

3 Basic PTC of OW-PMSM Drive

The stator flux and motor torque are the basic control variables in PTC. After measuring motor speed, DC link voltage and phase currents, the stator flux estimation and current one step prediction are accomplished as (13) and (14) respectively. The stator current (15) and flux (16) two step predictions are realized using Euler's discretization. From them, torque prediction is derived as (17). Using effective 19 VVs of dual two-level VSI, (15)–(17) are computed to obtain prediction control variables. In final stage, cost-function (CF) is evaluated (18), which is function of

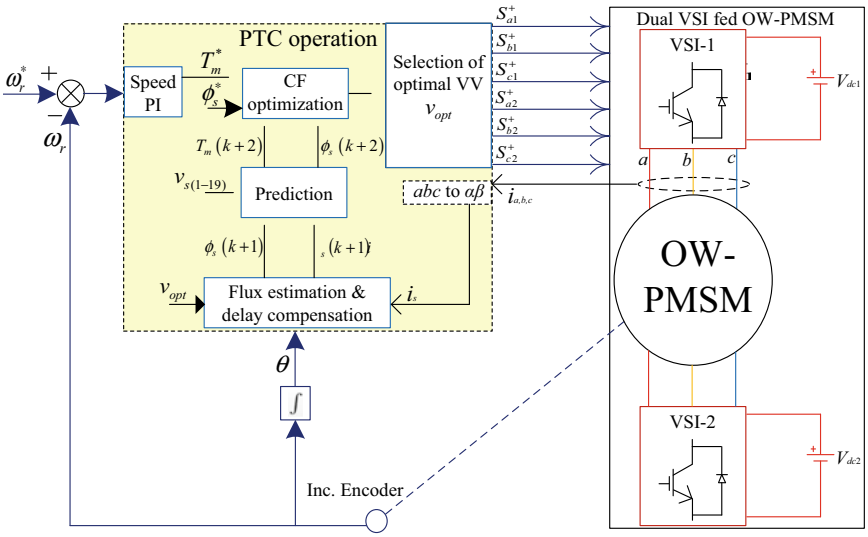

Fig. 2 Basic PTC function of OW-PMSM drive

reference and prediction control variables. The reference flux ($\varnothing_s^*$) is set to motor rated flux value and reference torque (T_m^*) is generated through speed PI controller. Therefore, the entire PTC working involves three key steps: estimation, prediction of torque and flux control variables and cost-function evaluation. Its block diagram is shown in Fig. 2.

$$\varnothing_s(k+1) = \left(v_{opt} - R_s i_s\right) T_s + \varnothing_s(k) \tag{13}$$

$$i_s(k+1) = \left(v_{opt} - \varnothing_r \omega_r e^{j\theta}\right) \frac{T_s}{L_s} + i_s\left(1 - \frac{T_s R_s}{L_s}\right) \tag{14}$$

$$i_s(k+2)_n = \left((v_s)_n - \varnothing_r \omega_r e^{j\theta}\right) \frac{T_s}{L_s} + i_s(k+1)\left(1 - \frac{T_s R_s}{L_s}\right) \tag{15}$$

$$\varnothing_s(k+2)_n = ((v_s)_n - R_s i_s(k+1)) T_s + \varnothing_s(k+1) \tag{16}$$

$$T_m(k+2)_n = (0.75P) \times \text{imag}(\overline{\phi}_s(k+2)_n \times i_s(k+2)_n) \tag{17}$$

CF formulation:

$$G_n = \left|T_m^* - T_m(k+2)_n\right| + W_\varnothing \left|\varnothing_s^* - |\varnothing_s(k+2)_n|\right| \tag{18}$$

In (13)–(18), variables at present sample instant are denoted by 'k' and prediction variables at one and two steps ahead are denoted by $(k+1)$ and $(k+2)$. T_s is sample time, subscript 'n' denotes prediction VV's number, $W_{\varnothing}$ is flux weighting factor, which is to be tuned by trial-and-error base.

From (18), it is evident that basic cost-function design lags control over CMV and switching frequency. To gain these controls, CMV and switching frequency control objectives with proper weights can be introduced in CF. However, it leads to a cumbersome control process due to a greater number of weighting factor tuning parameters.

4 Proposed PTC of OW-PMSM Drive

The main intent of this paper is to design a simple PTC operation to provide CMV elimination and switching frequency reduction. Its block diagram is presented in Fig. 3. Proposed PTC uses basic CF (18) having flux weighting factor only. In control operation, VVs are priorly selected which produces zero CMV. This can be identified from Table 1, where 7 VVs (V_0, V_8, V_{10}, V_{12}, V_{14}, V_{16}, V_{18}) are known to be optimal for CMV elimination. These seven VVs (as shown in Fig. 4) acts as prediction VV sets for computing torque, flux predictions and finally CF evaluation. The VV providing optimized minimum valued CF is chosen for basic control of torque and flux. In addition, proposed PTC operation offers low complexity, since only 7 VVs are involved in computational process out of 19 VVs.

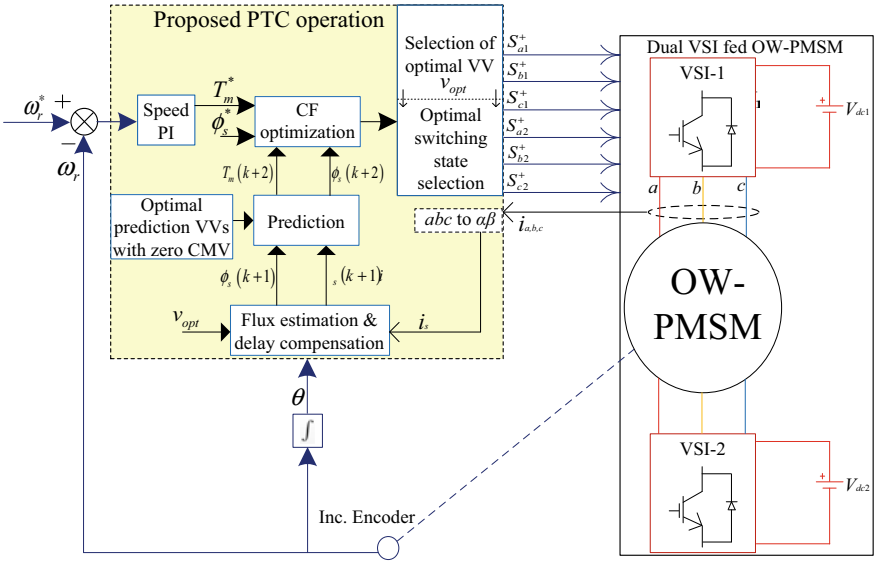

Fig. 3 Proposed PTC function of OW-PMSM drive

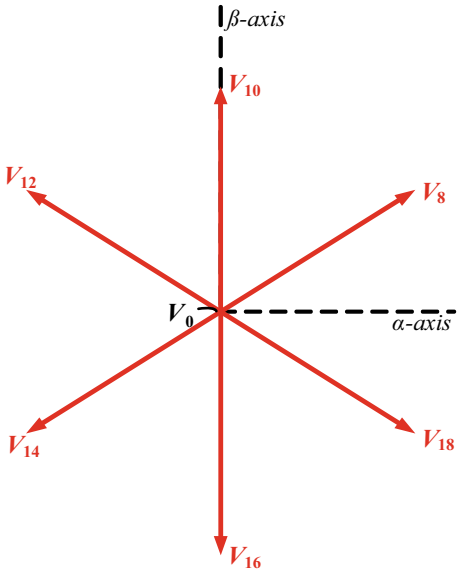

Fig. 4 Optimal prediction VVs with zero CMV

After evaluating the final optimal VV for control operation, switching state selection procedure is followed for the operation of dual two-level VSI fed OW-PMSM drive. From Table 1, it is identified that each prediction VV of proposed PTC has redundant switching states. Thus, concept of redundancy is utilized to gain minimum switching state transitions. This can be accomplished with the evaluation of (19), where optimal VV's redundant switching states are compared with previous instant switching state.

Among possible redundant switching states of optimal VV, the switching state which provides minimum value of 'F' (19) is applied for the control operation. Therefore, gaining minimum switching state transitions consequences an overall reduction in switching frequency of OW-PMSM drive operated with proposed PTC.

$$F_r = \left| S_{opt}(k-1) - S(k)_r \right| \tag{19}$$

In (19), $S_{opt}(k-1)$ is optimal switching state applied in previous sample instant and $S_{opt}(k)_r$ is present optimal VV's redundant switching states having 'r' numbers.

From the entire discussion of proposed PTC for OW-PMSM drive, the notable features are listed as: CMV elimination, low complexity in operation and switching frequency reduction. Thus, significant advancements in proposed PTC operation are perceptible.

5 Results and Discussion

Matlab/Simulink simulation tests are carried out to validate the efficacy of the proposed PTC. The OW-PMSM drive parameters are listed in Table 2. Test 1 analyses the performance of proposed PTC versus basic PTC in steady state at different speeds such as 50 rpm, 300 rpm and 800 rpm, with the load torque of 12.5 N-m. The captured results of speed, torque, flux, switching pulses and CMV are displayed in Figs. 5, 6 and 7.

Similarly, test 2 and 3 analyses the dynamic performance obtained for proposed PTC versus basic PTC. Test 2 in Fig. 8 indicates dynamic performance with respect to step changes in speed from 200 to 800 rpm. From this, the observed speed transient time is 0.33 S for both basic and proposed PTC. Test 3 in Fig. 9 indicates dynamic performance with respect to a step change in load torque from 12 N-m to 20 N-m. From this, the observed speed transient time is 0.8 S for both basic and proposed PTC. Therefore, proposed PTC retains high dynamic performance of basic PTC.

In Table 3, the displayed results are quantitatively analyzed in terms of CMV (rms), switching frequency and losses, ripple content of flux and torque. Using standard deviation concept, ripple content of flux and torque are calculated. By measuring the

Table 2 OW-PMSM drive parameters

Parameter	Value
Stator resistance- R_s	1.12 Ω
Stator inductance- L_s	10.5 mH
Rotor flux	0.7 Wb
Inertia	0.0615 kg-m^2
Rated power	5 HP
Combined DC-link voltage ($V_{dc} = V_{dc1} + V_{dc2}$)	600 V
Proportional and integral gains	18 and 36
Rated flux	0.705 Wb
Flux weighting factor	75

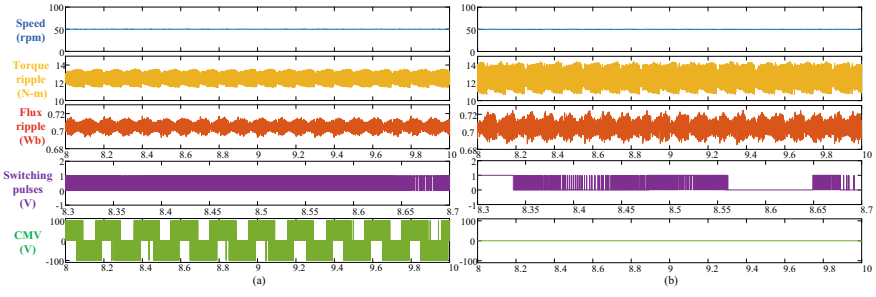

Fig. 5 Test 1 analysis at 50 rpm. **a** basic PTC and **b** proposed PTC (X-axis: Time (S))

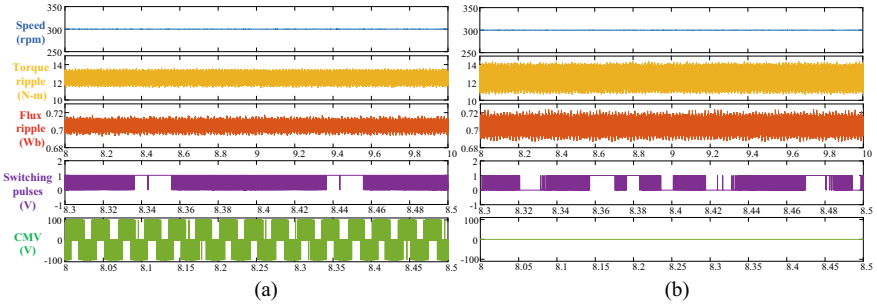

Fig. 6 Test 1 analysis at 300 rpm. **a** basic PTC and **b** proposed PTC (X-axis: Time (S))

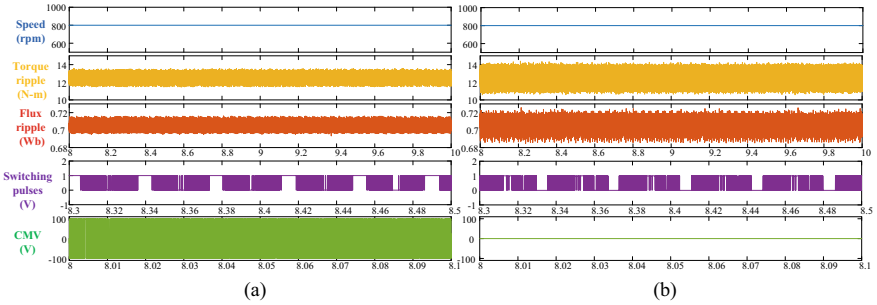

Fig. 7 Test 1 analysis at 800 rpm. **a** basic PTC and **b** proposed PTC (X-axis: Time (S))

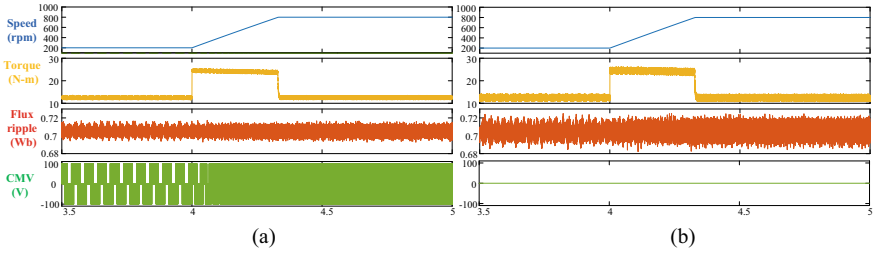

Fig. 8 Test 2 analysis with speed dynamics. **a** basic PTC and **b** proposed PTC (X-axis: Time (S))

number of state transitions per switch in a second, average switching frequency values are provided. Considering IGBT model SKM75GB12T4, switching loss estimation is provided. The mathematical analysis to evaluate average switching losses is given in [21].

From the achieved quantitative values, comparative analysis between basic and proposed PTC is performed. It is noticed that proposed PTC lags in torque and flux response with more ripple. This is due to utilization of reduced VVs in proposed PTC operation. However, the key contributions of proposed PTC are complete CMV

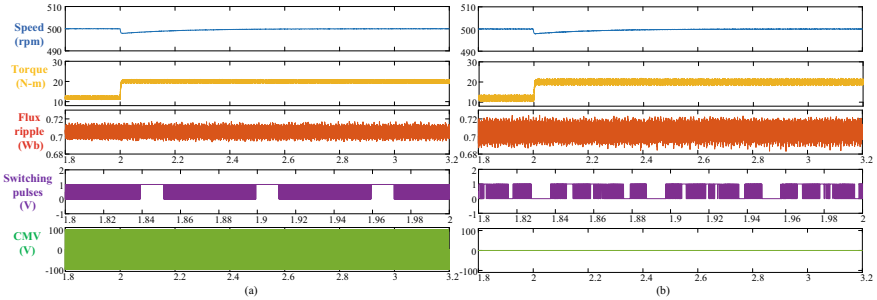

Fig. 9 Test 3 analysis with load dynamics. **a** basic PTC and **b** proposed PTC (X-axis: Time (S))

Table 3 Performance comparisons

Speeds (rpm)	Torque ripple (N-m)	Flux ripple (Wb)	Avg. switching frequency (Hz)	Avg. Switching losses (W)	CMV (V) in rms
Basic PTC					
50	0.451	0.0044	1235	1.23	11.00
300	0.453	0.0041	4108	4.07	55.17
800	0.450	0.0046	4428	4.40	47.84
Proposed PTC					
50	0.720	0.0063	**508**	**0.50**	**0**
300	0.785	0.0061	**1711**	**1.70**	**0**
800	0.782	0.0064	**4096**	**4.06**	**0**

elimination, switching frequency and loss reduction. Owing to zero CMV performance, the proposed PTC operated OW-PMSM drive is ideal for industrial applications, where CMV mitigation is of prime importance to attain electrical safety. The obtained values shown in Table 3 validates the significance of proposed PTC. Besides this, number of computations for proposed PTC operation is reduced. This can be evident from Table 4.

Finally, a design of proposed PTC of OW-PMSM drive with low complexity, CMV elimination, switching frequency and loss reduction is attained. The future scope of this research is to implement zero CMV along with improved steady state performance such as torque and flux response of OW-PMSM drive.

Table 4 Computational comparisons

Scheme	Number of CF evaluations
Basic PTC	19
Proposed PTC	**7**

6 Conclusion

This paper presents a low complexity PTC operated OW-PMSM drive with CMV elimination. The proposed PTC uses basic CF without additional involvement of weighting factors. Using priorly selected optimal VVs for CMV elimination, proposed PTC is operated. In addition, final optimal VV's switching states redundancy is utilized to gain minimum switching state transitions. Thereby, achieving reduction in switching frequency and losses. According to Matlab/Simulink simulation results, the proposed PTC of OW-PMSM drive shows zero CMV, less switching frequency and losses. These benefits are achieved by sacrificing steady state performance such as torque and flux response of OW-PMSM drive. However, zero CMV performance of proposed PTC ensures electrical safety, which is crucial in industries. Therefore, it can be concluded that the low complexity proposed PTC operation is ideal for CMV elimination in OW-PMSM drive along with switching frequency and loss reduction, which is well suitable for electric traction and industrial electric drive applications.

References

1. X. Sun, C. Hu, G. Lei, Z. Yang, Y. Guo, J. Zhu, Speed sensorless control of SPMSM drives for EVs with a binary search algorithm-based phase-locked loop. IEEE Trans. Veh. Technol. **69**(5), 4968–4978 (May2020)
2. Z. Wang, T.W. Ching, S. Huang, H. Wang, T. Xu, Challenges faced by electric vehicle motors and their solutions. IEEE Access **9**, 5228–5249 (2021)
3. C. Gong et al., Hybrid DC-bus capacitor discharge strategy using internal windings and external bleeder for surface-mounted PMSM-based EV powertrains in emergency. IEEE Trans. Industr. Electron. **68**(3), 1905–1915 (March 2021)
4. A. Poorfakhraei, M. Narimani, A. Emadi, A review of multilevel inverter topologies in electric vehicles: current status and future trends. IEEE Open J. Power Electr. **2**, 155–170 (2021)
5. S. Pal et al., A cascaded nine-level inverter topology with T-type and H-bridge with increased DC-bus utilization. IEEE Trans. Power Electron. **36**(1), 285–294 (Jan. 2021)
6. R.E.K. Meesala, S. Athikkal, Evaluation of predictive torque controlled two-level and multilevel permanent magnet synchronous motor drive for electric vehicles. IEEE International Power and Renewable Energy Conference (IPRECON) 2021, 1–6 (2021)
7. U.R. Muduli, A.R. Beig, R.K. Behera, K.A. Jaafari, J.Y. Alsawalhi, Predictive control with battery power sharing scheme for dual open-end-winding induction motor based four-wheel drive electric vehicle. IEEE Trans. Industr. Electron. **69**(6), 5557–5568 (June 2022)
8. R. E. Kodumur Meesala and V. K. Thippiripati, "An improved direct torque control of three-level dual inverter fed open-ended winding induction motor drive based on modified look-up table," in *IEEE Transactions on Power Electronics*, vol. 35, no. 4, pp. 3906–3917, April 2020
9. Ravi Eswar, Kodumur Meesala, Chokkalingam Bharatiraja, and Jayakumar Vinoth. "Assessment of various vector control schemes for PMSM drive application." In *Proceedings of International Conference on Power Electronics and Renewable Energy Systems*, pp. 49–60. Springer, Singapore, 2022
10. C. Dang, M. Dou, Y. Wang, Model predictive direct torque control for PMSM drives in M-T frame. IEEE International Conference on Predictive Control of Electrical Drives and Power Electronics (PRECEDE) 2021, 138–141 (2021)

11. M. Wu, X. Sun, J. Zhu, G. Lei and Y. Guo, "Improved model predictive torque control for PMSM drives based on duty cycle optimization," in *IEEE Transactions on Magnetics*, vol. 57, no. 2, pp. 1–5, Feb. 2021, Art no. 8200505
12. A. Nasr, C. Gu, G. Buticchi, S. Bozhko and C. Gerada, "A low-complexity modulated model predictive torque and flux control strategy for PMSM drives without weighting factor," in *IEEE Journal of Emerging and Selected Topics in Power Electronics*, https://doi.org/10.1109/JESTPE.2022.3152652
13. H. Xie, F. Wang, Y. He, J. Rodríguez, R. Kennel, Encoderless parallel predictive torque control for induction machine using a robust model reference adaptive system. IEEE Trans. Energy Convers. **37**(1), 232–242 (March 2022)
14. A. Hota, V. Sonti, S. Jain, V. Agarwal, Common mode voltage elimination in single-phase multilevel inverter using a 3rd Leg. International Conference on Sustainable Energy and Future Electric Transportation (SEFET) **2021**, 1–5 (2021)
15. G. Mirzaeva, D. Carter, S. M. M. Uddin and P. Stepien, "Common mode voltage elimination in variable speed drives for improved electrical Safety," in *IEEE Transactions on Industry Applications*, vol. 56, no. 4, pp. 4365–4374, July–Aug. 2020
16. Kumar, Kunisetti V. Praveen, and Thippiripati Vinay Kumar. "Predictive torque control of open-end winding induction motor drive fed with multilevel inversion using two two-level inverters." *IET Electric Power Applications* 12, no. 1 (2018), pp. 54–62
17. N. S. P. Musunuru and S. Srinivas, "Elimination of dead time effects on common mode voltage in an open-end winding induction motor drive under low speed operation using a simplified model predictive control," in *IEEE Journal of Emerging and Selected Topics in Industrial Electronics*, https://doi.org/10.1109/JESTIE.2022.3151555
18. K.D. Pham, N.V. Nguyen, A reduced common-mode-voltage pulsewidth modulation method with output harmonic distortion minimization for three-Level neutral-point-clamped inverters. IEEE Trans. Power Electron. **35**(7), 6944–6962 (July 2020)
19. A.G.F. da Silva et al., SVPWM technique with reduced common mode voltage for three-phase voltage source inverter. IEEE Applied Power Electronics Conference and Exposition (APEC) **2020**, 2499–2505 (2020)
20. H. Qamar, H. Qamar and R. Ayyanar, "Performance analysis and experimental validation of 240°-clamped space vector PWM to minimize common mode voltage and leakage current in EV/HEV traction drives," in *IEEE Transactions on Transportation Electrification*, https://doi.org/10.1109/TTE.2021.3108957
21. Meesala RE, Athikkal S, Aruldavid R, "Improved direct torque controlled PMSM drive for electric vehicles," in Journal of The Institution of Engineers (India): Series B. 2022 Feb 1:1–2

Comparative Analysis of Conventional and Intelligent Methods for Speed Control of Induction Motor

Ashwani Srivastav, M. Rizwan, and Vinod Kumar Yadav

Abstract Induction motor drives are widely preferred for speed control applications because of its simpler construction, robustness and development in power electronics. Most of these applications need faster response and intelligent speed control logic to achieve higher efficiency along with high dynamic performance. The primary goal is to effectively manage the speed and flux independently in order to achieve good dynamics performance. To decouple the torque and flux we try to make ac motor analogous to dc motor, as the field current and armature current are independent of one another in dc motor i.e. when torque is controlled, flux will not be altered and quick dynamic response is assured. Because of inherent coupling problem the response of the induction motor is sluggish. Sensor less Direct Torque Control and Field Oriented Control drives require knowledge of stator and rotor flux and torque. These estimations are generated by using the stator line voltage and current and machine stator and rotor electrical parameters. The estimation of torque and flux are also considered to model the drive. In this paper, both conventional and intelligent methods of speed control are reviewed and then their comparative analysis is done on the basis of performance, maintenance cost, complexity and area of applications.

Keywords Induction motor Drive · V/f method · Field oriented control · Direct torque control · Intelligent control

A. Srivastav (✉) · M. Rizwan · V. K. Yadav
Department of Electrical Engineering, Delhi Technological University, Delhi, India
e-mail: ashwanisrivastav_2k20pes06@dtu.ac.in

M. Rizwan
e-mail: rizwan@dce.ac.in

V. K. Yadav
e-mail: vinodkumar@dtu.ac.in

J. Kumar et al. (eds.), *Control Applications in Modern Power Systems*, Lecture Notes in Electrical Engineering 974, https://doi.org/10.1007/978-981-19-7788-6_5

1 Introduction

The Induction motor drives are widely used in around 90% of the application in different fields like commercial, industrial and other utility applications. It is because of the advantages provided by induction motors which make it superior compared to other electrical motors. Some of the benefits are listed below [1]:

- The robust construction and low manufacturing cost make it more suitable compared to any other motor drive.
- Cost of maintenance is comparably low because of its simple construction
- The efficiency and reliability of it is high.

In induction motor drive, the development and advancement are more focused on the speed control mechanism. The motor speed is controlled to perform variety of operations. Previously, variable speed drives had several problems, such as low efficiency, unstable speed control, poor dynamic characteristics, and so on. These issues are gradually being resolved by the advancement of power electronics [2].

Power electronics and electrical drives controlled through power electronic are seeing tremendous growth. As power electronic and electrical drives are used as actuators or energy converters in larger engineering systems, their use often necessitates careful engineering. To achieve the desired characteristics of the power electronic and electrical drive systems, as well as the overall application, control systems are required. The diversity of applications is reflected in the vast number of control techniques available [3].

To achieve high dynamic response in any critical application, where user wants to drive the motor strictly following the desired speed-time characteristics, we need a control algorithm that store the speed-time relation (specified by the user) which is strictly followed by the induction motor. Also, Induction motors have inherent non-linear coupling because flux and torques both change on varying voltage and on changing current speed and flux both changes. It means that torque and flux are not decoupled due to which we get a sluggish response if we directly feed the response in control circuit. So, we use different algorithms to decouple flux and torque which results in faster dynamic response.

Earlier, v/f control (Scalar Control) was employed for conventional applications due to its simplicity; however, for high dynamic response and torque retention in the low-speed area, vector control is chosen.

FOC operation is based on managing flux and torque independently through adjusting the Park components of the input current. DTC is based on the principle of directly controlling the induction motor's stator flux and torque by applying the proper stator voltage space vector [4]. FOC method is a bit complex as compared to the DTC method as it includes various transformations. It depends on physical parameters, since these parameters are continuously changing on operation from no load to full load, we cannot specify parameters to the control logic thus accuracy is suffered so we need to continuously update the parameter during operation which

makes the system more complex. For this reason, we go for DTC method, as in DTC performance does not depend on the parameters.

In this paper, comparison between different algorithms is done which are used for speed control of induction motors and then conclude which is better for the different applications.

2 Basic Principle of Speed Control

An induction motor's revolving magnetic field rotates at a synchronous speed determined solely by its supply frequency and the magnetic poles. Synchronous speed is the theoretical speed of a motor when there is no friction in the bearings and no load on the shaft. [2]. The synchronous speed is given numerically by the relationship described in Eq. 1:

$$N_s = \frac{120f}{p} \tag{1}$$

where,
p = Number of poles.
f = Frequency in Hz.

Now the rotor is trying to rotate at synchronous speed but slips back by a factor called slip due to which the motor always rotates at a speed lower than synchronous speed [5]. The slip of induction motor is defined as, percentage difference between synchronous speed and shaft speed:

$$s = \frac{N_S - N_R}{N_S} \tag{2}$$

where,
N_r = Rotor speed.
N_s = Synchronous speed.

We may deduce from Eq. (1) that synchronous speed is inversely proportional to number of magnetic poles and directly proportional to supply frequency. Since most of the application use squirrel cage induction motor, once the machine is manufactured the number of poles become fixed hence the speed can only be controlled by varying the frequency only [6].

3 Speed Control Methodologies

Different Speed control techniques are broadly classified as scalar control, field oriented and direct torque control.

3.1 Scalar Control (V/F Control)

Using scalar control method, we can change the value of frequency or voltage of the Induction motor in order to keep motor torque closer to specified torque at given frequency while maintaining the constant air gap flux (φ). If there is a drop in supply frequency without a change in supply voltage, it will increase air gap flux and motor will be saturated. This raises the magnetizing current and increases core and copper losses, causing the system to overheat and have excess vibration. To avoid these issues, we adjust the supply voltage and frequency of supply simultaneously [7].

The scalar control method involves adjusting the supply voltage and frequency while maintaining the ratio (Voltage to frequency) constant. The motor will not run at very low supply voltages, although the ratio will be the same at low voltages and frequencies.

The voltage of induction motor is related to speed and flux:

$$V = kf\varphi \tag{3}$$

where:
f = frequency.
φ = air gap flux.
k = constant.

From Eq. (1), we can say that frequency is proportional to the speed hence from Eq. (3) we concluded that supply voltage is 'proportional to both frequency and stator flux. So the flux and torque can be maintained fixed for all speeds by altering the voltage and frequency by the same ratio. As a result, the constant v/f method is the most commonly used induction motor speed control method. [7]. Scalar control ignores the coupling effect in machine, and have somewhat inferior performance than vector control technique but scalar control is simple to execute, gives good running & transient performance therefore it is favored when accuracy is not a concern (Fig. 1).

Using closed loop system with a controller can ensure better speed control. Proportional integral controller is generally used for its simpler model but then requires a detailed mathematical modeling of system. Fuzzy logic controller can also be used in which human expertise is required. So, using a better controller can breach the simplicity of scalar system. In [8], a method was presented that does not require human expertise or mathematical modeling, but rather relies on a linear relationship between the load torque and the slip speed of the induction motor at constant stator-flux linkage produced under rated conditions.

3.2 Field Oriented Control

Major shortcoming of scalar control is that flux and torque are not decoupled which creates a sluggish response leads to system instability. If torque is increase by varying

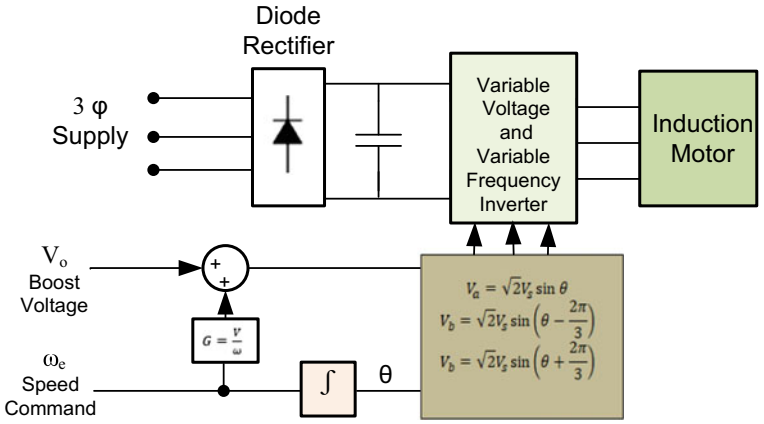

Fig. 1 Schematic diagram of open loop scalar method

the supply frequency, the flux will decreases in transient condition. Additional voltage is fed along with supply to compensate this decrease in flux. This delay affects the dynamic response.

In comparison with scalar method, the Field oriented control method has a better range of speed and good dynamic response. The Vector control method controls the flux and torque independently similar to that in separately excited DC motor. In FOC method we make ac motor analogous to separately excited DC motor. Also in DC motor, operating magnetic flux is controlled with the help of excitation current separately, whereas armature current controls the torque of motor independently. So, the two currents are magnetically as well as electrically decoupled. Unlike DC motor, the torque and magnetic field both are affected by armature current of the stator in AC motor. In a rotor reference rotating frame, flux and torque are decoupled by converting the instantaneous current into two orthogonal components: the current associated with torque development and the field current [9].

This problem is rectified by opting the vector control method in which control is done by the transformation of a rotating three phase system into a rotating two coordinate system using Parks and Clarks transformation. These projections and transformations results in a structure resembling DC motor control. In DC machine two fluxes, field and armature, are orthogonal or decoupled with respect to one another i.e., when torque is controlled by armature flux, field flux is not affected. During transient conditions to achieve better performance, a direct vector control technique is being used in which decoupling between flux and torque is ensured resulting in advancement of the dynamic performance of AC motor drive [10]. Various advantages of the FOC method are:

- Torque control at lower speed and lower frequencies.
- Improved torque response.

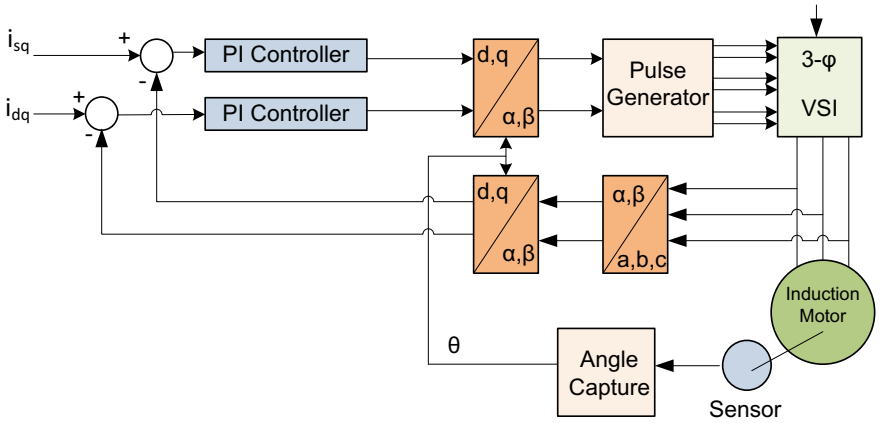

Fig. 2 Schematic diagram of FOC method

- Dynamic speed accuracy.
- Short term overloading capability.
- Decrease motor size, cost and power consumption.

This configuration is bit complex as there is a need to continuously transform the coordinate of stationary frame to rotating frame and vice versa and PI regulators. The process of flux measurement also increases equipment costs but still we do not get the desired result. Due to its complexity and less accuracy, we need a better algorithm so we go for Direct Torque Control method for speed control (Fig. 2).

In [11] suggested an adaptive mechanism-based technique for predicting induction motor speed. The state observer provides the poles arbitrarily, even in low-speed regions used in indirect FOC. The cons of this technique are: it is difficult to use precise parameters, as the resistance of the rotor and stator changes as the temperature of the motor. Speed and flux were observed close to the references. It contains overshoots during transition response. In conventional v/f, at high speeds the motor experience frictional torque which shifts as per the conditions of load and bearing state. As a result the motor sometimes fails to start so the method was proposed and used successfully implemented based on the current controlled v/f control system, with switch mode, start mode and normal v/f control mode. Starting mode cope with starting problems and transition mode assures smooth voltage transition to get a smooth current profile [12]. Also it was experimentally proved in [12] that this technique do not produce any peak current at starting and goes well at high speed with air bearings.

Induction motor has a non-linear characteristic which makes it difficult to control. A method was proposed to get suitable control using PID control which was based on Indirect Field Oriented Control. Using this method, one can get an improved output response with faster dynamic response [13]. In [14], According to the simulation results, for operating at a reference speed of 700 rpm, it takes 0.18s to reach reference

speed and to reach steady state speed it takes 0.95s. Then, for 800 rpm it takes 0.19s to reach the reference speed and 0.88s for steady state speed. For 900 rpm it takes 0.2s to reach reference speed and 1s for steady state speed. This strategy gives a good system response while requiring less time to attain the reference speed and steady state speed conditions. In [15] it was shown that the Indirect Field Oriented Control model with fuzzy-PID gives better dynamic performance as compared with induction motor without control. The controller gives good dynamic performance, less starting time and less overshoot.

3.3 Direct Torque Control (DTC)

In FOC, three phase stator currents are transformed into two orthogonal components but it is highly sensitive to stator flux which makes it dependent on machine parameters. To achieve the expected performance, it is necessary to continuously track the variation in parameters accurately, as it changes from no load to full load. This results in making the FOC a bit complex and cumbersome method. So, the new method is developed called Direct torque Method. Its main advantage is that in DTC, there is no need to convert the stationary frame coordinates to the rotating frame coordinates, voltage modulator block is absent and torque response time is minimum [16]. This makes the method simpler, highly dynamic and robust.

The DTC controller contains two hysteresis band controls to decide the switching voltage vector to establish torque and flux between the lower and upper extremities. A suitable estimator is used to compare torque and stator flux. The DTC system requires torque and stator flux measurements for the hysteresis comparator, as well as measurement of rotor speed for controlling speed of motor. The torque and flux magnitude references are obtained using a space vector modulator. Then hysteresis controller generates the necessary flux and torque change, following which the switching table selects requisite state of the inverter to generate a voltage vector that will vary the torque and flux as needed [6] (Fig. 3).

Conventional DTC method suffers few disadvantages like high flux and torque ripples, slower speed response during lower speed, accurate estimation of torque and flux command and variable switching frequency. Over the recent years, many solutions are proposed to overcome these problems, most suitable of which is multilevel inverters but it has the issue of high switching losses. Another method involves replacement of hysteresis band with constant switching controllers.

Adaptive PI controller is proposed to reduce the shortcomings of common PID controllers such as over-shooting, gain constants and slow response. Advances in area of Artificial intelligence leads to advancement of controller based on fuzzy logic concepts that are consistent, simple and that do not require a detailed mathematical modeling of system. Design of the fuzzy logic controller is done through trial and error approach. From various studies it was noted that fuzzy logic controller offers better performance than standard controls. Conventional DTC also improved by discrete space vector modulation technique but they require accurate design of flux

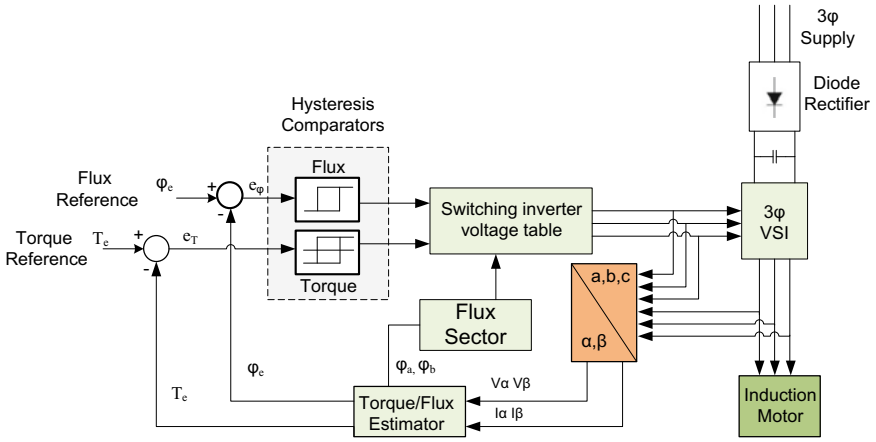

Fig. 3 Schematic diagram of DTC

and torque loop of PI controller. It results in much better transient response but not much improvement in flux and torque ripples under steady state [17]. Reduced computational time, less errors and fast learning, are the benefits that makes fuzzy logic controller a better option.

In [18–20], an artificial neural network is used to control the reference torque of an induction motor drive. It suggests that superior torque characteristics and a speed controller can be developed using an Adaline neural network. For stator current, it also compares the performance of PI controllers in conventional DTC and neural network controllers. From which it can be observed that although the dynamic response is faster, ripples also increased, due to which we do not get smoother operation.

3.4 New Intelligent Methods

The traditional PI controllers could be replaced by Fuzzy Logic Controller in Conventional DTC, as this technique gives a good dynamic response with much simpler design. Also, it is free from the high flux and torque ripple that was created due to PI controller. The Fuzzy Logic Controller ensures precise speed tracking while also increasing resilience against disturbance and ambiguity [21, 22]. In [23] it was shown that by using fuzzy logic, transient response can be improved greatly maintaining advantages of conventional DTC characteristics including low complexity, good dynamic response, and great robustness. Another algorithm is proposed in [24], in which not only speed is controlled but also reactive power is controlled in both motoring and field weakening mode using fuzzy logic. Fuzzy logic can also be used to generate the PID coefficients under most of the condition as conventional PID is unable to change its parameter according to new conditions. Also it was seen in [25]

that, Fractional PID is able to control the speed faster and more robustly and also it reached the steady state rapidly when compared to conventional or fuzzy PID.

Another disadvantage of conventional DTC is that the voltage source inverter has variable switching frequency which results in making its filtration process bit difficult, in turn leads to a higher level of interference [26]. As a result, in [27], a possible solution to this problem is proposed by adding a pulse width modulator into the induction motor drive's control structure. DTC ensures that the voltage source inverter's switching frequency remains consistent. However, the disadvantages of this technology include an increase in stator currents during the excitation phase of an induction motor. This control method ensures that torque ripple is reduced without generating any complacency. Another method to improve this issue is synchronised pulse width modulation (Syn-PWM) which is a successful solution for lowering current harmonics while also lowering torque ripples by retaining voltage pulse symmetry [28]. In this method, the period of control is adjusted online to fastly respond to a step load.

Another technique introduced to replace PI controller is Adaptive sliding mode controller for the outer speed loop. The space vector modulation method is used to maintain the constant switching frequency of the inverter. Also, taking into account the unknown load torque during the operation of the induction motor, a torque observer is proposed. The result was verified in [29] that the designed control scheme significantly reduces flux and torque ripple, along with strong robustness. One can enhance the performance of drive using sliding mode adaptive fuzzy controllers. Using adaptive fuzzy sliding mode, one may get fast reaction and good disturbance rejection. The superiority of adaptive fuzzy sliding mode controller over PI is demonstrated in [30], and it was clearly deduced that using adaptive fuzzy sliding mode controller, improved dynamic response along with minimal ripples in torque and minimum harmonics in stator current is achieved during transient conditions as compared to PI controller.

A new method of measuring motor speed on the basis of Model Reference Adaptive System was recently proposed. To measure motor speed the proposed method uses the motor impedance angle at input side of the reference. Reference angle is calculated by finding the angle difference between terminal current vector and voltage terminal vector using the Double Phase Locked Loop and variable angle is calculated instantly using the equivalent circuit of motor of each phase. This scheme naturally decouples reference and dynamic models; this has led to the acquisition of high performance at high speeds and low speeds. The ease of use of references and the adaptive schemes make it easy to analyze and implement the design. The concept of speed measurement presented is validated under a variety of operating conditions [31, 32]. The stability of the speed observer is studied, and the parameters of the PI controller are then determined based on the stability constraints, reducing the complexities of the pole placement technique and the empirical approach while also having high portability [33]. Another approach is using fuzzy logic controller for reference speed in MRAS observer, this improves the drive characteristics and also reduces the ripples shown in [34].

Another simpler method of speed control is suggested in [35]. In this, author suggested variable frequency drive in which the input supply is fed through PWM inverter and its frequency is controlled through it. This facilitates speed control with lesser energy consumption making it cost effective method and this is successfully proved by the author through hardware results.

3.5 Sensorless Methods for Speed Control

The problems related to multilevel inverters rectify through some modifications in technique as done in [36], author proposed a modified SVPWM technique in using multilevel inverters which improves dynamic performance and switching losses created by it can be decreased by using proposed modified circuit which uses neural network as speed observer and predictive controller as speed controller. This reduces the switching state from 12 to 18 thus also decreasing power losses.

For sensor less method, the speed sensors are replaced by an estimation algorithm which depends on voltage and current values. In [37] a disturbance observer based speed estimator is used, it works successfully for lower speed range but for higher speed, it do not work thus not suggested for high speed application. In [38] another predictive control method is proposed for sensor less speed control. It continuously supplies switching signal to spontaneously make motor speed as desired speed. In [39], sliding mode observer is suggested which motor speed, flux and angular position are estimated through motor voltage and current without complicating the system. In [40] a new observer is designed by combining linear super-twisting algorithm and sliding mode observer. Then the flux compensation is added to further improve the performance. The proposed method is also suitable for high speed range.

4 Conclusion

Advancement of various speed control methods and analysis of its performance is compared. First the basic speed control system is explained than in the next section various speed control methods are compared. Finally, the comparative analysis is concluded in Tables 1 and 2. Vector control method is much more advantages than the scalar method as it is could be used for wide range of frequencies with very low switching loss and harmonics also the dynamic response of the system is very high. By intelligently selecting the speed control method, according to the application, the dynamic performance and efficiency. Recently new techniques are used for speed control but they require more research to be used for large applications.

Table 1 Comparison of speed control methods

Parameters	Scalar control method	Vector control method
Switching losses	High	Low
Harmonics	High	Low
Switching frequency	2–15 kHz	Varies widely around average frequency
Efficiency	Low due to switching losses	High
Dynamic response	Moderate	Very high

Table 2 Comparing DTC and FOC method

Parameters	DTC method	FOC method
Coordinate transformation	No	Yes
Requirement of rotor position	No	Yes
Dynamic response of torque	Faster	Slower
Switching frequency	Variable, depend upon operating point	Constant
Complexity and processing requirement	Lower	Higher
Frame of reference	stationary	Synchronous rotating
Controller	Hysteresis controller for stator flux and torque	Linear controllers for stator currents
Implementing complexity	Medium complexity as no coordinate transformation	High complexity as coordinate transformation is necessary

References

1. S. Rahman, A.A.B.Z. Abidin, A review on induction motor speed control methods, In: International Journal of Core Engineering & Management (IJCEM) (2016)
2. G. Lin, Z. Xu, Direct torque control of induction motor based on fuzzy logic, In: 2nd International Conference on Computer Engineering and Technology, Chengdu, China, V4–651-V4–654 (2010)
3. T.Y. Abdalla, H.A. Hairik, A.M. Dakhil, Direct torque control system for a three phase induction motor with fuzzy logic based speed controller, In: 1st International Conference on Energy, Power and Control (EPC-IQ), Basrah, Iraq, pp. 131–138 (2010)
4. Z.A. Alnasir, A.H. Almarhoon, Design of direct torque controller of induction motor (DTC), In: International Journal of Engineering and Technology (IJET), pp.54–70 (2012)
5. A.Z. Latt, N.N. Win, Variable speed drive of single phase induction motor using frequency control method, In: International Conference on Education Technology and Computer, Singapore, pp. 30–34 (2017)
6. B.K. Bose, *Modern power electronics and ac drives* (Prentice Hall, Book, 2002)
7. P.S. Dorale, M. Zubair, K.K. Rajput, V.A. Ghodeswar, A.S. Kakad, Speed control of induction motor by using v/f control method in matlab simulink, In: National Conference on Innovative Trends in Science and Engineering, Vol. 4, No. 7, pp. 29–31 (2016)
8. A. Shaltout, O.E.M. Youssef, Speed control of induction motors using proposed closed loop Volts/hertz control scheme, In: Nineteenth International Middle East Power Systems Conference (MEPCON), Cairo, Egypt, pp. 533–537 (2017)

9. S. Manias, Power electronics and motor drive systems, In: Academic Press (2016)
10. A. Kumar, T. Ramesh, Direct field oriented control of induction motor drive, In: Second International Conference on Advances in Computing and Communication Engineering, Dehradun, India, pp. 219–223 (2015)
11. V.T. Ha, N.V. Thang, D.A. Tuan, P.T. Hanh, Sensorless speed control of a three-phase induction motor: An experiment approach, In: International Conference on System Science and Engineering (ICSSE), Ho Chi Minh City, Vietnam, pp. 694–698 (2017)
12. J.W. Lee, Novel current control assisted V/F control method for high speed induction motor drives, 10th International Conference on Power Electronics and ECCE Asia (ICPE 2019-ECCE Asia), Busan, Korea (South), pp. 1293–1296 (2019)
13. A.N. Mohammed, G.A.-R. Ghoneim, Fuzzy-PID speed controller model-based indirect field oriented control for induction motor, In: International Conference on Computer, Control, Electrical, and Electronics Engineering (ICCCEEE), pp. 1–6 (2021)
14. Ferdiansyah, L.P.S. Raharja, D.S. Yanaratri and E. Purwanto, Design of PID controllers for speed control of three phase induction motor based on direct-axis current (Id) coordinate using IFOC, In: 4th International Conference on Information Technology, Information Systems and Electrical Engineering (ICITISEE), Yogyakarta, Indonesia, pp. 369–372 (2019)
15. A.N. Mohammed, G.A.-R. Ghoneim, Fuzzy-PID speed controller model-based indirect field oriented control for induction motor, In: International Conference on Computer, Control, Electrical, and Electronics Engineering (ICCCEEE), Khartoum, Sudan, pp. 1–6 (2021)
16. Wahab, H.F. Abdul, H. Sanusi, Simulink model of direct torque control of induction machine, In: American Journal of Applied Sciences, pp. 1083–90 (2008)
17. S.V.K. Arun, U. Subramaniam, S. Padmanaban, M.S. Bhaskar, D. Almakhles, Investigation for performances comparison PI, adaptive PI, fuzzy speed control induction motor for centrifugal pumping application, In: IEEE 13th International Conference on Compatibility, Power Electronics and Power Engineering (CPE-POWERENG), Sonderborg, Denmark, pp. 1–6 (2019)
18. K. Sundararaju, R.S. Kumar, I.G.C. Raj, Modeling and simulation of neural based speed controller for direct torque control of three phase induction motor, In: TENCON IEEE Region 10 Conference, Penang, Malaysia, pp. 1439–1444 (2017)
19. A.H. Kumar, R. Ramchand, Analysis on the extend of application of artificial neural networks in direct torque control-space vector modulated drives, In: IEEE International Conference on Power Electronics, Smart Grid and Renewable Energy (PESGRE2020), Cochin, India, pp. 1–5 (2020)
20. M.I. Mosaad, F.A. Banakher, Direct torque control of synchronous motors using artificial neural network, In: IEEE International Conference on Electro Information Technology (EIT), Brookings, SD, USA, pp. 1–6 (2019)
21. V.R. Metha, S.S. Karvekar, Speed control of induction motor using a fuzzy logic controller and direct torque controller, In: 4th International Conference for Convergence in Technology (I2CT), Mangalore, India, pp. 1–5 (2018)
22. H.B. Noura Rezika, Fuzzy logic based topological approach for monitoring speed reversal in induction motor, In: International Conference on Electrical, Computer and Energy Technologies (ICECET), pp. 1–6 (2021)
23. J. Dhanaselvam, A.B. Singh, S. Deebika, S. Surendar, Controlling of torque and flux for 3φ induction machine drive system (IMDS) using fuzzy controller (theory and introductory concepts), In: IEEE International Conference on Power, Control, Signals and Instrumentation Engineering (ICPCSI), Chennai, India, pp. 929–933 (2018)
24. H. Mohan, M.K. Pathak, S.K. Dwivedi, Reactive power based speed control of induction motor drive using fuzzy logic for industrial applications, In: IEEE International Conference on Power Electronics, Smart Grid and Renewable Energy (PESGRE2020), Cochin, India, pp. 1–5 (2020)
25. M. Vahedpour, A.R. Noei, H.A. Kholerdi, Comparison between performance of conventional, fuzzy and fractional order PID controllers in practical speed control of induction motor, In: 2nd International Conference on Knowledge-Based Engineering and Innovation (KBEI), Tehran, Iran, pp. 912–916 (2015)

26. P. Brandstetter, M. Kuchar, H.H. Vo, C.S. Thien Dong, Induction motor drive with PWM direct torque control, 18th International Scientific Conference on Electric Power Engineering (EPE), Kouty nad Desnou, Czech Republic, pp. 1–5 (2017)
27. Gourikrishna, V.R. Bindu, PWM direct torque control of induction motor drive with reduced torque ripple, In: International CET Conference on Control, Communication, and Computing (IC4), Thiruvananthapuram, India, pp. 33–38 (2018)
28. X. Wu, W. Huang, X. Lin, S. Zhu, An initial trial to drive induction motors by synchronized SVPWM-based direct torque control, In: IEEE 9th International Power Electronics and Motion Control Conference (IPEMC2020-ECCE Asia), Nanjing, China, pp. 342–345 (2020)
29. N. Wang, H. Yu, X. Liu, DTC of induction motor based on adaptive sliding mode control, In: Chinese Control and Decision Conference (CCDC), Shenyang, China, pp. 4030–4034 (2018)
30. A. Sahu, K.B. Mohanty, R.N. Mishra, D.R. Nayak, Adaptive fuzzy sliding mode based torque and speed compensator for DTC IM Drive, In: IEEE 29th International Symposium on Industrial Electronics (ISIE), Delft, Netherlands, pp. 247–252 (2020)
31. G. Tarchała, T. Orłowska Kowalska, Equivalent-signal-based sliding mode speed MRAS-type estimator for induction motor drive stable in the regenerating mode, In: IEEE Transactions on Industrial Electronics, vol. 65, no. 9, pp. 6936–6947 (2018)
32. H.A. Hamed, Z.M. Elbarbary, M.S.E. Moursi, P.K. Chamarthi, A new δ MRAS method for motor speed estimation, In: IEEE Transactions on Power Delivery, vol. 36, no. 3, pp. 1903–1906 (2021)
33. Y. Wang, X. Deng, C. Wu, A new method for PI parameter adjustment of induction motor based on MRAS, In: IEEE 4th Advanced Information Technology, Electronic and Automation Control Conference (IAEAC), Chengdu, China, pp. 500–504 (2019)
34. M.F. Elmorshedy, W. Xu, M.M. Ali, Y. Liu, S.M. Allam, High performance speed sensorless finite-set predictive thrust control of a linear induction motor based on MRAS and fuzzy logic controller, In: IEEE 9th International Power Electronics and Motion Control Conference (IPEMC2020-ECCE Asia), pp. 3039–3044 (2020)
35. P.V. Patil, S.A. Naveed, Implementation of VFD application for speed control of induction motor, In: International Conference on Smart Innovations in Design, Environment, Management, Planning and Computing (ICSIDEMPC), Aurangabad, India, pp. 168–170 (2020)
36. S. Hussain, M.A. Bazaz, Modified SVPWM technique for a sensorless controlled induction motor drive using neural network observer and predictive controlle, In: International Journal of Advanced Intelligence Paradigms,16(2), pp. 172–89, 202
37. K. Indriawati, B.L. Widjiantoro, N.R. Rachman, Disturbance observer-based speed estimator for controlling speed sensorless induction motor, In: 3rd International Seminar on Research of Information Technology and Intelligent Systems (ISRITI), Yogyakarta, Indonesia, pp. 301–305 (2020)
38. A. Wakodikar, M.V. Aware, Speed sensorless finite set model predictive speed control of induction motor, In: IEEE First International Conference on Smart Technologies for Power, Energy and Control (STPEC), Nagpur, India, pp. 1–6 (2020)
39. L. Zhang, Z. Dong, L. Zhao, S. Laghrouche, Sliding mode observer for speed sensorless linear induction motor drives, In: IEEE Access, vol. 9, pp. 51202–51213 (2021)
40. S. Mao, H. Tao, Z. Zheng, Sensorless control of induction motors based on fractional-order linear super-twisting sliding mode observer with flux linkage compensation, In: in IEEE Access, vol. 8, pp. 172308–172317 (2020)

Design of Novel Complex Fractional Order Controller Using Genetic Algorithm for Fractional Order System

Omar Hanif, R. Ranganayakulu, G. Uday Bhaskar Babu, and Sumanta Kundu

Abstract In this paper, a Novel Complex Fractional Order Proportional Integral Derivative (CFOPID) controller structure is developed of the form $PI^{x+iy}D^{a+ib}$ for fractional order systems. This novel type of controller has more (seven) parameters to tune than the conventional PID and fractional order PID controllers, resulting in a higher degree of control freedom. However, the complexity of CFOPID is due to many tuning parameters, making design and tuning cumbersome. Therefore, this work uses a Genetic algorithm optimization technique with cost function as Integral Absolute Error (IAE). The performance of the proposed CFOPID controller is compared to that of PID and fractional order PID controllers, and then validated on an identified real heat exchanger system. In terms of performance measures such as rise time, settling time, and IAE, the results reveal that the CFOPID controller outperforms integer and fractional order PID controllers for set point and disturbance rejection. Also, the stability is investigated through frequency response using Bode plot.

Keywords Complex fractional order proportional integral derivative · Fractional order proportional integral derivative · Fractional order system · Genetic algorithm · Relative stability

O. Hanif
The University of Sheffield, Western Bank, Sheffield, UK
e-mail: ohanif1@sheffield.ac.uk

R. Ranganayakulu · G. U. B. Babu (✉) · S. Kundu
National Institute of Technology Warangal, Telangana 506004, India
e-mail: udaybhaskar@nitw.ac.in

R. Ranganayakulu
e-mail: rayalla.ranga@student.nitw.ac.in

S. Kundu
e-mail: skch20211@student.nitw.ac.in

J. Kumar et al. (eds.), *Control Applications in Modern Power Systems*, Lecture Notes in Electrical Engineering 974, https://doi.org/10.1007/978-981-19-7788-6_6

1 Introduction

The prominent tuning of controllers was introduced by Zeigler and Nicholas based upon the ultimate period cycle, which is still being implemented today where primitive control strategy is needed [1]. The Proportional integral derivative (PID) controller is the most used for industrial and commercial purposes but this controller suffers inaccuracy. This is because it is an integer-order type controller which signifies limited degrees of freedom and restricted controller actions.

The advancement of computational sciences led to the application of fractional-order calculus [2, 3], which structured a new controller called Fractional order PID (FOPID) controller [4] of the form $PI^{\lambda}D^{\mu}$, a PID variant controller. Podlubny et al. devised a technique for Fractional-order controller structure formulation [5]. A novel approach was suggested to tune FOPID controller fulfilling gain and phase margins criterion [6]. However, FOPID controllers still lag the performance quality when compared with the novel variant of PID controller, i.e., Complex fractional-order controller. A complex controller was designed to ensure dynamic performance using complex fractional integrator [7]. The Commande Robuste d'Ordre Non-Entier (CRONE) innovated a complex structure and added another level in the PID controller hierarchy. The frequency representation of the transfer function based on complex-order is given by Eq. (1):

$$\epsilon = C_0\left(\text{Real}\left[\left(\frac{\omega_{cg}}{s}\right)^{a+ib}\right]\right)^{-\text{sign(a)}} \tag{1}$$

where Laplace frequency is represented by 's', gain crossover frequency is denoted by 'ω_{cg}', 'C_0' is the unity gain at 'ω_{cg}'. The term 'Real' acts as the real operator for (1), 'a' and 'b' stand for real and imaginary parts respectively of the complex fractional order given in (1). The first novel complex fractional order controller was devised in the form 'PI^{x+iy}' [8]. The noise attenuating capability of the former complex fractional-order controller is enhanced by adding the derivative controller making the structure '$PI^{x+iy}D$' also known as Complex fractional order PID (CFOPID) controller [9]. There was limited advancement in the tuning CFOPID controller for integer order systems [10, 11] but not for fractional order systems. The CFOPID controller has more tuning parameters than the classical PID and FOPID, subsequently attaining a better output of the closed-loop controlled system (faster response, accuracy, and sensitivity). However, due to the excessive number of parameters that need to be adjusted and the increased computational complexity, CFOPID [12] tuning is not easy. Once properly tuned, it can control most systems better than PID and its variants. Genetic Algorithm (GA) is an evolutionary optimization algorithm that runs on probabilistic transition rules. It takes into account the population of likely known chromosomes and generates new values. The cost function to be optimized can be error performance specifications. After the simulation is completed, mutation, crossover, and reproduction begin until the best solution is obtained [13, 14]. The GA proves to be useful than the other classical tuning algorithms [16] owing to its,

ability to find the local optimization faster than the classical tuning methods, i.e., convergence rate is fast. Subsequently, the large number of controllers' parameters makes the classical tuning algorithm quite a complex task to tune the controllers' parameters. Therefore, by using the GA optimization algorithm to obtain the tuning parameters of the new driver, the mathematical complexity is reduced.

In this article, a new CFOPID controller structure in the form of $PI^{x+iy}D^{a+ib}$ is proposed to improve the performance of fractional order systems. To overcome the complexity of tuning, GA optimization technique is used with cost function as the Integral absolute error (IAE). In addition, it compares with traditional PID and FOPID responses (servo and regulation) by simulating different fractional order systems. To the best of authors' knowledge, it is the first time to introduce the design of the CFOPID controller using GA for fractional order systems.

2 Preliminaries

2.1 Fractional Order Systems

The fractional order systems are characterized by fractional order differential equations. A typical fractional-order differential Eq. (2) with input u(n) is:

$$\propto_n D_t^{\beta_n} y(n) + \ldots\ldots\ldots\ldots\ldots \propto_1 D_t^{\beta_1} y(n) + \propto_0 D_t^{\beta_0} y(n) = u(n) \tag{2}$$

where 'n' is the representation of continuous-time, y is the output and D_t^i is the differential operator. On taking Laplace Transform the following transfer function (3) is obtained:

$$\frac{Y(s)}{U(s)} = \frac{1}{\propto_0 s^{\beta_0} + \propto_1 s^{\beta_1} + .. + \propto_n s^{\beta_n}} \tag{3}$$

2.2 Controllers

The PID and FOPID controllers used in the present work are defined in (4) and (5):

$$\text{PID: } k_p + \frac{k_i}{s} + k_d s \tag{4}$$

$$\text{FOPID: } k_p + \frac{k_i}{s^{\lambda}} + k_d s^{\mu} \tag{5}$$

k_p, k_i and k_d are the proportional, integral and derivative gains respectively; λ and μ are the fractional orders of the integrator and differentiator.

The structure of the CFOPID controller denoted as $PI^{(complex)}D^{(complex)}$ is given in (6)

$$\text{CFOPID} : \mathrm{K_p} + \mathrm{K_i}\left(\mathrm{Real}_{/i}\left[\frac{1}{s^{f+ig}}\right]\right) + \mathrm{K_d}\left(\mathrm{Real}_{/i}\left[s^{q+ir}\right]\right) \tag{6}$$

where, $\mathrm{Real}_{/i}$ denotes the real component of the expression

3 Proposed Control Approach

The proposed method uses feedback structure intended to minimize the error. The proposed controller i.e., CFOPID and the PID/FOPID [15] controllers are tuned through the GA optimization technique for fair comparison. In this work, the error performance function namely IAE is employed as the cost function. The proposed control algorithm is presented in Fig. 1 and Table 1 shows the GA properties used while tuning the system.

4 Results and Discussion

The proposed approach is verified by a fractional order system and validated experimentally through heat exchanger.

4.1 Example 1

Consider a fractional order system given by (7). The ranges of the parameter of PID/FOPID/CFOPID controller gains for example 1 are given in the Table 2.

$$\mathrm{G(s)} = \frac{1}{39.86s^{1.25}+0.598} \tag{7}$$

The controllers tuned using GA are given in (8) (9) and (10).

$$\text{PID: } 19.331+\frac{1.003}{s}+39.231s \tag{8}$$

$$\text{FOPID: } 19.563+\frac{11.899}{s^{0.103}}+38.731s^{0.4365} \tag{9}$$

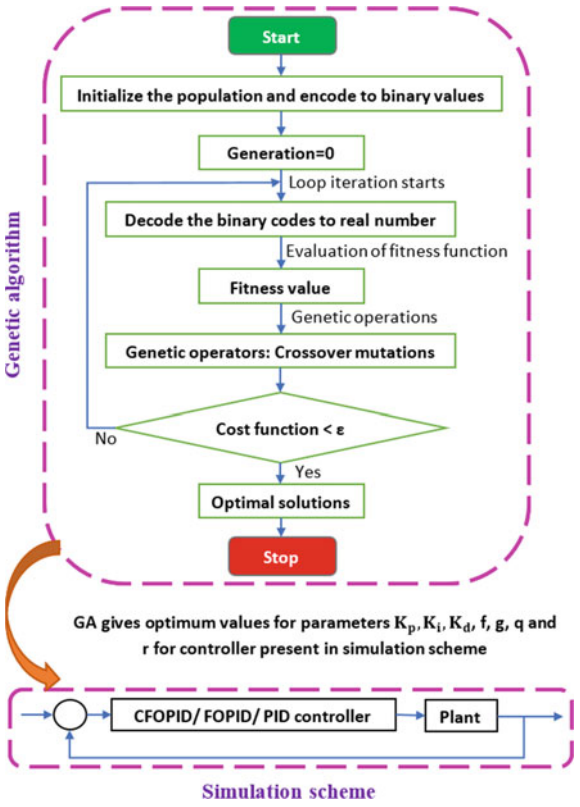

Fig. 1 GA optimized controlled system

Table 1 GA properties used in tuning the parameters

Parameter	Types/value
Maximum generation	100
Population size	100
Encoding	Binary
Selection	Uniform
Crossover fraction	0.65
Mutation fraction	0.35

Table 2 Controller tuning parameter ranges

Controller	Parameter	K_p	K_i	K_d	Re	Im	Re	Im
PID	Minimum	1	1	1	–	–	–	–
	Maximum	20	20	40	–	–	–	–
FOPID	Minimum	1	1	1	0.1	–	0.1	–
	Maximum	20	20	40	2	–	2	–
CFOPID	Minimum	1	1	1	0.1	0.1	0.1	0.1
	Maximum	20	20	40	2	2	2	2

$$\text{CFOPID: } 19.981 + 18.099\left(\text{Re}/_{\text{i}}\left[\frac{1}{s^{0.6213 + i0.4633}}\right]\right) + 34.655s^{0.3744 + i0.8065} \quad (10)$$

The servo response for unit step signal is shown in Fig. 2 and the performance specifications are recorded in Table 3. The regulatory response for a disturbance applied at t = 2 s is in Fig. 3 and the respective metrics are in Table 3. It is evident from Table 3 that CFOPID has a fastest rise time although FOPID shows better settling, tacking and disturbance rejection capability than PID and CFOPID controlled plant.

It is evident from Bode plot in Fig. 4 that although all the controllers have infinite GM but the PID controller is having better PM than other fractional/complex

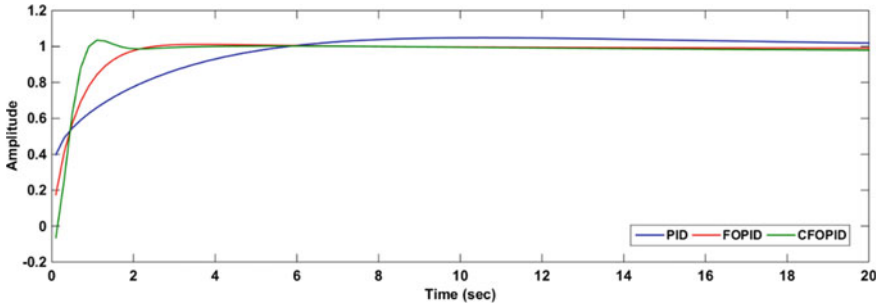

Fig. 2 Comparison of servo response for fractional order system

Table 3 Comparison of controllers based on servo and regulatory response

Controllers	Servo response			Regulatory response		
	t_r	t_s	IAE	t_r	t_s	IAE
PID	4.03	21.45	1.64	0.070	24.8	0.85
FOPID	1.23	5.76	0.73	0.006	7.7	0.41
CFOPID	0.51	12.37	0.78	0.003	15.5	0.49

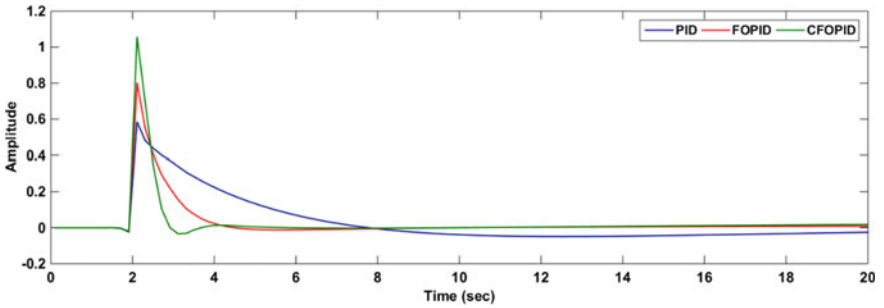

Fig. 3 Comparison of disturbance rejection for fractional order system

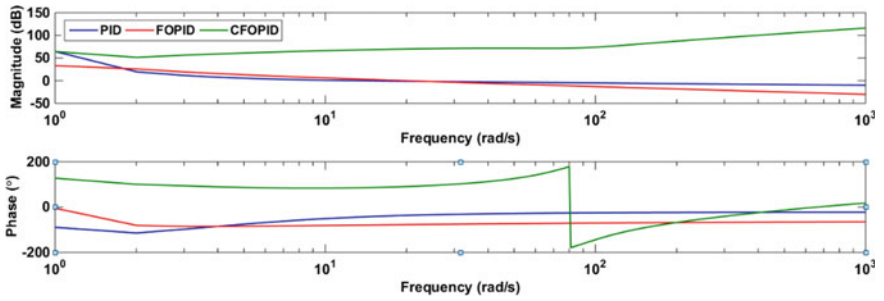

Fig. 4 Bode plot of fractional order system

fractional controllers, therefore, it is relatively more stable. Hence for fractional order transfer function, it can be stated that the FOPID controlled plant has better servo response and regulatory responses in terms of IAE. In general, fractional order controllers (any of the FOPID or CFOPID) are better than the integer order controller (PID).

4.2 Example 2

A real time heat exchanger system [17] is considered for validation. The input percentage valve opening (manipulated variable U) with the temperature maintained in the exchanger (controlled variable Y) is recorded in Table 4 with as many as 1423 readings taken. Using input–output data the heat exchanger model is identified as a fractional order system. The fractional order transfer function (FOTF) is identified by FOMCON toolbox in MATLAB. The identified FOTF is denoted by T_{FO} and is given in (11). The GA is acted upon the FOTF model to tune the controller parameters. The boundaries of search for the parameters of three controller gains are given in Table 5.

$$T_{FO}(s) = \frac{30.761 \times s^{0.008209}}{74.739 \times s^{1.1689} + 653.13 \times s^{1.0004} + 1.2526} e^{-9.5 \times 10^{-3} s} \tag{11}$$

Table 4 Input–output raw data

S. no	Y (temp. in °C)	U (% of valve opening)
1	32.496	71.385
2	32.497	71.583
3	32.501	70.978
1423	……	……

Table 5 Controllers' parameter ranges

Controller	Parameter	K_p	K_i	K_d	Re	Im	Re	Im
PID	Minimum	0	0	0	–	–	–	–
	Maximum	50	50	70	–	–	–	–
FOPID	Minimum	0	0	0	0.1	–	0.1	–
	Maximum	50	50	70	2	–	2	–
CFOPID	Minimum	0	0	0	0.1	0.1	0.1	0.1
	Maximum	50	50	70	2	2	2	2

The tuned controllers are given by (12) (13) and (14)

$$\text{PID: } 49.789 + \frac{49.889}{s} + 0.007s \tag{12}$$

$$\text{FOPID: } 49.998 + \frac{49.712}{s^{0.0579}} + 23.861s^{0.2267} \tag{13}$$

$$\text{CFOPID: } 49.519 + 49.997\left(\text{Re}/_{\text{i}}\left[\frac{1}{s^{0.326 + \text{i}0.1822}}\right]\right) + 69.864s^{0.0769 + \text{i}0.4189} \tag{14}$$

Set point tracking of the FO system for a step input is shown in Fig. 5. Similarly, disturbance rejecting ability of the controller for a perturbation of 0.5 amplitude at a delay of 1 s is shown in Fig. 6. The observations are tabulated in Table 6. The servo and the regulatory responses in Figs. 5 and 6 show that CFOPID has the fastest t_r, t_s and IAE followed by the FOPID controller (although in disturbance rejection case CFOPID controller shows a slower t_s than FOPID controller). A relative stability check is performed through Bode plot with the FOTF in (11) as shown in Fig. 7. It is observed that CFOPID controlled plant is having a better GM and PM than fractional order PID or the classical PID controller. Hence practically CFOPID controlled plant is relatively more stable than other PID variants.

5 Conclusion

In this work, a novel CFOPID controller is designed based on GA for fractional order systems and compared with conventional PID and FOPID controllers in terms of performance indices such as t_r, t_s and IAE. This CFOPID controller has a higher degree of control freedom with seven tuning parameters. The performance of the proposed controller is validated through two fractional order systems. The closed loop performance is compared in terms of trajectory tracking, disturbance rejection and relative stability of the system. The simulation results show that CFOPID controller is better with low IAE followed by the FOPID controller. This shows that the CFOPID

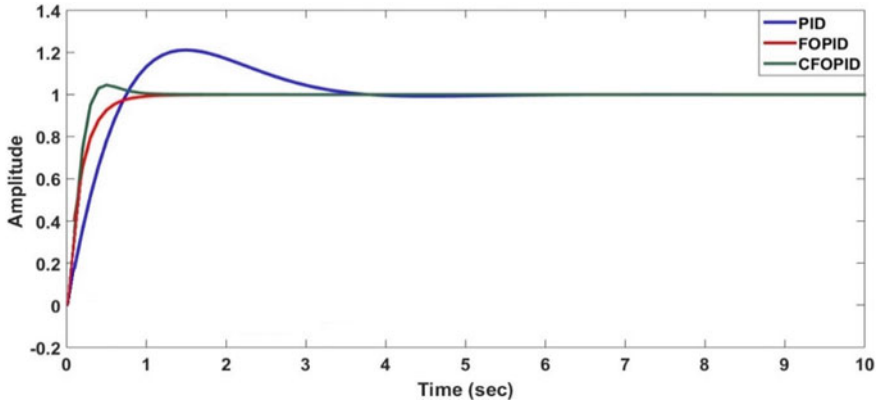

Fig. 5 Comparison of servo response for heat exchanger

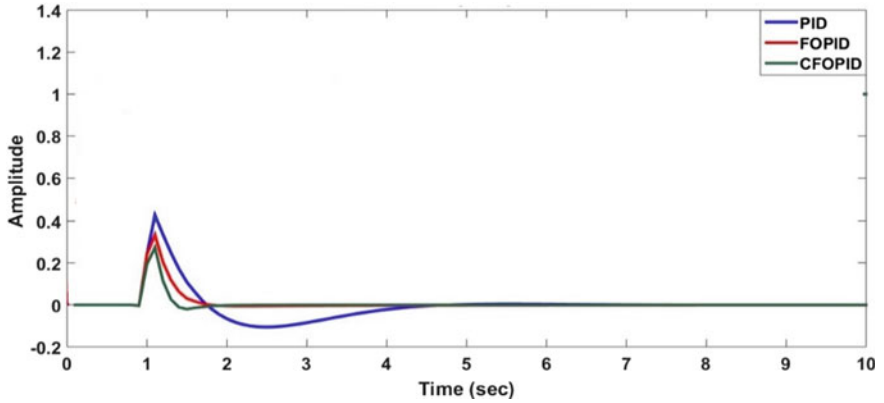

Fig. 6 Comparison of regulatory response for heat exchanger

Table 6 Performance comparison of heat exchanger

Controllers	Servo response			Regulatory response			GM	PM
	t_r	t_s	IAE	t_r	t_s	IAE		
PID	0.49	3.37	0.61	0.04	4.36	0.33	1	-1.3×10^{-5}
FOPID	0.43	0.90	0.15	0.02	1.69	0.12	0.9998	1.0384
CFOPID	0.17	0.84	0.12	4.8×10^{-5}	1.82	0.07	0.999	1.05

controller can be considered as a future replacement for conventional PID or FOPID controllers.

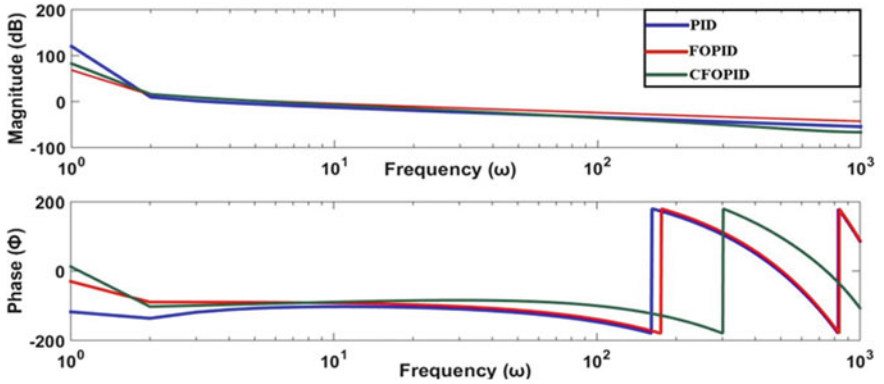

Fig. 7 Bode plot for heat exchanger

References

1. J.G. Ziegler, N.B. Nichols, Optimum settings for automatic controllers. J. Dyn. Syst. Meas. Contr. **115**(2B), 220–222 (1993)
2. K.S. Miller, B. Ross, *An Introduction to the Fractional Calculus and Fractional Differential Equations* (John Wiley & sons, New York, 1993)
3. S. Das, *Functional Fractional Calculus* (Springer, Berlin Heidelberg, 2011)
4. D. Valério, J.S. Da Costa, Introduction to single-input, single-output fractional control. IET Control Theory Appl. **5**(8), 1033–1057 (2011)
5. I. Podlubny, I. Petras, B.M. Vinagre, Y. Chen, P. O'Leary, L. Dorcak, Realization of fractional order controllers. Acta Montanistica Slovaca **8**(4), 233–235 (2003)
6. H.S. Ahn, V. Bhambhani, Y. Chen, Fractional-order integral and derivative controller design for temperature profile control, in *2008 Chinese Control and Decision Conference*, (IEEE, Yantai, China, 2008), pp. 4766–4771
7. A. Oustaloup, V. Pommier-Budinger, P. Lanusse, Design of a fractional control using performance contours. Application to an electromechanical system. Fract. Calcul. Appl. Anal. **6**(1), 1–24 (2003)
8. M. Shahiri, A. Ranjbar, M.R. Karami, R. Ghaderi, New tuning design schemes of fractional complex-order PI controller. Nonlinear Dyn. **84**(3), 1813–1835 (2016)
9. A. Guefrachi, S. Najar, M. Amairi, M. Aoun, Tuning of a $PI^{x+iy}D$ fractional complex order controller, in *2017 25th Mediterranean Conference on Control and Automation (MED)*, (IEEE, Valletta, Malta, 2017), pp. 643–648
10. O.W. Abdulwahhab, Design of a complex fractional order PID controller for a first order plus time delay system. ISA Trans. **99**, 154–158 (2020)
11. M.G. Moghadam, F. Padula, L. Ntogramatzidis, Tuning and performance assessment of complex fractional-order PI controllers. IFAC-PapersOnLine **51**(4), 757–762 (2018)
12. A. Guefrachi, S. Najar, M. Amairi, M. Aoun, Tuning of fractional complex order PID controller. IFAC-PapersOnLine **50**(1), 14563–14568 (2017)
13. A. Jayachitra, R. Vinodha, Genetic algorithm based PID controller tuning approach for continuous stirred tank reactor. Adv. Artif. Intell. 1–8 (2014)
14. B.K. Mukherjee, S. Metia: Fractional order modeling and GA based tuning for analog realization with lossy capacitors of a PID controller, in Proceedings of the International MultiConference of Engineers and Computer Scientists (IMECS), (Hong Kong, 2009), pp. 18–20

15. A. Tepljakov, E. Petlenkov, J. Belikov, FOMCOM: A MATLAB toolbox for fractional order system identification and control. Int. J. Microelectron. Comp. Sci. **2**(2), 51–62 (2011)
16. S. Katoch, S.S. Chauhan, V. Kumar, A review on genetic algorithm: past, present, and future. Multimedia Tools Appl. **80**(5), 8091–8126 (2021)
17. S. Chakraborty, S. Ghosh, A.K. Naskar, I-PD controller for integrating plus time-delay processes. IET Control Theory Appl. **11**(17), 3137–3145 (2017)

Optimal Power Management in a Grid-Connected PV System with an Efficient Controller: Firefly Algorithm

Kamaraju Vechalapu and Chintapalli V. V. S. Bhaskara Reddy

Abstract Optimal power management is achieved in a grid-connected solar system model. The system model was designed by combining an updated Series Capacitor high conversion ratio (USC-HCR) converter, a maximum PowerPoint tracker (MPPT), and an efficient controller with an effective control method, which is the Firefly algorithm (FFA). The FFA generates an accurate control signal database for optimal performance of the system. The main objective of this work is to enhance the utilization of power at the consumer end. The system outcomes are represented in terms of voltage, current, and power. The power banks, such as batteries, are connected to the system to get a constant and uninterrupted power supply to the consumer. Under ideal conditions, different cases are studied, and among them, two cases with changing solar irradiance at constant load and constant solar irradiance at variable load are presented in this work. The recommended simulation was run in MATLAB/Simulink, and the system's efficiency was analyzed by using existing technologies. The convergence characteristics of control techniques used in this model for system optimality.

Keywords Solar energy · PV system · Microgrid · SC-HCR · MPPT · FFA · BSO · PSO · PI · Equality and inequality constraints

1 Introduction

Solar energy has the potential to provide limitless electricity at a low cost. These are more powerful, reliable, and pollution-free, so they are better for the environment [1]. As a result of increasing demand on the electrical infrastructure, electricity usage has risen dramatically in recent days. Renewable energy sources are the only option to satisfy power demands. Two of the most important energy sources, for example, are photovoltaics and wind [2]. PV systems connected to microgrids are capable

K. Vechalapu (✉) · C. V. V. S. Bhaskara Reddy
Department of Electrical Engineering,
Andhra University College of Engineering (A), Andhra University, Visakhapatnam, Andhra Pradesh 530003, India
e-mail: raju.vechalapu@gmail.com

J. Kumar et al. (eds.), *Control Applications in Modern Power Systems*, Lecture Notes in Electrical Engineering 974, https://doi.org/10.1007/978-981-19-7788-6_7

of supplying enough power to meet load requirements [3]. Due to the intermittent nature of the PV system, which is due to bad weather, solar power generation is being disrupted. Matching PV power with a continuously changing load is the most challenging, along with its intermittency [4]. The peak load occurs at night, particularly in the city's industrial and residential districts. As a result, PV is commonly combined with energy storage devices such as batteries. The most important thing is to maintain power flowing to the load during times of heavy consumption, especially at night. Batteries play an important role in maintaining an uninterrupted power supply as power backup devices [5]. During off-peak hours, generally during the day, they are charged with a large amount of energy and then used to produce power during peak hours [6]. Traditional generation has become more costly, less efficient, and even unavailable in recent years. As a result, non-conventional electricity production is getting more popular [7]. The Maximum PowerPoint Tracker (MPPT) is for sending precise signals to the PWM unit in order to maintain the duty ratio of switches in the Integrated DC/DC converter so that the PV module may produce the maximum amount of power [8]. I investigated the updated SC high conversion ratio (SC-HCR) converter by its operation. In the modelling of the SC-HCR converter, the modes of operation are examined, as well as the average DC current input and voltage transfer gain [9]. The state-space averaging approach is used to simulate the converter [10]. To get optimal power, the switching loss of the converter must be reduced, which will enhance the converter's efficiency. Because the batteries are designed to store excess energy generated by the PV system [11]. The inspiration for the Firefly algorithm (FFA) comes from the natural characteristics of fireflies [12–14]. With the FFA control method, the gains of the PI controller have been fine-tuned. The configured system is coded in the MATLAB Simulink working environment, and the performance of the suggested system using the FA approach is compared to current techniques. To evaluate the effectiveness of the presented approach, many scenarios were investigated and analyzed, including irradiance fluctuation under stable load and changing load at constant irradiance. For both scenarios, the current, voltage, and power responses were investigated and compared to established techniques such as BSO [14, 15], and PSO [16].

The remainder of this project is covered in the parts that follow. The architecture of the grid-connected solar system, as well as solar power characteristics with changes in solar irradiation and temperature, are covered in the second section. Section 3 discusses the converter's modelling and operational modes. Section 4 discusses the methodology of current heuristic optimization methods. Section 5 examines the MATLAB/Simulink results. The present work concluded in Section 6.

2 The Architecture of the Grid-Connected PV System

The system architecture of the grid-connected solar system affiliated with the microgrid, the HCR Converter, and the selected controller is presented in Fig. 1. The interconnection of the grid-connected PV system, battery system, is achieved by

a novel model of HCR Converter, the designed controller by the approach of the Firefly algorithm, DC-Microgrid, and electrical loads in the system. To begin with, the photovoltaic cell uses a solar module to generate power from light energy, which is then transferred to the DC microgrid via the DC-DC Converter. The traditional MPPT device controls the converter output by altering the PWM unit's pulse widths using PV-Voltage and PV-Currents as reference values. A bi-directional DC/DC converter connects the battery system to the DC-Microgrid. With the help of a DC to AC converter, the DC-Bus is connected to the AC-Bus. If solar energy is available, the power is drawn from the solar system, and the batteries are also charged. If the sun doesn't shine, especially at night, the batteries are used to keep the lights on.

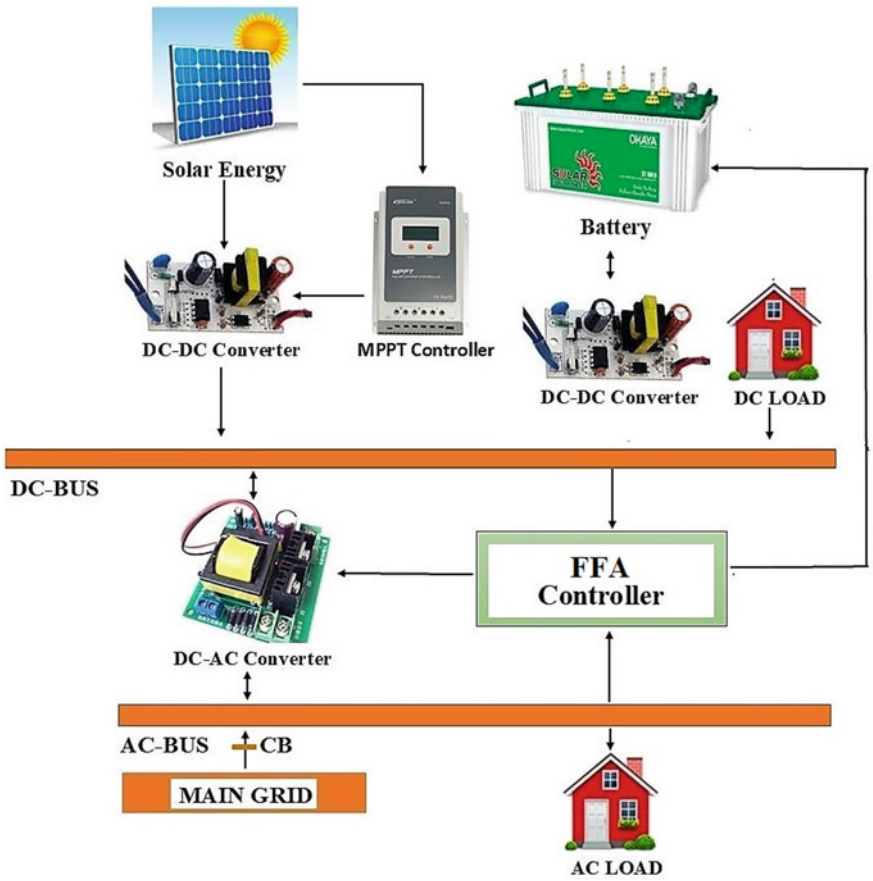

Fig. 1 The architecture of the grid-connected PV system with FFA controller

2.1 Photovoltaic Cell Modelling

To make the best photovoltaic cell possible, a freewheeling diode is connected in parallel with a source of light-generated electricity. In practical terms, all available PV cells are non-ideal. So, having a resistor in parallel is known as shunt resistance, and the other resistance that is in series is series resistance (Fig. 2).

$$\tilde{I}_{pv} = [\tilde{I}_{sc} + K_I(T - T_{ref})]\frac{G}{G_{ref}} \tag{1}$$

$$\tilde{I}_{sat} = \tilde{I}_{rs}\left[\frac{T_c}{T_{ref}}\right]^3 Exp\left[\frac{qE_g}{nk}\left(\frac{1}{T_{ref}} - \frac{1}{T_c}\right)\right] \tag{2}$$

$$\tilde{I} = \tilde{I}_{pv} - \tilde{I}_d - \tilde{I}_{sh} \tag{3}$$

$$\tilde{I} = \tilde{I}_{pv} - \tilde{I}_{sat}\left[\text{Exp}\left(\frac{V + \tilde{I}R_s}{nV_T}\right) - 1\right] - \left[\frac{V + \tilde{I}R_s}{R_{sh}}\right] \tag{4}$$

where, $\tilde{I}_{pv}$ is the photocurrent, $\tilde{I}_{sat}$ is the cell saturation Current, $\tilde{I}_d$ is the current in diode, $\tilde{I}_{sc}$ is the short circuit current, $\tilde{I}_{sh}$ is the current in shunt resistor, R_{sh} is the shunt resistor, R_s is the series resistor, G is the solar irradiance (W/m^2), G_{ref} is the reference irradiance (W/m^2), $V_T = kT_c/q$ is the thermal voltage.

3 Modelling and Design of an USC-HCR DC-DC Converter

The interleaved buck converter (IBC) is used in many commercial applications that need a lot of power [9]. The interleaved technique reduces the need for input and output filters while improving converter dynamics. All of the switches must be closed

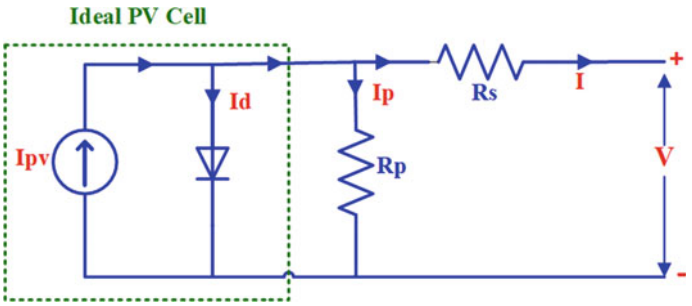

Fig. 2 Circuit diagram of photovoltaic cell

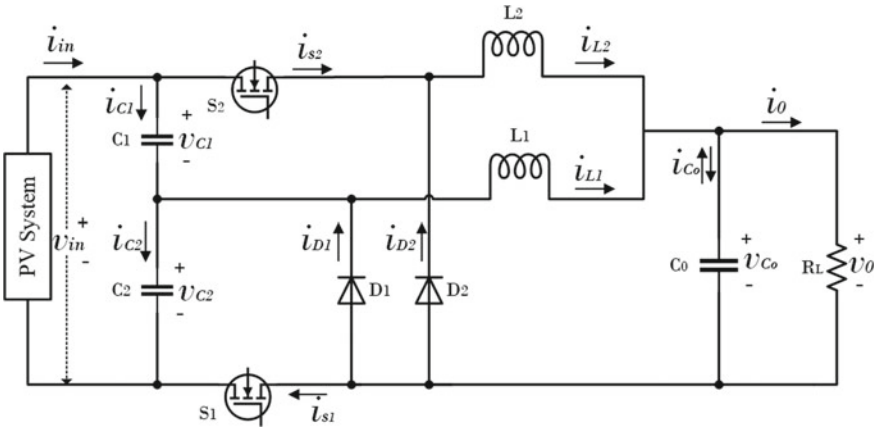

Fig. 3 Circuit diagram of an updated SC-HCR converter

when there is a need for a lot of voltage conversion. This is because the IBC has a very low duty ratio when there is a lot of voltage to convert. A special method is also needed to balance the two inductor currents (iL1 and iL2) so that they are equal. The series-capacitor buck (SCB) converter was made to fix problems with the traditional IBC. It was made to fix problems with the IBC. The SCB converter, also known as the double step-down buck converter, is a kind of buck converter that has two steps [17, 18].

To limit the input voltage, the S2 voltage is necessary. The currents in the two inductors are also balanced because C1 is good at balancing charges. Due to the presence of switch S1, at the start-up of the converter, the capacitor C1 starts charging from zero voltage. As a result, during this instant, all switches must block the input voltage Vin. As a result, the aforementioned factor determines the switch's voltage rating. To address the issue of voltage stress at start-up, this study presents an upgraded SC-HCR dc-dc converter.

Figure 3 depicts the recommended converter. When the switches are open, capacitors C1 and C2 are connected in series and parallel to the input voltage, then Vc1 + Vc2 = Vin and Vc2 becomes (Vin-Vc1). Later, the capacitors are drained to keep the switch voltages constant. It's easier to just think of the capacitance values of the two capacitors as being equal, so they're both called C1 and C2. The voltage across each is also the same Vc1 = Vc2 = Vin/2. The operation of the upgraded converter was investigated using its four operation modes. The functioning of the improved converter is identical to that of the SC buck converter.

3.1 Operational Modes of an Updated SC-HCR Converter

The operational modes are described briefly below with the help of Fig. 3.

Mode I: The switch S1 is switched on and the switch S2 is switched off, with diode D1 not conducting and diode D2 conducting. The inductor L1 is charged through switch S1, while the inductor current iL2 passes through the diode D2. The capacitors C1 and C2 are correspondingly charged and discharged. In this mode, the input voltage "Vin" is equal to the sum of VC1 and Vc2, so Vc1 + Vc2 = Vin.

Mode II: Both S1 and S2 are switched off, whereas both the diodes D1 and D2 are in conduction. The two inductor currents (iL1, iL2) passing through the body diodes D1 and D2, and the current flowing through the capacitors C1 and C2 are almost zero.

Mode III: In this mode, the switch S2 is switched on, whereas S1 is switched off, whereas diode D1 is conducting, but diode D2 is not in a conduction state. The capacitor "C1" is charging and the capacitor "C2" is discharging. The diode D1 continues to freewheel the inductor current IL1, while the inductor L2 is charged through S2. In this, the diode "D1" receives the total of the currents in the inductors (id1 = iL1 + iL2), which is nothing but output current (io = iL1 + iL2).

Mode IV: This mode of operation is same as the operation of mode II.

3.2 Voltage Transfer Gain

From the voltages of the inductors, the voltage transfer gain for the proposed converter can be found:

$$(0.5V_{in} - V_{out})dT_s = V_{out}(1-d)T_s \tag{5}$$

$$V_{Tg} = \frac{V_{out}}{V_{in}} = \frac{d}{2} \tag{6}$$

The duty ratio here ranges from zero to one hundred percent. As a result, at high conversion ratios, the aforementioned converter acts as a buck converter. The output voltage of the recommended converter is half that of the input voltage. This means the suggested converter converts at its maximum conversion level. This type of converter is mainly used for high current and high-power applications.

4 Firefly Algorithm

The Firefly Technique (FFA) is a nature-inspired metaheuristic optimization algorithm. The Firefly Algorithm was created by Dr. Xin-She Yang of Cambridge University in 2007 and is based on the social flashing behavior of fireflies, or lighting bugs, in the summer sky in tropical temperature zones [12–14]. Although it shares many characteristics with other swarm intelligence algorithms, such as the well-known Particle

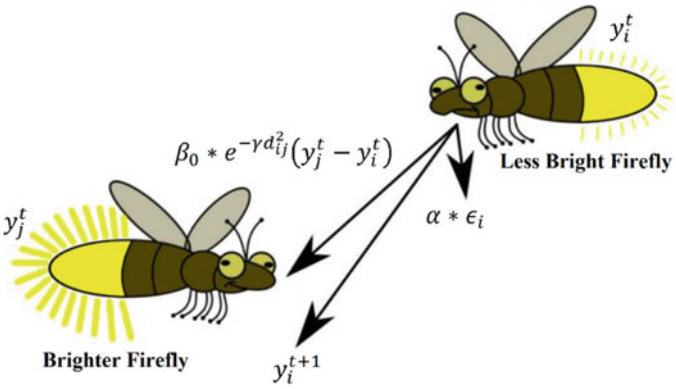

Fig. 4 The attractiveness and movement of Firefly

Swarm Optimization (PSO), Artificial Bee Colony Optimization (ABC), and Bacterial Foraging (BFA) algorithms, the firefly algorithm is far more straightforward in terms of concept and execution. According to recent research, the approach is exceedingly efficient and can outperform other algorithms, such as genetic algorithms, in tackling specific optimization issues (Fig. 4).

The Firefly Algorithm (FFA) approach is distinguished by three characteristics: 1. Each firefly attracts other fireflies regardless of gender since it is unisex. 2. The brightness of a firefly affects its attractiveness; the brighter the firefly, the more attracted it is to the less brightness. The attraction between two fireflies reduces as the distance between them expands. 3. A firefly's brightness is influenced by or determined by the geography of the target function. The value of the objective function of a problem determines the brightness or light intensity of a firefly. The light intensity in maximization problems is proportional to the value of the objective function.

4.1 Implementation of FFA for Getting Optimal Control Signal

Step 1: Initialization

During the initialization procedure, the input proportional and integral gain parameters, such as K_p and K_i, are created at random. Here it is two-dimensional since it has two gain parameters.

Step 2: Random Generation

The random behavior of gain parameters is generated based on the start-up step.

Step 3: Fitness Function

The fitness of the function is determined by the location of the firefly. The needed objective function is in terms of error signal and is given in the following equation:

$$\mathrm{U} = \min\{\mathrm{e(t)}\} \tag{7}$$

where "U" is the objective function, "e" error signal, "t" time period of signal

Step-4: Attractiveness

The Attraction between any two fireflies may be expressed as follows,

$$\beta(d) = \beta_0 e^{-\gamma d^m}, (\mathrm{m} \geq 1) \tag{8}$$

here β_0 is the attractiveness at d = 0, It varies monotonically with 'd', for a fixed coefficient of absorption 'γ', the characteristic length λ is expressed as:

$$\lambda = \gamma^{-1/m} \to 1, \ \mathrm{m} \to \infty \tag{9}$$

Step-5: Distance

The distance 'd' between two fireflies i and j are y_i and y_j computed as follows:

$$d_{ij} = \|y_j - y_i\| = \sqrt{\sum_{k=1}^{n} (y_{jk} - y_{ik})^2} \tag{10}$$

The letters 'i' and 'j' are supposed to be two fireflies, and 'n' represents dimension; The kth element of the vector y_i is denoted by the symbol y_{jk}. If the firefly 'j' is brighter than the firefly 'i', then as a result of its attraction, firefly 'i' has migrated to wards firefly 'j':

Step-6: Movement

The movement of a firefly i which is attracted by a more attractive (i.e., brighter) firefly j is given by the following equation:

$$y_i^t = \beta_0 * e^{-\gamma d_{ij}^2} \left(y_j^t - y_i^t\right) \tag{11}$$

Step-7: Upgraded position

The best optimum solution is updated based on the value of the Objective function after each individual's fitness calculation.

$$y_i^{t+1} = y_i^t + \alpha * \epsilon_i \tag{12}$$

The third term contains the random variable ϵ_i which may be substituted by rand-1/2, and is the randomization parameter 'α'.

Step 8: Obtain best output

The low bright firefly reached brighter by travelling an optimal distance and obtained an optimal function value (Figs. 5 and 6).

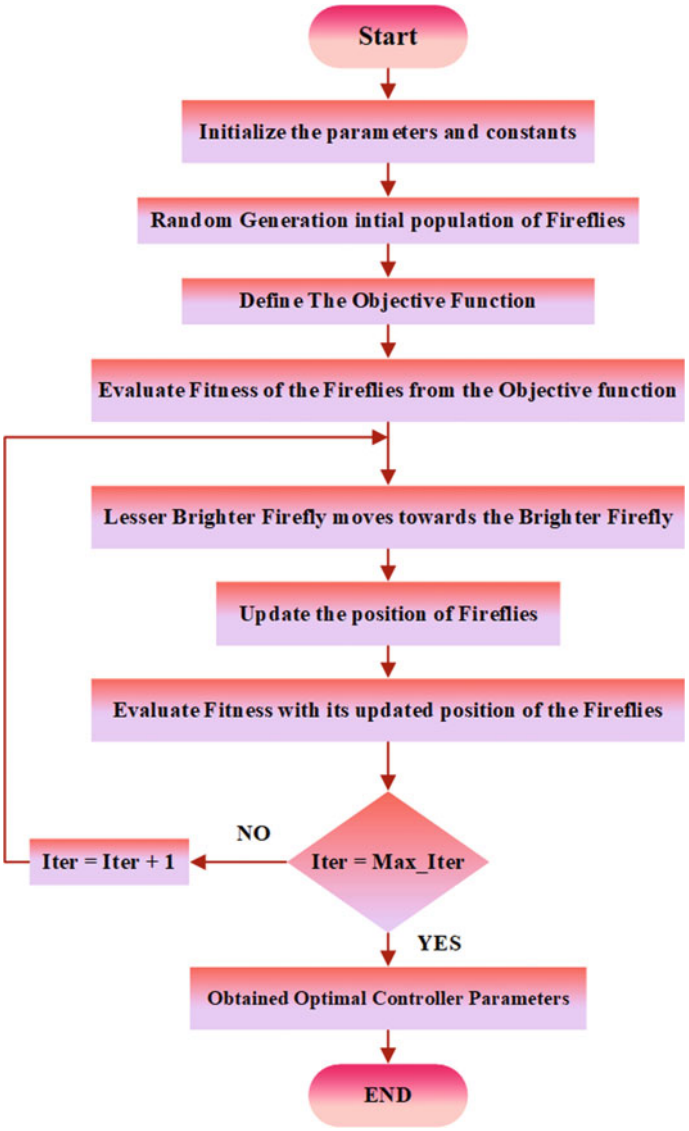

Fig. 5 Flow chart of the FFA algorithm

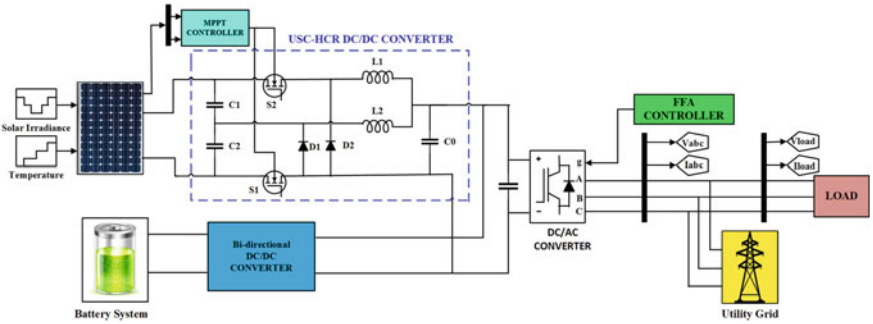

Fig. 6 MATLAB-simulation diagram grid connected system with FFA controller

5 System Outcomes and Its Analysis in MATLAB/Simulink Environment

This part evaluated the efficacy of several optimization methods on grid-connected solar systems and demonstrated the efficiency of the system and HCR converter by measuring the output. The FFA control system model is implemented in the MATLAB/Simulink environment. In this application FFA framed a precise control signal for optimal utilization power. The efficiency of the FFA-affiliated grid-connected solar system is assessed based on the photovoltaic output, and variation of load demand. The system is examined in a variety of operating modes and events.

Case 1: Changing of solar irradiance under Steady Load

In terms of voltage, current, and power, Case 1 represents a grid-connected solar system with a proposed HCR converter. This will be examined when the solar irradiance is changed while the load remains constant. Figure 7a shows that the PV irradiance of 1000 W/m2 at time interval 0 that is maintained for the next 0.2 s. Following that, it will decrease linearly to 800 W/m2 at 0.2 s maintained at the same amplitude up to 0.4 s, following that, it will decrease linearly to 600 W/m2 at 0.4 s maintained at the same amplitude up to 0.6 s, later it increased again to 800 W/m2 at 0.6 maintained at the same amplitude up to 0.8 s, and finally it reaches up to 1000 W/m2 as same as the initial amplitude.

Figure 8 demonstrates the analysis of power outcomes of the grid connected solar system with a proposed SC-HCR converter and FFA controller. The PV is illustrated in subplot 8(a) shows that photovoltaic power and it flows from 0 W to 1.5 KW at 0.01 s time interval and decreases up to 0.7 KW at 0.5 s. The PV converter power is illustrated in subplot 8(b) shows that PV converter power and flows from 0 W to 0.95 KW at 0.01 s time interval and decreases up to 0.5 KW at 0.5 s. The battery power illustrated in subplot 8(c) shows the battery power and it flows from 0 W to 3.25 KW at 0.01 s and increases up to 3.3 KW at 0.5 s. The load power is illustrated in subplot 8(d) shows the Battery converter power and it flows from 0 W to 3.1 KW at 0.01 s and increases up to 3.2KW at 0.5 s. 8(e) shows the grid power and it flows

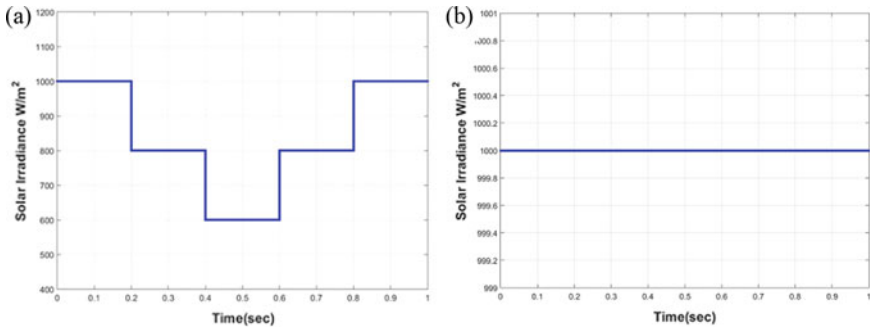

Fig. 7 **a** Changing of PV irradiance, **b** Steady PV irradiance with respect to time

from 0 W to 3.2 KW at 0.01 s and decreases up to 3 KW at 0.5 s. 8(f) shows the load power and it flows from 0 W to 10 KW at 0.01 s and is maintained at a constant value.

Figure 9 demonstrates the comparison of the converter and load power using a proposed controller designed by approaching the FFA technique with the other existing techniques like BSO, PSO under case1. Figure 9a represents the comparison of PV Converter power. The system with PSO approach has produced the maximum power of 713 W at 0.8 s time. The system with BSO approach has produced the maximum power of 715 W at 0.8 s time. The system with the proposed FFA technique has produced the maximum power of 721 W at 0.8 s time. In this observation, the output power of the proposed converter with the FFA approach is high, with low switching loss. Figure 9b represents a comparison of load power with existing and

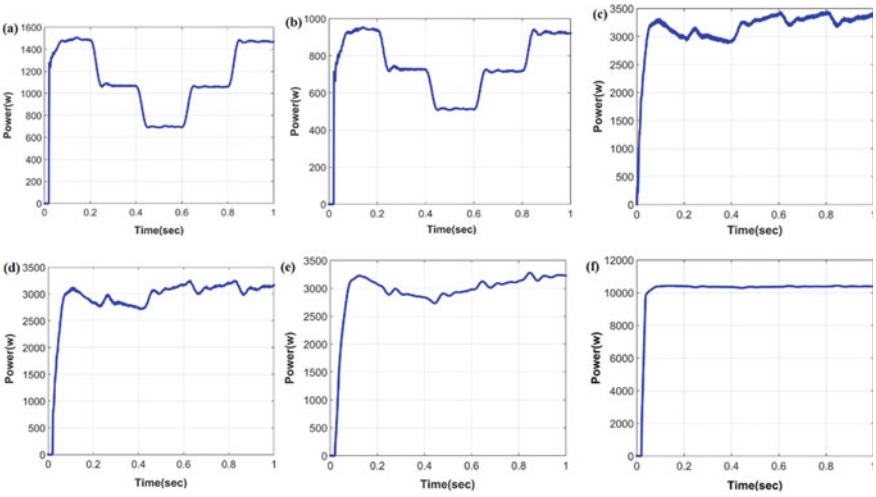

Fig. 8 Under Case.1, The power outcomes of the system using BSO controller **a** PV source, **b** PV Converter, **c** Battery, **d** Battery converter, **e** Grid, **f** load

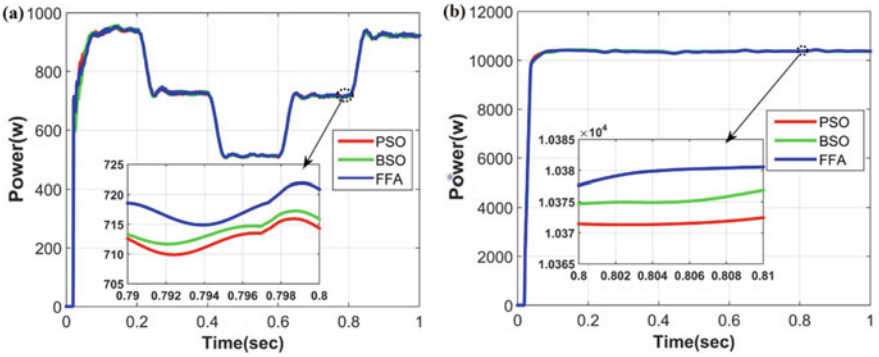

Fig. 9 Comparison of powers **a** PV Converter power **b** load power

proposed approaches. The system with the PSO approach has produced the maximum power of 10,371 W at 0.8 s time. The system with the BSO approach has produced the maximum power of 10,374 W at 0.8 s time. The system with the proposed FFA technique has produced the maximum power 10,379 W at 0.8 s time. The utilizing power with the proposed approach is high compared with other existing approaches. It is observed that when the power is available at load, the utilization of power in a system with the proposed FFA approach is higher than the other existing methods.

Case 2: Changing Load under Steady PV irradiance

In Case 2, we analyzed the power outcomes of the PV source, PV converter, Battery, Battery Converter, Grid and load of a solar system with a proposed SC-HCR converter and FFA controller at changing load with respect to time under constant solar irradiance of 1000 W/m2. Figure 7b depicts the variation in system load as the power demand varies over time under a constant irradiance of 1000 W/m2. In this case, the battery will go into charging mode if the power demand is lower than the generation. If the power demand is higher than the generation, then it will go into the discharging mode and supply power to the load.

Figure 10 demonstrates the analysis of power outcomes of the PV source, PV converter, battery, and load of a solar system with a proposed SC-HCR converter and FFA controller. The PV power is illustrated in subplot 10(a) shows the photovoltaic power and flows from 0 W to 1.5 KW at 0. 1 s time interval and is decreased up to 1.48 KW at 0.8 s. The PV converter power is illustrated in subplot 10(b) shows the PV converter power and flows from 0 W to 0.95 KW at 0. 1 s time interval and is decreased up to 0.93 KW at 0.8 s. The battery power illustrated in subplot 10(c) shows the battery power and it flows from 0 W to 3.3 KW at 0. 1 s and is increased up to 3.5 KW at 0.8 s. The battery converter power is illustrated in subplot 10(d) shows the battery converter power and it flows from 0 W to 3 KW at 0. 1 s and is increased up to 3.2 KW at 0.8 s. The grid power is illustrated in subplot 10(e) shows the grid power and it flows from 0 W to 3.1 KW at 0.1 s and is increased up to 3.2 KW at 0.8 s time interval. The load power is illustrated in subplot 10(f) shows the

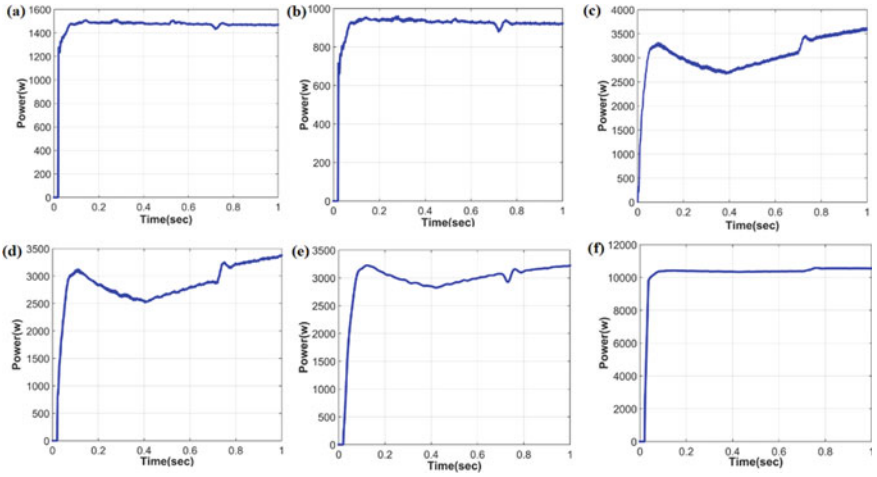

Fig. 10 Under Case.2 The power outcomes of the system using FFA controller **a** PV source, **b** PV Converter, **c** Battery, **d** Battery converter, **e** Grid, **f** load

load power and it flows from 0 W to 10.2 KW at 0.1 s and is increased up to 10.5 KW at 0.8 s time interval.

Figure 11 demonstrates the comparison of the SC-HCR converter output power and load power using a proposed controller designed by approaching the FFA technique with the other existing techniques like BSO, PSO under case2. Figure 11a represents the comparison of PV Converter power under case 2. The system with PSO approach has produced the maximum power of 922 W at 0.8 s time. The system with BSO approach has produced the maximum power of 924 W at 0.8 s time. The system with the proposed FFA technique has produced the maximum power of 928 W at 0.8 s time. In this observation, the output power of the proposed SC-HCR converter with the FFA approach is high, with low switching loss. Figure 11b represents a comparison of load power with existing and proposed approaches. The system with the PSO approach has produced the maximum power of 10.54 KW at 0.8 s time. The system with the BSO approach has produced the maximum power of 10.542 KW at 0.8 s time. The system with the proposed FFA technique has produced the maximum power 10.55 KW at 0.8 s time. Compared to the existing approach, the load power of proposed approach is high. In this observed that power available at load, utilization of power in a system with the proposed FFA approach is higher than other existing methods.

Figure 12 demonstrates the convergence characteristics of control techniques used in this model for system optimality. Subplot 12(a) depicts the FFA control technique conversed after 30 iterations. The fitness value of this technique is 0.792 when used to minimize the system fitness function. Subplot 12 (b) represents the comparisons of effectiveness and convergence characteristics of the FFA control technique along with BSO and PSO. From this subplot, we observed that the FFA control technique is

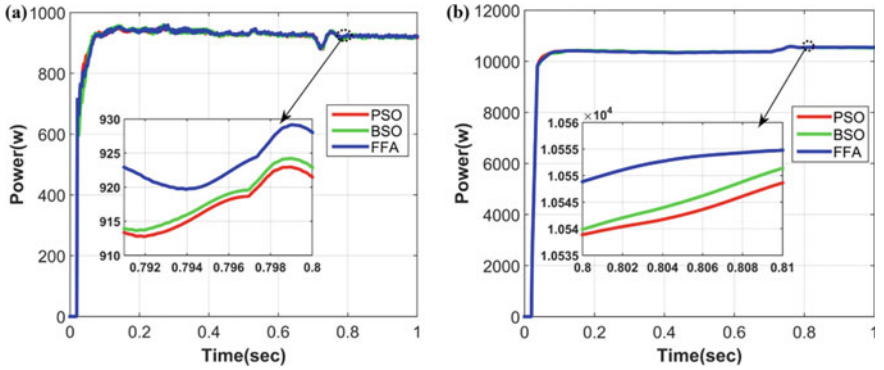

Fig. 11 Comparison of powers under case-2 **a** PV Converter power **b** load power

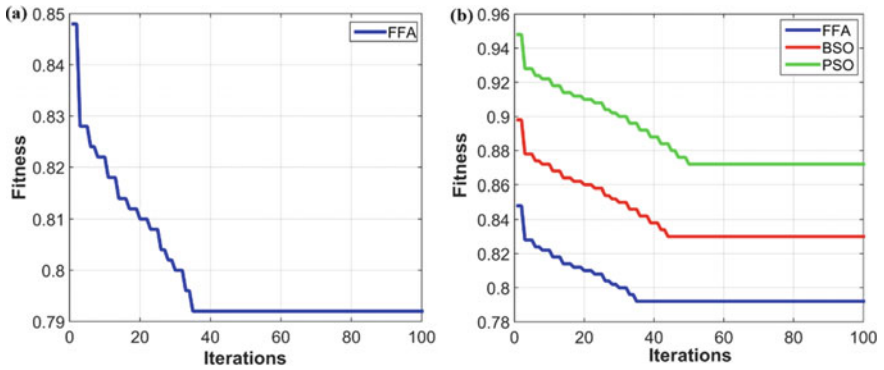

Fig. 12 Convergence characteristics active power using proposed and the existing techniques **a** Fitness of GWO control technique, **b** Fitness comparison of proposed and the existing techniques

more effective and converged earlier than the other two techniques. The FFA, BSO, and PSO have fitness values of 0.792, 0.828, and 0.873, respectively.

6 Conclusion

This work modelled and constructed a unique controller for a grid-connected solar system using the novel control strategy Firefly Algorithm (FFA) to achieve optimal power management in the system. The grid-connected system is associated with an updated SC-HCR dc-dc converter, which leads to reduced switching losses and also improved converter efficiency. The MATLAB/Simulink work site is used to investigate the system's performance. The proposed system's performance is assessed by

comparing it to existing control strategies such as BSO and PSO. The FFA demonstrated that it is a very competitive and promising control strategy in addressing optimization of the suggested power system model in terms of both accuracy and execution time, whereas the BSO control strategy is competitive but its execution time is high. BSO control strategy's accuracy scores in some of the test functions were not especially good. This system model was tested in two scenarios: variation of PV irradiance at constant load and variation of load at a constant PV irradiance. In both situations, the FFA control technique improved the system model's responsiveness in terms of current, voltage, and power during load. The simulation results of the recommended model demonstrate that the system efficiency increased. As a result, the proposed method is effective and efficient for power management.

References

1. N. Priyadarshi et al., Dynamic operation of grid-connected photovoltaic power system, in *Advances in Greener Energy Technologies* (Springer, Singapore, 2020), 211–218
2. A. Rezvani et al., Intelligent hybrid power generation system using new hybrid fuzzy-neural for photovoltaic system and RBFNSM for wind turbine in the grid connected mode. Front. Energy **13**(1), 131–148 (2019)
3. S. Goel, R. Sharma, Analysis of measured and simulated performance of a grid-connected PV system in eastern India. Environ. Dev. Sustain. **23**(1), 451–476 (2021)
4. A.Q. Al-Shetwi et al., Grid-connected renewable energy sources: review of the recent integration requirements and control methods. J. Clean. Prod. 253, 119831 (2020)
5. S. Lenka, S. Pampa, J. Chitralekha, An improvement review on power quality of grid connected PV with lithium-ion and super capacitor based hybrid energy storage system using a new control strategy, in *Renewable Energy Optimization, Planning and Control: Proceedings of ICRTE 2021*, vol. 1 (2021)
6. S.K. Sharma, D.K. Palwalia, V. Shrivastava, Performance analysis of grid-connected 10.6 kW (commercial) solar PV power generation system. Appl. Solar Energy **55**(5), 269–281 (2019)
7. M.D. Raj et al., Amelioration of power quality in a solar PV fed grid-connected system using optimization-based selective harmonic elimination. Electr. Eng. 1–18 (2022)
8. B. Babes, A. Boutaghane, N. Hamouda, A novel nature-inspired maximum power point tracking (MPPT) controller based on ACO-ANN algorithm for photovoltaic (PV) system fed arc welding machines. Neural Comput. Appl. **34**(1), 299–317 (2022)
9. K. Kim, H. Cha, S. Park, I.-O. Lee, A modified series-capacitor high conversion ratio DC–DC converter eliminating start-up voltage stress problem. IEEE Trans. Power Electron. **33**(1), 8–12 (2018)
10. P. Azer, A. Emadi, Generalized state space average model for multi-phase interleaved buck, boost and buck-boost DC-DC converters: transient, steady-state and switching dynamics. IEEE Access **8**, 77735–77745 (2020)
11. H. Fakham, L. Di, B. Francois, Power control design of a battery charger in a hybrid active PV generator for load-following applications. IEEE Trans. Industr. Electron. **58**(1), 85–94 (2010)
12. X.-S. Yang, Firefly algorithm, stochastic test functions and design optimisation. Int. J. Bio-inspir. Comp. **2**(2), 78–84 (2010)
13. H. Shukla, S. Gudhe, PSO and firefly algorithm applied to EV-based hybrid renewable energy system for load frequency control considering time-delay effect, in *Topical Drifts in Intelligent Computing: Proceedings of International Conference on Computational Techniques and Applications (ICCTA 2021)*, vol. 426 (Springer Nature, 2022)

14. V.-O. Sai, C.H. Shieh, Y.C. Lin,M.-F. Horng, T.-T. Nguyen, Q.-D. Le, J.-Y. Jiang, Comparative study on recent development of heuristic optimization methods, in IEEE 2016 *Third International Conference on Computing Measurement Control and Sensor Network (CMCSN)* (Matsue, Japan, 2016), pp. 68–71
15. Y. Shi, Brain storm optimization algorithm in objective space, in 2015 IEEE Congress on Evolutionary Computation (CEC), (IEEE, Sendai, Japan), pp. 1227–1234
16. H. Saeed et al., An improved search ability of particle swarm optimization algorithm for tracking maximum power point under shading conditions. Electr. Eng. Electromech. **2**, 23–28 (2022)
17. K. Yao, Y. Qiu, M. Xu, F.C. Lee, A novel winding-coupled buck converter for high-frequency, high-step-down DC–DC conversion, in *IEEE Trans. Power Electron., vol. 20, no. 5, pp. 1017–1023, Sep. 2005, Fuzzy Controller of Luo Converter for Controlling of DC Motors Speed 4th Power Electronics, Drive Systems & Technologies Conference (PEDSTC2013)*, (Tehran, Iran, 2013)
18. K. Nishijima, K. Harada, T. Nakano, T. Nabeshima, T. Sato. Analysis of double step-down two-phase buck converter for VRM, in *Proceedings of the IEEE Telecommunication. Energy Conf*, (2005), pp. 497–502

Constant Voltage Controlled MPPT for PV Fed Water Pumping System

Aditya Nath Jha, Bhavnesh Kumar, and Arjun Tyagi

Abstract This paper presents a study about a constant voltage-controlled photovoltaic (PV) water pumping system and compares it with a directly controlled PV water pumping system. The voltage-controlled PV system employs a constant voltage maximum power point tracking algorithm because of its easy implementation for both digital and analog circuits whereas a directly connected PV system, directly connects the PV array to the DC motor through a DC-DC converter. To study the advantages and disadvantages of each system, this paper analyzes the system performance for different irradiance and energy associated with it. Simulation results were obtained using a solar panel (4.2 kW, 8 × 3 A10 green technology A10J-S72-175) connected to 3.7 kW of separately excited DC motor. To compensate the losses of the DC-DC converter and separately excited the DC motor provides excess power from PV array.

Keywords DC-DC converter · Direct current (DC) separately excited motor · Photovoltaic (PV) array · Proportional–Integral (PI) controller

1 Introduction

In today's scenario, the cost of conventional energy is increasing day by day, along with the demand for electrical energy. To meet this increasing demand economically, the utilization of renewable energy sources such as PV(Photovoltaic), wind, tidal, geothermal, etc. must be increased [1]. In all of these renewable energy sources, for countries like India where a considerable amount of solar radiance is present, PV systems are the most suitable renewable energy source [2]. One of the major applications of PV standalone systems is in the agriculture sector for water pumping. PV systems can be utilized to drive electric motors with different types of loads [3].

A. N. Jha (✉) · B. Kumar
Department of Instrument and Control Engineering, Netaji Subhas University of Technology, New Delhi, India
e-mail: adityan.ie20@nsut.ac.in

A. Tyagi
Department of Electrical Engineering, Netaji Subhas University of Technology, New Delhi, India

J. Kumar et al. (eds.), *Control Applications in Modern Power Systems*, Lecture Notes in Electrical Engineering 974, https://doi.org/10.1007/978-981-19-7788-6_8

Electric machines consume more power as compared to other industries' equipment (about 40% of total power) [4–6]. In electric machine, DC motor is one of the most used equipment in industries due to its advantages like cheaper in cost than other available motors, simpler design, speed control of DC motor is very easy, full torque available at zero speed, free from harmonics, etc., [7]. The applications of the DC motor are in most of the industries, agriculture sector for water pumping, rolling mill, paper mill, conveyor belt, etc. [8]. These motors are also best for application where a very low-speed variation and high accuracy are required. The DC motor also performs very well at dynamic braking and reversing application [9].

DC Motors when directly connected to a PV system may not be able to function at the maximum power point (MPP). They work at the meeting of the current–voltage (I–V) curve of PV system and load line of a separately excited DC motor [10]. Because of a mismatch between the load line and I–V curve, it loses a substantial part of accessible solar power. In this work, to overcome this problem, maximum power point tracking (MPPT) technique is utilized to control the duty ratio of DC-DC converter. By this, the voltage of the motor and speed of the motor can be controlled [11].

In this paper, Constant Voltage Controlled MPPT technique applied because of its simplicity among various MPPT algorithm available and low cost [12]. A standalone system, like the water pumping system, needs to be simple and cost effective because it has application in agriculture industries where cost is one of the important factors. Constant Voltage controlled MPPT technique is the most suitable MPPT in Standalone PV systems because of its simple and low cost implementation. It can easily be designed in both Digital and Analog Systems.

In this paper, a constant voltage control PV pumping system is compared with a directly connected PV pumping system.

2 System Modelling

An appropriate selection of the DC motor, PV array and DC-DC converter is needed for getting the desired result. The selection of components in the system is such that it does not get affected by any external disturbances.

2.1 Design of PV Array

Solar modules are reconfigured together to form PV Array to convert solar energy into electrical energy to serve the electrical demand. These cells are reconfigured in series, parallel grouping to compensate the energy, voltage, and current demand of the system [13].

The PV array A10 Green technology A10J-S72-175 is chosen for the research. It has 8 series and 3 parallel strings. Voltage (V) versus current (I) and voltage (V)

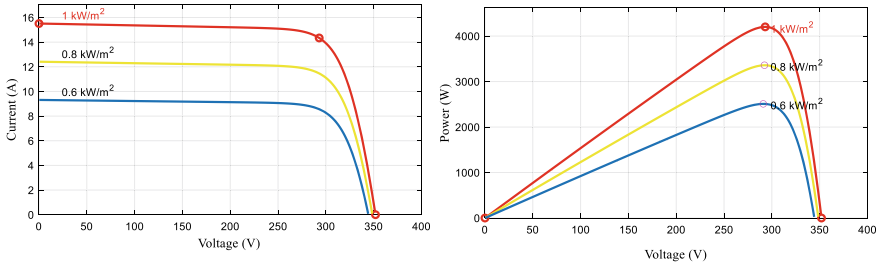

Fig. 1 V–I and V–W of 8 ×3 A10 Green technology A10J-S72-175 for 1000–800–00600 W/m^2

Table 1 Details parameters of module A10 green technology A10J-S72-175

S. no	Parameters	Value
1	Maximum power	175 W
2	Cells per module	72
3	Open circuit voltage Voc	44
4	Short circuit current Isc	5.17
5	Voltage at maximum power point Vmp	37
6	Current at maximum power point Imp	4.78

versus power (W) responses of the selected PV array for insolation of 600, 800, 1000 W/m^2 at 25 ºC are shown in Fig. 1. Maximum power obtained for 1000 W/m^2 is 4.2 kW and using a technique the gate pulse of the step-down converter is adjusted to acquire maximum power. Table 1 shows the data of module A10 Green technology A10J-S72-175 which is selected for the study. The 4.2 kW PV array is designed for the 3.7 kW DC Motor due to compensating losses of the DC-DC converter and motor.

2.2 Constant Voltage MPPT Algorithm

In the Constant voltage-controlled MPPT algorithm [14] a reference voltage for MPP voltage is assumed. Value of reference voltage is calculated at standard test conditions (STC). This standard voltage value is used as a reference for the PI controller which controls the duty ratio of the DC-DC converter [15] as shown in Fig. 2. This algorithm only measures the array voltage and can easily be implemented in both digital and analog circuits.

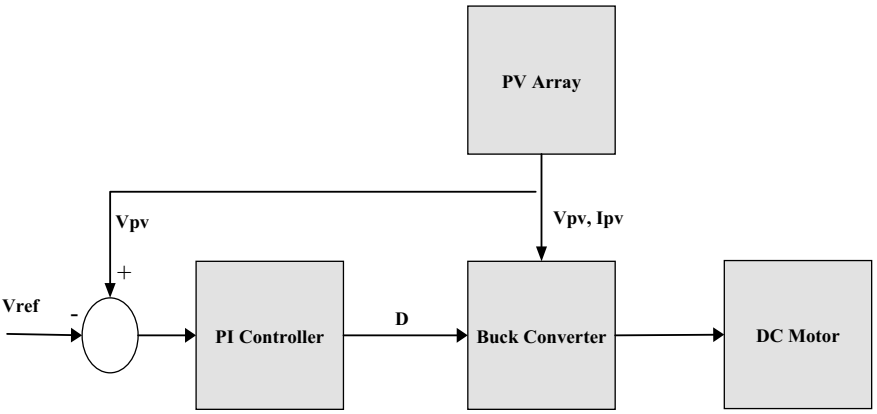

Fig. 2 Block diagram of constant control voltage MPPT for PV fed water pumping system

2.3 *Separately Excited DC Motor*

The circuit diagram of a separately excited DC motor is shown in Fig. 3, where V is armature voltage, R is resistance of the armature, L is inductance of the armature, E_b is the back emf of the motor and i_a is the current flown through the armature [16].

The mathematical model of a separately excited DC motor is given by Eqs. (1), (2), (3), (4) and (5).

$$V - E = Ri_a + L\frac{dia}{dt} \tag{1}$$

$$E = \alpha w \tag{2}$$

$$Ia = \frac{V}{L} - \frac{\alpha}{L} - w - \frac{R}{L}i_a \tag{3}$$

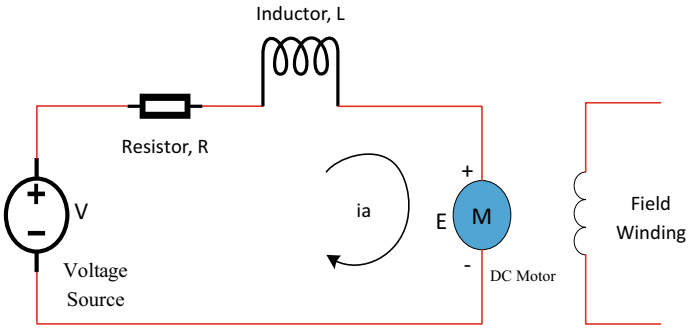

Fig. 3 Circuit diagram of separately excited DC motor

Table 2 Ratings of Selected Separately Excited DC Motor

Separately Excited DC Motor Ratings	Rated armature voltage	Rated field voltage	Rated speed (rad/s)	Rated power (W)	Armature resistance
	240 V	300 V	182.2	3730 W or 5HP	2.581Ω

$$T = T_1 + M\frac{dw}{dt} + Bw \tag{4}$$

$$T = \beta i_a \tag{5}$$

where, w represents the speed of the DC motor in rad/sec. T represents the torque of the separately excited DC motor in N-m. T_l represents the load torque in N-m applied to the separately excited DC motor. B represents friction of the DC Motor. M represents inertia of separately excited DC motor in kg-m^2/s^2. β represents the coefficient of torque in N-m/A and α represents the coefficient of back emf in Vs/rad.

The separately excited motor DC motor was selected and implemented using MATLAB. The motor ratings are given in Table 2.

3 Simulation Result

3.1 Direct Connected PV Pumping System

In a directly connected PV system, the duty cycle of the DC-DC converter is controlled through a pulse generator as shown in Fig. 4. The Load torque of the DC Motor is directly proportional to the square of the speed of the DC motor in case of the water pumping system. In this system, firstly the transient analysis of the directly connected PV fed water pumping system at constant irradiance and constant cell temperature (1000 W/m^2 and 25 °C respectively) is studied. It has been observed that PV array voltage and current settle at 0.7 s. as shown in Fig. 5.

In a directly connected PV system at constant irradiance and constant cell temperature (1000 W/m^2 and 25 °C) results of the DC Motor parameter were observed as shown in Fig. 6. It is observed that the motor draws high current from the link capacitor initially, however, as the current decreases in the motor the voltage across the link capacitor decreases. Motors generally possess higher mechanical time constant, due to this the motor speed takes more time to settle. The ripple in high frequency can easily be damped by the inertia of the motor and it does not affect the speed of the motor.

In order to observe the behavior of the DC motor and PV array characteristics with different irradiance, in directly connected PV systems, solar irradiance varies from 400 to 1000 W/m^2 to again 400 W/m^2 with constant cell temperature of 25 °C

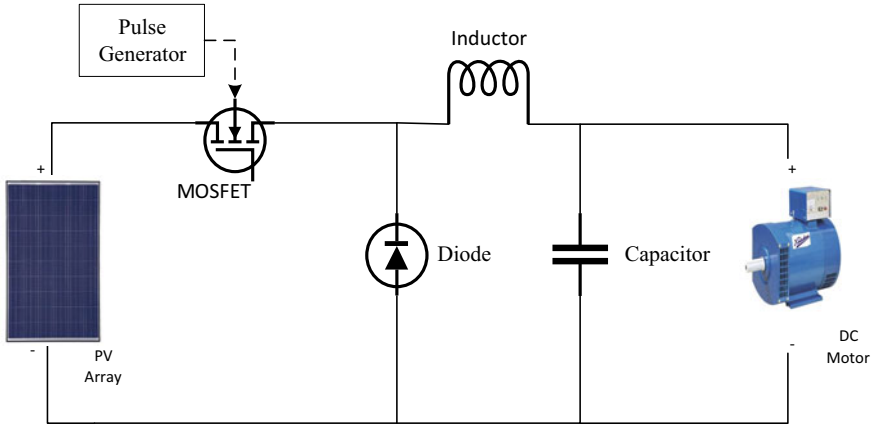

Fig. 4 Block diagram of directly connected PV fed water pumping

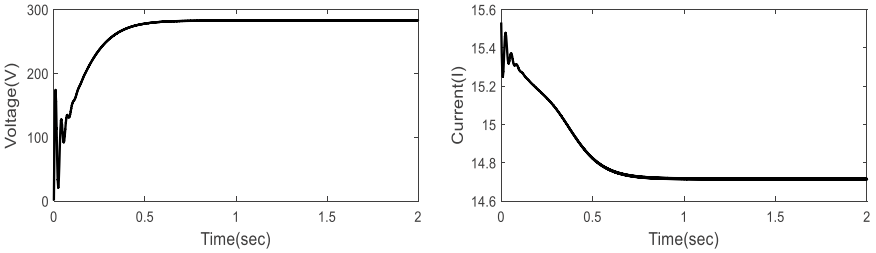

Fig. 5 Simulation result showing **a** PV array voltage, **b** PV array current waveform for the directly connected PV system

as shown in Fig. 7. The simulation result of PV array current and voltage, and the DC motor armature voltage, armature current, speed, and load torque for variations of solar irradiance with time are shown in Fig. 8 and in Table 3.

The energy utilization of directly connected the PV fed Water Pumping System is calculated. The lowest energy utilization of PV Array is 60.40% at 400 W/m^2 and the lowest energy utilization of Separately Excited DC Motor is 23.10% at same solar irradiance. The Calculation of energy utilization of PV Array is done by Eq. (6) and calculation of energy utilization of Separately Excited DC motor is done by Eq. (7)

$$Energy\ Utilization\ of\ PV\ Array = \frac{Actual\ Power\ of\ PV\ Array}{Theoritical\ Power\ of\ PV\ Array} \quad (6)$$

$$Energy\ Utilization\ of\ DC\ Motor = \frac{V.I_a - I_a^2 R}{Rated\ Power} \quad (7)$$

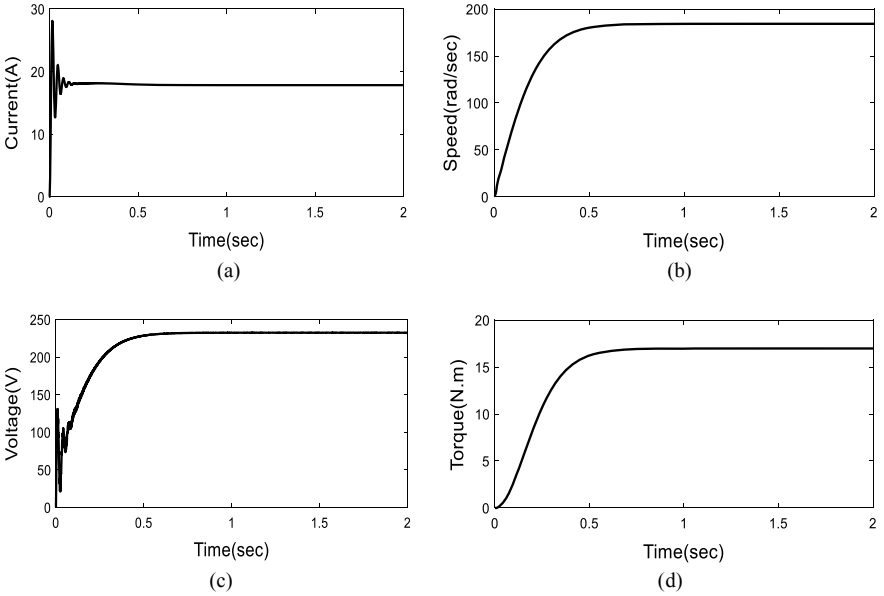

Fig. 6 **a** Motor current, **b** Motor speed, **c** Armature voltage and **d** M load torque simulation result of PV pumping for directly connected PV system

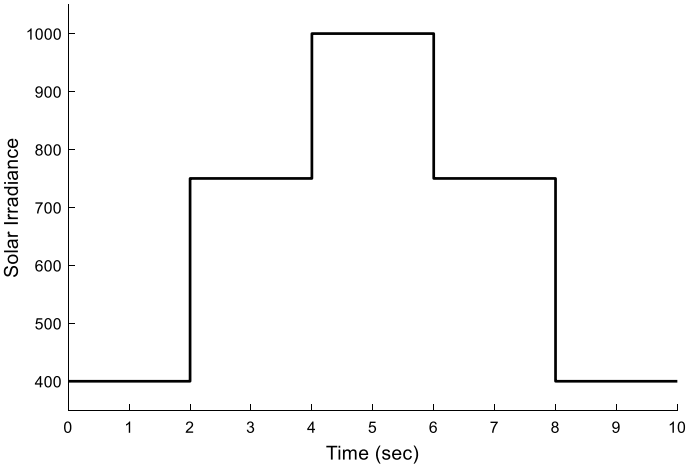

Fig.7 Variation of solar irradiance with time

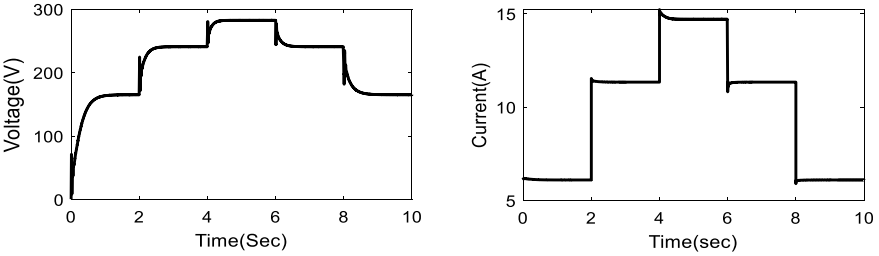

(a) PV array Voltage and current for irradiance 400, 750, 1000 W/m^2

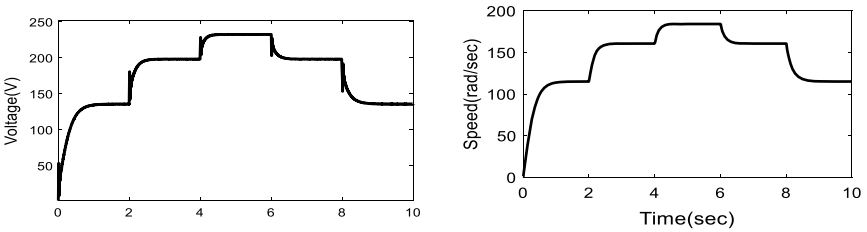

(b) DC Motor Voltage and Speed for irradiance 400, 750, 1000 W/m^2

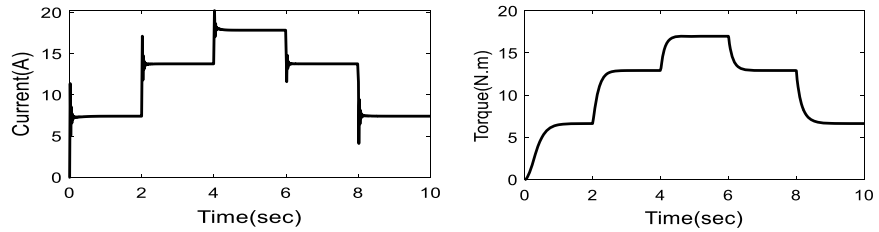

(c) DC Motor Current and Torque for irradiance 400, 750, 1000 W/m^2

Fig. 8 **a**, **b** and **c** show the simulation result of the PV system for the the directly connected PV water pumping system when solar irradiance varies

Table 3 Measured values of motor current & speed, load torque, PV array voltage & current for directly connected PV system at different solar irradiances

Solar irradiance (W/m^2)	Measured armature voltage (V)	Measured armature current Ia (A)	Motor speed w(rad/s)	Load torque Tl (N.m)	PV array Vmpp voltage (V)	PV array Impp current (A)
400	135.5	7.40	113.9	6.5	163.8	6.11
750	198.1	13.76	160.8	12.92	241.0	11.35
1000	232.4	17.84	184.3	16.7	282.8	14.71

where V is the armature voltage, I_a is the armature current and R is the armature resistance.

3.2 *Constant Voltage Controlled PV Pumping System*

The system with a constant voltage-controlled MPPT algorithm consists of a step-down converter, PV array, Proportional and Integral controller, and a separately excited DC motor as shown in Fig. 9. Step down converter's duty cycle is controlled by the PI controller to maintain PV array voltage fixed at the STC voltage using constant voltage controlled MPPT Technique.

Firstly, the transient analysis of the PV array at specific solar irradiance and cell temperature (1000 W/m^2 and 25 °C) is shown in Fig. 10, are carried out. At the point when PV array begin their operation, it has been seen that the reaction of the PV system is its open circuit that moves towards reference voltage in less than 0.01 s.

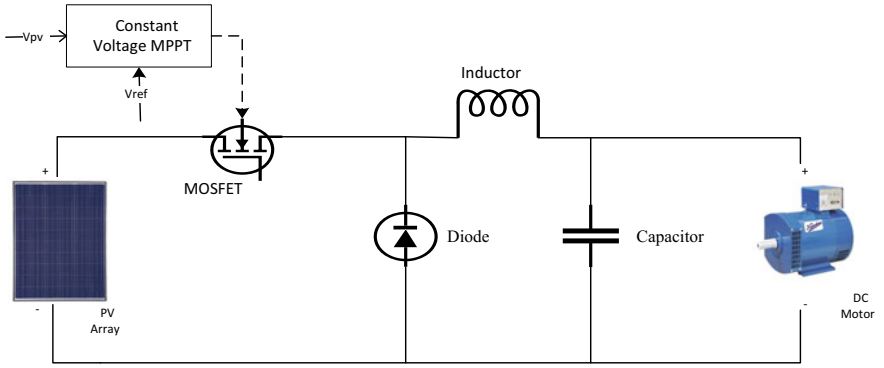

Fig. 9 Block diagram of constant controlled MPPT PV fed water pumping

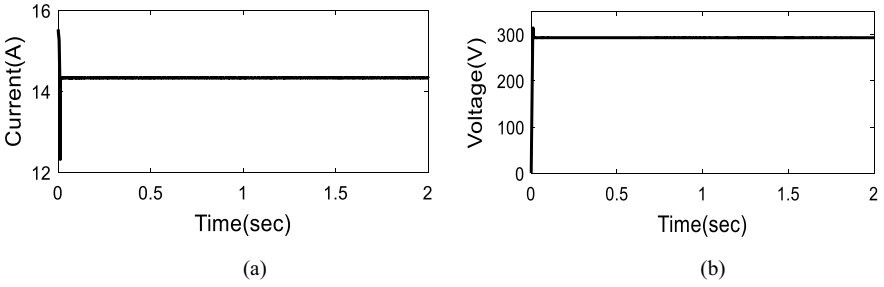

Fig. 10 Simulation result showing **a** PV array current, **b** PV array voltage waveform for constant voltage-controlled system at constant solar irradiance and constant cell temperature

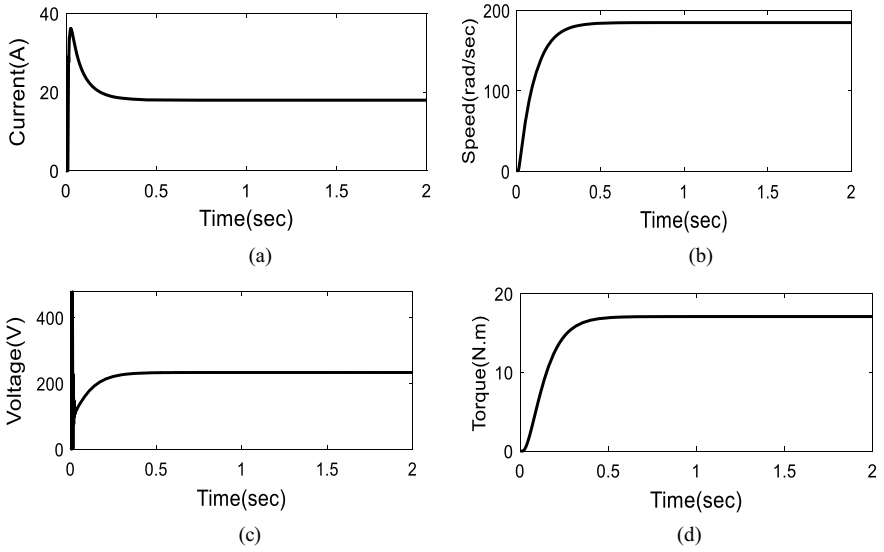

Fig. 11 **a** Motor current, **b** Speed **c** Voltage **d** Load torque waveform of PV pumping for constant voltage-controlled control at constant solar irradiance and constant cell temperature

At constant solar irradiance and specific cell temperature (1000 W/m^2 and 25 °C) the simulation result of the parameters of the DC Motor is shown in Fig. 11. Initially, the separately excited DC motor draws large amount of current from the link capacitor, as voltage in the capacitor started to decrease as the current in the motor also started to decrease. Motors, generally, have a higher mechanical time constant. Therefore, the motor speed takes a longer time to settle. The ripple in high frequency can easily be damped by the inertia of the motor and it does not affect the speed of the motor. The square of motor speed is directly proportional to the load torque.

For a constant voltage-controlled set, the reference voltage is 293 V (solar irradiance of 1000 W/m^2 and cell temperature is at 25 °C) and is compared with voltage at different solar irradiances. In order to observe the behavior and efficiency of the DC Motor and PV Array, the solar irradiance varies from 400 to 1000 W/m^2 again to 400 W/m^2 as shown in Fig. 7. Then the PV array voltage, PV array Current and different Parameters of the DC Motor are measured and compared with the calculated value and the energy efficiency is determined as shown in Fig. 12 and Table 4.

With a Constant Voltage PV System, we simulate the system with different irradiances for the minimum energy utilization we achieved is 98% at 400 W/m^2. PI controller has a very fast response change as compared to the speed of irradiance change and because of this reason energy utilization does not affect greatly with irradiance or temperature transient.

On simulation with a constant voltage PV system, the PV array achieves 98% energy utilization at 400 W/m^2 whereas energy utilization for solar irradiance is 38.37% using Eqs. (6) and (7).This can be additionally improved by choosing the

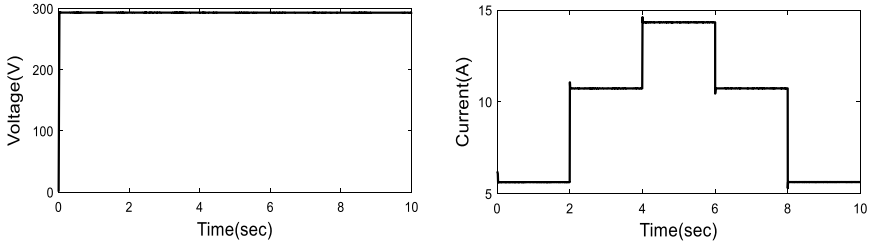

(a) PV array Voltage and current for irradiance 400, 750, 1000 W/m^2

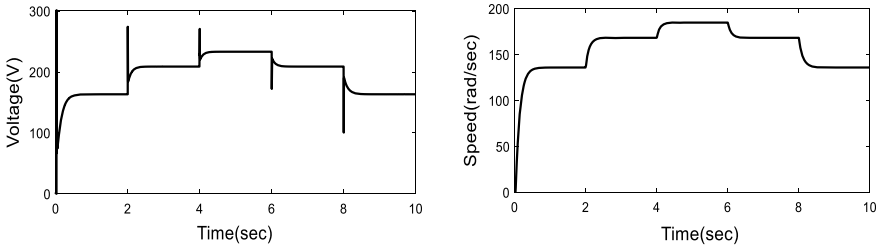

(b) DC Motor Voltage and Speed for irradiance 400, 750, 1000 W/m^2

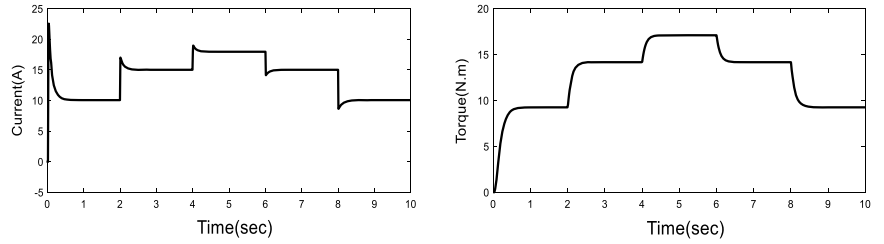

(c) DC Motor Current and Torque for irradiance 400, 750, 1000 W/m^2

Fig. 12 **a**, **b** and **c** shows simulation result of PV system for constant voltage-controlled PV water pumping system for different solar irradiances

Table 4 Measured values of motor current & speed, load torque, PV array voltage & current for constant controlled voltage at different solar irradiance

Solar irradiance (W/m^2)	Measured armature voltage (V)	Measured armature current Ia (A)	Motor speed w(rad/s)	Load torque Tl (N.m)	PV array Vmpp voltage (V)	PV array Impp current (A)
400	163.4	10.5	136.0	9.243	293.3	5.7
750	208.9	15.0	168.3	14.16	293.3	10.73
1000	233.3	17.95	184.9	17.09	293.3	14.33

Table 5 Comparison between constant controlled voltage PV pumping system and directly connected PV pumping system

	Energy utilization of PV array at 400 W/m^2 and 25 °C	Energy utilization of separately excited DC motor at 400 W/m^2 and 25 °C	Settling time at 1000 W/m^2 and 25 °C
Constant controlled voltage PV pumping system	98%	38.37%	<0.01 s
Directly connected PV pumping system	61%	23.10%	<0.7 s

reference voltage as per local temperature and normal irradiance as opposed to selecting Standard Test Condition for MPPT Voltage.

In a constant controlled voltage PV pumping system, energy utilization of the PV array and separately excited DC Motor achieved is 98 and 38.37%, respectively, and the settling time of the PV array is less than 0.01 s, whereas in a directly connected PV pumping system energy utilization of PV array and separately excited DC Motor is 61 and 23.10% respectively and the settling time of the PV array is 0.7 s. as shown in Table 5.

4 Conclusion

This research paper presents an investigation of a Constant Voltage controlled PV fed water pumping system, and it is compared with a directly connected PV fed water pumping system. On variation of solar irradiance with time, effects on PV Array and DC motor for both types of systems are examined. The transient analysis of both the systems are compared, in a constant voltage-controlled system with a settling time of less than 0.01 s for the PV array, whereas in a directly connected system the PV array settling time is 0.7 s. The Directly connected PV System has low energy utilization as compared to a constant controlled voltage PV system. A directly connected PV system produces 61% of energy utilization while a constant voltage connected PV system produces 98% at 400 W/m^2 and 25 °C. In case of energy utilization of the Separately Excited DC Motor it gives 38.37% and 23.10% for constant Control Voltage PV fed water pumping system and directly connected PV fed water pumping system, respectively, at 400 W/m^2 and 25 °C. Moreover, the efficiency of the system can be further improved by selecting the reference voltage in accordance with the local temperature or using a more sophisticated algorithm which is present in the market or literature. But if a standalone PV system is applied with a sophisticated algorithm it will lose its advantage which is, it is very simple to apply in both digital and analog circuits.

References

1. K. Anand, N. Singh, A. Singh, D. Singh, A. Kumar, Standalone hybrid power generation using photovoltaics, battery and bio-gas, in *2018 5th IEEE Uttar Pradesh Section International Conference on Electrical, Electronics and Computer Engineering (UPCON)*, (IEEE, 2018), pp. 1–6
2. B. Kumar, K.C. Yogesh, V. Shrivastava, A comparative study of maximum power point tracking methods for a photovoltaic-based water pumping system. Int. J. Sustain. Energ. **33**(4), 797–810 (2014)
3. S. Shukla, B. Singh, Reduced current sensor based solar PV fed motion sensorless induction motor drive for water pumping. IEEE Trans. Industr. Inf. **15**(7), 3973–3986 (2018)
4. R.K. Munje, M.R. Roda, B.E. Kushare, Speed control of DC motor using PI and SMC, in 2010 Conference Proceedings IPEC, (2010) pp. 945–950
5. D. Shobha Rani, M. Mahankali, Boost converter fed high performance BLDC drive for solar PV array powered air cooling system. Adv. Electr. Electr. Eng. **15**(2), 154–168 (2017)
6. K. Rajan, B. Singh, Solar PV powered BLDC motor drive for water pumping using Cuk converter. IET Electr. Power Appl. **11**, 222–232 (2017)
7. K. Rajan, B. Singh, Single stage solar PV fed brushless DC motor driven water pump. IEEE J. Emerg. Select. Top. Power Electr. **5**(3), 1377–1385 (2017)
8. R. Najet, A. Hmidet, R. Gammoudi, O. Hasnaoui, Implementation of photovoltaic water pumping system with MPPT controls. Front. Energy **9**, 187–198 (2015)
9. S.Y. Kim, Y.J. Park, I. Ali, T.T.K. Nga, H.C. Ryu, Z.H.N. Khan, S.M. Park, Y.G. Pu, M. Lee, K.C. Hwang, Y. Yang, Design of a high efficiency DC–DC buck converter with two-step digital PWM and low power self-tracking zero current detector for IoT applications. IEEE Trans. Power Electr. **33**(2), 1428–1439 (2017)
10. D. Tufan, N. Tan, Design of PI controller using optimization method in fractional order control systems. IFAC-Papers **51**(4), 841–846 (2018)
11. M. Poovizhi, M.S. Kumaran, J.A. Roseline, M. Kullan, An optimized design modelling of PV integrated SEPIC-based four-switch inverter for sensorless PMBLDC motor control. Automatika **63**(1), 90–101 (2022)
12. J.-S. Ko, J.-H. Huh, J.-C. Kim, Overview of maximum power point tracking methods for PV system in micro grid. Electronics **9**(5), 816 (2020)
13. S. Singh, B. Singh, Solar PV water pumping system with DC-link voltage regulation. Int. J. Power Electr. **7**(1–2), 72–85 (2015)
14. E. Mohammed Ali, B. Zahawi, A.D. John, Comparison of directly connected and constant voltage controlled photovoltaic pumping systems. IEEE Trans. Sustain. Energy **1**(3), 184–192 (2010)
15. R. Kumar, B. Singh, Grid interactive solar PV-based water pumping using BLDC motor drive. IEEE Trans. Ind. Appl. **55**(5), 5153–5165 (2019)
16. K. Viji, K. Chitra, T. Someswari, M. Raichel Ruby, P. Sandhya, Solar powered DC motor speed control by MPPT and discrete controller, in IEEE Third International Conference on Intelligent Communication Technologies and Virtual Mobile Networks (ICICV), (2021) pp. 651–655

Enhancement of Oscillatory Stability of a Grid Integrated Microgrid by Optimized Governor Damping Action

Narayan Nahak, Jyotiswarup Samal, Santosh Kumar Swain, Samarjeet Satapathy, and Akshaya Kumar Patra

Abstract An optimized mechanical damping torque is proposed in the present work provided by the synchronous generator governor to improve oscillatory stability for a grid integrated micro grid. Small signal modelling of micro grid with grid has been considered here with uncertain variations in solar and wind power generations. The gains of the governor are optimized by the Random Walk Grey wolf optimizer (RWGO) in contrast to PSO and GWO algorithms. Pertained to uncertain variations in solar and wind variations, time and frequency analysis have been conducted to observe effective damping by governor action. It has been found that intermittency in solar and wind generation variations create a challenge for oscillatory instability and the governor can impart adequate damping torque if its gains are properly set by an efficient control law. The excitation system of the generator is kept fixed at an initial operating condition by RWGO. The ITAE criterion is selected for the minimization problem for which a step change of 10percent of input mechanical power is executed. The aggravation of oscillations due to variations in renewable penetration can be damped and compensated by the phase lead provided by tuned governor action.

Keywords Governor · Wind source · SPV · Random walk GWO · Oscillatory stability

N. Nahak (✉) · J. Samal · S. K. Swain · S. Satapathy
Department of Electrical Engineering, Siksha 'O'Anusandhan Deemed to be University, Bhubaneswar, Odisha 751030, India
e-mail: narayannahak@soa.ac.in

A. K. Patra
Department of Electrical and Electronics Engineering, Siksha 'O'Anusandhan Deemed to be University, Bhubaneswar, Odisha 751030, India
e-mail: akshayapatra@soa.ac.in

J. Kumar et al. (eds.), *Control Applications in Modern Power Systems*, Lecture Notes in Electrical Engineering 974, https://doi.org/10.1007/978-981-19-7788-6_9

1 Introduction

Microgrid (MG) plays a vital role for reliable and economic operation of a power system. The reliability includes stabilising voltage and frequency. When a MG is connected to a grid, there are several challenges for a system operator out of which an important issue is the dynamical interaction of low inertia MG with the conventional grid. The MG may be of AC, DC or hybrid type and may include synchronous generation, induction generation or generation based on different power electronics converters. For the dynamic stability study of MG a linearized model of MG along with other power system components is needed. The linear modelling of various power systems has been reported by different researchers [1–3]. The low frequency Heffron Phillips modelling of the power system has been employed in many research studies for linear modelling [4–7]. In [8], a generalised modelling of MG has been reported and in [9] KVL and KCL have been employed for MG modelling. But estimating the MG and control action parameters are reported [10, 11]. The equivalent model of MG has been reported in many research studies including black box theory as in [12–14] or using mathematical modelling as in [15]. A linear equivalent model of MG connected to the grid has been presented in [16] which has been considered in this work with optimal tuning of the governor parameters for the synchronous generator of MG. An important issue is selection of proper gains for creating an effective damping torque and for which a suitable algorithm can be applied. In [5] a modification of the GWO algorithm called random walk GWO is proposed as a challenging technique in contrast to prevailing algorithms. This algorithm is proposed here to tune governor gains and has been compared with PSO and GWO algorithms for justification of tuning efficacy.

2 Low Frequency Model of Micro Grid

2.1 Synchronous Generator-Based MG Modelling

The low frequency MG model considered here is based on modification of the small signal Heffron Phillips model [5] including the governor and excitation system. Figure 1 represents the single line diagram of MG connected to an infinite bus. Figure 2 shows the IEEE ST6B excitation system considered in this work and Fig. 3 depicts the equivalent turbine governor model. Equations describing the MG are presented by [16]

$$\frac{dw}{dt} = \frac{1}{2H}(T_m - T_e - T_D)$$

$$\frac{d\delta}{dt} = \omega_b(\omega - 1)$$

$$\frac{de'_q}{dt} = \frac{1}{T'_{d0}}\left[E_{fd} - e'_q - \left(X_d - X'_d\right)i_d\right] \tag{1}$$

$$i = i_d + ji_q$$

$$v_t = v_d + jv_q$$

$$V_{pcc} = v_{pcc}(\sin\delta + j\cos\delta)$$

$$Z = R + jX\ Y = G + jB$$

$$C_1 + jC_2 = 1 + ZY$$

$$R_1 = R - C_2X'_d,\ R_2 = R - C_2X_q$$

$$X_1 = X + C_1X_q,\ R_2 = R - C_2X_q$$

$$X_1 = X + C_1X_q,\ X_2 = X - C_1X'_d$$

$$Z_e^2 = R_1R_2 + X_1X_2$$

$$Y_d = (C_1X_1 - C_2R_2)/Z_e^2$$

$$Y_q = (C_1R_1 - C_2X_2)/Z_e^2 \tag{2}$$

$$v_{do} = P_o v_{t0}\left[P_0^2 + \left(Q_0^2 + v_{t0}^2/X_q\right)^2\right]^{-1/2}$$

$$V_{q0} = \left(V_{t0}^2 - V_d^2\right)^{1/2}$$

$$i_{q0} = \frac{vd0}{X_q}i_{d0} = \left(P_0 - i_{q0}v_{q0}\right)/v_{d0}$$

$$e'_{q0} = v_{q0} + X'_d i_{d0}$$

$$v_{pccd0} = C_1 v_{d0} - C_2 v_{q0} - R i_{d0} + X i_{q0}$$

$$v_{pccq0} = C_2 v_{d0} + C_1 v_{q0} - X i_{d0} - R i_{q0}$$

$$\delta_0 = \tan^{-1}\left(\frac{v_{pccd0}}{v_{pccq0}}\right)$$

$$i_{Ld0} = G v_{d0} - B v_{q0}\, i_{Lq0} = G v_{q0} + B v_{d0}$$

$$i_{Lined0} = i_{d0} - i_{Ld0} i_{Lineq0} = i_{q0} - i_{Lq0} \tag{3}$$

By Kirchoff's voltage law the parameters are presented as:

$$Zi = (1 + ZY) v_t - v_{pcc}$$

$$\begin{bmatrix} R & -X \\ X & R \end{bmatrix} \begin{bmatrix} i_d \\ i_q \end{bmatrix} = \begin{bmatrix} C_1 & -C_2 \\ C_2 & C_1 \end{bmatrix} \begin{bmatrix} v_d \\ v_q \end{bmatrix} - v_{pcc} \begin{bmatrix} \sin\delta \\ \cos\delta \end{bmatrix} \tag{4}$$

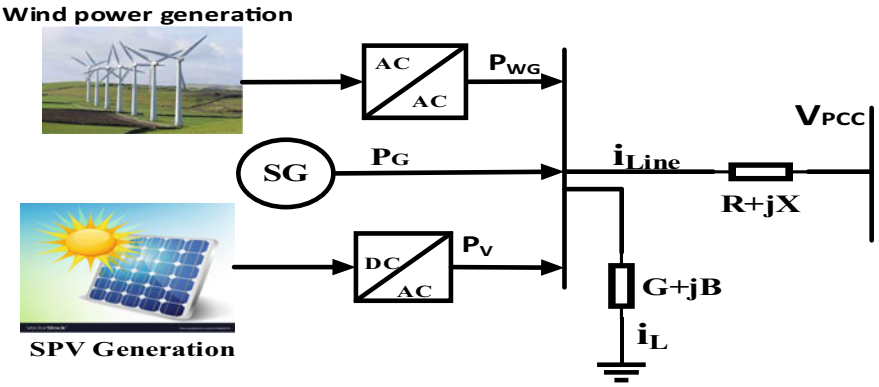

Fig. 1 SG with SPV and wind source connected to infinite bus

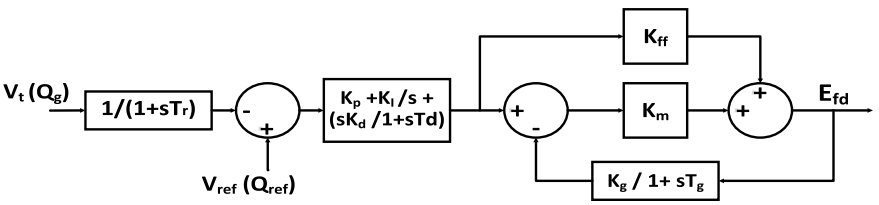

Fig. 2 IEEE-ST6B excitation system

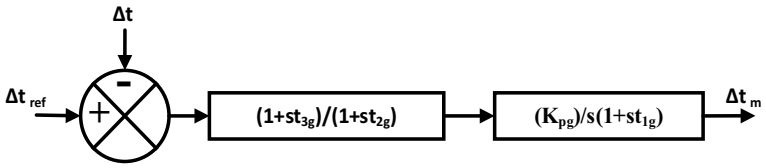

Fig. 3 Equivalent turbine governor modelling

As per the voltage and currents in d and q axis are stated as:

$$\begin{bmatrix} v_d \\ v_q \end{bmatrix} = \begin{bmatrix} 0 \\ 1 \end{bmatrix} e'_q - \begin{bmatrix} 0 & -X_q \\ X'_d & 0 \end{bmatrix} \begin{bmatrix} i_d \\ i_q \end{bmatrix} \tag{5}$$

By combining Eqs. (4) and (5) the equations are presented as

$$\begin{bmatrix} i_d \\ i_q \end{bmatrix} = \begin{bmatrix} Y_d \\ Y_q \end{bmatrix} e'_q - \frac{v_{pcc}}{Z_e^2} \begin{bmatrix} R_2 & X_1 \\ -X_2 & R_1 \end{bmatrix} \begin{bmatrix} \sin\delta \\ \cos\delta \end{bmatrix} \tag{6}$$

And which can be linearized as

$$\begin{bmatrix} \Delta i_d \\ \Delta i_q \end{bmatrix} = \begin{bmatrix} Y_d \\ Y_q \end{bmatrix} \Delta e'_q + \begin{bmatrix} F_d \\ F_q \end{bmatrix} \Delta\delta \tag{7}$$

For which

$$\begin{bmatrix} F_d \\ F_q \end{bmatrix} = \frac{v_{pcc}}{Z_e^2} \begin{bmatrix} -R_2 & X_1 \\ X_2 & R_1 \end{bmatrix} \begin{bmatrix} \cos\delta_0 \\ \sin\delta_0 \end{bmatrix} \Delta e'_q \tag{8}$$

In the Heffron–Phillips model, the input signals have relations with the variables by the K-constants. So the torque and real powers are presented as:

$$T_e = p = i_d v_d + i_q v_q$$

$$\Delta T_e = K_1 \Delta\delta + K_2 \Delta e'_q$$

$$\begin{bmatrix} K_1 \\ K_2 \end{bmatrix} = \begin{bmatrix} 0 \\ i_{q0} \end{bmatrix} + \begin{bmatrix} F_d & F_q \\ Y_d & Y_q \end{bmatrix} \begin{bmatrix} (X_q - X_d) i_{q0} \\ e'_{qo} + (X_q - X'_d) i_{d0} \end{bmatrix} \tag{9}$$

The equation of internal voltage in Eq. (1) is linearized as

$$(1 + sT'_{d0}) \Delta e'_q = \Delta E_{fd} - (X_d - X'_d) \Delta i_d \tag{10}$$

And using Eq. (7) we can write Eq. (11) as:

$$\left(1 + sT'_{d0}\right)\Delta e'_q = K_3\left[\Delta E_{fd} - K_4\Delta\delta\right]$$

$$K_3 = 1/\left[1 + \left(X_d - X'_d\right)Y_d\right]$$

$$K_4 = \left(X_d - X'_d\right)F_d \tag{11}$$

The state variables can be linked with output reactive power as Eq. (12).

$$Q = i_d v_q - i_q v_d$$

$$\Delta Q = K_5\Delta\delta Z + K_6\Delta e'_q$$

$$\begin{bmatrix} K_5 \\ K_6 \end{bmatrix} = \begin{bmatrix} 0 \\ i_{d0} \end{bmatrix} + \begin{bmatrix} F_d & F_q \\ Y_d & Y_q \end{bmatrix}\begin{bmatrix} e'_{q0} - 2X_d i_{d0} \\ -2X_q i_{q0} \end{bmatrix} \tag{12}$$

K_1 to K_5 are constants for small signal model of the generator. The equivalent model of grid integrated MG can be formed by Eqs. (9), (11) and (12). The small signal model of MG is presented in Fig. 4 where the governor parameters are to be set optimally to provide adequate damping torque. Here the SPV and wind sources are integrated. K_v, T_v are gain and time constants for the SPV system, K_{wg}, T_{wg} are gain and time constants for the wind energy conversion system.

The active and reactive powers at PCC are given by Eqs. (13) and (14):

$$P_{pcc} = v_{pcc}i_{Lined} + v_{pccq}i_{Lineq}$$

$$Q_{pcc} = v_{pcc}i_{Lined} - v_{pccd}i_{Lineq} \tag{13}$$

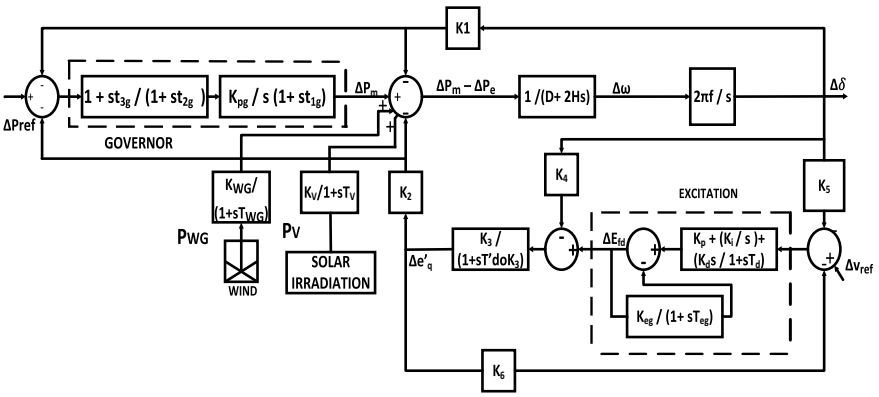

Fig. 4 Small signal MG modelling

$$\Delta P_{pcc} = \Delta v_{pcc} i_{Lined0} + v_{pccd0} \Delta i_{Lined} + \Delta v_{pccq} i_{Lined} + v_{pccq0} \Delta i_{Lineq}$$

$$\Delta Q_{pcc} = \Delta v_{pccq} i_{Lined0} + v_{pccq0} \Delta i_{Lined} - \Delta v_{pccd} i_{Lineq0} - v_{pccd0} \Delta i_{Lineq} \quad (14)$$

3 Governor Control Action and Objective Function

In the small signal model of Fig. 4, the governor parameters are Kg, t_{1g}, t_{2g}, t_{3g} and t_{4g} that represent the governor control action and these parameters are to be tuned by the RWGO algorithm. The flow chart of the proposed control scheme is presented in Fig. 5. The objective of the present work is to damp out the electromechanical oscillations followed by disturbances. So, an ITAE based objective function is chosen here.

$$J = \int_0^{tsim} t|\Delta\omega|dt \quad (15)$$

Subject to constraint

$$K_{pg}^{min} \leq K_{pg} \leq K_{pg}^{max},$$

$$t_{1g}^{min} \leq t_{1g} \leq t_{1g}^{max},\ t_{2g}^{min} \leq t_{2g} \leq t_{2g}^{max}$$

$$t_{3g}^{min} \leq t_{3g} \leq t_{3g}^{max}$$

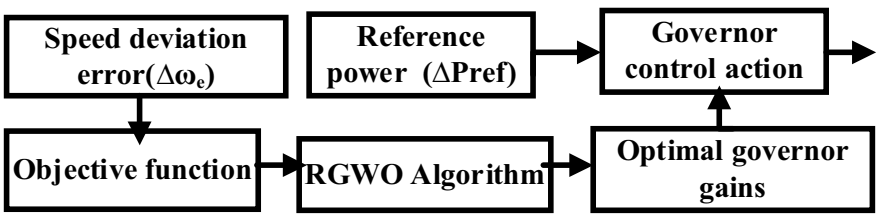

Fig. 5 Flow chart of proposed control scheme

4 Random Grey Wolf Optimiser Algorithm

GWO has been implemented by many researchers in different areas of applications which involve around 5–11 wolves in a group which are divided as per their participation in the hunting process. There are certain merits and demerits of GWO. The demerit is that the decision regarding the group which will guide the positions of the alpha group because this group dominates the wolf pack and also the problem is whether the alpha group takes the guidance of the guidance of the lower group or not. Due to this, for each iteration in the GWO, the position of different individual wolf packs needs updation, hence premature convergence may occur in GWO. To avoid this, certain changes may be implemented in the leader pack of GWO. Also, to avoid stagnation in local optimum, in [5] the leaders explore the searching space by random walk known as Random path Grey Wolf Optimisation (RGWO) followed by finally omega wolves being presented as:

$$W_N = \sum_{i=1}^{N} S_i \tag{16}$$

Si being a random step can be obtained by random distributions.

Two consecutive random wolves are related as

$$W_N = \sum_{i=1}^{N} S_i = \sum_{i=1}^{N-1} S_i + X_N = W_{N-1} + S_N \tag{17}$$

Initiation point of wolf denoted as x_0 & final as x_N, so the random wolves are represented as: -

$$x_n = x_0 + \alpha_1 S_1 + \alpha_2 S_2 + \cdots + \alpha_N S_N = x_0 + \sum_{i=1}^{N} \alpha_i S_i \tag{18}$$

where $\alpha_i > 0$ is a condition controlling step size Si.

The algorithm RW-GWO step size is taken from Cauchy distribution. As the variance of Cauchy distribution is infinity, it might take longer jump sometimes which is very effective at the time of stagnation and very useful from the leader wolves exploring the search space for getting the prey and guiding other wolves. Pseudcode for RGWO is given in Table 1.

5 Result and Analysis

Different case studies have been conducted in the present work to justify the optimal governor actions for power oscillation damping. These case studies include sudden and discrete variations in solar and wind generations. RWGO has been implemented

Table 1 Pseudo code of RGWO

Initializing Populations of grey wolf x_i(i = 1,2,3……., n)
Initializing c, b &μ
Initializing l = 1, the ITER number
Evaluating separate wolves fitness
Selecting α = fit wolf pack
β = best second wolf
δ = best third wolf
While l < ITER of maximum number
Evaluating each wolf fitness
For individual wolf leader
To find new position of y_i of leader x_i by randomising wolf
if $f(x_i) > f(y_i)$
leaders updatation
end
for individual wolf ω
updation of position & apply greedy move in present and updated position
end

to set the governor parameters optimally. The initial stage of synchronous generators is set at 0.8 pu and 0.17 pu for real and reactive power generations, respectively. In case 1, solar generation is a step raised by 0.3 pu and the system response is presented in Fig. 6. Bode plot is presented in Fig. 7 with the RGWO algorithm. Also, in case-1 wind source is varied suddenly by 0.4 pu and eigen values depicted in Table 2. Table 3 depicts optimal governor parameters with fixed PID excitation gains. The performance of RWGO has been compared with PSO, GWO techniques. In case 2, the solar and wind powers are varied discretely as per the pattern shown in Fig. 8. The system response has been represented in Figs. 9 and 10. From the results obtained in discrete variations of solar and wind penetrations, it has been observed that the parameters of the governor when tuned by RGWO provide better damping efficacy as compared to PSO, and GWO. Also the capability of the governor can be significantly improved by properly tuning of its parameters.

6 Conclusion

In a micro-grid, the oscillations brought by uncertain solar and wind penetrations create challenge for maintaining oscillatory stability, which has been presented in this work. The variations in solar and wind sources are executed with step and random pattern for a micro-grid integrated with grid, and subject to this the governor gains are set optimally by the RWGO algorithm in contrast with PSO and GWO algorithms. A random walk being incorporated with GWO makes it more robust for the optimization problem and the additional lead compensation brought by governor action can provide a better damping torque to enhance oscillatory stability of the micro-grid system. System eigen analysis and frequency response plots are obtained

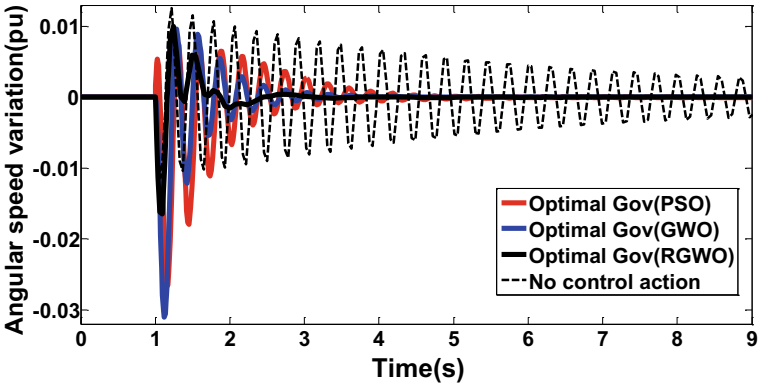

Fig. 6 Angular frequency variations

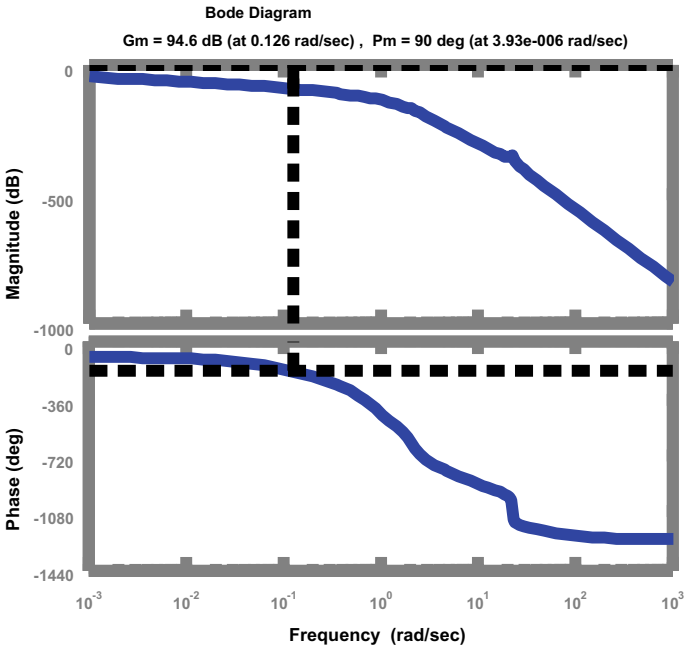

Fig. 7 Bode plot for case-1

for sudden variations in solar and wind generations. It has been concluded that synchronous generator's governor can improve oscillatory stability if its parameters are efficiently tuned by a suitable algorithm. This work was further extended with more renewable penetrations using the 33-bus micro-grid system.

Table 2 Prominent system eigen values with SPV/wind variations

Pv = 0.3 pu	*Pw = 0.4 pu*	*Pv = 0.3 pu*	*Pw = 0.4 pu*	*Pv = 0.3 pu*	*Pw = 0.4 pu*
PSO		GWO		RGWO	
−12.9729	−12.4374	−14.5330	−14.3472	−24.4627	−12.7238
−7.3532	−4.1811	−7.3470	−3.4602	−6.3470	−3.4602
−19.8917	−1.2721 + 8.3590i	−20.3417	−2.9923 + 8.1191i	−18.6417	−3.2423 + 2.0793i
−13.3909	−1.2721−8.3590i	−11.3209	−2.9923−8.1191i	−10.4909	−3.2423−2.0793i
−12.7067	−16.5580	−11.3206	−12.4120	−10.4406	−11.7744
−1.4711 + 3.7140i	−11.8351	−2.8211 + 3.7220i	−10.3451	−3.4801 + 2.2880i	−9.7851
−1.4711−3.7140i	−2.4422	−2.8211−3.7220i	−2.2289	−3.4801−2.2880i	−1.2243
−1.4244	−2.1633	−1.3666	−2.4332	−1.47667	−2.6443
−1.8883	−0.4043	−1.07661	−0.4438	−1.0798	−0.4469
−1.5419	−0.4969	−1.0762	−0.2026	−1.0766	−0.2067
−0.0959	−1.1790	−0.0723	−1.2470	−0.6799	−1.2442
0.0000	−0.0972	0.0000	−0.0421	0.0000	−0.0701
−0.9252	0.0000	−0.9529	0.0000	−0.9912	0.0000

Table 3 Optimized parameters

Gains	Excitation parameters fixed at $Kp = 26.4988$, $Kd = 2.5221$, $Ki = 87.8001$		
	PSO	GWO	RGWO
K_{pg}	1.8778	4.1277	7.2980
t_{1g}	0.9987	0.6142	0.1581
t_{2g}	0.1704	0.2788	0.6311
t_{3g}	0.4099	0.6788	0.8278

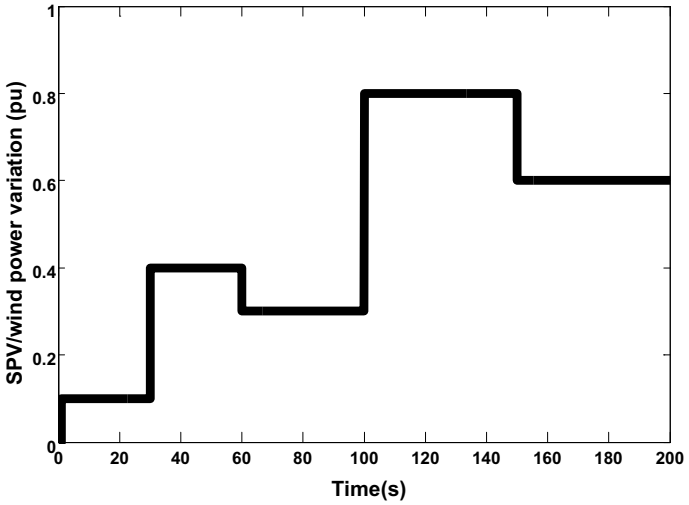

Fig. 8 SPV/wind power random variations

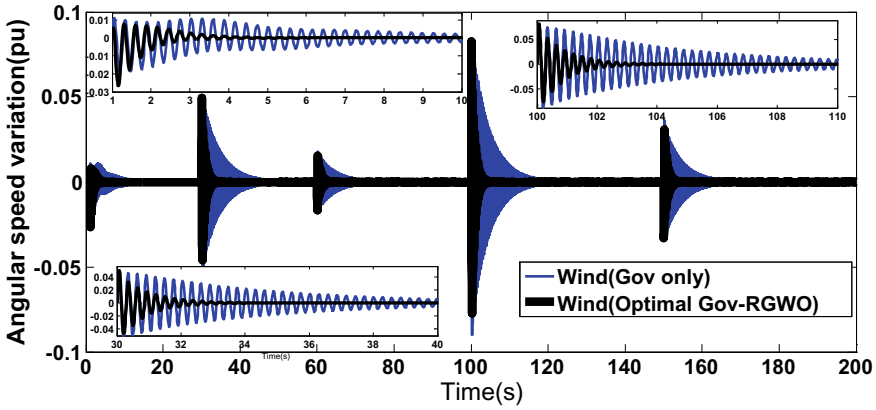

Fig. 9 Angular speed variations for case-2 for varying wind source

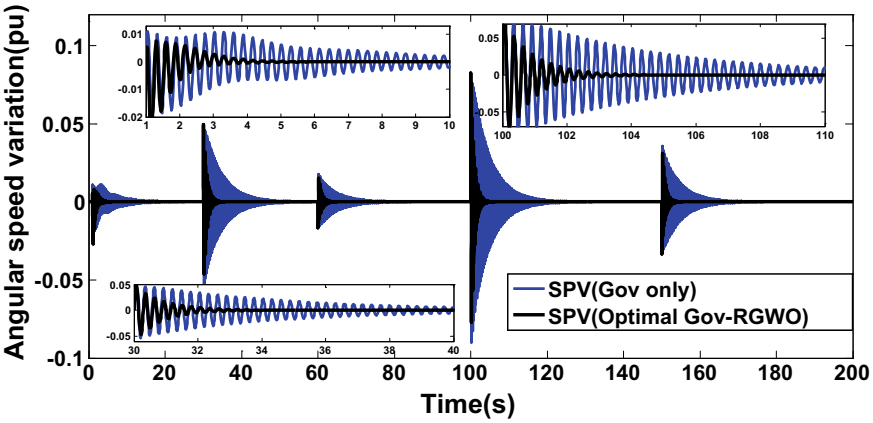

Fig. 10 Angular speed variations for case-2 for varying SPV source

References

1. B. Zaker, G.B. Gharehpetian, N. Moaddabi, Parameter identification of Heffron-Phillips model considering AVR using on-line measurements data, in *International. Conference on Renewable Energies and Power Quality (ICREPQ'14)*, (Cordoba, Spain, 2014)
2. M. Dehghani, S.K.Y. Nikravesh, State-space model parameter identification in largescale power systems. IEEE Trans. Power Syst. **23**(3), 1449–1457 (2008)
3. E. Ghahremani, M. Karrari, O.P. Malik, Synchronous generator third-order model parameter estimation using on-line experimental data. IET Gener. Transm. Distrib. **2**(5), 708–719 (2008)
4. N. Nahak, O. Satapathy, P. Sengupta, A new optimal static synchronous series compensator-governor control action for small signal stability enhancement of random renewable penetrated hydro-dominated power system. Optim. Control Appl. Method **43**(3), 593–617 (2022). https://doi.org/10.1002/oca.2844
5. N. Nahak, O. Satapathy, Investigation and damping of electromechanical oscillations for grid integrated micro grid by a novel coordinated governor-fractional power system stabilizer, in *Energy Sources, Part A: Recovery, Utilization, and Environmental Effects* (2021). https://doi.org/10.1080/15567036.2021.1942596
6. N. Nahak, S.R. Sahoo, R.K. Mallick, Small signal stability enhancement of power system by modified GWO optimized UPFC based PI-lead-lag controller, in *Advances in Intelligent System and computing*, vol. 817 (Springer, 2019). https://doi.org/10.1007/978-981-13-1595-4_21
7. N. Nahak, M.M. Nabi, D. Panigrahi, R.K. Pandey, A. Samal, R.K. Mallick, Enhancement of dynamic stability of wind energy integrated power system by UPFC based cascaded PI with dual controller. IEEE Int. Conf. Sustain. Energy Technol. Syst. (ICSETS) , 150–155 (2019)
8. T.N. Preda, N. HadjSaid, Dynamic equivalents of active distribution grids based on model parameters identification, in PES general meeting conference & exposition, (IEEE, 2014) pp. 1–5
9. C. Changchun, C. Xiangqin, Equivalent simplification method of micro-grid. TELKOMNIKA **11**(9), 5461–5470 (2013)
10. B. Zaker, G.B. Gharehpetian, M. Karrari, N. Moaddabi, Simultaneous parameter identification of synchronous generator and excitation system using online measurements. IEEE Trans. Smart Grid **7**(3), 1230–1238 (2016)
11. B. Zaker, G.B. Gharehpetian, M. Karrari, Improving synchronous generator parameters estimation using d-q axes tests and considering saturation effect. IEEE Trans. Ind. Inf. **14**(5), 1898–1908 (2018)

12. P.N. Papadopoulos, T.A. Papadopoulos, P. Crolla, A.J. Roscoe, G.K. Papagiannis, G.M. Burt, Measurement-based analysis of the dynamic performance of microgrids using system identification techniques. IET Gener. Transm. Distrib. **9**(1), 90–103 (2015)
13. A.M. Azmy, I. Erlich, P. Sowa, Artificial neural network-based dynamic equivalents for distribution systems containing active sources. IEE Proc. Gener. Transm. Distrib. **151**(6):681–688 (2004)
14. A.M. Azmy, I. Erlich, Identification of dynamic equivalents for distribution power networks using recurrent ANNs, in *Power systems conference and exposition*, (IEEE PES, 2004), pp. 348–53
15. J.V. Milanovic, Z.S. Mat, Validation of equivalent dynamic model of active distribution network cell. IEEE Trans. Power Syst. **28**(3), 2101–2110 (2013)
16. B. Zaker, G.B. Gharehpetian, M. Karrari, Small signal equivalent model of synchronous generator-based grid connected microgrid using improved Heffron-Phillips model. Electr. Power Energy Syst. **108**, 263–270 (2019)
17. S. Gupta, K. Deep, A novel random walk grey wolf optimizer. Swarm Evol. Comput. (2017). https://doi.org/10.1016/j.swevo.2018.01.001

Classical PID Based Speed Control of DC Machines with Voltage Controlled DC/DC Converter

A. Jaswanth, D. S. V. Saravana, V. Bharath Kumar, Y. V. Pavan Kumar, D. John Pradeep, and Ch. Pradeep Reddy

Abstract A DC-DC converter usually converts fixed DC voltage to variable DC output voltage. In a chopper-based control, the motor can be also used as a generator in the absence of mechanical energy. To achieve better results for mechanical works, speed control plays a crucial role owing to the fact that it provides a range of speeds that can reduce the maintenance and servicing costs consequently saving time and finances. Classical PID controllers are used to controlling the speed of the DC-DC converter as they are more feasible and easy to use. In this paper, to obtain precise gain parameters, PID tuning methods like OLTR, EPI, overshoot, and closed-loop are implemented to control the speed of the DC motor. The model design and the control methods are done in MATLAB/Simulink software. The results depict the optimum method to be used for tuning the controller to achieve the best stable response of the DC machine.

Keywords DC-DC converter · Two quadrant chopper drive · Speed control · PID controller

A. Jaswanth · D. S. V. Saravana · V. B. Kumar · Y. V. P. Kumar (✉) · D. J. Pradeep
School of Electronics Engineering, VIT-AP University, Amaravati, Andhra Pradesh-522237, India
e-mail: pavankumar.yv@vitap.ac.in

A. Jaswanth
e-mail: jaswanth.18bec7076@vitap.ac.in

D. S. V. Saravana
e-mail: saravana.18bec7091@vitap.ac.in

V. B. Kumar
e-mail: bharath.18bec7093@vitap.ac.in

D. J. Pradeep
e-mail: john.darsy@vitap.ac.in

Ch. P. Reddy
School of Computer Science and Engineering, VIT-AP University, Amaravati, Andhra Pradesh-522237, India
e-mail: pradeep.ch@vitap.ac.in

J. Kumar et al. (eds.), *Control Applications in Modern Power Systems*, Lecture Notes in Electrical Engineering 974, https://doi.org/10.1007/978-981-19-7788-6_10

1 Introduction

DC-DC converters are used to get a variable voltage from a fixed voltage and are used in many industrial applications. Analogous to a transformer, the voltage can be stepped up or stepped down depending on the application. The advantage of DC-DC converters is high efficiency with control over acceleration and quick dynamic response. In the dc-to-dc converter which is also known as a chopper, the motor can also be used as a generator. In the absence of any mechanical energy as input, the DC machine can be used as a generator with the help of a chopper device. The application of these converters can be seen in electric vehicles because of regenerative braking, which results in saving energy. Furthermore, these converters are used in cellular phones, laptops, automobiles, tram cars, and fork trucks.

In the context of their applications, these converters are used because of their flexibility, low cost, and high reliability, where position and speed control of a motor is required. Due to the disturbances that occur in a converter, the load may not result in a desired constant output. Therefore, to attain a constant gain, a controller is needed. Different types of controllers are used to improve stability as well as efficiency. Speed control is a productive and profitable alternative with regard to energy consumption and it provides many options to operate the machines with almost no heat losses. PID controllers are used traditionally to control the DC machine. The best results obtained for a controller cannot be generalized to other models. Moreover, PID is an offline controller which neglects real-time disturbances. To resolve this limitation, online controllers which are based on AI are used. Using these intelligent speed control methods, the servicing costs and maintenance of the system are reduced favourably which eventually leads to saving energy, time, and cost. In this paper, a PID controller is used to achieve the required speed from a two-quadrant chopper device. To find a suitable method that provides a fast and stable response along with accuracy, different PID methods mentioned in Fig. 1 are used. The acronyms used in the paper are mentioned in Table 1.

A chopper works at very high speeds and it attaches and detaches the load from the source to provide a chopped DC output. A chopper is a semiconductor device. The chopper devices are classified into 5 types namely Class A, B, C, D, and E based on the V-I plane characteristics. These types of choppers are reported in [1].

There are different types of regulations and each has its pros/cons. Different types of topologies are reported in [2]. However, to find the effectiveness of any topology, all the critical factors should be considered with qualitative and quantitative analysis, and this analysis is reported in [3]. In [4], a study of DC-DC converters is reported where the advantages, classification, simulation, filters, limitations, and topologies are given. In order to select the best filter for a converter, different analyses are done as reported in [5]. As stated earlier about the usage of a chopper in automobiles, the use of a chopper in an electric vehicle is reported in [6]. In this paper, a two-quadrant chopper device is used and the operation of a two-quadrant chopper is reported in [7]. The speed control of the chopper device without using a PID controller has been reported in [8]. In [9], the speed regulation of the DC motor is obtained without

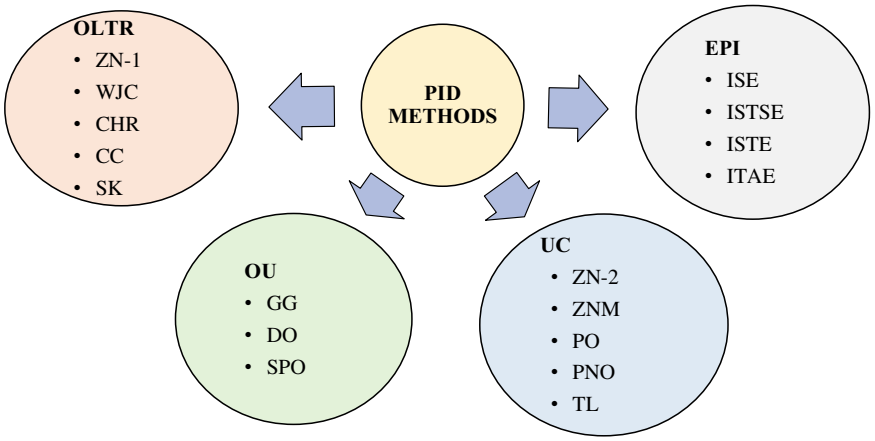

Fig. 1 Methods for tuning (designing) PID gains

Table 1 Methods applied to compute PID parameters

OLTR = Open loop transient response	WJC = Wang-Jang-Chan
ZN-1 = Ziegler–Nichols Method 1	CHR = Chien Hrones Reswick
EPI = Error performance index	CC = Cohen Coon
ISTE = Integral of squared time multiplied by square error	SK = Skogestad
ITAE = Integral time absolute error	ISE = Integral square error
UC = Ultimate gain/cycle method	ZNM = Pessen overshoot
ZN-2 = Ziegler Nichols method 2	TL = Tyreus Luyben
ZN3 = Ziegler Nichols modified	GG = Good gain
PNO = Pessen no overshoot	DO = Damped oscillations
OU = Overshoot/undershoot method	SPO = Set point overshoot

considering all the PID tuning methods. In order to achieve the best results, all the PID tuning methods need to be tested. In designing the controller only Tyreus–Luyben, Modified Ziegler-Nichols, and Ziegler-Nichols are used in a closed-loop and Cohen-Coon, Chien, Hrones, and Reswick, Ziegler-Nichols are used in open-loop tuning ignoring other methods as given in [10]. In this paper, all methods viz., OLTR, Closed-loop, EPI, and Overshoot are implemented. By considering the time response and the stability analysis, the best method is reported. In order to address the limitations of the PID controllers, ANN methods can be realized as given in [11].

2 System Modelling

The two quadrant chopper consists of two controllable semiconductors with two diodes as shown in Fig. 2. If two switches are fired together, the supply voltage becomes short-circuited. It consists of 2 modes, motoring mode and regenerative braking mode. A pair of transistor and diode (T1 & D1) operate to provide control for motoring operation and another pair of Transistor and Diode (T2 & D2) operate to provide control for regenerative braking operation. Initially, when T1 is 'on', the motor operation is initiated, during which, the inductor gets charged. When switching takes place from T1 to T2, the inductor discharges, and EMF is established at the armature. When T2 is 'on', the inductor charges and while switching from T2 to T1 the established EMF and the inductor voltage are greater than the source voltage, so, it acts as a generator. The source voltage, generally a battery is discharged in motor operation and it gets charged during generator operation. Shifting of control from T1 to T2 shifts operation from motoring to regenerative braking and vice versa. A 2-quadrant chopper's operation is given in [7].

When the voltage given to the armature circuit of the dc/dc converter is controlled through the duty cycle(k), it is called a voltage-controlled dc/dc converter. Due to the usage of a permanent magnet, the field equation is removed and L_{af}*I_f (where 'L_{af}' is mutual inductance and 'I_f' is field current) is replaced with a constant term k_v. The block illustration for controlling the speed with a voltage-controlled chopper is referred to in Fig. 3. Here w_r* is the reference speed, and the error value is fed to the PID controller. The output of the PID controller is the duty cycle 'k'. This signal is multiplied by the source voltage and fed to the summer block. The output signal of the summer is passed to another block which gives the armature current as output I_a. When this current signal is passed through a gain block with gain k_v, we get the output T_e. This signal is passed to the summer block along with load torque T_l. The output is passed through a gain block which gives the speed w_r which is taken as output and also feedback to the system. The procedure of OLTR, UC, and OU methods in order to find the gain parameters is reported in [12] and for EPI methods the procedure is reported in [13]. The system parameters [14] are considered as

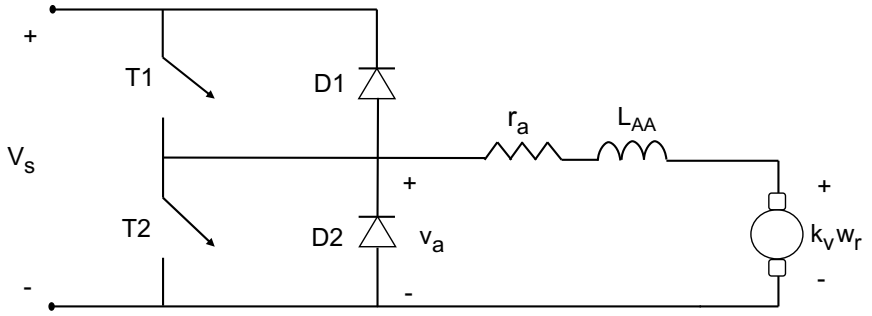

Fig. 2 Two-quadrant chopper drive system

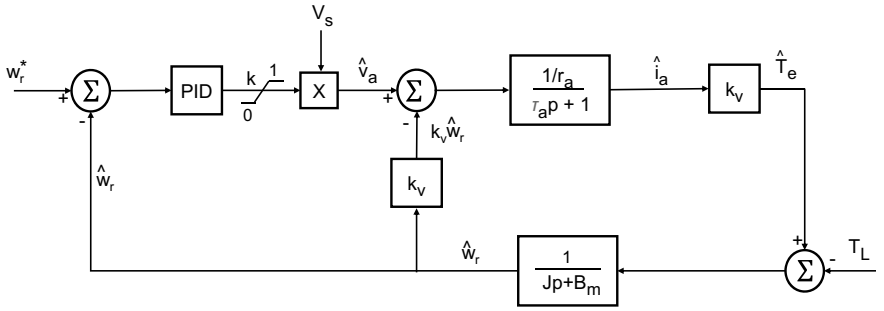

Fig. 3 Block diagram of machine speed regulation with DC/DC converter

$T_l = 5$ Nm, $B_M = 0.002953$ N/m(rad/sec), $J = 0.0607$ kgm^2, $k_v = 1.25$, $R_a = 0.65$ Ω, $L_{aa} = 0.008$ H, $v_s = 10$ V, $w_r* = 1500$ rpm.

3 Results and Discussion

The PID methods are classified into 4 categories that contain these gain computational methods. There are 17 methods in total and the gain results of Proportional Gain (K_p), Derivative Gain (K_d), and Integral Gain (K_i), obtained will be different for each method. To reduce the cost of implementation, we need to keep the gain parameters as low as possible. From Table 2 we can see that ITAE has low K_p, K_i and SK has low K_d values, thus these are the superior methods among all the PID methods.

3.1 Transient Analysis with Time Domain Parameters

Various methods give different transient responses in their time-domain analysis. To find the superior method, several factors considered are rise time, delay time, peak time, settling time, and peak over-shoot (%). The method with low values is considered to be superior. Figure 4 depicts the time response of the ZN1 method and the system enters the steady-state around 0.25 s. Figure 5 depicts the time response of the WJC method and the system enters the steady-state around 0.6 s. Figure 6 illustrates that the system response of the CC method reaches the steady-state around 0.9 s. The system response of the SK method enters into a steady state around 1.25 s and it is shown in Fig. 7. Figure 8 illustrates that the system reaches the steady-state around 5 s for the CHR method. Figure 9 depicts the unstable time response of the PNO method. Figure 10 illustrates that the system response of the ZNM method reaches the steady-state at 0.2 s. Figure 11 depicts the unstable time response of the ZN2 method.

Table 2 Calculated PID gain values with various methods

Methods		K_P	K_I	K_D	T_I	T_D
OLTR methods	1.ZN-1	7.48	576.09365	0.0242	0.01298	0.00324
	2.WJC	540	6086.15200	3.4565	0.08873	0.00640
	3.CHR	0.005	0.12398	0.0000162	0.04033	0.00324
	4.CC	0.0113	0.71538	0.0000269	0.01584	0.00237
	5.SK	0.1781	0.95119	0.0000000	0.18720	0.00000
EPI methods	1.ISTSE	0.0044828	0.10546510	0.0000133	0.042505	0.002958
	2.ITAE	0.0038094	0.07296764	0.0000086	0.052207	0.002269
	3.ISTE	0.0042182	0.09794073	0.00001051	0.043069	0.002491
	4.ISE	0.0045087	0.12699406	0.0000176	0.035503	0.003883
OU methods	1.GG	0.28	6.00214	0.003266	0.0467	0.011663
	2.DO	0.26	0.17978	0.093870	1.4452	0.361301
	3.SPO	0.22	4.69835	0.001853	0.0470	0.008397
UC methods	1.ZN-2	120	22,748.82	0.1583	0.00528	0.0013188
	2.ZNM	90	3877.64	0.1507	0.02321	0.0016746
	3.PO	66	12,511.85	0.2321	0.00528	0.0035167
	4.PNO	40	11,374.41	0.2110	0.00352	0.0052750
	5.TL	90	3877.64	0.1507	0.01055	0.0016746

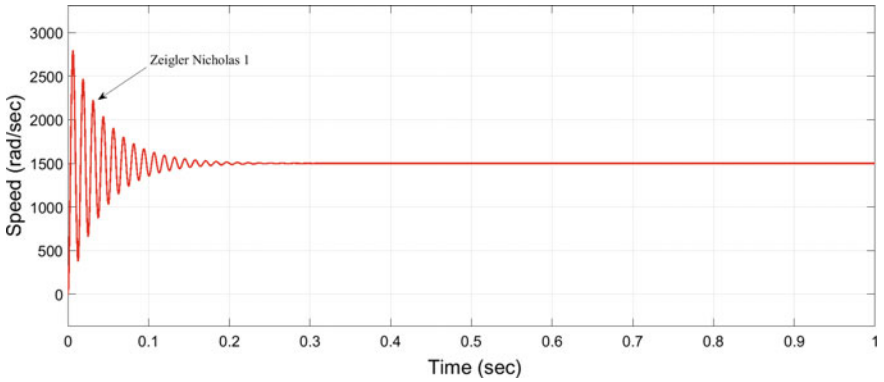

Fig. 4 Time response of the system for the ZN1 method

The system response of the TL method enters into a steady state around 0.2 s and it is shown in Fig. 12. Figure 13 depicts the unstable time response of the PO method. Figure 14 illustrates that the system reaches the steady-state around 8.5 s for the ITAE method. Figure 15 illustrates that the system response of the ISTSE method reaches the steady-state around 0.5 s. The system response of the ISTE method enters into steady-state around 0.5 s and it is shown in Fig. 16. Figure 17 depicts the time

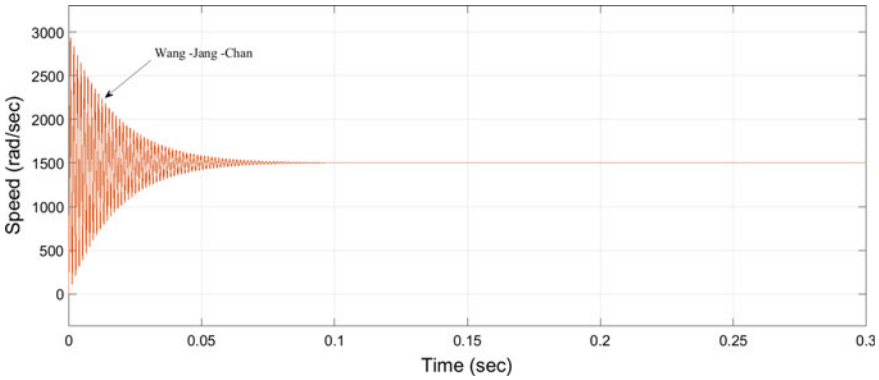

Fig. 5 Time response of the system for the WJC method

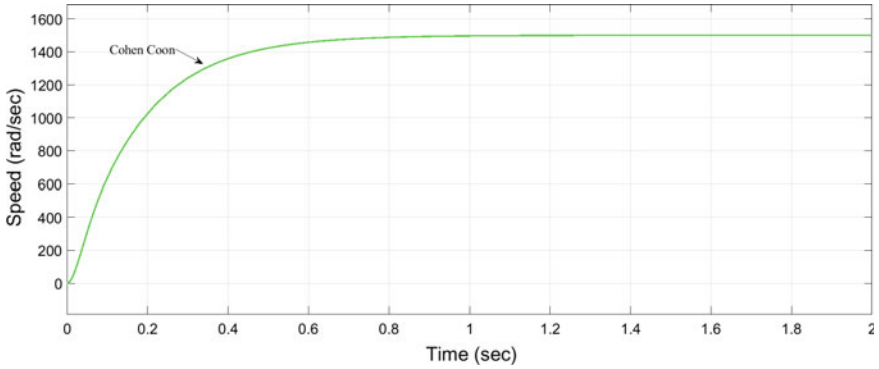

Fig. 6 Time response of the system for the CC method

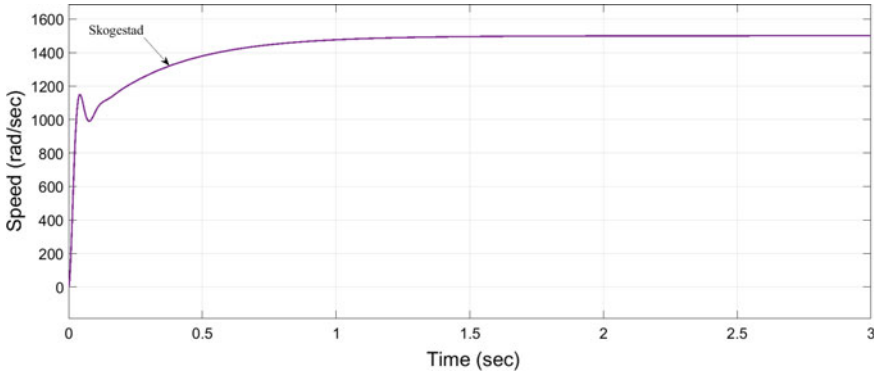

Fig. 7 Time response of the system for the SK method

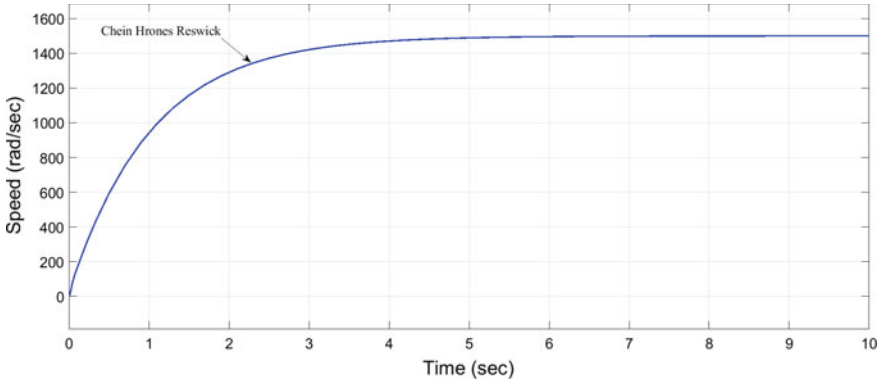

Fig. 8 Time response of the system for the CHR method

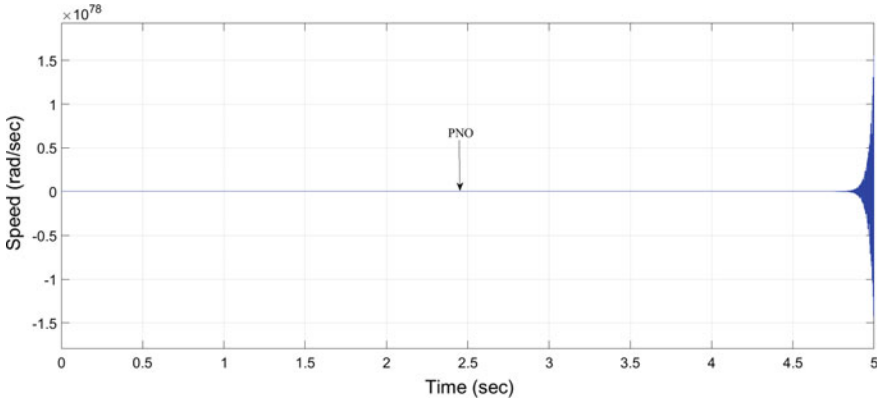

Fig. 9 Time response of the system for the PNO method

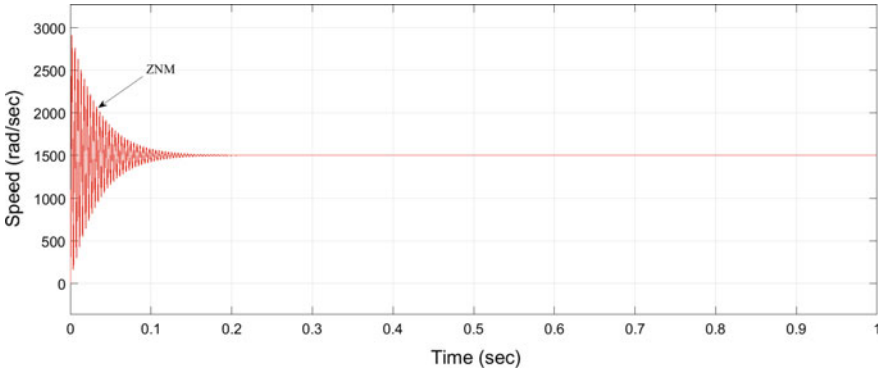

Fig. 10 Time response of the system for the ZNM method

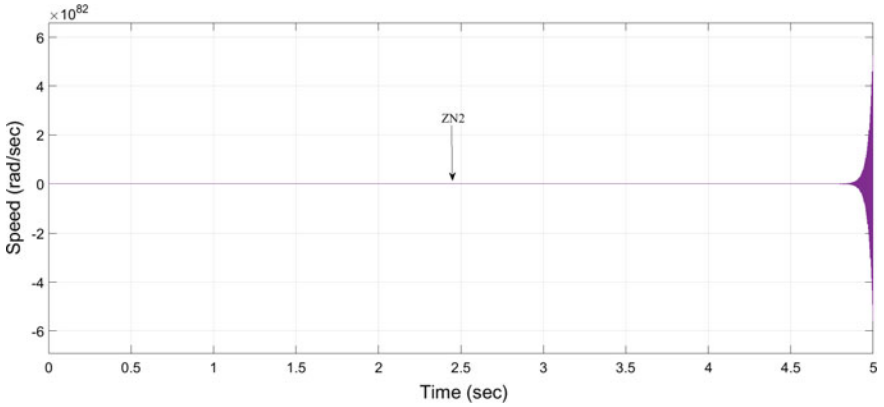

Fig. 11 Time response of the system for the ZN2 method

response of the ISE method and the system enters the steady-state around 4.5 s. Figure 18 illustrates that the system response of the DO method reaches the steady-state around 7 s. The system response of the SPO method enters into steady-state at around 0.225 s and it is shown in Fig. 19. Figure 20 illustrates that the system response of the GG method reaches the steady-state around 0.175 s. From Table 3 we can find that WJC gives an improved response in terms of peak time, rise time, delay time, and settling time. And, the DO method shows an improved response in terms of Peak Overshoot (%).

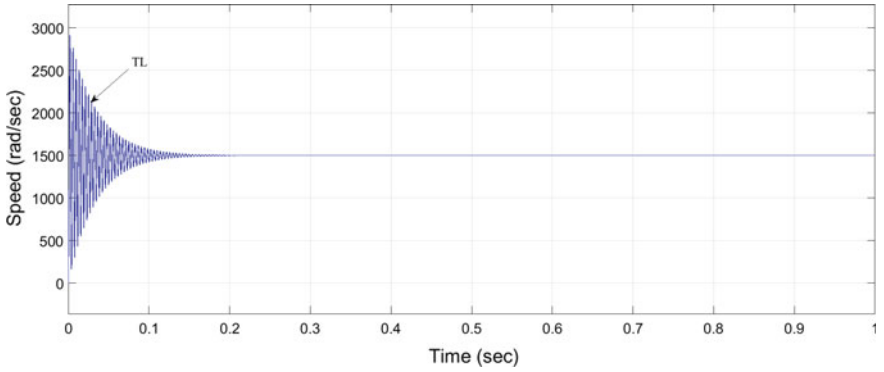

Fig. 12 Time response of the system for the TL method

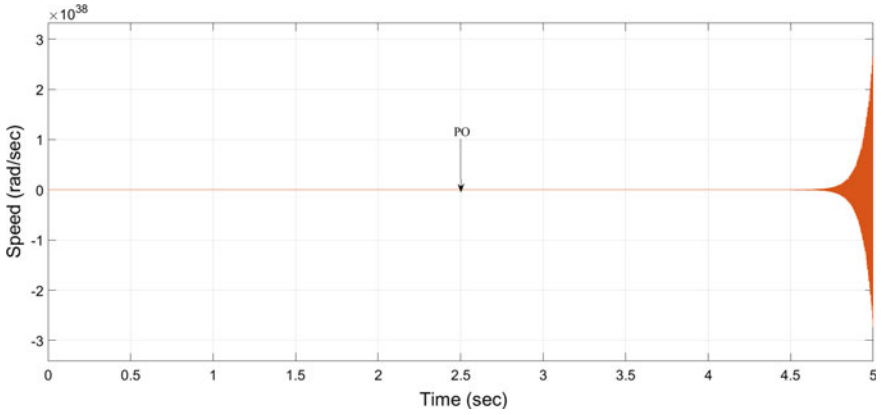

Fig. 13 Time response of the system for the PO method

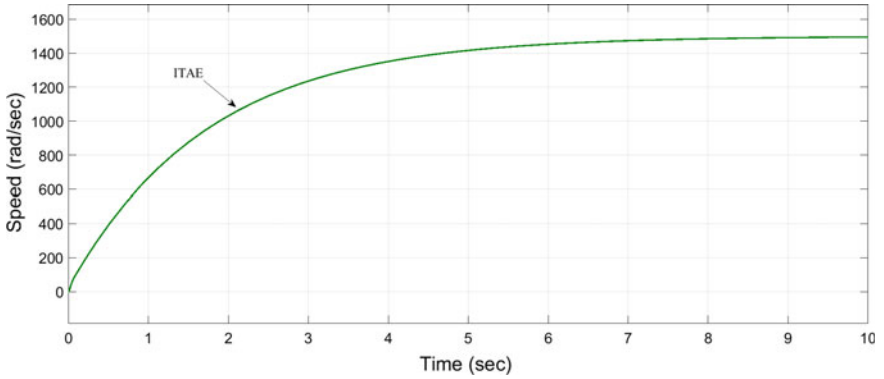

Fig. 14 Time response of the system for the ITAE method

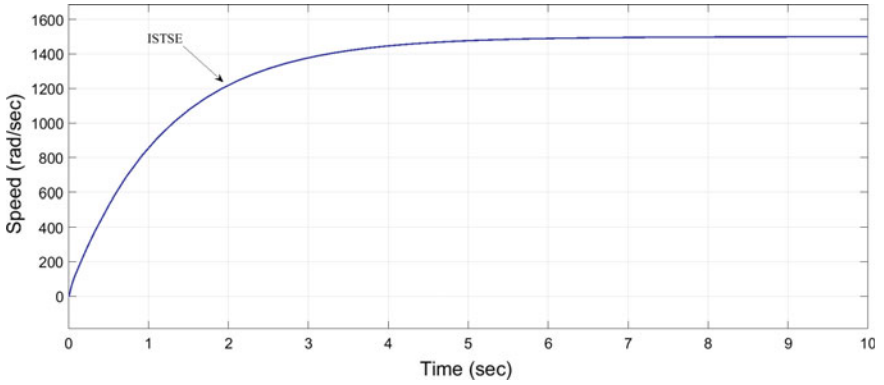

Fig. 15 Time response of the system for the ISTSE method

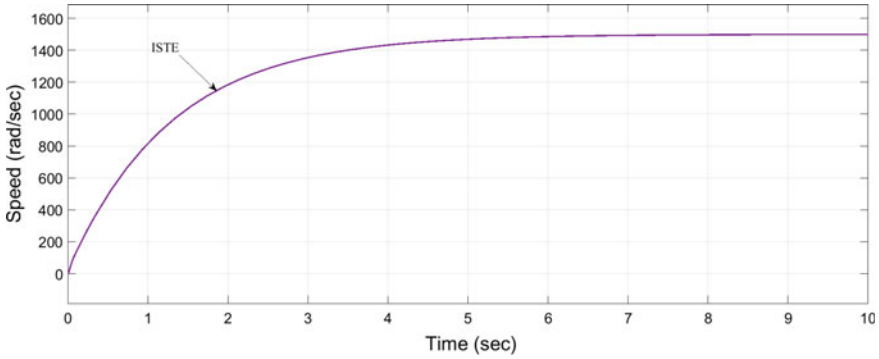

Fig. 16 Time response of the system for the ISTE method

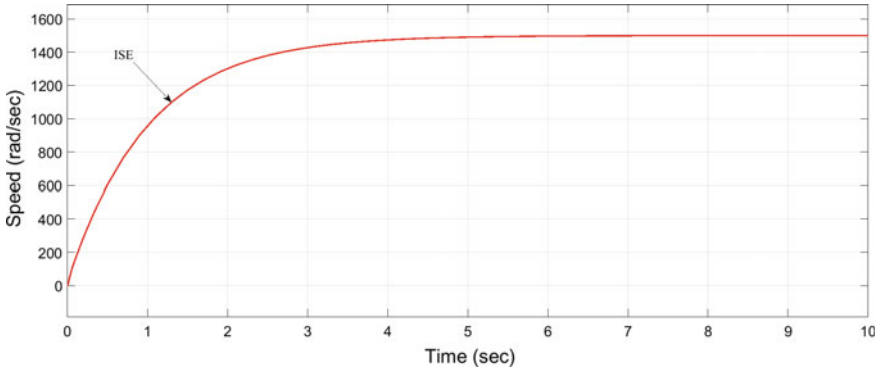

Fig. 17 Time response of the system for the ISE method

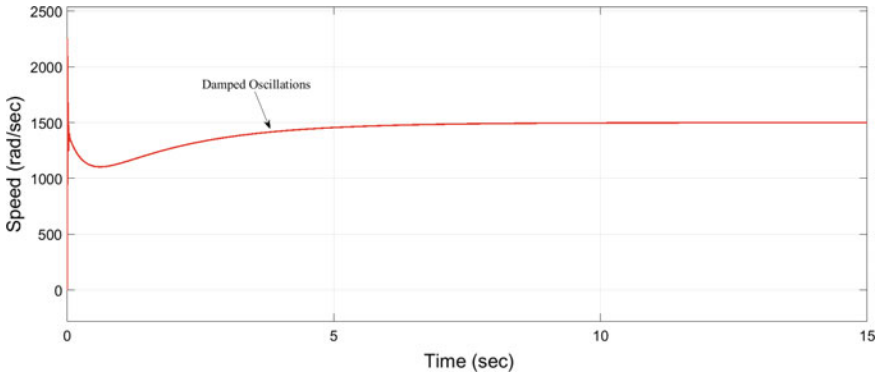

Fig. 18 Time response of the system for the DO method

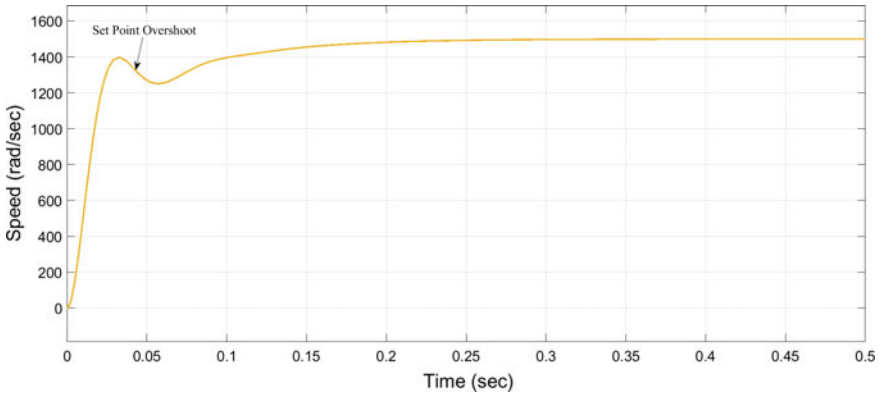

Fig. 19 Time response of the system for the SPO method

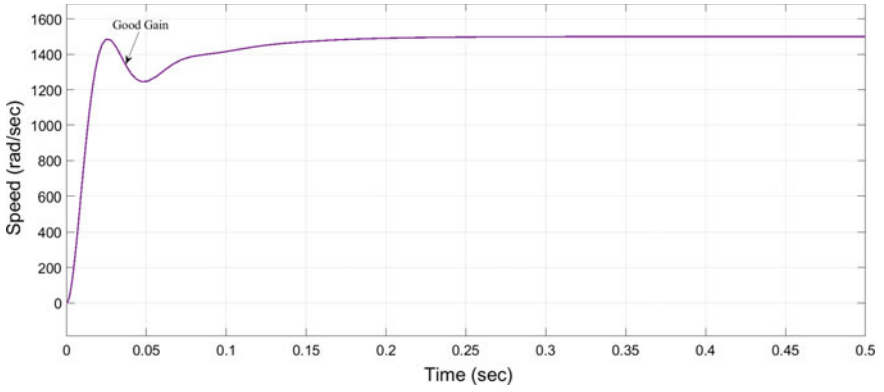

Fig. 20 Time response of the system for the GG method

3.2 Stability Analysis

To check the stability of the system, several types of analysis can be performed [15–17]. In this paper, the analysis is performed using Pole Zero Plot. For the classification of the system as stable, all poles should lie on the left of the s-plane, in this way all the requirements are reported in [15, 16]. In Table 4, the values of poles and zeroes of all methods are obtained after performing the stability analysis. Figure 21 shows that all poles lie on the left part of the s-plane indicating the CC method is a stable system. Figure 22 illustrates that the system using the CHR method is stable as all the poles lying on the left part of the s-plane. The stability response for ITAE provides that the system is stable with the fact that all the poles are located on the left half of the s-plane and this is depicted in Fig. 23. Figure 24 shows all poles lying on the left part of the s-plane indicating the ISTE method as a stable system.

Table 3 Time domain parameters calculated for all methods

Tuning Methods		Delay Time (sec)	Rise Time (sec)	Peak Time (sec)	Peak Overshoot (%)	Settling Time (sec) (Tolerance–5%)	Settling Time (sec) (Tolerance–2%)
OLTR methods	1.ZN1	0.002108	0.003211	6.053119	1295	0.1265715	0.17061
	2.WJC	0.00022	0.00033191	0.0006442	1441.02748	0.0518325	0.06596388
	3.CHR	0.695754	2.25350905	NA	NA	3.055502	3.9945827
	4.CC	0.12348	0.3609522	NA	NA	0.5051932	0.6567612
	5.SK	0.02116	0.4261106	NA	NA	0.647144	0.9281528
EPI methods	1.ISTSE	0.82171	2.6466603	NA	NA	3.591592	4.9103
	2.ITAE	1.18435	3.82963607	NA	NA	5.195	7.106
	3.ISTE	0.88381	2.8476000	NA	NA	3.866	5.288
	4.ISE	0.682255	2.1884505	NA	NA	2.9747214	4.0661020
OU methods	1.GG	0.01059	0.01506855	NA	NA	0.1062555	0.14783
	2.DO	2.26082	3.6131011	6.2221809	755.65947	4.033	5.7236
	3.SPO	0.013438	0.0218373	NA	NA	0.122524	0.17277241
UC methods	1.ZN2	Unstable					
	2. ZNM	0.0006401	0.00096744	0.0018609	1,412.40	0.100322	0.1319368
	3.PO	Unstable					
	4.PNO	Unstable					
	5.TL	0.0006401	0.00096744	0.0018609	1,412.40	0.1003222	0.1319368
Superior Method		WJC	WJC	GG	GG	WJC	WJC

Table 4 Poles and zeros calculated for all methods for stability analysis

Tuning methods		Poles	Zeros
OLTR methods	1.ZN-1	−23.4 + 50.3i, −23.4–50.3i, −67.3 + 36.5i	−67 + 36.8i, −67–36.8i, −67.3−36.5i
	2.WJC	−56.7 + 4.77e + 03i, −56.7–4.77e + 03i, −55.5, −12.4	−55.5, −12.4
	3.CHR	−99.2, −40.6 + 40.7i, −0.975	−65.8, −28.5, −40.6–40.7i
	4.CC	−98.6, −38.3 + 40.4i, −38.3–40.4i, −6.03	−65.9 + 27.5i, −65.9–27.5i
	5.SK	−39 + 77.6i, −39–77.6i, −3.24	−5.34,
EPI methods	1.ISTSE	−99.3, −40.6 + 40.6i, −0.83, −40.6–40.6i	−69, −26.3,
	2.ITAE	−99.6, −40.6 + 40.5i, −40.6–40.5i, −0.574	−76.8, −20.3,
	3.ISTE	−99.5, −40.5 + 40.5i, −0.771, −40.5–40.5i	−73.3, −25.4
	4.ISE	−99.1, −40.6 + 40.5i, −40.6–40.5i, −1	−56.2, −36.1,
OU methods	1.GG	−61.8 + 123i, −61.8-123i, −33.2, −24.5	−28 + 14.3i, −28–14.3i
	2.DO	−88.7 + 501i, −88.7-501i, −3.3, −0.541	−1.36–0.158i
	3.SPO	−56.1 + 99.9i, −56.1–99.9i, −51.2, −18	−33 + 8.39i, −33–8.39i
UC methods	1.ZN-2	−128 + 19.8i, −128–19.8i, 37 + 1.87e + 03i, 37–1.87e + 03i	−128 + 19.6i, −128–19.6i
	2.ZNM	−29.4 + 1.64e + 03i, −29.4–1.64e + 03i, −53.1, −69.4,	−53.2, −69.3,
	3.PO	16.4 + 1.52e + 03i, 16.4–1.52e + 03i, −107 + 50.3i, −107–50.3i	−107 + 50.5i, −107–50.5i
	4.PNO	34.9 + 1.26e + 03i,34.9–1.26e + 03i, −125 + 52.4i, −125–52.4i	−126 + 52.8i, −126–52.8i
	5.TL	−29.4 + 1.64e + 03i,−29.4–1.64e + 03i,−53.1,−69.4	−53.2, −69.3
Superior method		ITAE	

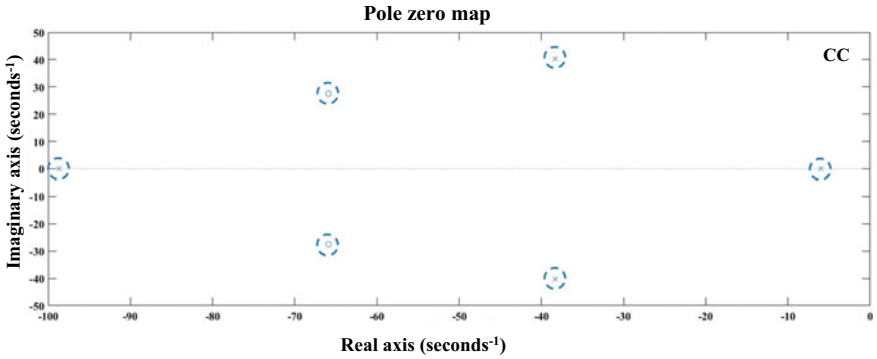

Fig. 21 System response with CC method for the stability study

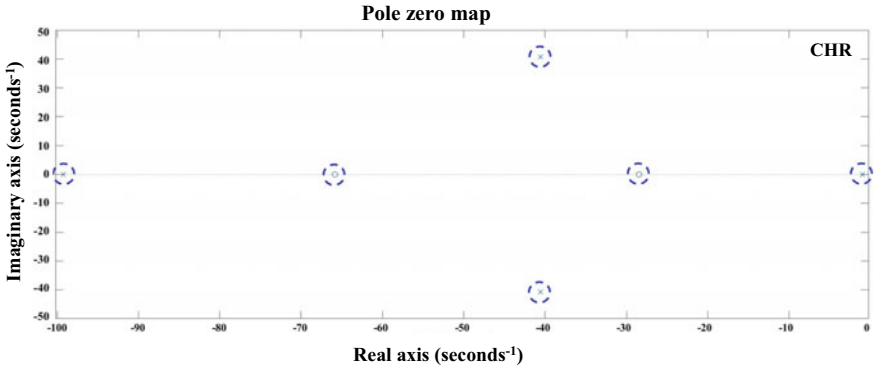

Fig. 22 System response with CHR method for the stability study

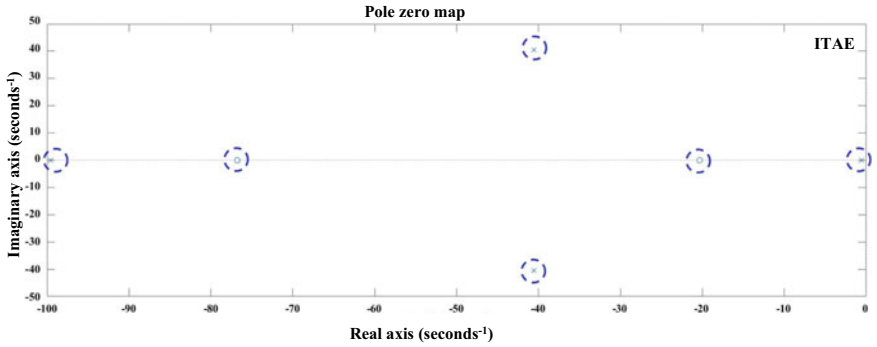

Fig. 23 System response with ITAE method for the stability study

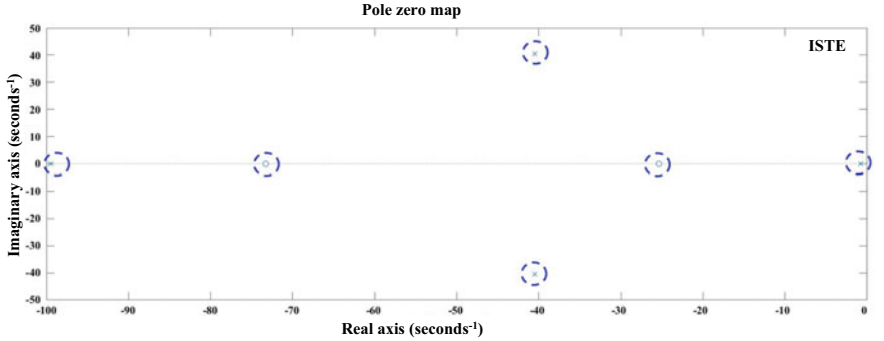

Fig. 24 System response with the ISTE method for the stability study

Figure 25 illustrates that the system using the TL method is stable as all the poles lie on the left part of the s-plane. The stability response for ZNM provides that the system is stable with the fact that all the poles lie on the left part of the s-plane and this is depicted in Fig. 26. Figure 27 illustrates that the system using the DO method is stable as all the poles lie on the left part of the s-plane. Figure 28 shows all poles lie on the left part of the s-plane indicating the GG method as a stable system. However, the poles lie on the right part of the s-plane in the stability response of ZN2 depicted in Fig. 29. From Table 4, it can be observed that the superior method is ITAE which indicates that ITAE is the most stable among all other methods because the pole lies far away from the origin on the left part of the s-plane.

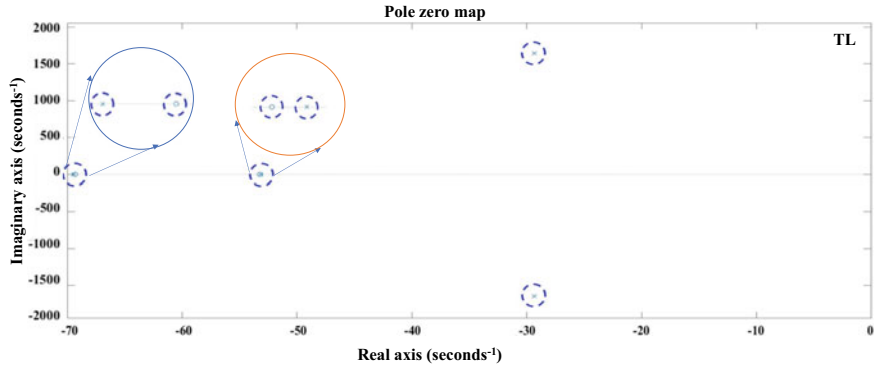

Fig. 25 System response with TL method for the stability study

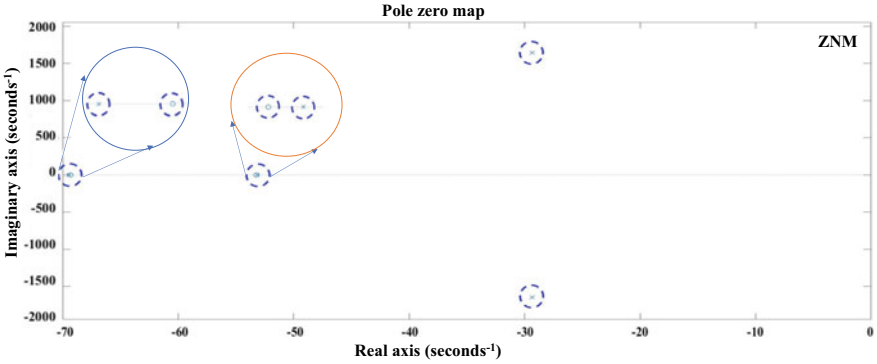

Fig. 26 System response with ZNM method for the stability study

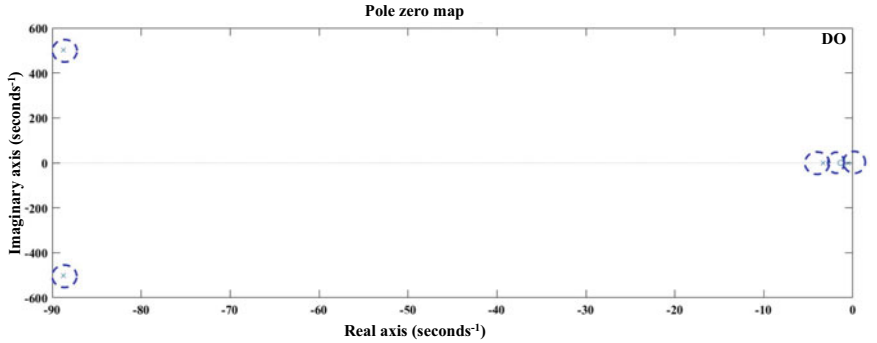

Fig. 27 System response with DO method for the stability study

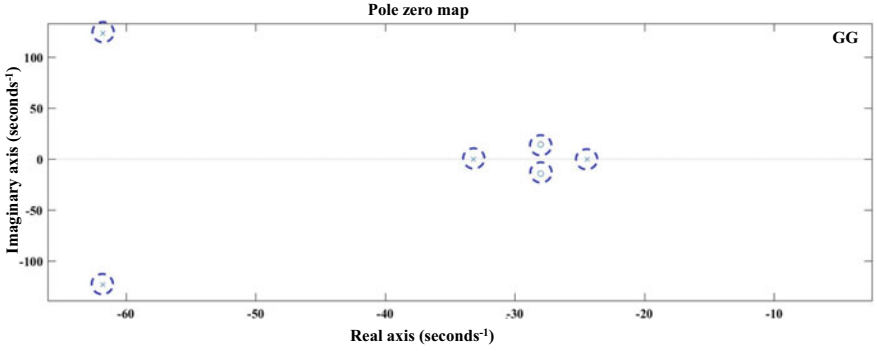

Fig. 28 System response with GG method for the stability study

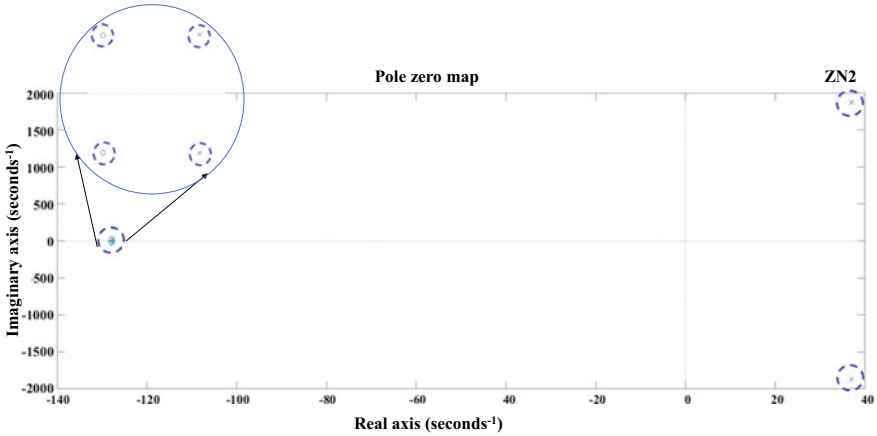

Fig. 29 System response with ZN2 method for the stability study

4 Conclusions

Thus, in this work, all the key classical methods of finding PID controller parameters for speed control of voltage-controlled DC-DC converter model are presented. To find the best method, the time domain analysis and stability analysis have been performed. From the time domain analysis, WJC is the best method among all the methods and GG gives the best peak time and peak overshoot as it does not have any peaks in the response. In the stability analysis, ITAE gives the best stability compared to all other methods.

Acknowledgements This work was supported by Project Grant No: SRG/2019/000648, sponsored by the Start-up Research Grant (SRG) scheme of the Science and Engineering Research Board (SERB), a statutory body under the Department of Science and Technology (DST), Government of INDIA.

References

1. N.B. Krishna, B. Nagaraju, P.V. Kumar, Design and implementation of four quadrant DC drive using chopper, in *International Conference on Electrical, Electronics, Signals Communication and Optimization (EESCO)*, (India, 2015), pp. 1–5
2. S.A. Lopa, S. Hossain, M.K. Hasan, T.K. Chakraborty, Design and simulation of DC-DC converters. Int. Res. J. Eng. Technol. (IRJET) **3**(1), 63–70 (2016)
3. S.U. Kiran, P.M. Kumar, Y.P. Kumar, Comprehensive analysis on critical factors for the operation of advanced high gain DC-DC converters used in renewable energy applications. Int. J. Renew. Energy Res. (IJRER) **11**(3), 1448–1459 (2021)
4. M. Biswal, S. Sabyasachi, A study on recent DC-DC converters. Int. J. Eng. Res. Appl. (IJERA) **2**(6), 657–663 (2012)

5. K. Ramireddy, J V.A.R. Sumanth, T.R.S. Praneeth, Y.P. Kumar, Analysis on filter circuits for enhanced transient response of buck converter, in *Advances in Clean Energy Technologies*, (Springer, Singapore, 2021), pp.1081–1097
6. M. Burridge, S. Alahakoon, The design and construction of a battery electric vehicle propulsion system-high performance electric Kart application. IOP Conf. Ser. Earth Environ. Sci. **73**(1), 1–11 (2017)
7. P.K. Saxena, G.K. Dubey, Comparative study of two quadrant choppers. Electr. Mach. Electromech. **6**(5), 407–422 (1981)
8. D. Singh, S. Kumar, S.S. Thakur, A technique to simulate two quadrant DC chopper fed drives. Int. J. Eng. Res. Technol. (IJERT) **3**(2), 1909–1912 (2014)
9. M.A. Ahmad, P. Rai, Speed control of a DC motor using controllers, in *Automation, Control and Intelligent Systems*, Special Issue: Impact of Gesture Recognition in the Technological Era, vol. 2(6) (2014), 1–9
10. P.V. Gopi Krishna Rao, M.V. Subramanyam, K. Satyaprasad, Study on PID controller design and performance based on tuning techniques, in *International Conference on Control, Instrumentation, Communication and Computational Technologies (ICCICCT)*, (India, 2014), pp. 1411–1417
11. K. Sandeep Rao, V.N. Siva Praneeth, Y.V. Pavan Kumar, D. John Pradeep, Investigation on various training algorithms for robust ANN-PID controller design. Int. J. Sci. Technol. Res. **9**(2) 5352–5360 (2020)
12. P.C. Krause, O. Wasynczuk, S.D. Sudhoff, S.D. Pekarek, *Analysis of Electric Machinery and Drive Systems*, 2nd edn. (IEEE, 2002)
13. V.B. Kumar, D. Sampath, V.N. Siva Praneeth, Y.V. Pavan Kumar, Error performance index based PID tuning methods for temperature control of heat exchanger system, in IEEE *International IOT, Electronics and Mechatronics Conference (IEMTRONICS)*, (Toronto, Canada, 2021), pp. 21–24
14. M. Sahana, S. Angadi, A.B. Raju, Speed control of separately excited DC motor using class a chopper, in *International Conference on Circuits, Controls, Communications and Computing (I4C)*, (Bangalore, India, 2016), pp. 1–6
15. D. Piriadarshani, S. Sathiya Sujitha, The role of transfer function in the study of stability analysis of feedback control system with delay. Int. J. Appl. Math. **31**(6), 728–136 (2019)
16. M.A.R. AboShady, M.A. Hindy, H. Shatla, R. Elsagher, M.S. Abdel-Moteleb, Novel transport delay problem solutions for gas plant inlet pressure control. J. Electr. Syst. Inform. Technol. **1**(2), 150–165 (2014)
17. K.V. Pavan Srikar, Y.V. Pavan Kumar, D. John Pradeep, C. Pradeep Reddy, Investigation on PID controller tuning methods for aircraft fuselage temperature control, in *IEEE 3rd International Symposium on Advanced Electrical and Communication Technologies (ISAECT)*, (Kenitra, Morocco, 2020), pp. 1–5

Design of Automatic Load Frequency Control Loop Using Classical PID Control Methods

A. Sree Vidya, V. Bharath Kumar, Y. V. Pavan Kumar, D. John Pradeep, and Ch. Pradeep Reddy

Abstract Regulation of voltage and frequency is essential in power plants, which further affects reactive and active power generation. These parameters are normally affected by load variations. Thus, an automatic load frequency controller (ALFC) is one such controller which is used to uphold the frequency of the power system at the desired level. This ALFC is a PID-based control loop, thus, the design of PID parameters plays a crucial role in ALFC operation. There are many design methods evolved in literature which are used in many industrial applications. However, the selection of a suitable design method for a particular application is not direct. Besides, one method may not be suitable for all operating conditions of the system. Thus, a detailed investigation is needed for the design of the PID controller according to the considered application. In this view, this paper implements several prominent PID tuning methods for the considered ALFC application. A comprehensive comparison is provided by computing transient time-domain index as well as frequency domain stability analysis to identify the most suitable design method. The entire simulation work has been carried out with the help of MATLAB/Simulink software. From the results, it is found that the "Wang Jang Chan" method is providing better responses under all conditions when compared to other key design methods for ALFC application.

A. Sree Vidya · V. Bharath Kumar · Y. V. Pavan Kumar (✉) · D. John Pradeep
School of Electronics Engineering, VIT-AP University, Amaravati, Andhra Pradesh, India
e-mail: pavankumar.yv@vitap.ac.in

A. Sree Vidya
e-mail: vidya.18bes7002@vitap.ac.in

V. Bharath Kumar
e-mail: bharath.18bec7093@vitap.ac.in

D. John Pradeep
e-mail: john.darsy@vitap.ac.in

Ch. Pradeep Reddy
School of Computer Science and Engineering, VIT-AP University, Amaravati, Andhra Pradesh, India
e-mail: pradeep.ch@vitap.ac.in

J. Kumar et al. (eds.), *Control Applications in Modern Power Systems*, Lecture Notes in Electrical Engineering 974, https://doi.org/10.1007/978-981-19-7788-6_11

Keywords Automatic load frequency controller · Power system control · PID controller · PID tuning · MATLAB/Simulink

Nomenclature

ALFC	Automatic load frequency controller
ZNM-1	Ziegler Nichols Method—(1)
ZNM-2	Ziegler–Nichols Method—(2)
MZNM	Modified-Ziegler–Nichols Method
WJCM	Wang Jang Chan Method
CHRM	Chien Hrones Reswick Method
CCM	Cohen coon Method
POM	Pessen's Overshoot Method
PIM	Pessen's Integral Method
TLM	Tyreus-Luyben Method
GGM	Good Gain Method
DCM	Damped cycling Method
ITAE	Integral-Time-Absolute-Error Method
ISEM	Integral-Square-error Method
ISTEM	Integral-Square-Time-error Method
ISTSEM	Integral-Square-Time-Square-error Method

1 Introduction

The main intention of the traditional power plant system operation and control is to dispense the power continuously to the consumers. The amount of power required at the consumer side must be equal to the amount of power that is generated. For maintaining a quality power factor, both real and reactive power should be balanced under any circumstances. Conventional power plants use fuels such as coal in order to produce energy in the form of steam. This steam will act as a driving force for the turbine movement. In the power system control, the Automatic Generation Control unit (AGC) plays a key factor in balancing the system. This AGC consists of two sub-control units, Automatic Voltage Regulator (AVR) and Automatic Load Frequency Control (ALFC). When there are any fluctuations in the voltage, then AVR is used in order to maintain a constant voltage. Similarly, in order to stabilize the frequency fluctuations, ALFC will be used.

In order to compose an efficient ALFC system, the design of the PID controller will be a crucial part. So, one needs to take prior attention while designing the PID gain parameters. There are various tuning methods available in the literature. The cuckoo search optimization (CS) algorithm is used to get optimized PID gain values

for the ALFC system. Further, the comparative analysis was done between CS and EPI methods [1]. Firefly algorithm was implemented to design gain values for the ALFC system. In addition to several loads, the disturbances were verified to check their performance [2]. To control the frequency deviations in hybrid power systems, a genetic and lightning search algorithm (LSA) was used. The response obtained from these algorithms is compared with traditional PID tuning methods [3]. ZN method was implemented to fabricate the tuning parameters of the controller for a multi-area power system and the results are compared with the NARMA-L2 controller [4]. Particle-Swarm-Optimization (PSO) algorithm was employed to enhance the gain values of the typical integral controller for Hydro-Thermal System application [5]. The trial and error based design of the controller is executed for single, two, and three-area interconnected power systems.

The output responses obtained from these interconnected systems are illustrated by considering performance parameters like settling time, peak overshoots etc. [6]. Several types of conventional PID tuning techniques were implemented in the liquid level control system. Further, the time domain analysis has been carried out to check the quality of the obtained system response [7]. In this work ZN, PL, PO, and TL methods are illustrated for the transfer function model of the heating furnace system. Further, the system responses were extensively analyzed by using performance metrics [8]. Thermal control of the Aircraft fuselage system was carried out by using various PID tuning methods. The effectiveness of the controller is estimated with the help of time-domain performance indices [9]. The flight attitude control system was implemented with the help of standard PID tuning methods by statistical analysis. Besides, the controller was practically implemented with the help of hardware in the loop technique and the efficiency is checked by Monte-Carlo analysis [10]. PI-based controller is implemented for the AVR system and its responses are compared with a fuzzy load frequency controller to control the frequency of the power system [11]. ANFIS based intelligent controller is used to control the frequency when there is a change in a load of a four area Hydro-thermal Interconnected power system and a comparison between the ANFIS, PI and PID-based control techniques was demonstrated in [12]. A tilted integral derivative (TID) controller is employed to stabilize the frequency of the ALFC system. Further, a comparative analysis has been done on the results of the PI controller, PID controller and TID controller [13]. Atom search Optimization algorithm was implemented for tuning the parameters of FOPID for the control of frequency in the Hybrid Power system. The results are compared with the different methods that are implemented in the literature earlier [14]. This paper tells the automatic frequency control of a two-area multisource Hybrid Power system. An attempt of implementing a cascade of PI-PD controllers has been carried out. Additionally, the results are compared with the AI-based methods [15]. To control the frequency of the two-area non-reheat thermal power system Fuzzy-PID and SMES controllers are implemented along with a chemical reaction Optimization Technique (CRO) [16]. In this paper, there is an implementation of the classical PID controller tuned by the ZN method to an interconnected microgrid to control the frequency of the system [17].

Even though there are many methods implemented for designing PID controllers in various applications, one particular method will not be suitable for all applications as well as under various operating conditions of the system. So, there is a need to do a detailed analysis of several important tuning methods to achieve a stable response for the considered system. With this motivation, this paper implements different key categories of PID tuning techniques for the ALFC system. Further, a suitable method will be suggested based on the time-domain and frequency-domain profiles. Thus, the identification of the most suitable PID controller design method for ALFC application is the major contribution of this paper.

2 Modelling of the ALFC System

ALFC system is mainly categorized into 3 main subunits, namely, governor, turbine, and generator. The total power in any electrical system will be constant as per the energy conservation theorem. However, it can transform from one form of energy to another form. Similarly, in the power system, the energy conversion takes place in different forms during the power generation as shown in (1).

$$P_{\text{fuel}} = P_{\text{steam}} = P_{\text{mechanical}} = P_{\text{electrical}} \tag{1}$$

where the electrical form of power can be represented by (2).

$$P_{\text{electrical}} = P = \sqrt{3} * VI \cos\theta \tag{2}$$

The mechanical form of power is represented by (3).

$$P_{\text{mechanical}} = P = \frac{2\pi N\tau}{60} = \tau * \omega \tag{3}$$

According to the equation mentioned in (2), the electrical power is directly proportional to voltage and current. When there is any change in load demand, the amount of current flow will vary accordingly. So due to this change in the current flow, the electrical power of the power system will get affected by assuming that constant voltage has been maintained in the system with the help of an automatic voltage regulator unit. As there is a change in the electrical power, the mechanical power (at the turbine) will get changed due to the energy conservation theorem.

Mechanical power is directly proportional to torque (τ) and no of rotations (N) of the turbine according to the relation shown in (3). Further, the number of rotations will directly depend on the amount of steam supplied to the turbine unit. If the steam input to the turbine is not regulated, then the torque of the system will get changed, such that there will be a change in the frequency of the system as mentioned in (4). So, the aim is to maintain the frequency constant by regulating the steam input to the turbine. This is the main idea behind the operation of the ALFC system. The transfer

Table 1 Output to input relation functions of each subunit in the ALFC system

S. No	Name of sub-block	Transfer function
1	Speed governor	$G(s) = \frac{1}{1+T_g s}$
2	Turbine	$G(s) = \frac{1}{1+T_t s}$
3	Rotation mass & load	$G(s) = \frac{1}{2Hs+D}$
4	Speed sensor	$G(s) = \frac{1}{R}$

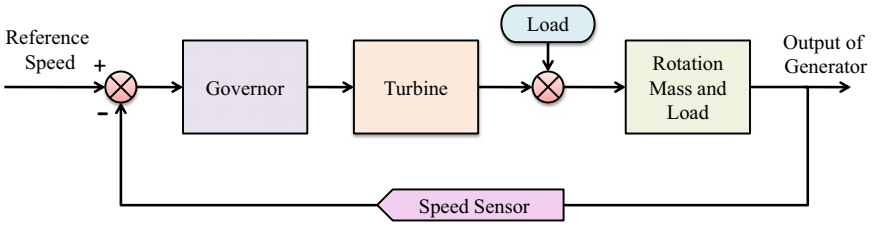

Fig. 1 Schematic diagram of ALFC system

functions of the speed governor, turbine, rotational mass and load, and speed sensor are represented in Table 1 [6].

$$\tau = J * \frac{d\omega}{dt} \tag{4}$$

The process flow of the ALFC system is represented in Fig. 1. The ALFC system is abide by desired turbine speed as an input, speed governor, turbine, rotation mass and load and feedback path which includes a speed sensor. The process of the ALFC system starts by setting up reference turbine speed, then this speed is supplied to the speed governor unit. This governor unit will adjust the steam which is given as input to the turbine. The mechanical output from the turbine is further supplied to the generator for getting the required electrical output.

3 Implementation of PID Controller for ALFC System

PID controller is a crucial controller, which is extensively used in many industrial applications. Designing a suitable tuning method for the PID controller is a crucial task. In a PID controller K_p, K_i, and K_d are the gain parameters of proportional (P), Integral (I), and Derivative (D) respectively. The proportional controller i.e., the P controller is used to raise the gain (K_p) of the system to the desired level, so that the system response reaches the setpoint value. To some extent increasing the K_p value of the P controller is acceptable until there are no oscillations in the system response. Sometimes the system may not reach the desired setpoint value even if

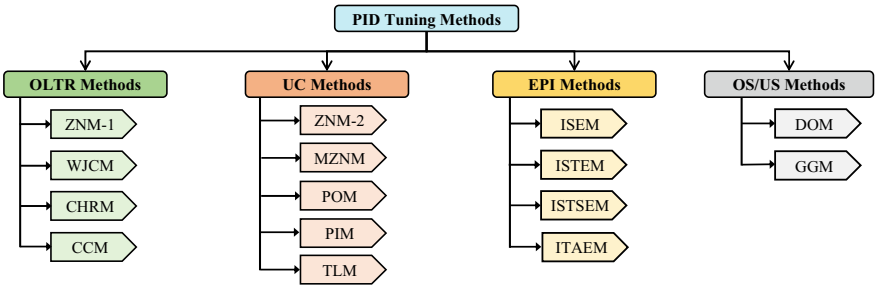

Fig. 2 Different categories of PID tuning methods

there is a drastic increase in the value of K_p, which results in a steady-state error. As the proportional constant K_p is limited to some extent, an integral constant can be added to the system i.e., the PI controller which increases the gain of the system to compensate for the error formed in steady-state. In the process of setting up the gain, some undesired oscillations and peak overshoots will occur in the system response. So, to get rid of those oscillations and peak overshoots, a derivative constant can be implemented in the system i.e., PID controller, which reduces the oscillations and further improves the settling time of the response. The output-input relation of PID is denoted by (5).

$$G(s) = K_p + \frac{K_i}{s} + K_d s \tag{5}$$

The important step in the process of PID controller design is to set up the gain values (K_p, K_i, K_d). There are different methods available to tune the PID gain value. There are different categories of the PID tuning methods implemented for the ALFC System as listed in Fig. 2. The detailed representation of each gain parameter that is designed for various tuning methods has been tabulated in Table 2.

3.1 Implementation of OLTR Methods

For implementing the OLTR methods the system should behave like an undamped system. To make the system operate in the undamped mode, there is a certain procedure that needs to be followed. S**tep-1**: Remove all feedback loops of the system such that no control operation can happen in the system. **Step-2**: Provide a step input to that open-loop system and record the response by connecting the output terminal to an oscilloscope. **Step-3**: Observe the system output in the oscilloscope, if the response of the system is stable continue the next steps, else the system can't be controlled using OLTR methods. **Step-4**: Make a tangent to the curve such that the

Table 2 Gain parameters for numerous PID tuning techniques

Category	Method name	K_p	K_i	K_d
OLTR	ZNM1	2.6901798	0.450390055	–
	WJCM	4.30942	0.2431266	–
	CHRM	2.621	1.20672	–
	CCM	0.17899	–0.08055	–
UCM	ZNM2	44.3856	46.7216	10.54158
	MZNM	14.7952	7.78694	9.36980016
	POM	24.6586667	25.9538	15.6171556
	PIM	51.7832	68.1357	14.758212
	TLM	33.2892	7.96392	10.0393
EPIM	ISEM	6.13066	0.3501	–
	ISTEM	6.157755	0.35207	–
	ISTSEM	5.80997435	0.328071055	–
	ITAEM	5.53485	0.25666965	–
OS/US	GGM	7.76	1.916	7.857
	DOM	8.28	4.805	3.567

tangent will completely align with that output waveform as shown in Fig. 3. **Step-5**: Note the parameters dead time (T_d), the slope of the tangent (M), saturation value (K_s) and time constant (T_c). Using these parameters, find the values of PID gains, K_p and K_i using the formulas in [18].

For implementing EPIM to the proposed ALFC system, initially, the system response should be critically damped, similar to that of OLTRM. The procedure to find the PID gain parameters is the same as finding gain parameters for OLTR methods. The only difference in the usage of EPIM & OLTRM is when there exists

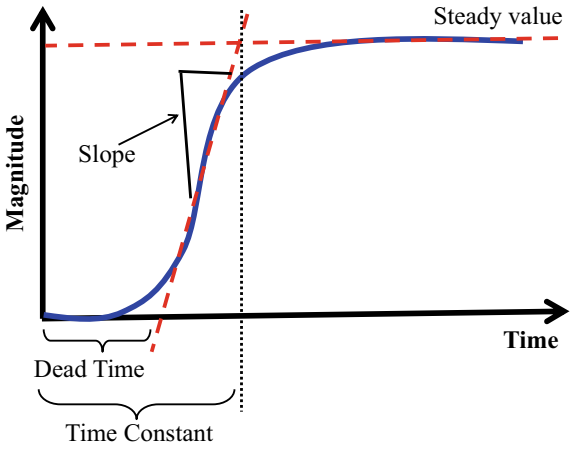

Fig. 3 Control free response of ALFC system

a steady-state error in the initial system response (open loop system response) then EPIM is a suitable method to be used for the control purpose of the system. By using the same procedure of OLTR methods the values of PI gains are calculated by using the formulae [19].

3.2 *Implementation of UC Methods*

To implement UC methods, the system response should get sustained oscillations. The Simulink model of the ALFC system to bring sustained oscillations in the system is shown in Fig. 4. To get sustained oscillations in the response, certain steps need to be followed. **Step-1**: Place a gain value K_p before the transfer function block. **Step-2**: Increase the gain value K_p until the system response gets the sustained oscillations. **Step-3**: Record the gain value (K_c) at which system response gets sustained oscillations. **Step-4**: Record the period (T_c) of the sustained oscillatory wave. **Step-5**: By using the values of K_c and T_c, find the value of K_p, K_i & K_d by substituting them into formulae. The output of the MATLAB/Simulink model obtained at a gain (K_c) of 73.976 is as shown in Fig. 5 with undamped oscillations. The time period (T_c) for these oscillations is 1.9.

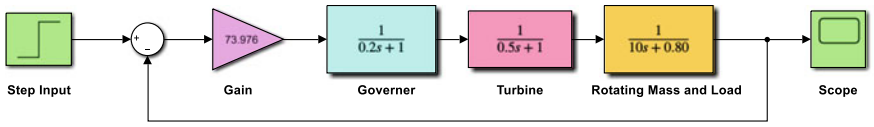

Fig. 4 Simulink model for obtaining sustained oscillations

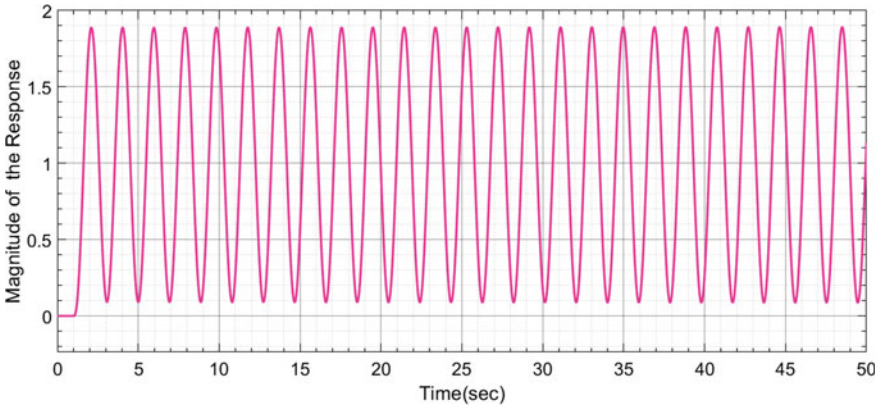

Fig. 5 Sustained oscillations

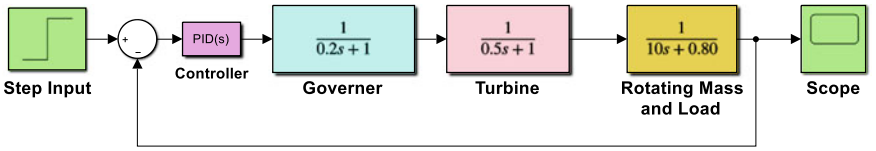

Fig. 6 Simulink model for getting underdamped oscillations

3.3 Implementation of the OS/USM

To implement the OS/US methods, the system should accomplish an underdamped system. In order to get the underdamped response in the system, there are certain steps to be followed. **Step-1**: Place a P controller before the transfer function block and unity gain feedback loop as shown in Fig. 6. **Step-2**: Increase the gain value (K_p) of the P controller until the system response will have its first peak overshoot and undershoot. **Step-3**: Record the gain value of the P controller at which the system behaves as an underdamped system. **Step-4**: From the response wave, find the time difference (T_{out}) between the first peak overshoot and the first undershoot. **Step-5**: Further, find the decay ratio P (ratio of first overshoot by second overshoot) and substitute these values into formulae [20, 21].

3.4 MATLAB/Simulink Model

The MATLAB/Simulink model of the ALFC system implementing all four categories of PID tuning methods is represented in Fig. 7. A step input of unity is given as an input to the Simulink model. Besides, the model consists of the transfer function blocks of governor, turbine, rotating mass and load. It also comprises of a feedback loop from the output end of the rotating mass and load block. The feedback loop and the step inputs are provided to the error comparator which measures the deviation in the frequency. The output of the error comparator is given as the input to the PID controller block. Further, PID gain parameters are tuned with different categories of the conventional methods. The controlled output from the PID controller is given to the transfer function block of the system. An oscilloscope is employed to view the response of the system.

4 Simulation Results

To achieve the objective of suggesting an apt tuning technique for the ALFC system, several tuning methods have been implemented in MATLAB/Simulink. Further, the responses obtained by these tuning methods are analyzed in transient and steady-state

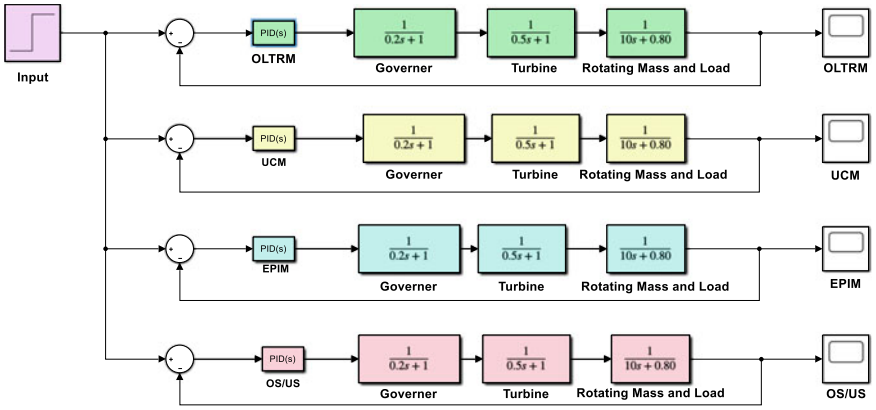

Fig. 7 MATLAB/Simulink model with different PID tuning methods

intervals. Various performance metrics are taken into contemplation for judging the stability of the ALFC system.

4.1 Time-Domain Analysis of the Proposed ALFC System

In this type of analysis, the x-axis represents simulation time and the y-axis represents the desired setpoint value of the ALFC system. There are various quality factors such as overshoot percentage, error in the steady-state interval, and settling time to judge the accurate conduct of the system response. All these quality factors are calculated and mentioned in Table 3. Among the open-loop response methods implemented for the ALFC system, ZN-1 and CHR method have attained overshoot in response compared to setpoint as shown in Figs. 8 and 9 respectively. Any system response which does not settle as per the setpoint level is treated as an undesirable response. So, here the ALFC system implemented with the CC method shows an undesirable response as shown in Fig. 10. The system response obtained with the WJC method doesn't have any peak overshoot. Besides, the settling time of the response obtained with the WJC method is maintained at acceptable limits as shown in Fig. 11. Further, all these OLTR responses are represented in one single frame for better comparative analysis as shown in Fig. 12.

Among UC methods that are implemented for the ALFC system, all methods are showing some peak overshoot in the transient space of the system response. But ZN-2 and PI methods are having high peak overshoot values when compared with others as shown in Figs. 13 and 14 respectively. The ALFC system responses obtained by MZN and PO methods have slight oscillations and peak overshoot in the transient state has been depicted in Figs. 15 and 16 subsequently. The only method

Table 3 Performance metrics for various tuning methods executed on the proposed system

Category	Method name	Rise time	%peak overshoot	Settling time	Delay time	Transient behavior
OLTRM	ZN1	4.37	11.23	28.5	3.7	Non-oscillatory
	WJC	4.15	No overshoot	50	3.05	Non-oscillatory
	CHR	2.8	38	40	3.3	Oscillatory
	CC	–	No overshoot		–	–
UCM	ZN2	0.405	60	10	1.375	Oscillatory
	MZN	0.908	17.555	12	1.52	Non-oscillatory
	PO	0.367	58.1	12.5	1.322	Oscillatory
	PI	0.49	23	7.5	1.365	Oscillatory
	TL	0.518	23.21	11.2	1.42	Oscillatory
EPIM	ISE	2.368	No overshoot	53	2.6	Non oscillatory
	ISTE	2.368	No overshoot	53.5	2.6	Non oscillatory
	ISTSE	2.65	No overshoot	56	2.65	Non oscillatory
	ITAE	2.745	No overshoot	75.5	2.72	Non oscillatory
OS/USM	GG	2.1515	9.4	24	1.72	Non-oscillatory
	DO	1.365	32.1	16.5	1.91	Oscillatory
Superior method	WJC	PO	WJC, EPI	PI	PO	All Non-oscillatory methods

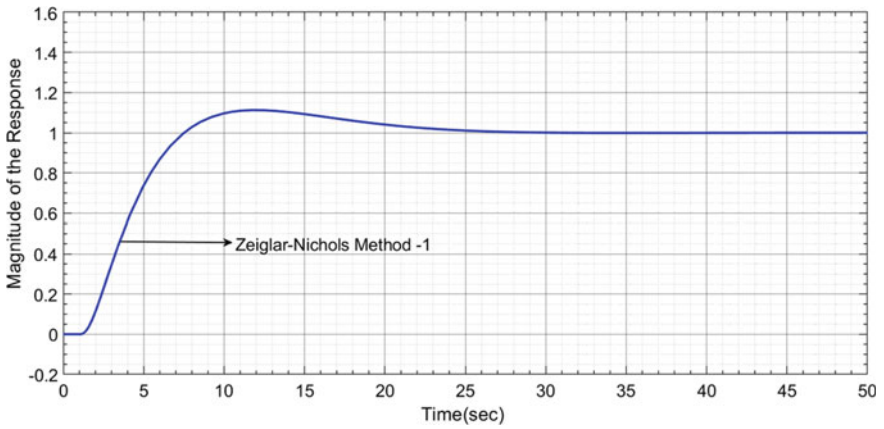

Fig. 8 Time versus setpoint response of ALFC system implemented with ZN tuning method

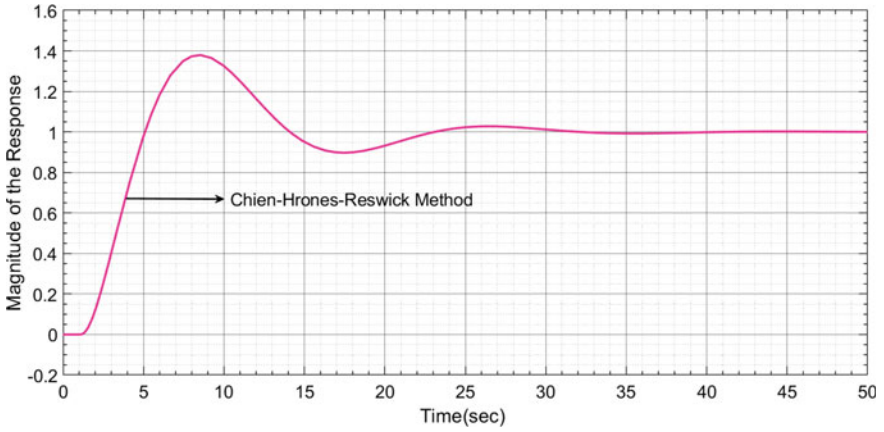

Fig. 9 Time versus setpoint response of ALFC system with CHR tuning method

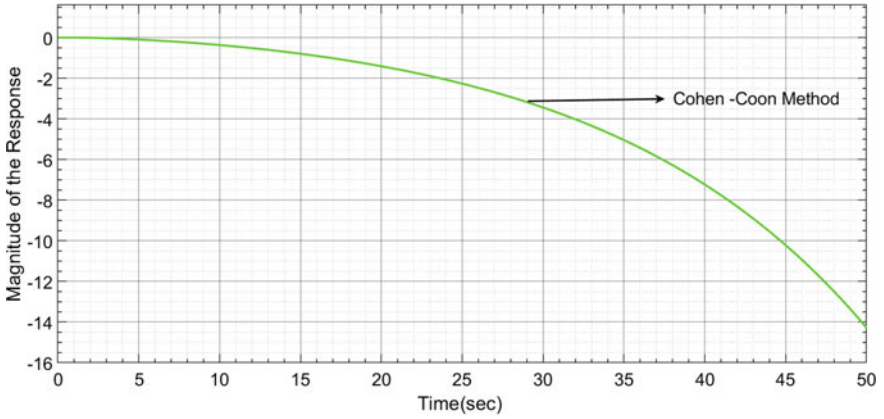

Fig. 10 Time versus setpoint response of ALFC system with CC tuning method

among all UC methods which has less settling and falls under optimum limits of quality factors is the TL method, where its response is shown in Fig. 17. Further, ZN-2 and PI tuning methods have oscillations in the transient state, the rest of the UC methods will not have any oscillations, which can be comparatively analyzed as shown in Fig. 18. All EPI tuning methods that are implemented for the proposed system will depict the same behavior in terms of transient and steady-state space. Figures 19, 20, 21 and 22 represents the system responses obtained by ISE, ISTE, ISTSE and ITAE respectively. But some minor deviations can be observed among the EPI responses in terms of percentage peak overshoot and system settling time which can be observed by the comparative visualization of responses shown in Fig. 23. Among all EPI methods, the ISE tuning method shows less settling time compared with others.

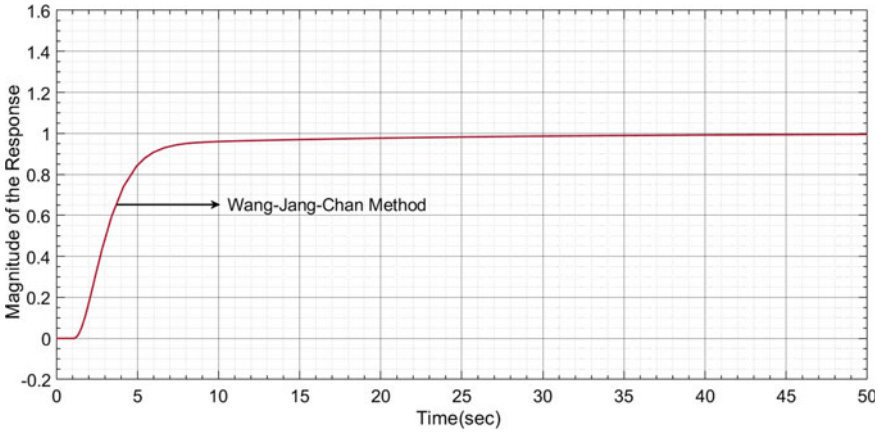

Fig. 11 Time versus setpoint response of ALFC system with WJC tuning method

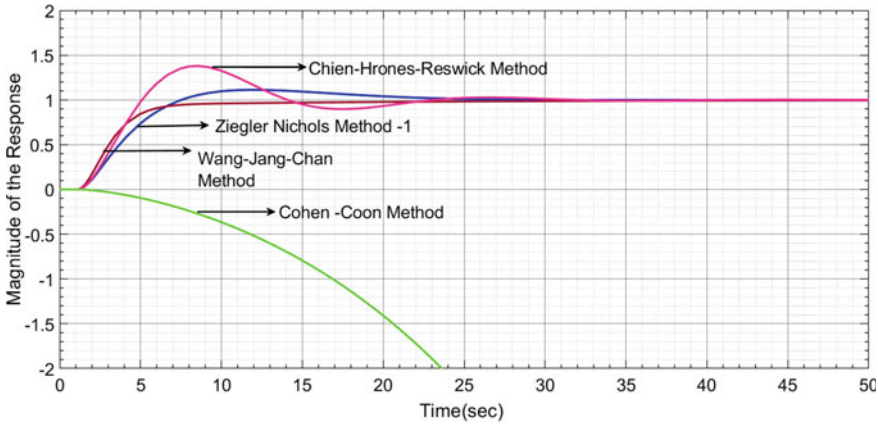

Fig. 12 Comparative responses of the system implemented with several OLTR tuning methods

The simulation responses for DO and GG methods are represented in Figs. 24 and 25 proportionately. The transient state of both these responses has a peak overshoot. When these two tuning method responses are visualized in a single frame, it can be concluded that the DO response shows some oscillatory behavior at the initial state of the system response as shown in Fig. 26.

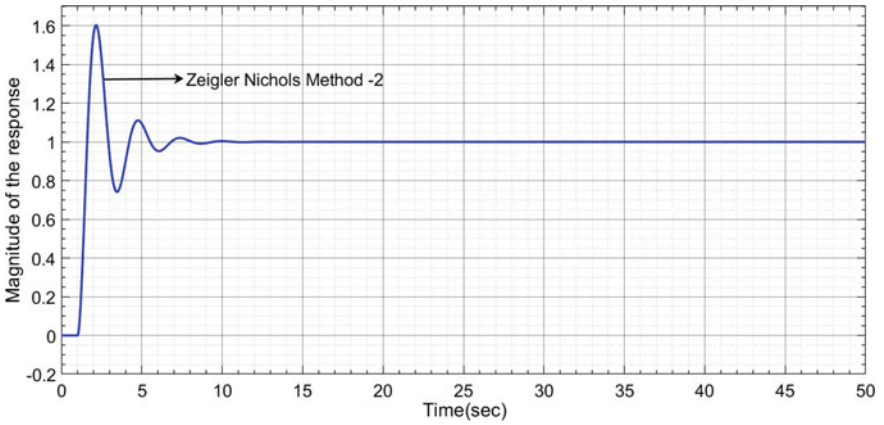

Fig. 13 Time versus setpoint response of ALFC system with ZN-2 tuning method

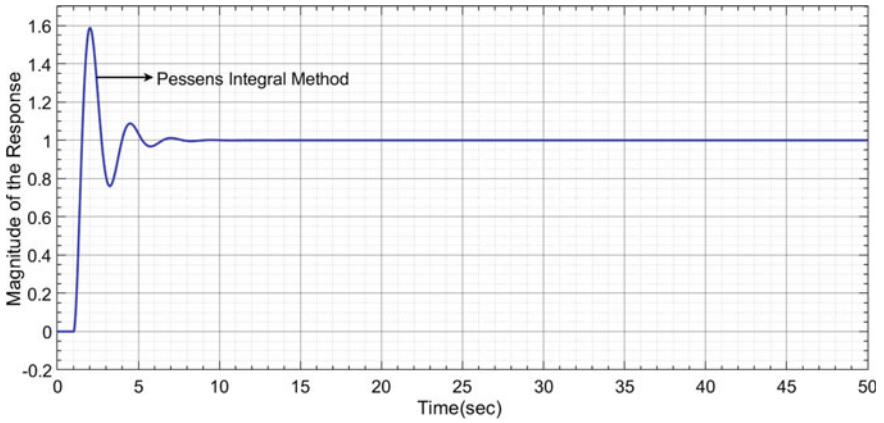

Fig. 14 Time versus setpoint response of ALFC system with PI tuning method

4.2 Frequency Domain Analysis for the Proposed ALFC System

In frequency domain analysis, the system responses will be analyzed in the s-domain. About time-domain analysis, here there are several quality factors like polar plot, bode plot and Nyquist plot which are useful for addressing the stability of any system. In this work, bode plots are chosen and analyzed for finding out the stability of

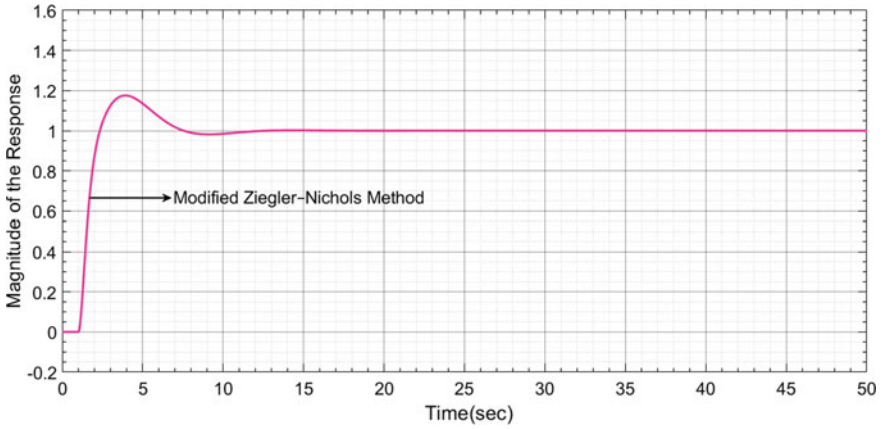

Fig. 15 Time versus setpoint response of ALFC system with MZN tuning method

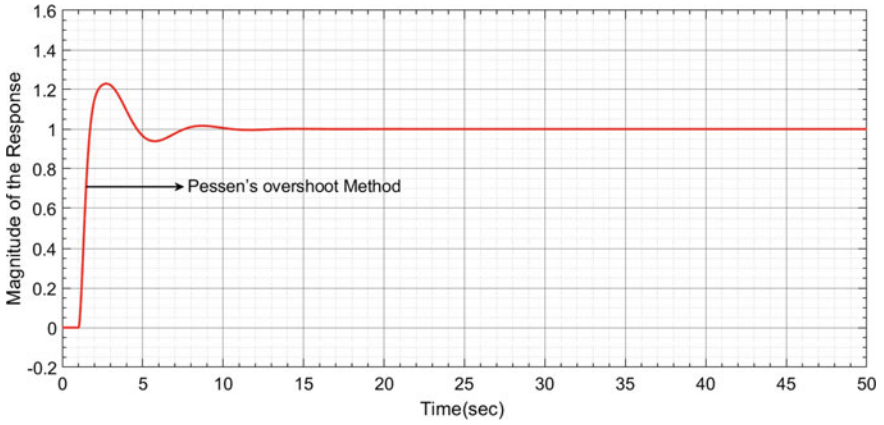

Fig. 16 Time versus set point response of ALFC system with PO tuning method

the system. Generally, the bode plot response which is having high gain and phase margins is considered a satisfactory response.

The responses which are declared as satisfactory based on time-domain quality factors are considered to be analyzed here with the help of bode plots. In the OLTR category, the system implemented with the WJC method has been chosen and observed the bode plot response is shown in Fig. 27. The gain margin for the WJC method was obtained as 23.8. In the UC category, the system implemented with the MZN method is chosen and observed the bode plot response as shown in Fig. 28. The gain margin and phase margin for the MZN method are 15.8 and 129, respectively. Under the EPI category, the ISE method is chosen for implementing

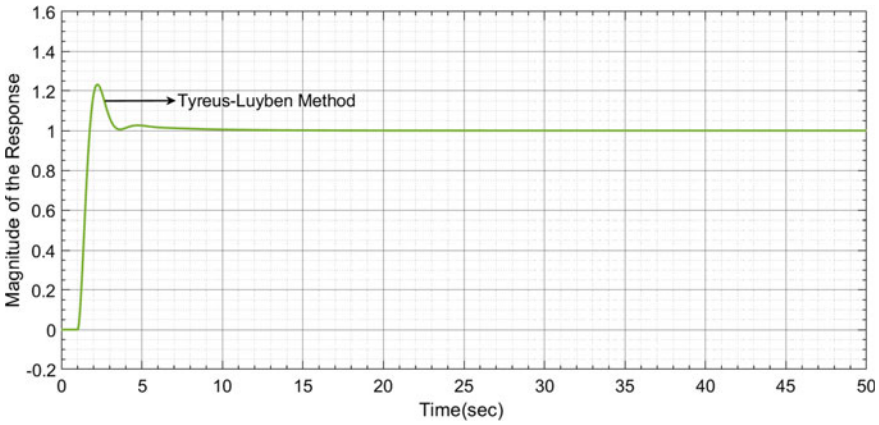

Fig. 17 Time versus set point response of ALFC system with TL tuning method

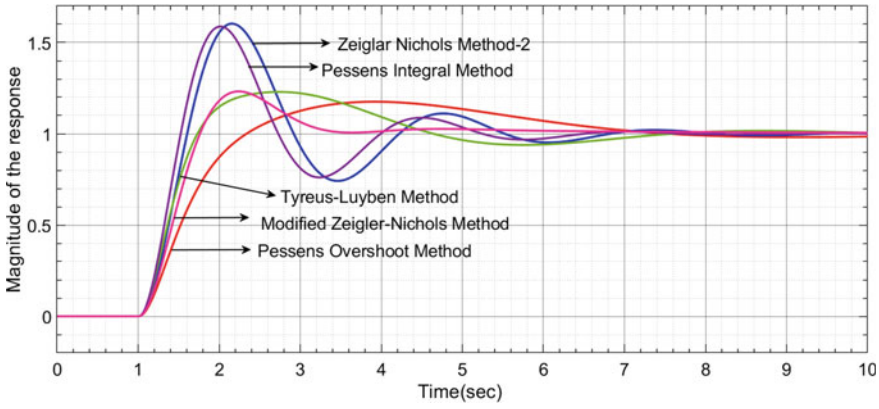

Fig. 18 Comparative responses of the system implemented with several UC tuning methods

bode plot analysis. The gain margin for the ISE method is 20.5 obtained by the response shown in Fig. 29. In OS/US category, the GG method was taken for implementing bode plot analysis. The gain and phase margin for the GG method are 19.5 and 149, respectively, which are obtained from the response shown in Fig. 30. The detailed frequency domain performance metrics for different tuning techniques were tabulated in Table 4.

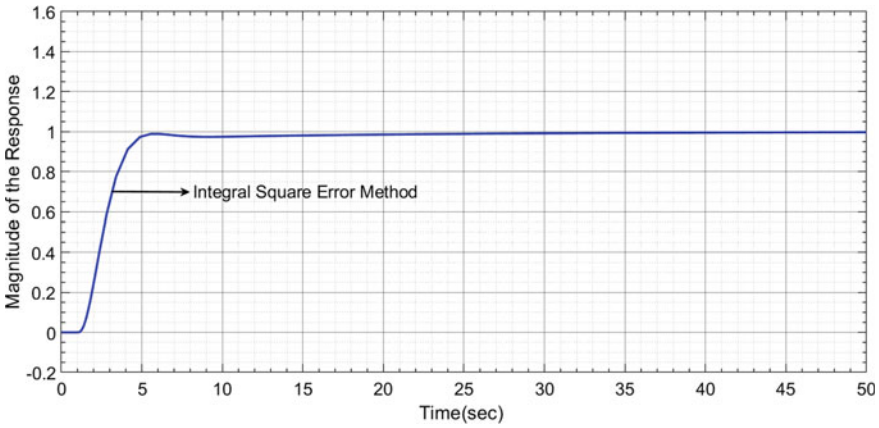

Fig. 19 Time versus setpoint response of ALFC system with ISE tuning method

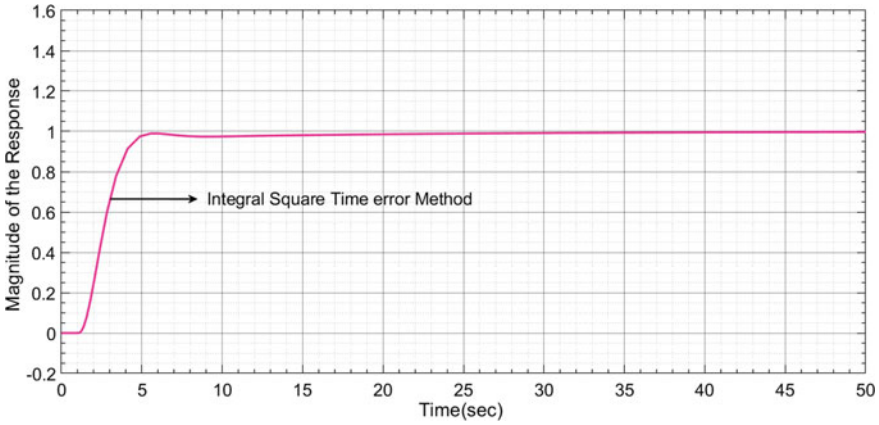

Fig. 20 Time versus set point response of ALFC system with ISTE tuning method

5 Conclusion

Thus, in this paper, a comprehensive analysis has been carried out in finding the best PID tuning method for controlling the frequency of a single area power system. Further, it also contains a detailed analysis of time and frequency domain specifications concerning simulation results obtained. The method which shows the smooth response in transient space and has less settling time and peak overshoot is considered to be the stable method that can make the ALFC system frequency constant.

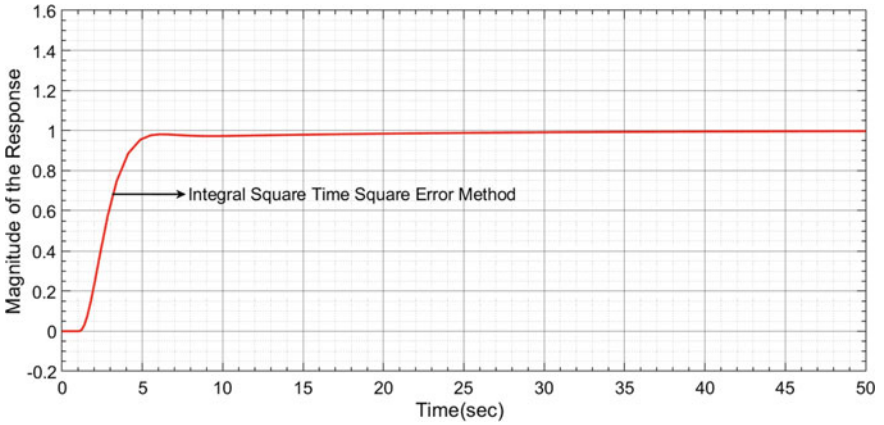

Fig. 21 Time versus setpoint response of ALFC system with ISTSE tuning method

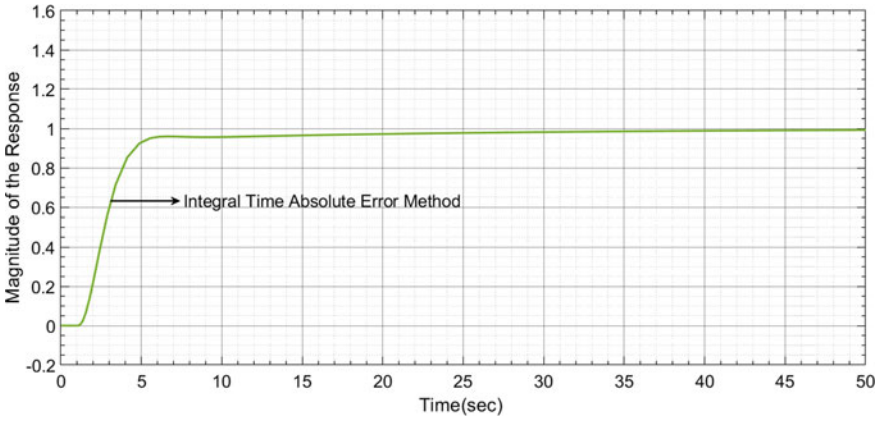

Fig. 22 Time versus setpoint response of ALFC system with ITAE tuning method

- Among OLTR methods, the WJC method is considered the best method because of having non-oscillatory behavior and less rise time and peak overshoot.
- Among UC methods, the MZN method is chosen as the superior method as it has less rise time, delay time and percentage peak overshoot.
- Among EPI methods, the ISE method is considered a suitable method because of having less settling time and no peak overshoot.
- Among OS/US methods, the GG method is chosen as the best method as it has fewer oscillations in transient space as well as less peak overshoot.
- In terms of frequency-domain WJC method will be chosen as stable as it has a high gain margin value.

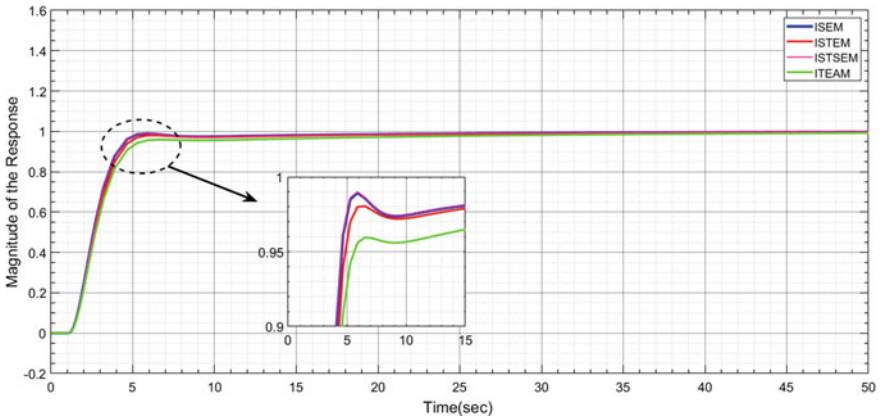

Fig. 23 Comparative responses of the system implemented with several EPI tuning methods

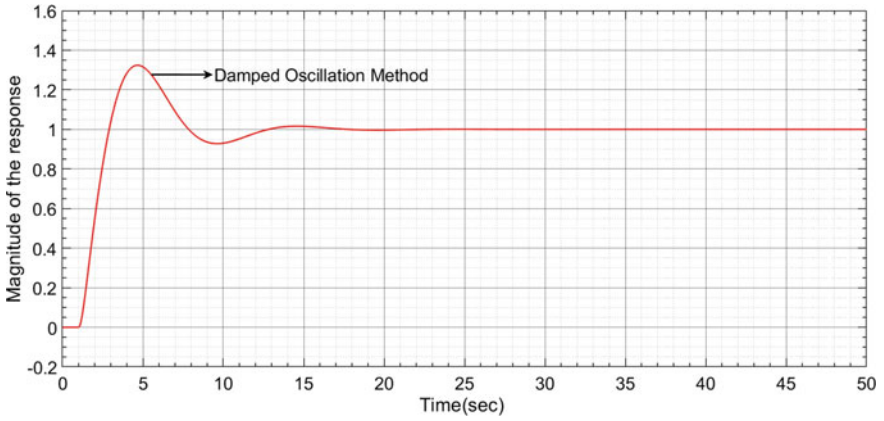

Fig. 24 Time versus setpoint response of ALFC system with DO tuning method

So, after doing an overall constructive analysis in both time domain and frequency domain profiles, the WJC method is chosen as the best method for the proposed ALFC system, as the quality factors of this method fall under standard limits.

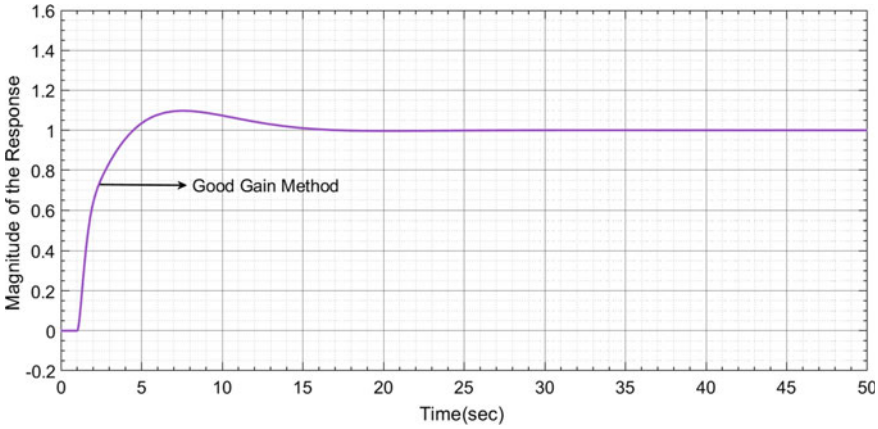

Fig. 25 Time versus setpoint response of ALFC system with GG tuning method

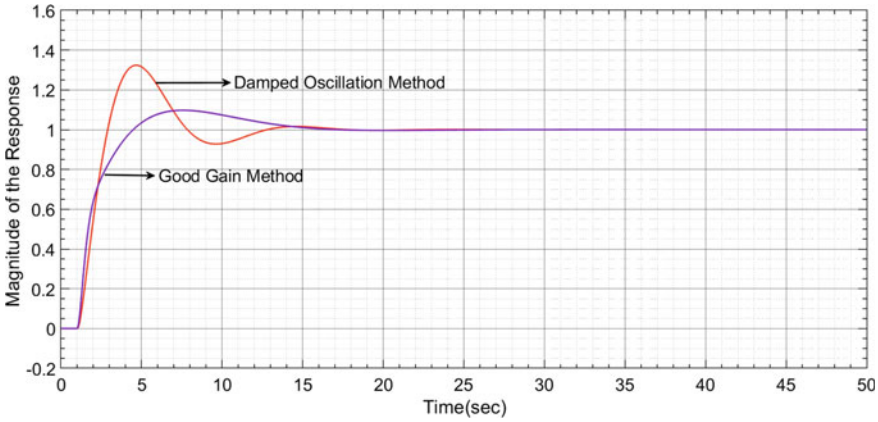

Fig. 26 Comparative responses of system implemented with several OS/US tuning methods

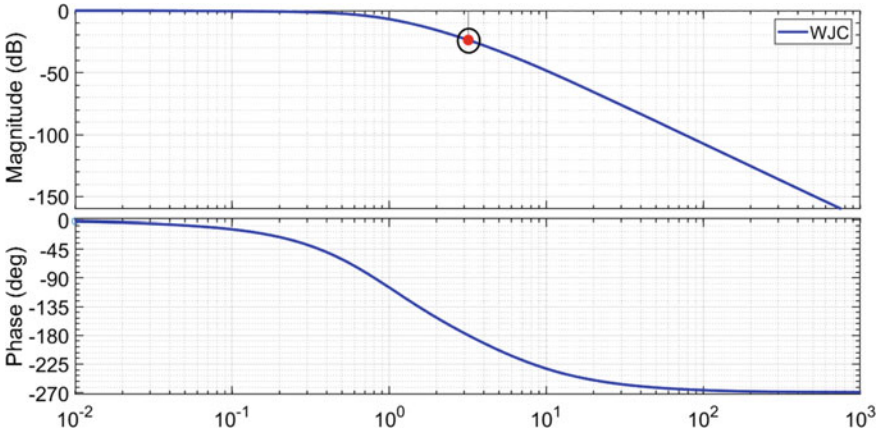

Fig. 27 Frequency domain response implemented with WJC tuning method

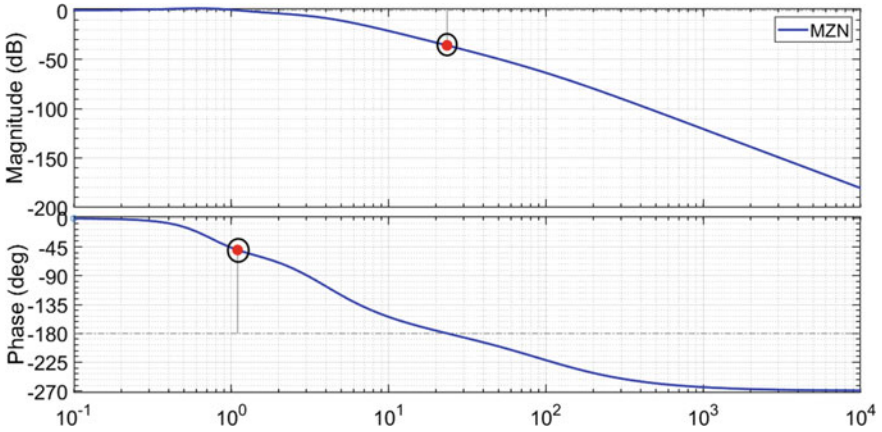

Fig. 28 Frequency domain response implemented with MZN tuning method

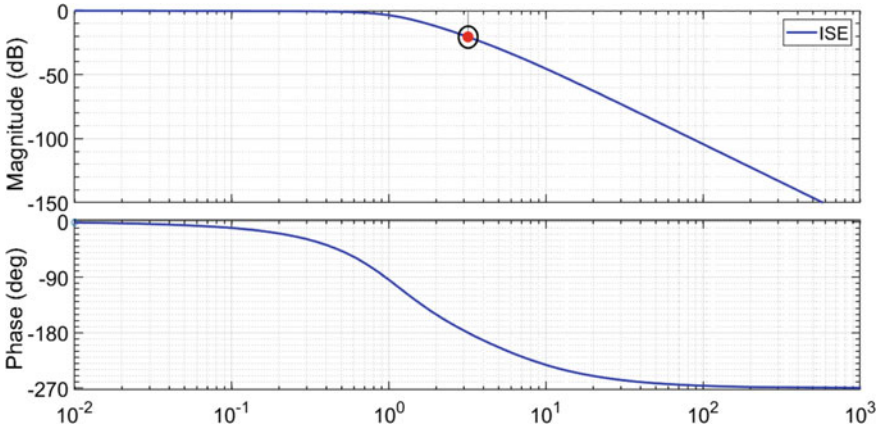

Fig. 29 Frequency domain response implemented with ISE tuning method

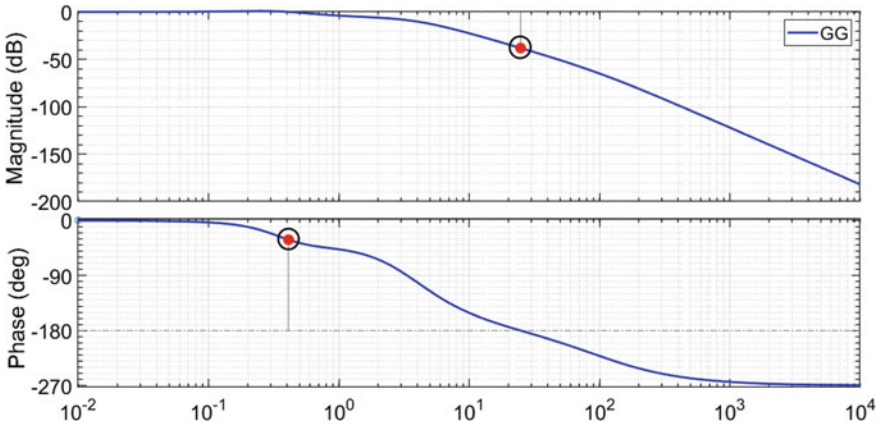

Fig. 30 Frequency domain response implemented with GG tuning method

Table 4 Frequency domain performance metrics for different tuning methods

Category	Method name	Gain margin	Phase margin
OLTRM	WJC	23.8	–
UCM	MZN	15.8	129
EPIM	ISE	20.5	–
OS/USM	GG	19.5	149
Superior methods	–	WJC	GG

References

1. P. Praveena, Basavareddy, S. Mishra, Optimization of multi objective load frequency control using cuckoo search algorithm, in *International Conference on Recent Innovations in Electrical, Electronics & Communication Engineering (ICRIEECE)*, Bhubaneswar, India (2018), pp. 2054–2059
2. M.K. Boddepalli, P.K. Navuri, Design and analysis of firefly algorithm based PID controller for automatic load frequency control problem, in *Technologies for Smart-City Energy Security and Power (ICSESP)*, Bhubaneswar, India (2018), pp. 1–5
3. A.K. Singh, P. Ahmad, N. Singh, N.K. Choudhary, Load frequency control of single area hybrid power system using fuzzy-PID (FPID) controller, in *Students Conference on Engineering and Systems (SCES)*, Allahabad, India (2019), pp. 1–6
4. D. K. Sambariya, V. Nath, Application of NARMA L2 controller for load frequency control of multi-area power system, in *International Conference on Intelligent Systems and Control (ISCO)*, Coimbatore, India (2016), pp. 1–7
5. S. Bhuyan, S.H.N. Dey, S. Paul, S. Chaine, Analysis of frequency regulation for a hydro-thermal system with ALFC-DR Model, in *International Conference on Power Electronics and Energy (ICPEE)*, Bhubaneswar, India (2021), pp. 1–5
6. S. Sharma, J. Bhadoriya, Automatic load frequency control in three area power system using the PID controller. Int. J. Innov. Res. Electr. Electron. Instrum. Control Eng. **3**(8), 138–143 (2015)
7. B. Vasu Murthy, Y.V. Pavan Kumar, U.V. Ratna Kumari, Application of neural networks in process control: automatic/online tuning of PID controller gains for $\pm 10\%$ disturbance rejection, in *International Conference on Advanced Communication Control and Computing Technologies (ICACCCT)*, Ramanathapuram, India (2012), pp. 348–352
8. B. Vasu Murthy, Y.V. Pavan Kumar, U.V. Ratna Kumari, Fuzzy logic intelligent controlling concepts in industrial furnace temperature process control, in *International Conference on Advanced Communication Control and Computing Technologies (ICACCCT)*, Ramanathapuram, India (2012), pp. 353–358
9. K.V.P. Srikar, Y.V.P. Kumar, D.J. Pradeep, C.P. Reddy, Investigation on PID controller tuning methods for aircraft fuselage temperature control, in *International Symposium on Advanced Electrical and Communication Technologies (ISAECT)*, Marrakech, Morocco (2020), pp. 1–5
10. Y.V. Pavan Kumar, R. Bhimasingu, M. Jyothi, B. Ramakrishna, Real time and high fidelity controller design for Hardware In the Loop (HIL) testing of flight attitude control, in *International Conference on Control, Instrumentation, Communication and Computational Technologies (ICCICCT)*, Kanyakumari, India (2014), pp. 1217–1222
11. M. Suman, M. Venu Gopala Rao, G.R.S. Naga Kumar, O. Chandra Sekhar, Load frequency control of three unit interconnected multimachine power system with PI and fuzzy controllers, in *International Conference on Advances in Electrical Engineering (ICAEE)*, Vellore (2014), pp. 1–5
12. D. Sharma, K. Pandey, V. Kushwaha, S. Sehrawat, Load frequency control of four-area hydro-thermal inter-connected power system through ANFIS based hybrid neuro-fuzzy approach, in *Second International Innovative Applications of Computational Intelligence on Power, Energy and Controls with their Impact on Humanity (CIPECH)*, Ghaziabad, India (2016), pp. 144–149
13. S.P. Behara, A. Biswal, B. Swain, S.S. Samantray, Hybrid power systems frequency regulation using TID based robust controller design and differential evolution (DE) algorithm, in *Technologies for Smart-City Energy Security and Power (ICSESP)*, Bhubaneswar, India (2018), pp. 1–6
14. A.X.R. Irudayaraj et al., A Matignon's theorem based stability analysis of hybrid power system for automatic load frequency control using atom search optimized FOPID controller. IEEE Access **8**, 168751–168772 (2020)
15. V. Veerasamy et al., A Hankel Matrix Based reduced order model for stability analysis of hybrid power system using PSO-GSA optimized cascade PI-PD controller for automatic load frequency control. IEEE Access **8**, 71422–71446 (2020)

16. A. Ghosh, S. Dutta, Chemical reaction optimization based fuzzy-PID controller for automatic load frequency control with SMES, in *National Conference on Emerging Trends on Sustainable Technology and Engineering Applications (NCETSTEA)*, Durgapur, India (2020), pp. 1–5
17. J. Kandasamy, R. Ramachandran, V. Veerasamy, Automatic load frequency control for interconnected micro-grid system, in *International Conference on Electronics and Renewable Systems (ICEARS)*, Tuticorin, India (2022), pp. 222–227
18. S.B. Prusty, S. Padhee, U.C. Pati, K.K. Mahapatra, Comparative performance analysis of various tuning methods in the design of PID controller, in *Michael Faraday IET International Summit*, Kolkata (2015), pp. 43–48
19. W. Tan, J. Liu, T. Chen, H.J. Marquez, Comparison of some well-known PID tuning formulas. Comput. Chem. Eng. **30**(9), 1416–1423 (2006)
20. A. O'Dwyer, *Handbook for PI and PID controller tuning rules*, 3rd edn. (World Scientific, Dublin Institute of Technology, Ireland, 2009)
21. G.C. Goodwin, S.F. Graebe, M.E. Salgado, *Control system design*, 1st edn. (Pearson, Prentice hall, 2015)

Design of Automatic Voltage Regulator Loop Using Classical PID Control Methods

Lella Purna Sri Sai Pallavi, V. Bharath Kumar, Y. V. Pavan Kumar, D. John Pradeep, and Ch. Pradeep Reddy

Abstract The voltage regulator finds importance across a wide range of applications such as computer power supplies, automotive alternators and power station generators. All these applications require regulation of the voltage to the desired level without any transients or deviations. Besides, the regulated voltage has to be attained within a short amount of time. The overall effectiveness of a voltage regulator depends on how well it is controlled. So, the design of a suitable controller provides better output from the regulator with minimum transients. Usually, PID (proportional plus integral plus derivative) controller has been used for implementing voltage regulator control operations. However, the PID controller performance depends on the design of the gain specifications/parameters precisely. There are many methods available in the literature to tune the PID gain parameters. However, choosing a unique method for different operating conditions of the voltage regulator system can't be fixed. So, the selection of a suitable method for the given application is a complex task. By keeping this issue in view, this paper executes a comprehensive quantitative analysis of all the important PID tuning methods and recommends a suitable method for voltage regulator control application. The analysis is supported by computing all time-domain performance specifications as well as frequency domain stability specifications. The analysis is carried out using MATLAB/Simulink software.

L. P. S. S. Pallavi · V. Bharath Kumar · Y. V. Pavan Kumar (✉) · D. John Pradeep
School of Electronics Engineering, VIT-AP University, Amaravati 522237, AP, India
e-mail: pavankumar.yv@vitap.ac.in

L. P. S. S. Pallavi
e-mail: pallavi.18bec7026@vitap.ac.in

V. Bharath Kumar
e-mail: bharath.18bec7093@vitap.ac.in

D. John Pradeep
e-mail: john.darsy@vitap.ac.in

Ch. Pradeep Reddy
School of Computer Science and Engineering, VIT-AP University, Amaravati, AP, India
e-mail: pradeep.ch@vitap.ac.in

J. Kumar et al. (eds.), *Control Applications in Modern Power Systems*, Lecture Notes in Electrical Engineering 974, https://doi.org/10.1007/978-981-19-7788-6_12

Keywords Automatic Voltage Regulator (AVR) · Conventional power plant · PID control · Performance metrics

1 Introduction

Most of the electrical and electronic equipment requires a constant voltage supply without any disturbances to function efficiently. Therefore, providing a regulated supply to the equipment is necessary and a complex task to achieve. Voltage regulators are used to providing regulated voltage to the desired levels. A voltage regulator is an electrical device that regulates the source voltage to provide a constant output voltage regardless of load changes, faults, input voltage changes, any disturbances, etc. In the world of electronic components, the voltage regulator is one of the most used components due to the requirement of multi-variety voltage levels. These days, electronic devices are getting more tightly packed than ever before with sensitive components like microcontrollers and integrated circuits (ICs). All such kinds of electronic devices will suffer due to unstable input voltage, which has to be addressed with the proper regulation facility. Therefore, voltage regulators became an important and necessary component for all these devices. However, the effectiveness of the voltage regulator depends on its control mechanism. Therefore, a suitable controller needs to be designed. Conventionally, PID Controllers are used for the control operations of the voltage regulators. The controller design will entirely depend on proper tuning up of PID gain parameters. There are many methods available to tune the gain parameters and there is no one particular method which can be applied to all the operating conditions of the voltage regulator. Therefore, deciding which method will best suit to voltage regulator is a tedious task. So, this paper focuses on implementing several important methods to tune the gain parameters using MATLAB/Simulink and suggests the best method for voltage regulator application by considering several performance metrics.

To get an optimum constant voltage output for the AVR system, tuning the PID controller is a very important task and there are various tuning methods available in the literature. Many Artificial Intelligence techniques, such as neural network technique, fuzzy logic and neuro-fuzzy system are available for tuning the PID controller but the problem with these techniques is that they are iterative processes. In addition to that, it requires a lot of time for their training process and execution. For example, Particle Swarm Optimization (PSO) is used in [1] where it is initialized with a group of random particles (or solutions). This technique is not recommendable because searching for the optimal values is much more difficult and also requires a lot of time when compared with other simpler methods. A manual method [2] can be used where it initially uses the values of K_p, K_i and K_d given by the soft computing techniques genetic algorithm and particle swarm optimization and then perform various experiments to obtain optimized gain values for the AVR system. Then there exists a TLBO method (Teaching Learning Based Optimization) for the AVR system in [3], which has a teaching phase and a learning phase. This TLBO

method will consume a lot of time as it is an iterative method. In [4], Haalman and Lambda-Tuning methods are used to tune the PID for the AVR system. According to the Ziegler-Nichols method, the reduction and validation of PID controller parameters with the help of MATLAB are discussed in [5] for the AVR system. In [6], pole placement and pole-zero cancellation methods are used to tune the analog type AVR system which is used to maintain the terminal voltage of the synchronous generator. Further, it concludes that the method of cancelling zeroes by poles is the best method to tune the PID controller of an excitation system.

A genetic algorithm (GA) is used to tune the PID controller for AVR in [7], where tuning is done using different population sizes and generation numbers to find the optimal values of the PID controller. Besides the simulation results of the PID controller based on GA has faster speed and stronger adaptability. A comparison between optimally tuned PID and self-tuned PID is done in [8], where both the methods produce a satisfactory response, but the IAE index shows that the self-tuned PID was better in comparison with the optimally tuned PID controller. In [9] a comparison between conventional PID and PI controllers is done for the AVR system. A Fractional Order PID controller is used to control AVR in [10] where Simulated Annealing (SA) algorithm is used to tune the FOPID. The algorithm is based on testing and examining different weighting factors to achieve optimum system response. Three optimization methods GA, PSO and HGAPSO are implemented and compared in [11] where it is found that the GA method is the most beneficial but the PSO is faster than GA. Fractional-order PID controller (FOPID) is implemented using Salp Swarm Algorithm (SSA) [12] where it is found that the FOPID outperformed the integer-order PID controller. By using the FOPID controller an improvement in settling time, rise time, peak overshoot and steady-state error is observed. The tuning of the FOPID controller for the AVR system using SFL, HS, PSO and GA techniques has been done in [13] where the SFL technique is found to be the best among all the techniques as it is less sensitive to disturbances from load disturbance analysis and also it is the most robust among the considered controllers. Particle Swarm Optimization Algorithm is used in [14] to get a novel fitness function that determines the most favorable PID controller parameters for an AVR system. An improved fitness function can let the PSO algorithm predict the best PID control variables with higher computational efficiency. Error Performance Index (EPI) methods are implemented to tune the PID controller for Temperature Control of Heat Exchanger System in [15] where it is concluded that the ITAE method is the superior method after comparative analysis. An automatic voltage regulator with a power system stabilizer system which is implemented for the power system is discussed. Further, the work proposed in the paper [16] will analyze the impact of damping circuits on the transient response of synchronous generators. In [17], a sin cosine based FOPID controller was designed for the automatic voltage regulator and obtained the step response. But, it was not analyzed for dynamic disturbances that occur in the system.

2 Modelling of AVR System

An Automatic Voltage Regulator (AVR) is used to maintain the terminal voltage of a generator in power systems. A typical AVR model consists of an amplifier, exciter and a generator. In order to maintain a constant output voltage, a sensor is used which senses the output terminal voltage of the generator. The difference between the voltage sensed by the sensor and the setpoint voltage gives the error signal. This error signal is then given to the controller. The controller generates an actuating signal which is amplified by the amplifier and then given to the exciter [18]. The parameters range of different components of AVR and also the values of these parameters used in this paper are depicted in Table 1 [19]. With the use of a PID controller, the output of the AVR system is enhanced by improving its transient and steady-state responses. A simple Automatic Voltage Regulator (AVR) system comprises four main blocks an amplifier, an exciter, a generator and a sensor. The typical AVR system can be represented using simplified block diagrams as shown in Fig. 1. Each of the blocks has been mathematically modelled to a simple first-order transfer function by linearizing each component and taking the major time constant into account and ignoring other non-linearity.

Table 1 AVR parameters and their limits

Block	Ranges	Values considered in this paper
Amplifier	$10 \leq K_{amp} \leq 40$	$K_{amp} = 25$
	$0.02 \leq T_{amp} \leq 0.1$	$T_{amp} = 0.06$
Exciter	$1 \leq K_{ex} \leq 10$	$K_{ex} = 5.5$
	$0.4 \leq T_{ex} \leq 1$	$T_{ex} = 0.7$
Generator	$0.7 \leq K_{gen} \leq 1$	$K_{gen} = 0.85$
	$1 \leq T_{gen} \leq 2$	$T_{gen} = 1.5$
Sensor	$K_{sen} = 1$	$K_{sen} = 1$
	$0.001 \leq T_{sen} \leq 0.06$	$T_{sen} = 0.003$

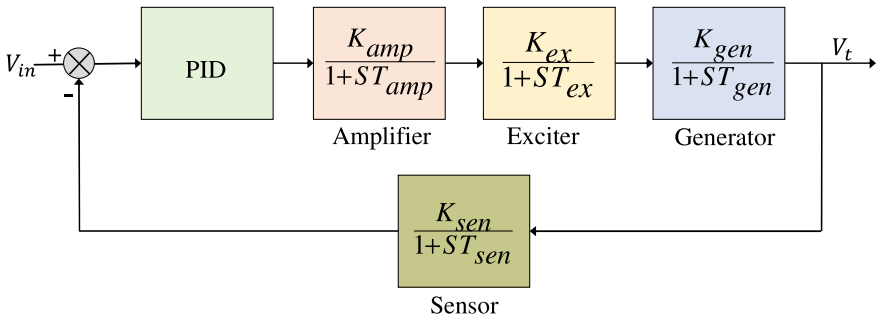

Fig. 1 Block diagram of AVR system

The amplifier block is represented by a first-degree Transfer function shown by (1) where K_{amp} is the gain of the amplifier and T_{amp} is the time constant. The output of the exciter block is a function of field voltage and it is non-linear due to the saturation effects in the magnetic circuit. The amplifier block after modelling and considering the major time constant and ignoring saturation or other non-linearity is represented by a first-degree Transfer function shown in (2) where K_{ex} is the gain of the exciter and T_{ex} is the time constant. The linearized generator model relating generator terminal voltage and its field voltage are given by the transfer function by (3) where K_{gen} is the gain of the generator block and T_{gen} is the time constant. The sensor block is represented by a first-degree Transfer function shown in (4) where K_{sen} is the gain of the amplifier and T_{sen} is the time constant. The general transfer function for a closed-loop system is represented as shown in (5).

$$TF_{amplifier} = \frac{K_{amp}}{1 + sT_{amp}} \tag{1}$$

$$TF_{exicter} = \frac{K_{ex}}{1 + s\,T_{ex}} \tag{2}$$

$$TF_{generator} = \frac{K_{gen}}{1 + sT_{gen}} \tag{3}$$

$$TF_{sensor} = \frac{K_{sen}}{1 + sT_{sen}} \tag{4}$$

$$\text{Transfer Function } TF = \frac{V_t}{V_{in}} = \frac{1 + G(s)}{1 + H(s)G(s)} \tag{5}$$

where $G(s)$ and $H(s)$ are represented as,

$$G(s) = \frac{K_{amp}K_{ex}K_{gen}}{\left(1 + sT_{amp}\right)(1 + sT_{ex})\left(1 + sT_{gen}\right)} \text{ and } H(s) = \frac{K_{sen}}{1 + sT_{sen}}$$

On substituting the above parameter values, the final TF of the AVR system is represented by (6) and (7). The final block diagram, which was used for the control analysis of the AVR system is shown in Fig. 2.

$$G(s) = \frac{116.875}{0.063s^3 + 1.182s^2 + 2.26s + 1} \tag{6}$$

$$H(S) = \frac{1}{1 + S\,0.03} \tag{7}$$

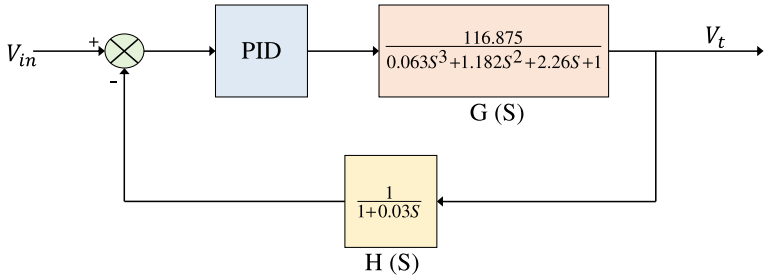

Fig. 2 Block diagram after substituting all values

3 PID Control Design for AVR System

The first-ever PID controller was developed by Elmer Sperry in 1911. But the first pneumatic controller with the fully tunable proportional controller was developed in 1933 by Taylor Instrumental Company. Then to eliminate the steady-state error found in the proportional controllers, they developed Proportional-Integral (P-I) controller. Then to reduce the overshooting issues, the first Proportional-Integral-Derivative (PID) controller was developed by TIC in 1940. It was not until 1942 when Ziegler and Nichols have come up with the tuning rules that the engineers were able to find and set appropriate control parameters for PID controllers. The automatic PID controllers were introduced in 1950s which are widely used in Industries to control various parameters.

A PID controller stands for Proportional-Integral-Derivative controller. It is a three-term controller with P, I and D control coefficients. PID controllers are used to regulating parameters like temperature, flow, pressure, speed etc. in various industrial control applications. For this, a feedback control loop is used to control the process variables. PID controllers use the closed-loop feedback control to get the actual output value as close as possible to the setpoint output or target output.

Tuning the PID controller is nothing but finding out the corresponding PID parameters (Kp, Ki, Kd) to achieve optimum performance from the process and this is a crucial part in all of the closed-loop control systems. There are a number of tuning methods which have been developed by different scientists over the years. But a single method can't be justified for all the operating conditions of the system, hence finding out the most appropriate method which gives an optimum result has become an important task. The PID Tuning methods can be broadly classified into Heuristic tuning, Rule-based tuning and model-based tuning. Heuristic tuning is where we used general rules to obtain approximate results, for example, the trial-and-error method. Model-based tuning is where a structured tuning process is used which considers both your process behavior and your control needs. Rule-based tuning methods assume a certain process response to obtain mathematical formulas that enable the tuning of a PID controller. But in this paper, rule-based PID tuning methods are used to

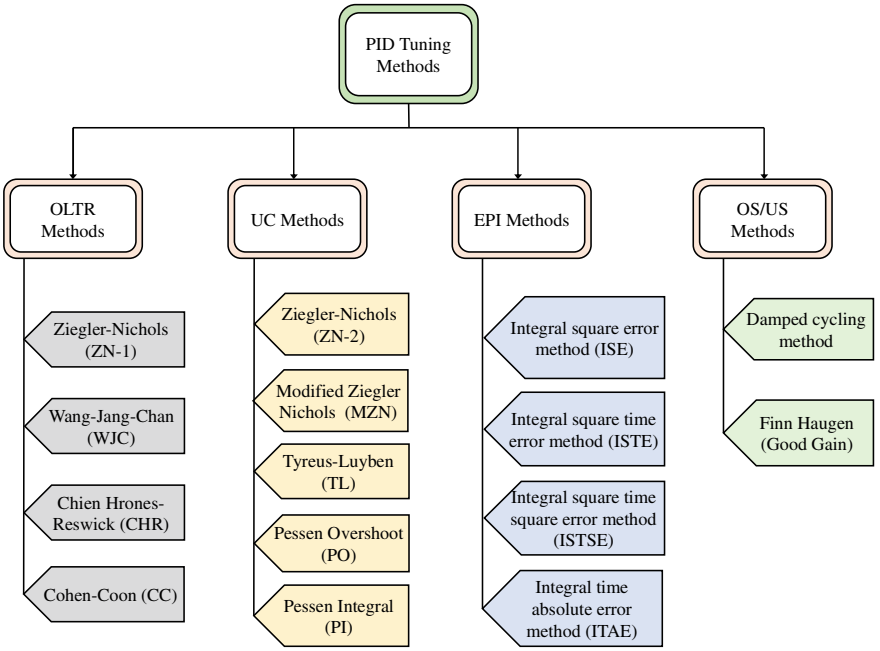

Fig. 3 PID tuning methods

find out the most optimal tuning method for the AVR system. The following are the categories of PID Tuning methods used in this paper to tune the AVR system as shown in Fig. 3.

3.1 Implementing OLTR Methods

In order to implement the OLTR methods the system needs to be undamped and for that all the feedback loops are removed; this makes the system act as a control free operation. Then the open loop system is given a step input and the output is observed by connecting the system to an oscilloscope. Then draw a tangent to the response curve at the inflection point. From this, the values of dead time ($T_d = 1.25$), time constant ($T_c = 3$), stationary gain ($K_s = 119$) and slope of the tangent (M = 36.36) as seen in Fig. 4. Using these values PI gain parameters are calculated as per the formulas mentioned in Table 2.

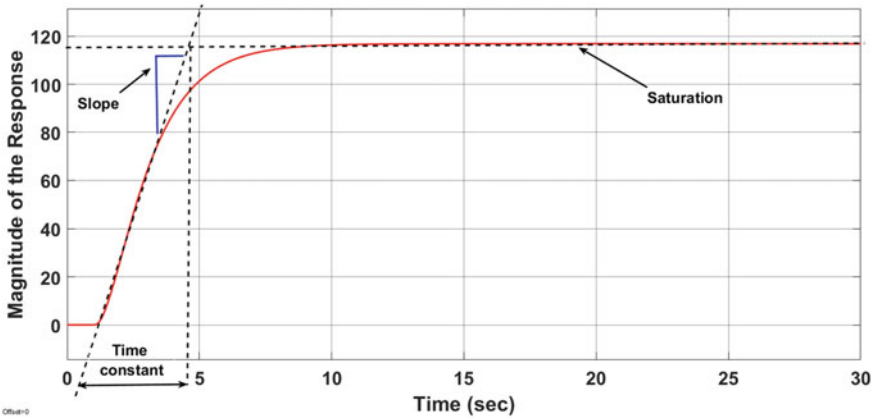

Fig. 4 Open loop response of the AVR system

Table 2 Formula for designing PI gain values of OLTR methods

Method	K_p		$K_i = K_p/T_i$	
	Formula	Value	Formula (T_i)	Value
ZN-1	$0.9/M\ T_d$	0.0198	$3.3\ T_d$	0.0048
WJC	$\left(0.73 + \frac{0.531T_c}{T_d}\right)\frac{(T_c+0.5T_d)}{K_s(T_c+T_d)}$	0.0043	$T_c + 0.5\ T_d$	0.0012
CHR	$0.35/M\ T_d$	0.0077	$1.2\ T_d$	0.0051
CC	$\frac{0.9}{M\ T_d}\left(1 + \frac{0.92T_c}{1-T_c}\right)$	−0.0075	$\frac{3.3+3\ T_c}{1+1.2\ T_c}T_d$	0.0049

3.2 Implementation of Ultimate Cycles Methods

To implement the UC methods, the system needs to behave as a sustainable oscillatory system and to achieve it the gain of the system is increased until a sustainable oscillatory response is obtained. The gain at which the desired oscillatory response is obtained is represented with K_c and the time period is represented with T_c. These gain and time period values are substituted into the formulas [20] to get K_p, K_I and K_d values. The Simulation model for getting sustained oscillations is represented as shown in Fig. 5. The sustained oscillations are obtained at a gain of 0.2304 and the time period is 1.3 as shown in Fig. 6. Using these gain and time periods, the values of PID controller parameters are calculated as per the formulas mentioned in Table 3.

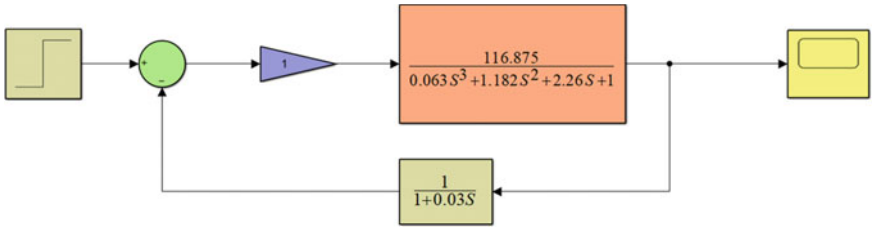

Fig. 5 MATLAB simulation model to obtain sustained oscillations

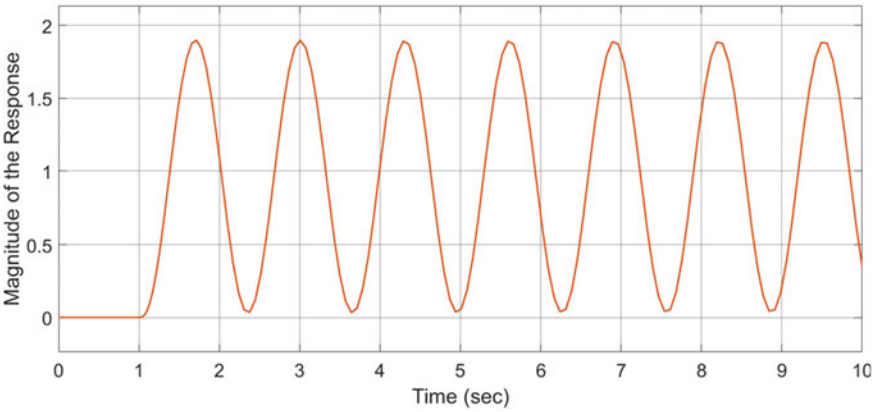

Fig. 6 MATLAB/SIMULINK model for obtaining the sustained oscillations for AVR system

Table 3 Formulas for designing PID gain values of UC methods

Parameters	Ziegler-Nichols PID controller tuning formula	Modified Ziegler-Nichols PID controller tuning formula	Tyreus-Luyben PID controller tuning formula
T_i	$T_c/2 = 0.65$	$T_c = 1.3$	$2.2T_c = 2.86$
T_d	$T_c/8 = 0.15$	$T_c/3 = 0.433$	$T_c/6.3 = 0.206$
K_p	$0.6\,K_c = 0.138$	$0.2\,K_c = 0.046$	$0.45\,K_c = 0.103$
K_i	$K_p/T_i = 0.212$	$K_p/T_i = 0.035$	$K_p/T_i = 0.036$
K_d	$K_p \times T_d = 0.020$	$K_p \times T_d = 0.019$	$K_p \times T_d = 0.021$

3.3 Implementation of EPI Methods

OLTR methods are limited with respect to the adjustment of steady-state error. For systems which are sensitive to transients, even a minor error can deviate the behavior of the system. In such systems, Error Performance Index methods provide a better

Table 4 Specifications used to calculate EPI methods

Method	a_1	a_2	b_1	b_2
ISE	1.048	1.195	−0.897	−0.368
ISTSE	0.968	0.977	−0.904	−0.253
ISTE	1.042	0.987	−0.897	−0.238
ITAE	0.965	0.796	−0.85	−0.1465

system response by effectively nullifying the steady-state errors [13]. The PID parameters are calculated using (8) and (9) and the values of a1, a2, b1 and b2 are given in Table 4.

$$K_p = \frac{a_1}{K_s}\left(\frac{T_d}{T_c}\right)^{b_1} \tag{8}$$

$$K_i = T_c\left(a_2 + b_2\left(\frac{T_d}{T_c}\right)\right)^{-1} \tag{9}$$

3.4 Implementation of Overshoot/Undershoot Methods

In order to implement the OS/US methods, an underdamped system is required. To get an underdamped response of the AVR system, the PID controller is replaced with a P-Controller and the feedback loop is replaced with unity gain feedback. The gain value of the P-controller is recorded as K_p when the system attains an undamped response and the time difference between the first overshoot and undershoot is termed as T_{out}. The delay ratio is calculated by dividing the first overshoot by the second overshoot and all these three values are substituted in to get the gain parameters of OS/US methods. The MATLAB model implementing different categories of tuning techniques is shown in Fig. 7. The detailed representation of each gain value of the PID controller obtained by various tuning methods is tabulated in Table 5.

4 Simulation Results

As the main objective of this paper is to find the most optimum tuning method for the AVR system, various parameters of all the obtained responses are compared to find the most appropriate method. Among the open-loop response methods, CHR and CC methods responses have a slight overshoot compared to the setpoint value as shown in Figs. 8 and 9 respectively. Whereas in the ZN-1 method, we observe a small peak before settling at the set value but the settling time in this method is smaller as

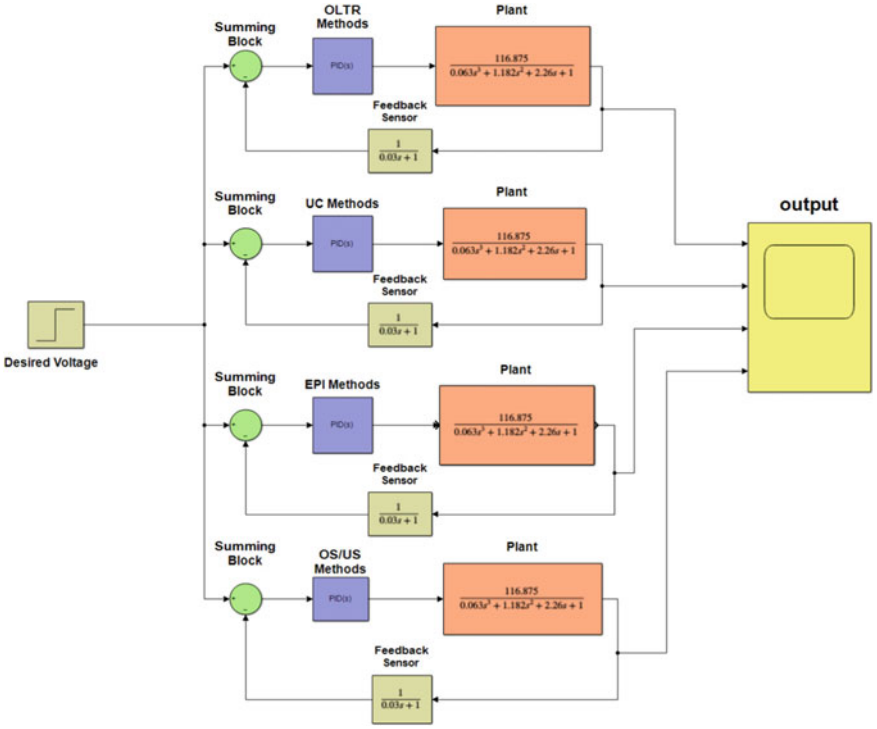

Fig. 7 MATLAB/Simulink model for OLTR methods

Table 5 PID gain parameters for all the methods

Category	Method name	K_p	K_i	K_d
OLTR	ZN-1	0.0198	0.0048	–
	WJC	0.0043	0.0012	–
	CHR	0.0077	0.0051	–
	CC	−0.0075	0.0049	–
UCM	ZN-2	0.13824	0.21267	0.020736
	MZN	0.04608	0.03544	0.01996
	TL	0.10368	0.03625	0.02138
	PO	0.0768	0.118035	0.03328
	PI	0.16128	0.310153	0.031449
EPIM	ISE	0.0199	0.0069	–
	ISTSE	0.018	0.0053	–
	ISTE	0.019	0.0058	–
	ITAE	0.017	0.0068	–
OS/US	DCM	0.15125	0.121124	0.047217
	GGM	0.028	0.01166	0.0168

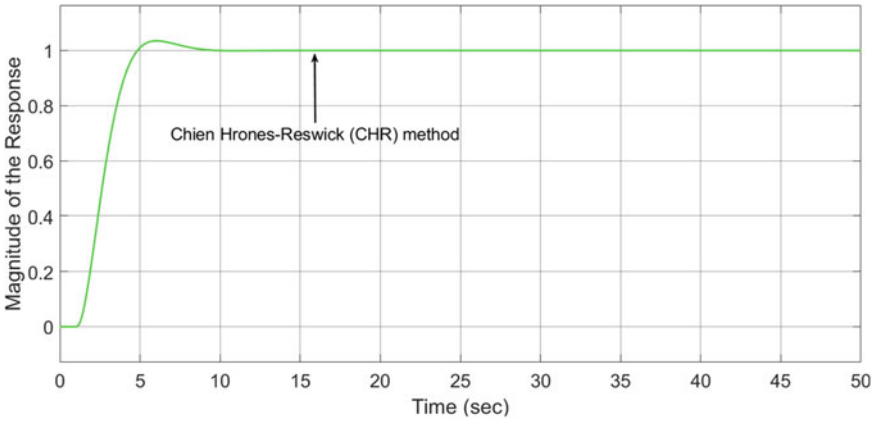

Fig. 8 AVR system response implemented with CHR method

compared to the settling time in the WJC method where there are no peaks observed by taking longer to settle as shown in Figs. 10 and 11 respectively. The time-domain response parameters comparison is done in Table 6. Also, all the OLTR method responses are represented in a single frame which gives a better understanding for comparison and analysis as shown in Fig. 12. All the UC methods have shown some peak overshoot in the transient state. But the highest peak overshoot is observed in the ZN-2 method as shown in Fig. 13 and the lowest is seen in the MZN method as shown in Fig. 14. A slight oscillatory response in the transient state is observed in both the ZN-2 method and PI method as shown in Fig. 15. Among all the UC methods, the TL method takes the least time to settle to the set value as shown in Fig. 16. The system response implemented with the PO method is shown in Fig. 17. Also, all the UC method results are shown in a single frame which gives a better understanding for comparison/analysis as shown in Fig. 18.

The responses of all the EPI tuning methods are almost equal except for some minute differences. The time-domain responses of ISE, ISTE, ISTSE AND ITAE methods are shown in Figs. 19, 20, 21 and 22. Among all the EPI methods, the ITAE method can be considered as an optimum method as it reaches the setpoint value exactly, whereas all the other three methods settle down to a value slightly less than the setpoint and all their settling times are almost the same. This can be observed in Fig. 23 where all the responses of EPI methods are cumulatively represented in one frame.

A peak overshoot is observed in the Damped Cycles method whose response is shown in Fig. 24. Whereas the Good gain method doesn't have any overshoot in its response and settles down to the setpoint value smoothly as shown in Fig. 25. But when it comes to settling time DCM method settles down much faster as compared to the GG method which can be observed in Fig. 26.

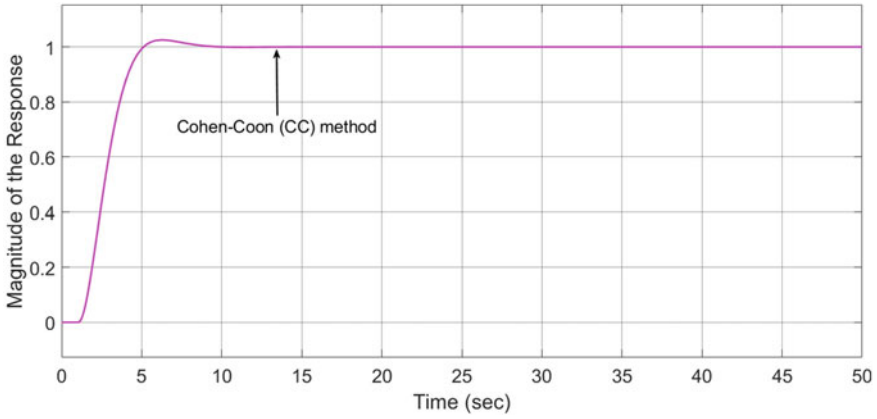

Fig. 9 AVR system response implemented with CC method

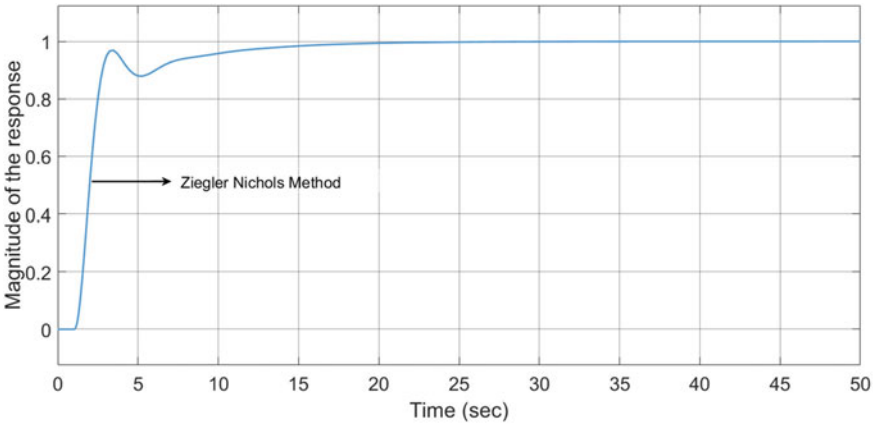

Fig. 10 AVR system response implemented with ZN-1 method

5 Conclusion

In this paper, a comprehensive analysis has been carried out in order to find the most optimum PID tuning method for the Automatic Voltage Regulator (AVR) system. The paper contains a detailed time-domain specifications analysis along with all the simulation results obtained. A method is considered optimum or stable when it has a smooth response with less peak overshoot and settling time. Such methods are suitable to tune the PID controller for the AVR system to maintain a constant voltage value.

In comparing all the OLTR methods, the CC method is considered the best as it has a non-oscillatory response, very less peak overshoot and less settling time.

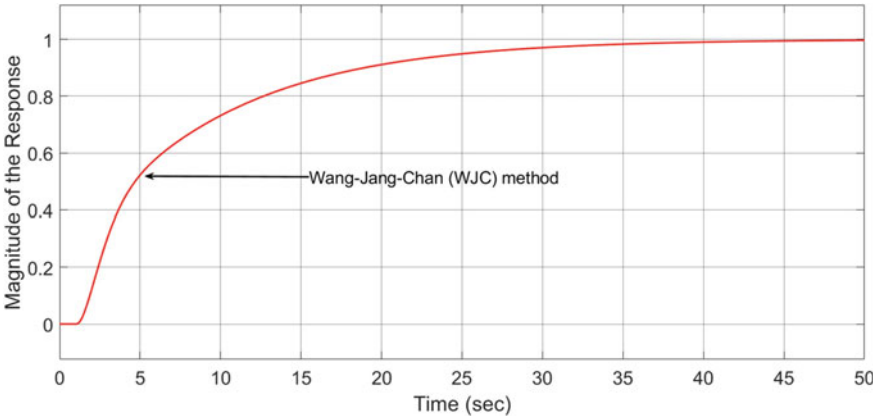

Fig. 11 AVR system response implemented with WJC method

Table 6 Performance metrics for various tuning methods implanted for the AVR system

Category	Method	Rise time	Peak Overshoot	Settling time	Delay time	Transient behavior
OLTRM	ZN1	2.765	No overshoot	18.112	1.98	Oscillatory
	WJC	18.968	No overshoot	42	4.728	Non-oscillatory
	CHR	4.009	3.4	9.735	2.601	Non-oscillatory
	CC	4.172	2.2	9.44	2.667	Non-oscillatory
UCM	ZN2	1.345	61.8	7.594	1.224	Oscillatory
	MZN	1.706	9	5	1.320	Non-oscillatory
	TL	1.423	21.6	3.873	1.248	Oscillatory
	PO	1.456	19.7	7.5	1.214	Oscillatory
	PI	1.319	64.7	6.306	1.188	Oscillatory
EPIM	ISE	2.636	4.3	7.5	1.955	Non-oscillatory
	ISTE	2.871	No overshoot	8.556	2.015	Non-oscillatory
	ISTSE	2.767	No overshoot	8.818	2.005	Non-oscillatory
	IAE	2.818	3.4	7.916	2.058	Non-oscillatory
OS/USM	DCM	1.261	22.7	3.994	1.156	Oscillatory
	GGM	2.682	No overshoot	6.087	1.418	Non-oscillatory
Superior Method	**GGM**	**DCM**	**ZN-1, WJC, ISTE, ISTSE, GGM**	**TL**	**GGM**	**WJC, CHR, CC, MZN, ISE, ISTE, ISISE, IAE, GGM**

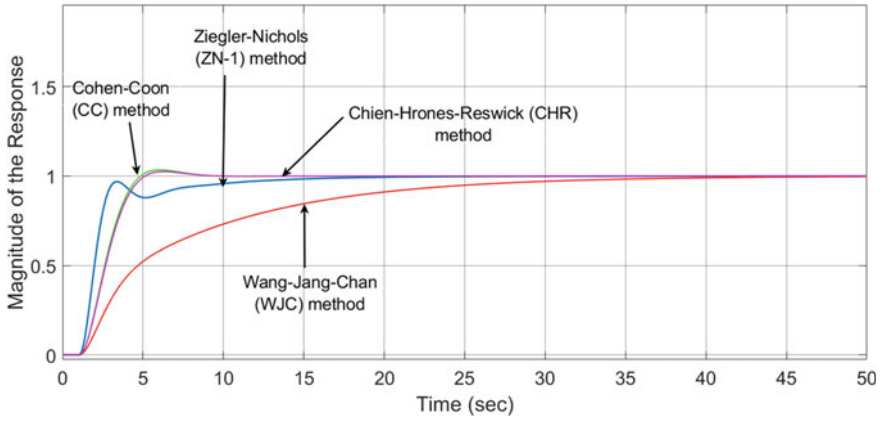

Fig. 12 Cumulative responses of AVR system implemented with OLTR methods

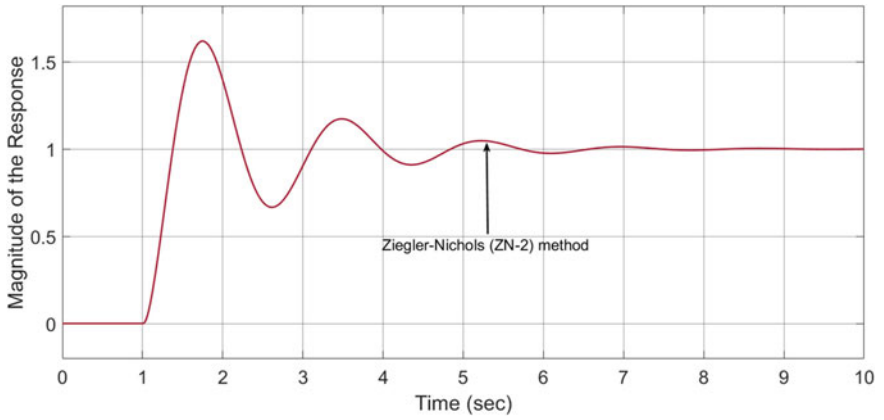

Fig. 13 AVR system response implemented with ZN-2 method

Similarly, the MZN method is considered the best among the UC methods because of less overshoot and settling time. Among EPI methods, the ITAE method can be considered as an optimum method as it reaches the setpoint value exactly whereas all the other three methods settle down to a value slightly less than the set point.

So, after doing an overall constructive time-domain analysis, Good Gain Method from Overshoot/Undershoot methods is chosen as the best method for the proposed AVR system as it gives a non-oscillatory response, has the least delay time of all the methods, has less settling time and no peak overshoot in the response. Hence, it is concluded that the Finn Haugen (Good Gain) method is the most optimal tuning method for the considered Automatic Voltage Regulator (AVR) system.

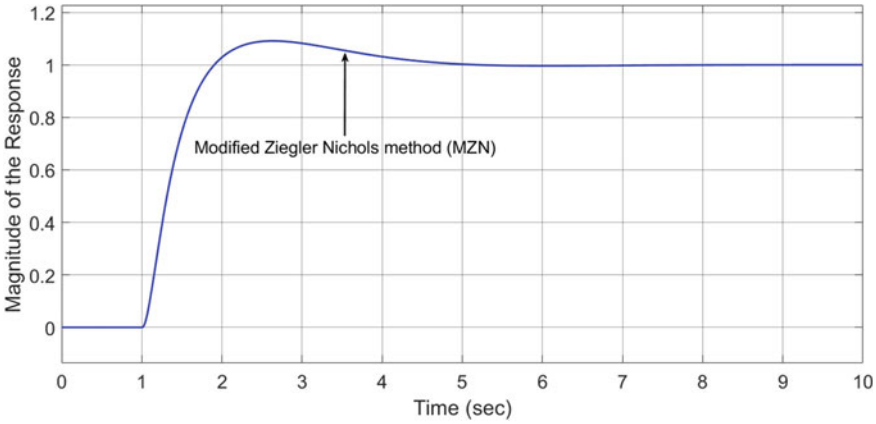

Fig. 14 AVR system response implemented with MZN method

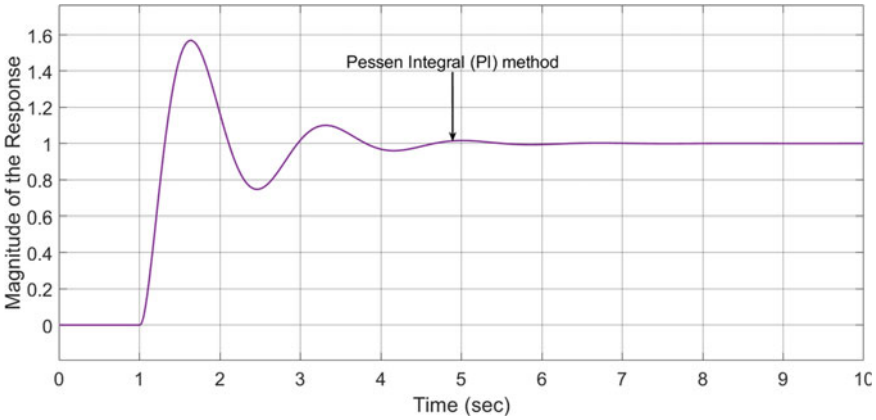

Fig. 15 AVR system response implemented with PI method

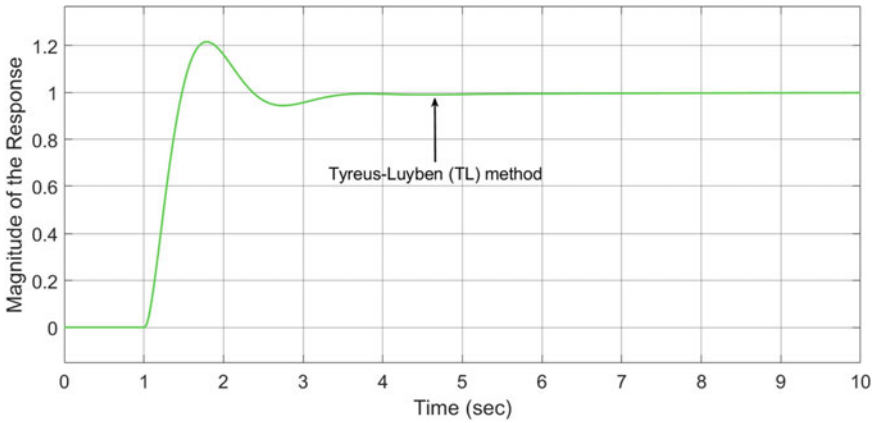

Fig. 16 AVR system response implemented with TL method

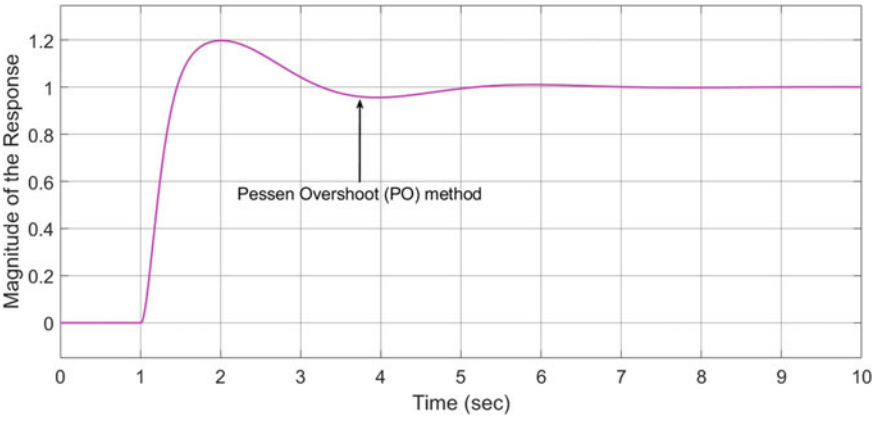

Fig. 17 AVR system response implemented with PO method

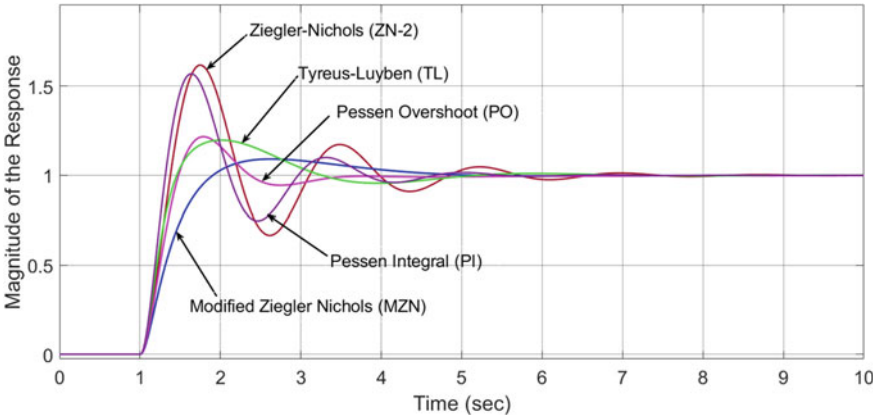

Fig. 18 Cumulative responses of AVR system implemented with UC methods

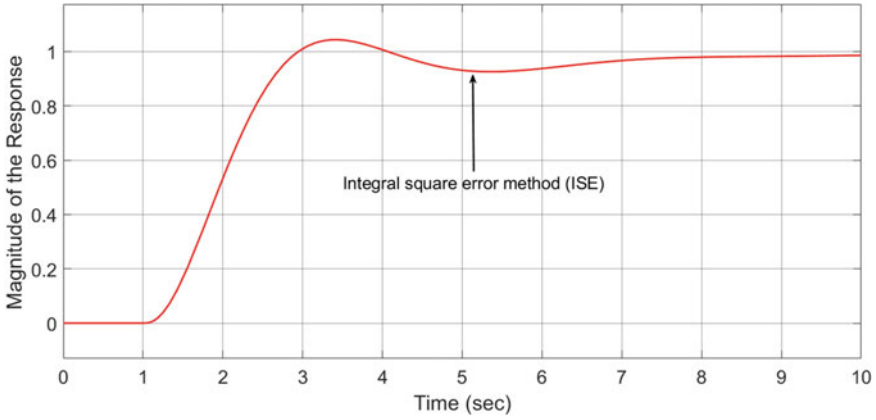

Fig. 19 AVR system response implemented with ISE method

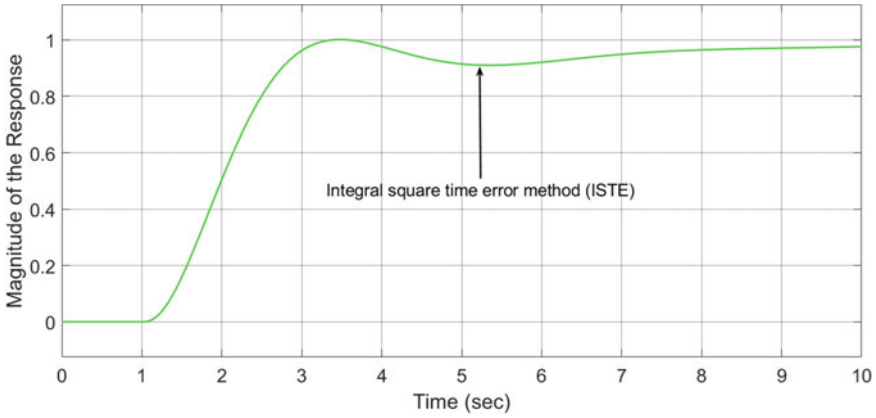

Fig. 20 AVR system response implemented with ISTE method

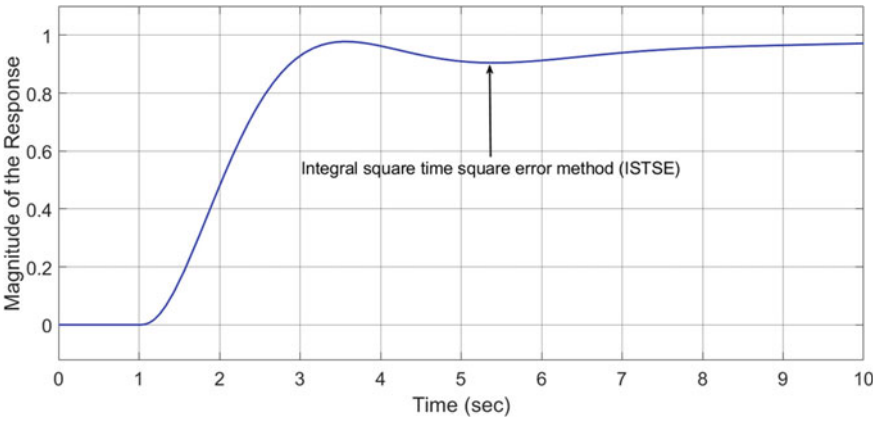

Fig. 21 AVR system response implemented with ISTSE method

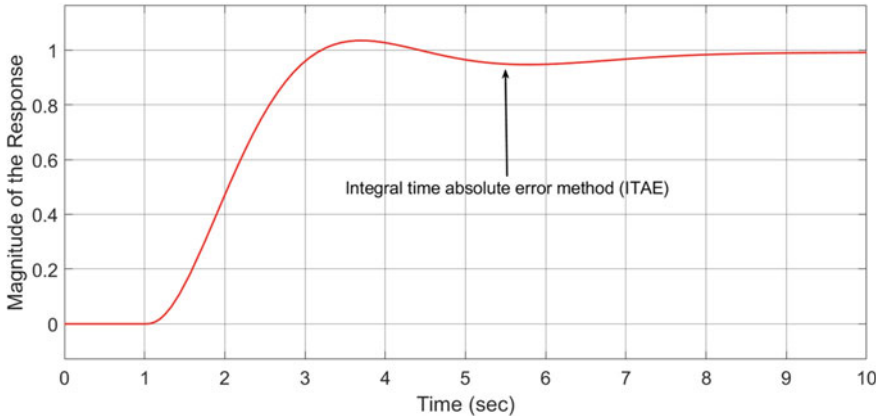

Fig. 22 AVR system response implemented with ITAE method

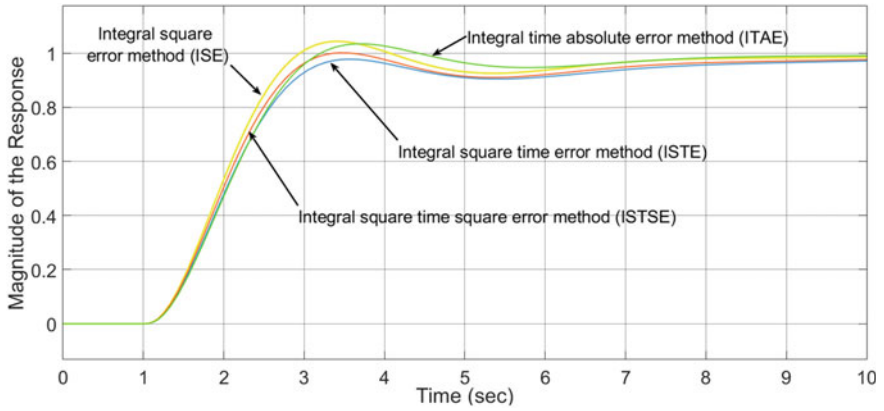

Fig. 23 Cumulative responses of AVR system implemented with EPI methods

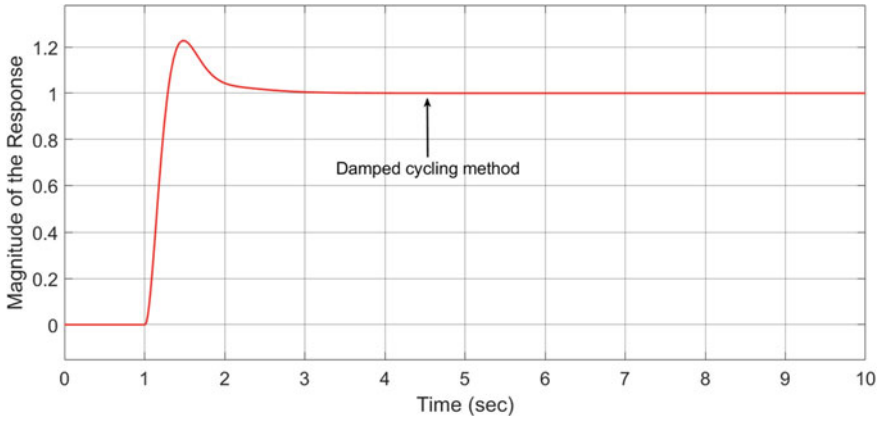

Fig. 24 AVR system response implemented with DCM method

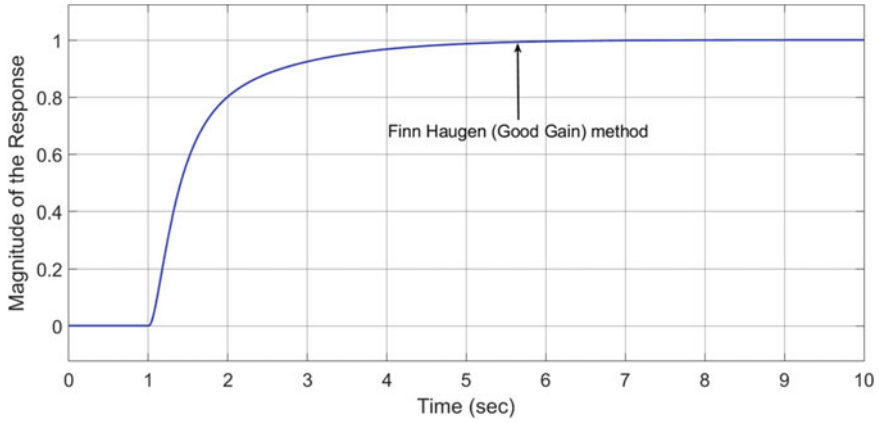

Fig. 25 AVR system response implemented with Finn Haugen (GG) method

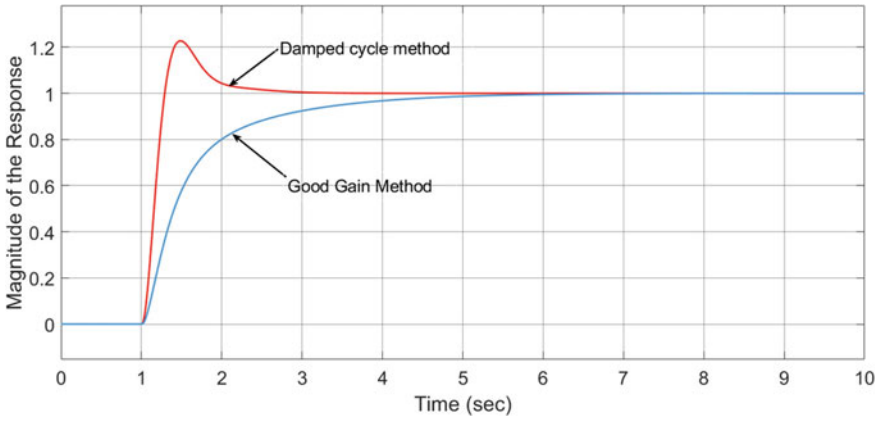

Fig. 26 Cumulative responses of AVR system implemented with US/OS methods

References

1. H.I. Kang, M.W. Kwon, H.G. Bae, PID coefficient designs for the automatic voltage regulator using a new third order particle swarm optimization, *2010 International Conference on Electronics and Information Engineering (ICEIE 2010)*, pp. 179–183, Kyoto, Japan (2018)
2. P. Andhare, N. Asati, PID controlled automatic voltage regulator with load frequency control. Int. J. Electr. Electron. Comput. Eng. **5**(2), 5–10 (2016)
3. M.M. Puralachetty, V.K. Pamula, V.N.B. Akula, Comparison of different optimization algorithms with two stage initialization for PID controller tuning in automatic voltage regulator system, *2016 IEEE Students' Technology Symposium (TechSym)*, pp. 152–156, Kharagpur, India (2016)
4. H. Wu, W. Su, Z. Liu, PID controllers: design and tuning methods, *2014 9th IEEE Conference on Industrial Electronics and Applications*, pp. 808–813, Hangzhou, China (2014)
5. S. Li, Q. Jiang, Study on PID parameters tuning method based on Matlab/Simulink, *2011 IEEE 3rd International Conference on Communication Software and Networks*, pp. 408–411, Xi'an, China (2011)
6. D.M. Saj nekar, S.B. Deshpande, R.M.Moharil, Efficient PID controller tuning method selection to be used in excitation system of brushless synchronous generator, *2016 International Conference on Computation of Power, Energy Information and Communication (ICCPEIC)*, pp. 413–418, Melmaruvathur, India (2016)
7. N.F. Mohammed, E. Song, M.A. Xiuzhen, Q. Hayat, Tuning of PID controller of synchronous generators using genetic algorithm, *2014 IEEE International Conference on Mechatronics and Automation*, pp. 1544–1548, Tianjin, China (2014)
8. M. Tajjudin, M.H.F. Rahiman, N. Ishak, R. Adnan, H. Ismail, Comparison between optimally-tuned PID with self-tuning PID for steam temperature regulation, *4th International Conference on Intelligent and Advanced Systems (ICIAS2012)*, pp. 551–556, Kuala Lumpur, Malaysia (2012)
9. A. Khalid, A.H. Shahid, K. Zeb, Comparative assessment of classical and adaptive controllers for automatic voltage regulator, *International Conference on Advanced Mechatronic Systems (ICAMechS)*, pp. 538–543, Melbourne, VIC, Australia (2016)
10. R. Lahcene, S. Abdeldjalil, K. Aissa, Optimal tuning of fractional order PID Controller for AVR system using simulated annealing optimization algorithm*, 5th International Conference on Electrical Engineering—Boumerdes (ICEE-B),* pp. 1–6, Boumerdes, Algeria (2017)

11. F. Aboura, Tuning PID controller using hybrid genetic algorithm particle swarm optimization method for AVR system, *2019 International Aegean Conference on Electrical Machines and Power Electronics (ACEMP) & 2019 International Conference on Optimization of Electrical and Electronic Equipment (OPTIM)*, pp. 570–574, Istanbul, Turkey (2019)
12. P. Sirsode, A. Tare, V. Pande, Design of robust optimal fractional-order PID Controller using Salp swarm algorithm for automatic voltage regulator (AVR) system, *2019 Sixth Indian Control Conference (ICC)*, pp. 431–436, Hyderabad, India (2019)
13. K. Gnaneshwar, R. Trivedi and P.K. Padhy, Optimal tuning of FOPID parameters with SFL algorithm for an AVR system, *2020 4th International Conference on Electronics, Communication and Aerospace Technology (ICECA)*, 2020, pp. 187–192, Coimbatore, India (2020)
14. K. Elumalai, S. Sumathi, Behavior modification of PID controller for AVR system using particle swarm optimization, *2017 Conference on Emerging Devices and Smart Systems (ICEDSS)*, 2017, pp. 190–195, Mallasamudram, India (2017)
15. V. Bharath Kumar, D. Sampath, V.N. Siva Praneeth, Y.V. Pavan Kumar, Error performance index based PID tuning methods for temperature control of heat exchanger system, *2021 IEEE International IOT, Electronics and Mechatronics Conference (IEMTRONICS)*, 2021, pp. 1–6, Toronto, ON, Canada (2021)
16. I.S. Zubkova, O.N. Kuznetsov, Electric power system stability conditions with automatic voltage regulator, *4th International Youth Conference on Radio Electronics, Electrical and Power Engineering (REEPE)*, pp. 1–6, Moscow, Russia (2022)
17. J. Sahu, P. Satapathy, M.K. Debnath, P.K. Mohanty, B.K. Sahu, J.R. Padhi, Automatic voltage regulator design based on fractional calculus plus PID controller, *International Conference on Computational Intelligence for Smart Power System and Sustainable Energy (CISPSSE)*, pp. 1–4, Keonjhar, India (2020)
18. N. Farouk, T. Bingqi, Application of self-tuning fuzzy PID controller on The AVR system, *IEEE International Conference on Mechatronics and Automation*, pp. 2510–2514, Chengdu, China (2012)
19. K. Eswaramma, Dr. G. Surya Kalyan, An automatic voltage regulator(AVR) system control using a P-I-DD controller. Int. J. Adv. Eng. Res. Dev. **4**(6), 499–506(2017)
20. S. Sharma, J. Bhadoriya. Automatic load frequency control in three area power system using the PID controller. Int. J. Innov Res. Electr. Electron. Instrumen. Control Eng. **3**(8), 138–143 (2015)

Tie-Line Bias Control for Frequency Deviation in the Presence of System Uncertainties with WTG and BESS: A Robust Control Approach

Shailendra Singh and M. K. Verma

Abstract In stand-alone mode, an AC power system such as microgrid can experience large frequency deviations arising due to RES (Renewable Energy Sources) power fluctuations. In this paper, a robust Proportional-Integral-Derivative (PID) tuner-based controller is proposed for mitigating the frequency transients arising from the variation in load and renewable energy resources power output. Conventional PID controllers are incapable of handling the system uncertainties. This work tries to develop robust control strategies for both the battery and conventional generation systems, with controllers designed to significantly reduce frequency variation, despite variable loads in the microgrid and the incorporation of a Wind Turbine Generator (WTG) source. Controllers are designed to cope with load transients, WTG output fluctuations and model uncertainties.

Keywords Load Frequency Control (LFC) · Tie-line bias control (TBC) · System uncertainties · Robust control

1 Introduction

Microgrids have gained wide attention in the past due to their benefits of higher system reliability, diverse generation possibility and reduced investment cost [1]. These systems are distinguished from traditional power systems wherein power is transmitted over a long distance. The penetration of renewable energy resources has reduced the dependency on combustible fuel. These renewables include Photovoltaics, wind energy systems, hydro energy systems etc. The higher cost-effective wind energy systems are being integrated into the conventional power system network at a higher pace [2]. The power output of the WTG system is in proportion with the cube of wind speed and hence can possibly cause large deviations in the system

S. Singh (✉) · M. K. Verma
Department of Electrical Engineering, IIT-BHU, Varanasi, India
e-mail: shailendras.rs.eee16@iitbhu.ac.in

M. K. Verma
e-mail: mkverma.eee@iitbhu.ac.in

J. Kumar et al. (eds.), *Control Applications in Modern Power Systems*, Lecture Notes in Electrical Engineering 974, https://doi.org/10.1007/978-981-19-7788-6_13

frequency. In this work, control over active power is deployed in order to achieve a reduction in frequency deviations [3]. Battery Energy Storage Systems (BESS) have been widely used for mitigating frequency deviation due to their capability of fast power injection. Due to the higher costs involved, the battery sizing poses a challenge while selecting the optimal capacity. For such a system configuration, existing control approaches are incapable of handling the frequency transients in the presence of system uncertainties. Various classical integral (I), proportional-integral (PI), and proportional-integral-derivative (PID) controllers are utilized for LFC problems in power systems [4]. Further, a robust output feedback based linear quadratic regulator (LQR) controller is proposed in [5] for LFC in the system. Recently, meta-heuristic approaches have been applied for tuning the controller [6–8]. Various research works have adopted fuzzy logic for controller tuning [9–11]. Different layered control strategies for BESS to damp out wind transients are proposed in [12, 13]. However, developing an accurate fuzzy logic model to deliver satisfactory performance is difficult. In this work, a robust tuned PID controller is developed that delivers satisfactory performance over the control parameters, thus ensuring system reliability. Large-scale integration of intermittent RES injects high-frequency transients taken care of by the BESS. Further, consideration of BESS size is also crucial due to the higher costs involved. Thus, different battery sizes are considered for obtaining the smallest size of the battery and being able to mitigate high-frequency transients.

The remaining paper is framed as follows. Section 2 discusses the test system modelling. Control design with various weighing parameters has been inked in Sect. 3. In Sect. 4, simulation results are presented, and the work is concluded in Sect. 5.

2 Test System Modelling

The typical setup of the test system is modelled using SIMULINK in MATLAB as shown in Fig. 1 with the parameters specified in Tables 1 and 2. The detailed model of the power system network was created consisting of generation units, loads and electricity grid while taking characteristics of generation unit and their response to drops in frequency into consideration. In the system, both types of energy sources, i.e., conventional and renewable Wind-Turbine-Generator (WTG) sources, are present. The green block over the component represents that the individual element is controllable. Low-frequency transients are taken care of by conventional sources. In contrast, Battery Energy Storage System (BESS), having the capability to quickly inject/absorb active power, takes care of the high-frequency transients often produced by RES. A mathematical model is utilized for analyzing the system and controller design for minimizing the frequency deviation (Δf). The developed model comprises the conventional generator system, WTG system and BESS, as shown in Figs. 2, 3 and 4.

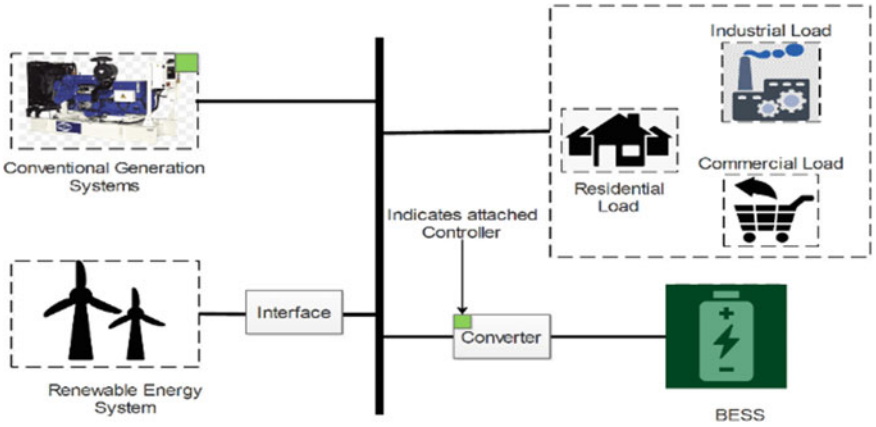

Fig. 1 Setup of microgrid with RES and BESS

Table 1 Parameters of conventional generator

Parameter	Value
Governor time constant T_g	0.1 s
Diesel engine time constant T_d	5.0 s
Inertia Constant M	0.15 pu MWs/Hz
Damping constant D	0.008 pu MW/Hz
Speed Droop R	3.0 Hz/pu

Table 2 Parameters of wind turbine generator (WTG)

Parameter	Value
Blade radius R_w	14 m
Inertia coefficient J	62.993 kgm^2
Air density ρ	1.225 kg/m^3
Rated output P_{wg}	350 kW
Phase Voltage V	692.82 V
Stator resistance R_1	0.00397 Ω
Stator reactance X_1	0.0376 Ω
Rotor resistance R_2	0.00443 Ω
Rotor reactance X_2	0.534 Ω

The power imbalance between load and generation causes the frequency deviation in the system, and hence it is normalized to per-unit (p.u.). The commanding power output of conventional generator and BESS are the error signals. The saturation block in the BESS model prevents overcharging and deepdischarging of the battery. The mechanical power output of the WTG (P_{wind}) is normalized to p.u. by generated power (P_{wg}). The output of the WTG system is uncontrolled by the

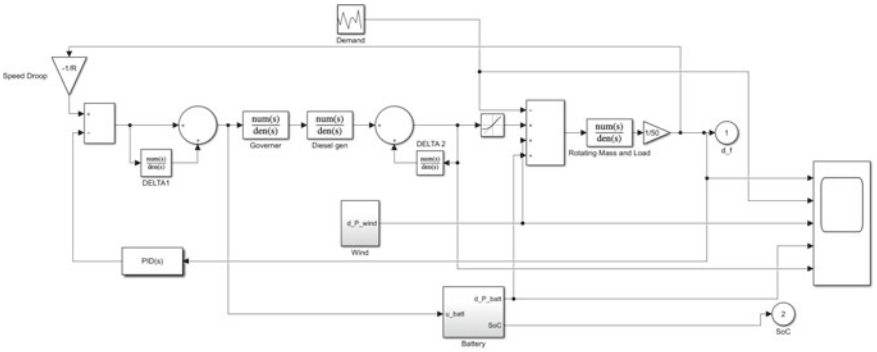

Fig. 2 Typical test system with WTG and BESS

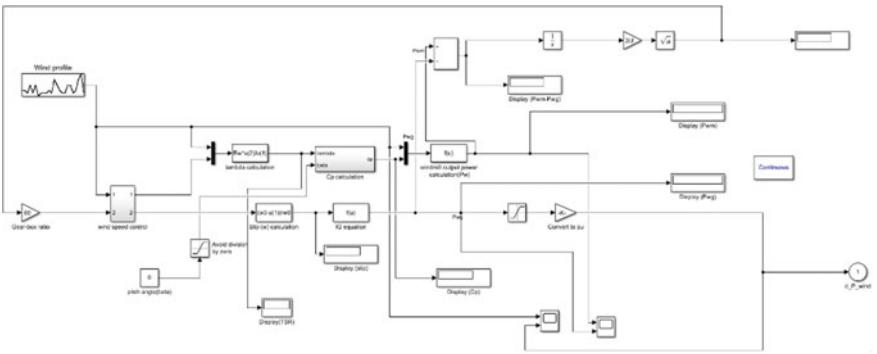

Fig. 3 Wind turbine generator (WTG) model

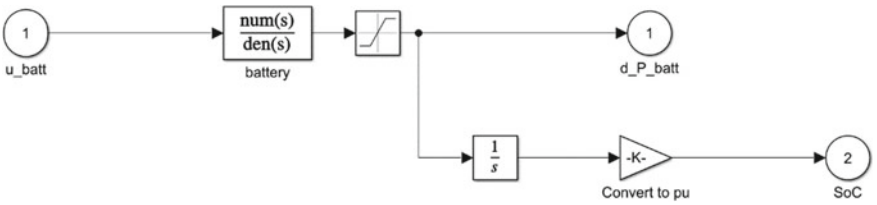

Fig. 4 Battery energy storage system model

proposed controller and hence, considered as a disturbance for the system. The power produced by the WTG is given as follows with the values of the parameters listed in Table 2:

$$\lambda = \frac{wR_w}{V_{wind}} \tag{1}$$

$$C_p = f(\lambda, \beta) \tag{2}$$

$$P_{wm} = \frac{C_p V_{wind}^3 \rho A}{2} \tag{3}$$

$$S_s = \frac{w_0 - w}{w_0} \tag{4}$$

$$P_{wg} = \frac{-3V^2 s_s (1 + s_s) R_2}{(R_2 - s_s R_1)^2 + s_s^2 (X_1 + X_2)^2} \tag{5}$$

2.1 Conventional Generator with WTG and BESS Modelling

See Fig. 2 and Table 1.

2.2 Wind Turbine Generator Modelling

See Fig. 3 and Table 2.

2.3 Battery Energy Storage System (BESS) Modelling

The mathematical model of BESS is shown in Fig. 4. The commanded power output, *u_batt* is in accordance with the battery capacity. A first-order lag system is utilized to incorporate the response of power electronic (P.E.) converter with $T_b = 0.1s$. . The State of Charge (SoC) of the battery is obtained by integrating the power output of BESS.

3 Controller Design with Uncertainties

3.1 Uncertainty in the System

Model uncertainty is the error between the actual physical system and its mathematical model developed for simulation. These modelling errors in the system are introduced in the form of multiplicative uncertainties. These can be lumped together to form an uncertainty parameter Δ, as shown in Fig. 5. The robustness of a system

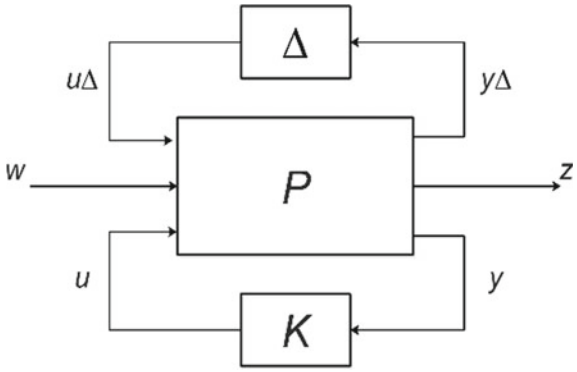

Fig. 5 Configuration of the robust control approach

can be quantified by the smallest Δ that yields singular $I - M\Delta$, where M is the linear fractional transform (LFT) of P and K.

3.2 Disturbance Signals on the System

In this system, two disturbance signals have been considered, i.e., changing load profile and uncertain WTG output. It is easily understood that load consumes power while WTG injects. Since WTG output is uncontrolled, which depends upon the wind speed profile, it acts as a disturbance in our system. Hence, both the signals are combined at the summer junction.

3.3 Performance Weights Selection

The net load profile in the system is a combination of the load drawing power from the system and WTG power output. This load consists of both high-frequency and low-frequency transients that are balanced by the conventional generator and BESS. Due to the fast power injection/absorption capability of BESS, the weight on the error control signal of BESS (W_b^e) is applied so that it primarily takes care of high-frequency transients. On the contrary, the error control signal of the generator (W_g^e) is weighted to deal with low-frequency transients. Weight is also applied to the battery SoC error control signal (W_{SoC}^e) to avoid overcharging and deep discharging of the battery.

$$W_g^e = \frac{20}{s + 0.0001} \tag{6}$$

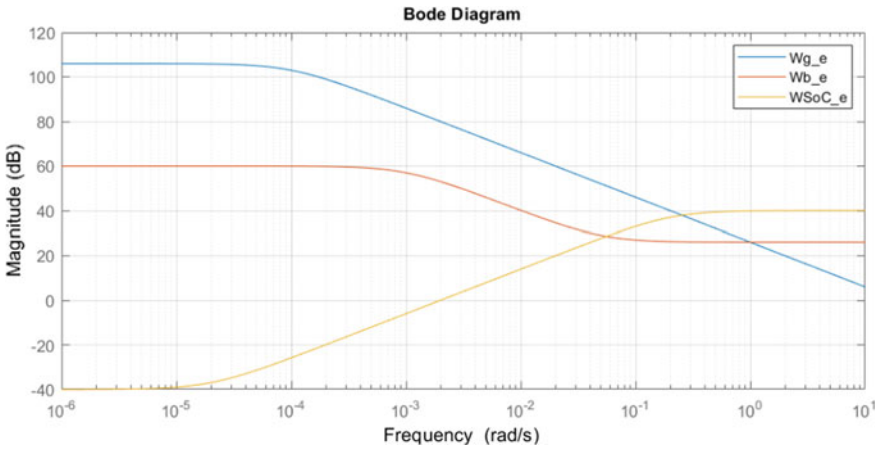

Fig. 6 Bode Plot (magnitude) of performance weight parameters

$$W_b^e = \frac{20s + 1}{s + 0.001} \tag{7}$$

$$W_{SoC}^e = \frac{50s + 0.001}{0.5s + 0.1} \tag{8}$$

The bode plot in Fig. 6 shows the control error signals magnitude over the frequency range $10^{-6} - 10^1 rad/s$. The generator signal has a large magnitude for the low-frequency region, while the battery signal magnitude is sufficiently high for the high-frequency range. The SoC signal magnitude is very low in the lower frequency range, where the battery is mostly inactive.

Two controllable inputs, i.e., conventional generator (W_g^c) and battery (W_b^c) weights have been assigned as:

$$W_g^c = \frac{s + 0.1}{5s + 1} \tag{9}$$

$$W_b^c = \frac{0.2s + 0.1}{100s + 0.1} \tag{10}$$

The bode plot in Fig. 7 shows that the generator control signal is heavily penalized in the lower frequency range and, hence, remains inactive for the load variation in the lower frequency range. The battery control signal weight amplitude is higher in this frequency range as the battery takes care of the fast transients in load change. Similarly, weights are adjusted such that, in the higher frequency range, the generator remains active and the battery is nearly inactive (Figs. 8 and 9).

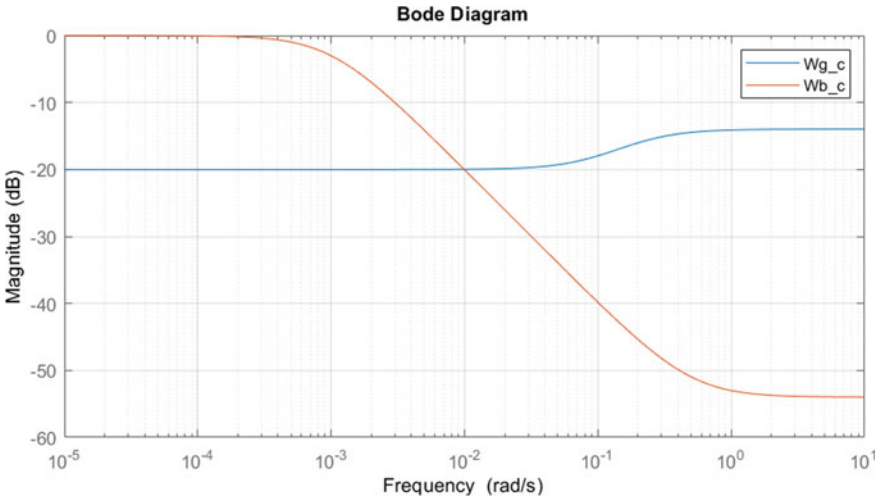

Fig. 7 Bode Plot (magnitude) of control signal weight

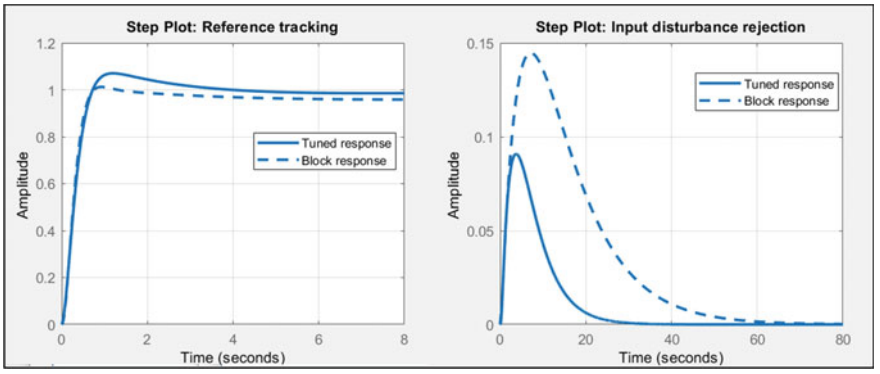

Fig. 8 Closed-loop step plot for reference tracking and input disturbance rejection

4 Simulation Results

4.1 With Model Uncertainties

This section presents simulation results under the developed control for frequency deviation for 24 h. The variation in load and wind power output is considered as disturbances in the system. The corresponding results with conventional PID control in the presence of system uncertainties have been presented in Fig. 10 wherein the frequency transients shoot near to 0.5 p.u. (i.e., 2.5 Hz) which is unacceptable.

Controller Parameters

	Tuned	Block
P	8.2603	4.9047
I	1.1322	0.3454
D	15.052	17.28
N	331.9203	54.85

Performance and Robustness

	Tuned	Block
Rise time	0.475 seconds	0.436 seconds
Settling time	2.8 seconds	NaN seconds
Overshoot	7.01 %	1.21 %
Peak	1.07	1.01
Gain margin	Inf dB @ Inf rad/s	33.7 dB @ 37.5 rad/s
Phase margin	69 deg @ 2.9 rad/s	69.6 deg @ 3.28 rad/s
Closed-loop stability	Stable	Stable

Fig. 9 Controller parameters for the closed-loop plant

It can be seen in Fig. 11; the maximum frequency deviation is 0.605% at 49200 s, which is much lesser than the security limits of 1%. It is conveniently observed that the tuned PID controller is able to sufficiently mitigate the frequency deviations in the presence of system uncertainties.

Frequency deviation with different battery sizes is presented in Fig. 12. Without battery, it can be seen that the frequency deviation reaches 1.4%, which violates the security constraint. In the absence of a battery, the conventional generator is forced to cope with the load change.

5 Conclusion

In this work, PID tuned robust controller is proposed to mitigate the frequency deviations in the system. It is shown that with small size of battery considered, robust control results in a significant reduction of frequency deviation(i.e., from 2.5 Hz deviation with conventional PID to 0.24 Hz with robust tuned PID controller). Various uncertainties arising due to mathematical modelling errors and unmodeled system

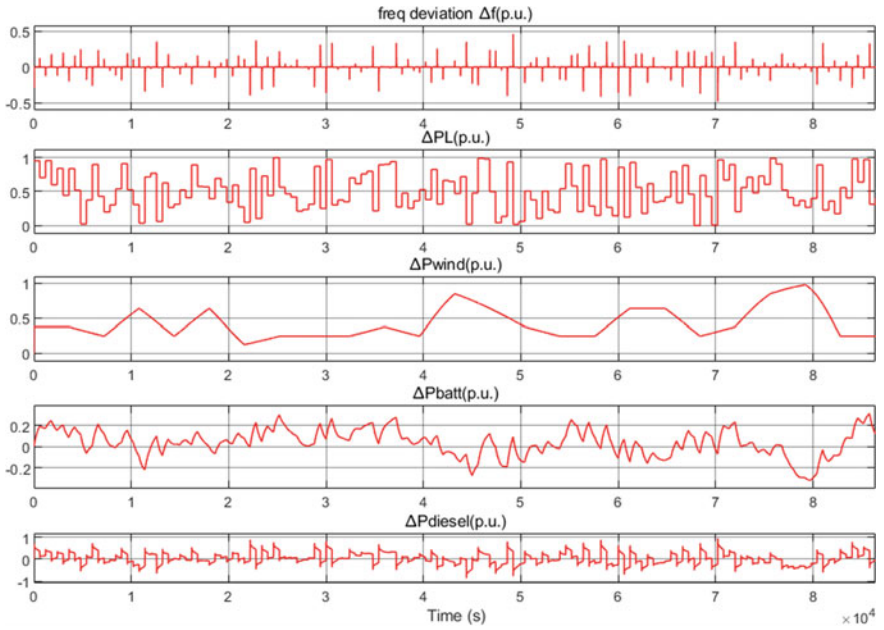

Fig. 10 Frequency variation with load change in the presence of system uncertainties with conventional PID

dynamics have also been considered. The proposed closed-loop controller simultaneously employs a conventional generator to cope up with slow transients while BESS model dampens out fast transients occurring due to renewable energy resources. Since the battery cost is size-dependent, it is a crucial factor while employing the BESS in the system. Further, different battery sizes were employed to assess the capability to suppress high-frequency transients.

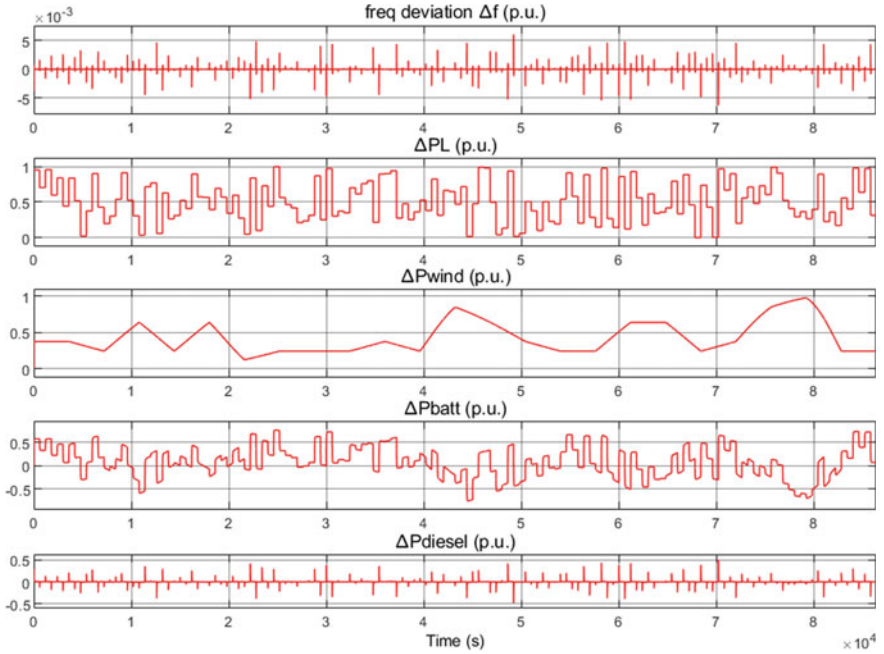

Fig. 11 Frequency variation with load change in the presence of system uncertainties with tuned PID

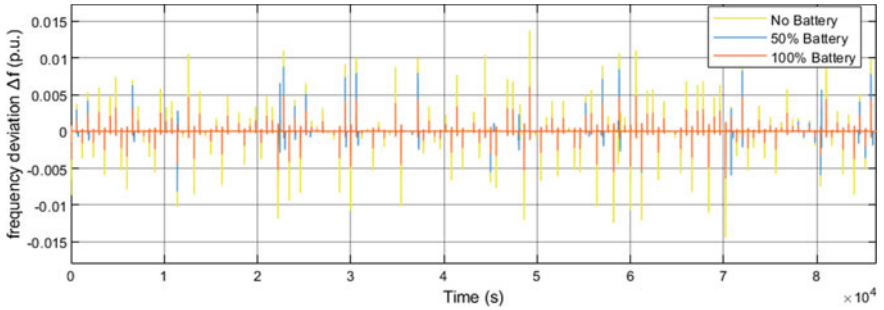

Fig. 12 Frequency deviation with varying battery size

References

1. C. Hernandez-Aramburo, T. Green, N. Mugniot, Fuel consumption minimization of a microgrid. IEEE Trans. Ind. Appl. **41**, 673–681 (2005)
2. T. Goya, E. Omine, Y. Kinjyo, T. Senjyu, A. Yona, N. Urasaki, T. Funabashi, Frequency control in isolated island by using parallel operated battery systems applying h-inf; control theory based on droop characteristics. IET Renew. Power Generat. **5**, 160–166 (2011)
3. A.M. Howlader, Y. Izumi, A. Uehara, N. Urasaki, T. Senjyu, A. Yona, A.Y. Saber, A minimal

order observer based frequency control strategy for an integrated wind-battery-diesel power system. Energy **46**(1), 168–178 (2012)
4. V. Sundaram, T. Jayabarathi, Load frequency control using PID tuned ANN controller in power system, in *Proceedings 1st International Conference Electrical Energy Syst. (ICEES)*, Jan. 2011, pp. 269–274
5. S. Sen, V. Kumar, Decentralized output-feedback-based robust LQR V-f controller for PV-battery microgrid including generation uncertainties. IEEE Syst. J. **14**(3), 4418–4429 (2020)
6. S.M. Abd-Elazim, E.S. Ali, Load frequency controller design of a two-area system composing of PV grid and thermal generator via firefly algorithm. Neural Comput. Appl. **30**(2), 607–616 (2018)
7. D. Guha, P.K. Roy, S. Banerjee, Symbiotic organism search algorithm applied to load frequency control of multi-area power system. Energy Syst. **9**(2), 439–468 (2018)
8. M. Gheisarnejad, M.H. Khooban, Design an optimal fuzzy fractional proportional integral derivative controller with derivative filter for load frequency control in power systems. Trans. Inst. Meas. Control **41**(9), 2563–2581 (2019)
9. R. Dhanalakshmi, S. Palaniswami, Application of multi stage fuzzy logic control for load frequency control of an isolated wind diesel hybrid power system, *in Proceedings International Conference Green Technology Environmental Conservat. (GTEC)*, Dec. 2011, pp. 309–315
10. F. Dupont, A. Peres, S. Oliveira, Fuzzy control of a three-phase step-up dc-dc converter with a three-phase high frequency transformer, *in Proceedings Brazilian Power Electronical Conference, COBEP '09.* , Oct. 27–1, 2009, pp. 725–732
11. R. Sakamoto, T. Senjyu, N. Urasaki, T. Funabashi, H. Fujita, H. Sekine, Output power leveling of wind turbine generators using pitch angle control for all operating regions in wind farm, *in Proceedings 13th International Conference Intelligent System Application Power Syst*em, Nov. 2005, p. 6
12. N. Mendis, K.M. Muttaqi, S. Perera, Management of low and high-frequency power components in demand-generation fluctuations of a DFIG-based wind-dominated RAPS system using hybrid energy storage. IEEE Trans. Ind. Appl. **50**(3), 2258–2268 (2014)
13. Q.Y. Jiang, Y.Z. Gong, H.J. Wang, A battery energy storage system dual-layer control strategy for mitigating wind farm fluctuations. IEEE Trans. Power Syst. **28**(3), 3263–3273 (2013)

Fractional Calculus Based PI-FOPID Controller for Frequency Deviation Control in Integrated Power System

Jyoti Ranjan Padhi, Moayad Ali Deeb, Sabita Tripathy, and Manoj Kumar Debnath

Abstract In this research analysis, we projected a new structure of controller configuration by hybridizing conventional PID and FOPID controllers. By using hybrid cascaded PI-FOPID controller we can double the benefit as it has the properties of two controllers. This will help to retain the frequency within acceptable limits during the faults or demand variations in an interconnected power system that contains various plants and a SMES (Superconducting magnetic energy storage) unit. The controller is tuned by the Sine–Cosine Optimization (SCO) algorithm considering ITAE as an objective function. Firstly, the outcome of the system is witnessed during Step Load Perturbation (SLP) of 1% in area 1 and it is compared with pre-published outcomes in terms of negative undershoots, settling time and positive overshoots. In the second case, the system response is analyzed in the presence of a SMES unit and the outcomes are monitored by comparing the performance of FOPID and PI-FOPID controllers tuned by sine cosine algorithm. The supremacy of the PI-FOPID controller is established over other mentioned controllers.

Keywords Multi-area power system · Fractional order controller · Automatic generation control · Hybrid cascaded controller · Sine–cosine optimization

1 Introduction

To make the systems more dependable and reliable, electric power networks are interconnected. In a unified multi-generations system, loads and generations are synchronized via the tie lines that connect the regions [1, 2]. The overall power demand of an electrical power system changes during the day and the balance is required between power producing units and loads. LFC acts on the load variations in order to retain frequency at the planned value known as frequency control. With

J. R. Padhi · M. A. Deeb · S. Tripathy · M. K. Debnath (✉)
Siksha 'O' Anusandhan Deemed to Be University, Bhubaneswar, Odisha, India
e-mail: mkd.odisha@gmail.com

J. Kumar et al. (eds.), *Control Applications in Modern Power Systems*, Lecture Notes in Electrical Engineering 974, https://doi.org/10.1007/978-981-19-7788-6_14

the neighboring control areas, the power flows at preferred values is known as tie-line control [3, 4].

According to a literature review, high voltage AC interlines are mostly utilized for the interconnection of multiple control areas in the power systems whereas AC-DC parallel tie lines received less attention [5, 5]. HVDC transmission has gained popularity due to its numerous technological and economic benefits. Operating a DC connection in parallel with an AC link joining two control regions to improve the system's dynamic performance with higher stability margins under tiny disturbances [7, 8]. The LFC of linked power systems model coupled by high voltage DC connection in tandem with AC link has received little attention [9]. A SMES was considered in several pieces of literature during the study of Frequency Deviation Control. SMES unit that can simultaneously control active and reactive power is utilized for effective stabilization of frequency fluctuation in article [10]. In the following research, the effect of TCPS and SMES on the stability of unified power systems is analyzed, considering governor nonlinear responses. Then in the dual-area power systems, SMES and TCPS are modeled, where at the end, simulation results are presented [11]. The impact of a superconducting magnetic energy storage (SMES) unit on the performance of an automated generation control (AGC) system is explored in this study [12]. The SCO algorithm has been used in many models of power systems to adjust the frequency changes. In the paper [13], the SCO algorithm is employed to adjust the PD + PI dual-loop controller's gains. These articles [14, 15], presented Sine Cosine Optimized (SCO) technique for LFC controller design to adjust the fractional-order PID (FOPID) controller coefficients. Frequency regulation with nonlinearity(GDB) and 2DOF-PID controller was analysed in article [16]. (1 + PD)-PID controller [17] was successfully employed for frequency regulation in diverse electric unified power system. Naladi Ram Babu [18] implemented CA Optimized PI-TID Cascade Controller for LFC investigation in a unified system with AC-DC link. Several integrated controllers were used and their effect on the power system was studied in relation to load frequency control with many algorithms. One of the efficient algorithm SCO was introduced by Mirjalili [19]. SMES and UPFC [20] can also be associated with the unified system for examining LFC. PID controller adjusted by Artificial neural network [21] was used for frequency deviations control in power systems with distributed energy resources. Adaptive dual mode PID controller adjusted by IMO algorithm is described in article [22]. PID-Fuzzy-PID hybrid controller [23] was introduced for successful frequency regulations. To eliminate unwanted signals PID controller with derivative filter was used in article [24]. Multi-staged PID controller is described in article [25] for frequency deviation control in interconnected multi-area systems.

According to the literature review, the majority of research effort focuses on PID controllers that limit control action. In order to extract best outcomes our present research work focuses on an optimum PI-FOPID controller which was optimized using the new optimization approach called SCO.

2 System Explored

In the presence of a PI-FOPID controller, an examination is conducted on a dual-area model. The simulation model for this proposed network is shown in Fig. 1. Each area of the implemented model contains several units such as Hydro unit, thermal unit and gas turbine unit with an HVDC link in both areas. The SMES is available in the first area. However, every unit has its own PI-FOPID controller to keep frequency within permissible limits. The system is experimented to observe its performance under two conditions: sudden load changes equal to 1% in area 1 only, secondly experimented in the presence of SMES unit in first area with SLP of 1% in area 1. These suggested system parameters' nominal values are derived from studies [6]. The ACE signal, which contains information on the frequency error for both area and tie-line power error of the relevant control area, is used as an input to the implemented PI-FOPID controller.

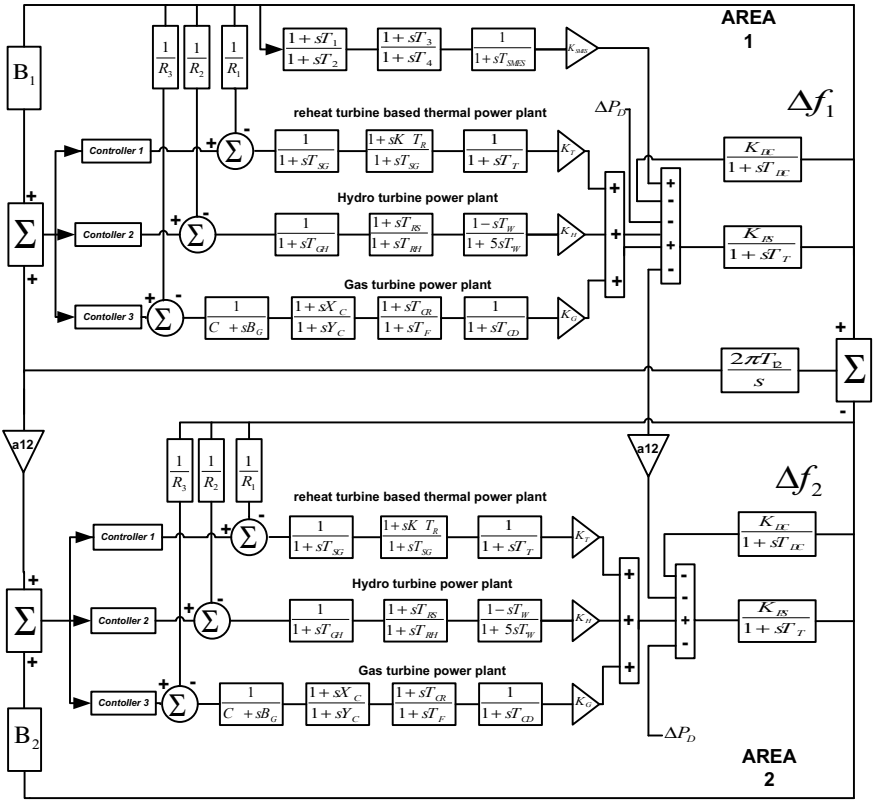

Fig. 1 Thermal-hydro-Gas based dual-area power system [6]

3 Controller Arrangement

Cascaded Controller

Alternative feedback compensation methods, such as the cascade control system, are well-known for enhancing disturbance rejection. The cascade control concept, on the other hand, is derived based on the sequential regulation of two methods, where the output of inner control actions provides the input to the outer control actions. Both the inner process output and the variable of the external process may be measured. The major goals of cascade or series control [11] are as follows: (i) The inner control actions are designed to reduce the impact of a supply outage or any kind of unwanted signal on the sequence's external processes, and (ii) The outside or exterior process measurement is used to regulate the ultimate outcomes of the process. Two control loops make up the simplest cascade control system as demonstrated in Fig. 2.

The outer loop

The exterior loop is basically treated as primary loop or master loop. It comprises the process output y(s), which is the main focus of control. G1(s) represent the exterior process and the entire process is subjected to load disturbance d1(s). The exterior loop equation is given:

$$\mathrm{y(s)} = \mathrm{G1(s)U1(s)} + \mathrm{d1(s)} \tag{1}$$

the equation above describes the operation of the outer process [11].

The inner/secondary loop

The interior loop is also treated as secondary loop and its role is like a slave. The said loop comprises the inside or supply process G2(s). The following equation describes the interior loop.

$$\mathrm{y2(s)} = \mathrm{G2(s)U2(s)} \tag{2}$$

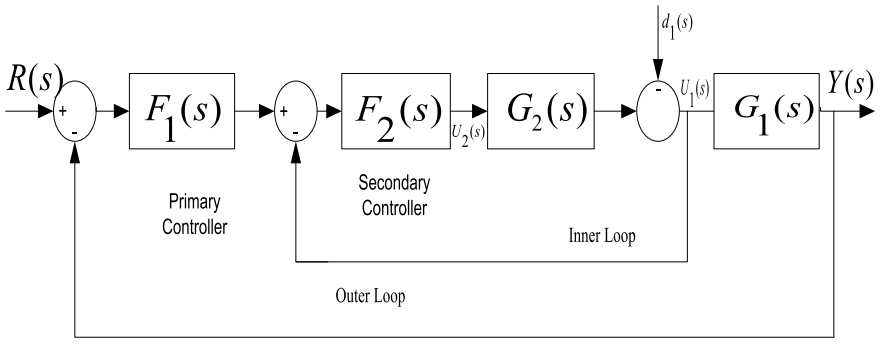

Fig. 2 Structure of cascaded controller

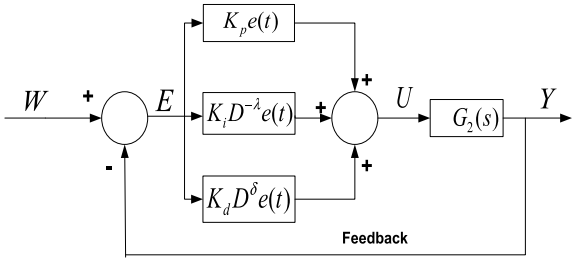

Fig. 3 Structure of FOPID controller

The equation above describes the operation of the interior process. The inner loop's main aim is to restrict the influence of changes in the internal gain of inner blocks upon the performance of the control system.

PI-FOPID Controller

The model is constructed using one loop control system with a fractional control system with a FOPID controller as demonstrated in Fig. 3. In several cases as reference tracking as well as disturbance rejection, the outcomes of both the control loops are matched. Two controllers are chosen and referred to as $F_1(s)$ and $F_2(s)$, respectively, as the primary and secondary controllers. Here, the *PI* controller is made as the primary controller and *FOPID* controller as the secondary controller and are expressed by the below equation.

$$F_{PID}(s) = K_P + \frac{K_I}{S} \tag{3}$$

$$F_{FOPID}(s) = K_P + K_I s^{-\lambda} + K_D s^{\delta} \tag{4}$$

$K_{P,\,I,\,Dmin}$ and $K_{P,\,I,\,Dmax}$ are the min and max values of the controller's parameters (PI-FOPID/FOPID), respectively and $\lambda_{min}, \delta_{min}$ $\lambda_{max}, \delta_{max}$ are the min and max values of fractional integral and derivative coefficients, respectively. For both bounds (min and max) in controllers' gains are chosen as 1 and 5 and that of the FOPID coefficients are 0.1 and 1.

Objective Function

The ITAE was chosen as an objective function in all the cases that were studied, as it is characterized by several characteristics like high sensitivity and the best selection than the other functions and producing smaller overshoots and oscillations over the other functions like (IAE), (ISE), (ITSE).

$$ITEA = \int_0^t \{(|\Delta f_1|) + (|\Delta f_2|) + (|\Delta P_{tie}|)\}.\, tdt \tag{5}$$

4 Overview of Sine–Cosine Optimization Algorithm

Mirjalili created the SCO algorithm [19]. The sine cosine algorithm (SCO) with the aid of a mathematical model based on sine and cosine functions, starts its search by randomly generating solutions and making them seek to and fro in the direction of the best solution. The different solutions are updated in response to sine and cosine functions in order to discover a new one. The algorithm's optimization procedure is completed after a maximum number of iterations has been satisfied. A fitness function evaluates each candidate solution, and their locations are updated using the following Eq. (6):

$$X_i^{g+1} = \begin{cases} X_i^g + r_1 \times \sin(r_2) \times \left| r_3 P_i^g - X_i^g \right| if\, r_4 < 0.5 \\ X_i^g + r_1 \times \cos(r_2) \times \left| r_3 P_i^g - X_i^g \right| if\, r_4 \geq 0.5 \end{cases} \tag{6}$$

where Pi denotes the position of intended points and Xit = present position of solution at tth iteration. r_1 governs the updated position, the amount of movement towards destination is governed by r_2, r_3 provides random numbers so as to stochastically underline the effect of updation. At the end the random number r_4 correspondingly changes between the sine and cosine parts. Sine cosine range in (6) is altered by (7)

$$r_1 = a - a\frac{t}{T} \tag{7}$$

where t is the latest iteration, T (constant value) is max number of iterations. More information on the algorithm is found in [19].

5 Result and Discussion

Application of 1% SLP in control area 1

In the first case, an abrupt demand variation of 1% is applied in control area 1, the PI-FOPID controller was tuned through the SCO algorithm and the results were compared to previously published outcomes [6], which involves tuning of the conventional PID controller through the SCO and TLBO algorithms. This experiment was performed with sudden load changes of 1% in area 1 and without the SMES unit. Table 1 displays the tuned gains of the controllers after using the proposed algorithm. In terms of negative undershoots, settling time and positive overshoots, the controllers' performance was compared and thus the outcomes showed the superiority of the proposed controller PI-FOPID tuned by algorithm SCO. Table 2 shows the results of the performance of the controllers.

The following Figs. 4 and 5 show the performance of the controllers clearly. These justifies the ascendency of the recommended PI-FOPID controller.

Table 1 Optimal values of parameters of PI-FOPID/PID controllers

	PI-FOPID controller SCO algorithm			PID controller SCO algorithm			PID controller [6] TLBO algorithm		
	Thermal plant	Hydro plant	Diesel plant	Thermal plant	Hydro plant	Diesel plant	Thermal plant	Hydro plant	Diesel plant
K_P	4.127	1.289	4.987	9.7744	9.8525	0.203	5.0658	0.7032	0.0264
K_I	4.825	2.097	5	1.3873	0.013	10	3.9658	0.0220	0.0264
K_D	3.709	3.408	1.127	4.1195	0.013	0.131	2.4170	0.0264	2.4181
λ	0.609	0.586	0.871	–	–	–	–	–	–
δ	1	0.534	0.892	–	–	–	–	–	–
$K_P 1$	4.289	3.481	4.447	–	–	–	–	–	–
$K_I 1$	4.546	5	2.296	–	–	–	–	–	–

Table 2 Performance evaluative indices for different controllers

Controller	Δf_1			Δf_2			ΔP_{tie}		
	U_{sh} (Hz)	O_{sh} 10^{-3} Hz	T_s Sec	U_{sh} Hz	O_{sh} 10^{-3} Hz	T_s Sec	U_{sh}	O_{sh} 10^{-3}	T_s Sec
PID TLBO [6]	0.0083	0.3037	8.1851	−0.0016	0.2194	13.3851	−0.0009	0.1613	8.9851
PID SCO [6]	0.0079	0.0791	2.5676	−0.0016	0.0284	6.1595	−0.0010	0.0522	4.5625
PI-FOPID SCO	0.0041	0.4507	3.7259	−0.0004	0.1468	5.2153	−0.0002	0.0770	1.3765

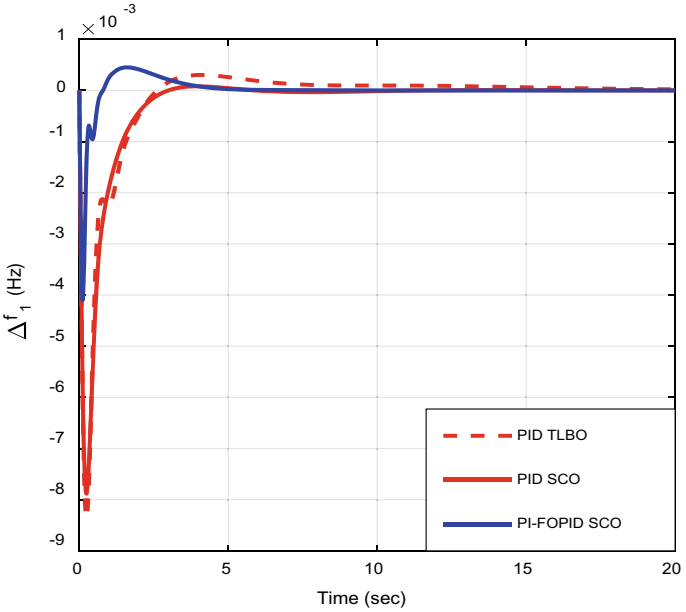

Fig. 4 Oscillations of frequency in control area 1

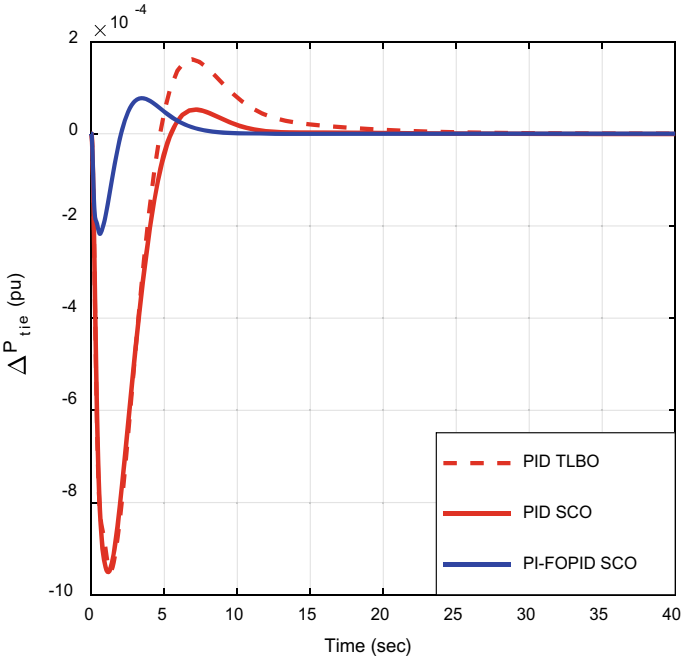

Fig. 5 Oscillations of interline power

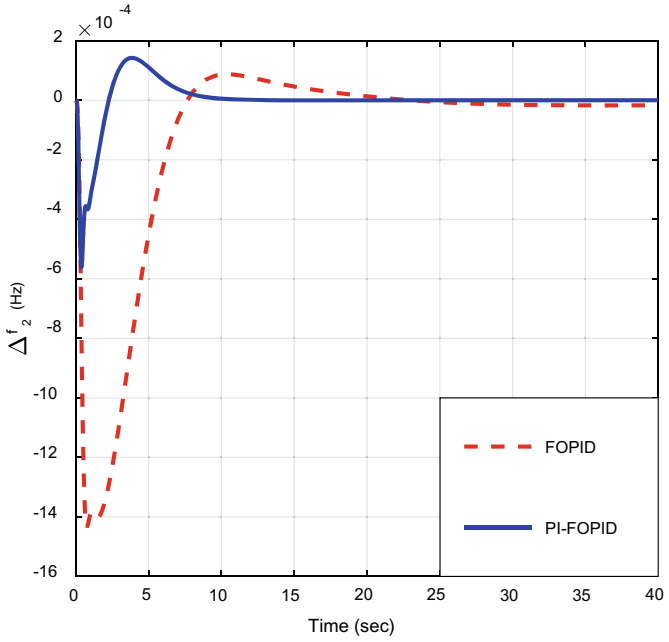

Fig. 6 Oscillations of frequency in control area 2 with SMES

Performance analysis in presence of SMES

In this case, both PI-FOPID controller and FOPID controller were tuned through the SCO algorithm, taking into account the presence of load changes of 1% in area 1 and also with the existence of the SMES unit in the first area. The outcomes show the superiority of the proposed controller in terms of negative undershoots, settling time and positive overshoots. The parameters of the PI-FOPID and FOPID controllers have been optimized by the SCO algorithm. The behavior of the controllers PI-FOPID and PID were viewed through the Figs. 6 and 7. As per the values of negative undershoots, settling time and positive overshoots, it can be judged the dominant nature of projected PI-FOPID controller over PID controller.

6 Conclusion

The above results proved the supremacy of the recommended PI-FOPID controller tuned by the SCO technique with ITAE as objective function. The designed PI-FOPID controller resulted from the hybridization of two cascaded controllers namely, PI controller and FOPID controller. The supremacy of recommended PI-FOPID controller tuned by SCO is confirmed in terms of negative undershoots, settling time and positive overshoots over FOPID and PID controllers optimized by the SCO and

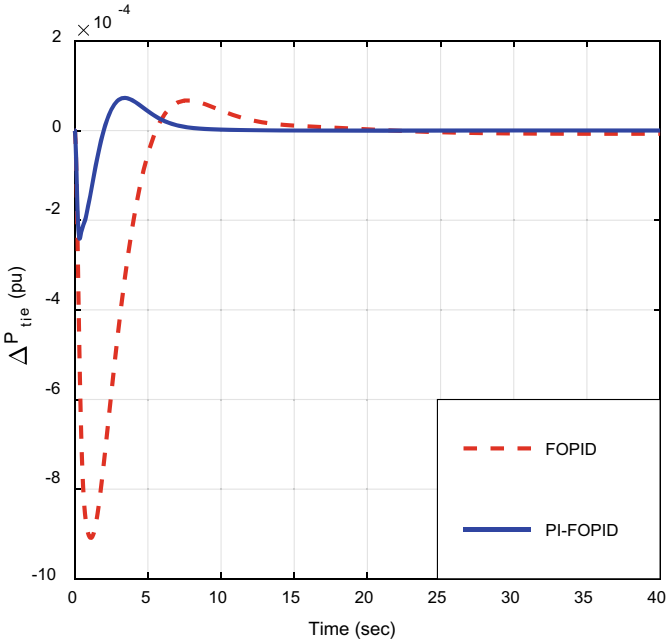

Fig. 7 Oscillations of interline power with SMES

TLBO algorithms. The scrutinized interconnected power system contains various power generating units, an HVDC links in both areas and a SMES unit in the first area. The analysis was done taking into account several procedures such as changing the load by about 1% SLP with the absence of a SMES unit and as well as with the presence of the SMES unit. By doing multiple analyses, the robustness of the proposed PI-FOPID controller tuned by the SCO algorithm was confirmed.

References

1. D.P. Kothari, I.J. Nagrath, *Modern Power System Analysis*. Tata McGraw-Hill Education (2003)
2. P. Kundur, *Power System Stability and Control*; 8th reprint. ed: New Delhi: Tata McGraw Hill (2008)
3. J. Machowski, Jan, Z. Lubosny, J.W. Bialek, J.R. Bumby, *Power System Dynamics: Stability and Control*. Wiley (2020)
4. Z.M. Al-Hamouz, Y.L. Abdel-Magid, Variable structure load frequency controllers for multi-area power systems. Int. J. Electr. Power Energy Syst. **15**(5), 293–300 (1993)
5. S. Ramesh, A. Krishnan, Fuzzy rule based load frequency control in a parallel AC-DC interconnected power systems through HVDC link. Int. J. Comput. Appl. **1**(4), 62–69 (2010)
6. N. Nayak, S. Mishra, D. Sharma, B.K. Sahu, Application of modified sine cosine algorithm to optimally design PID/fuzzy-PID controllers to deal with AGC issues in deregulated power system. IET Gen. Trans. Distrib. **13**(12), 2474–2487 (2019)

7. N.J. Vinoth Kumar, M. Mohamed Thameem Ansari. A new design of dual mode Type-II fuzzy logic load frequency controller for interconnected power systems with parallel AC–DC tie-lines and capacitor energy storage unit. Int. J. Electr. Power Energy Syst. **82**, 579–598 (2016)
8. K.Y. Lim, Y. Wang, R. Zhou, Decentralised robust load-frequency control in coordination with frequency-controllable HVDC links. Int. J. Electr. Power Energy Syst. **19**(7), 423–431 (1997)
9. P. Kumar, D.P. Kothari, Recent philosophies of automatic generation control strategies in power systems. IEEE Trans. Power Syst. **20**(1), 346–357 (2005)
10. P. Chandra Pradhan, R. Kumar Sahu, S. Panda, Firefly algorithm optimized fuzzy PID controller for AGC of multi-area multi-source power systems with UPFC and SMES. Eng. Sci. Technol. Int. J. **19**(1), 338–354 (2016)
11. P. Bhatt, R. Roy, S.P. Ghoshal, Comparative performance evaluation of SMES–SMES, TCPS–SMES and SSSC SMES controllers in automatic generation control for a two-area hydro–hydro system. Int. J. Electr. Power Energy Syst. **33**(10), 1585–1597 (2011)
12. R.R. Shukla, M.K. Maharana, D. Das, Effect of CES and SMES on AGC in presence of different controllers and ramp disturbances. *2015 IEEE Power, Communication and Information Technology Conference (PCITC)*. IEEE (2015)
13. N.C. Patel, M. Kumar Debnath, B.K. Sahu, P. Das, Solution of LFC problem using PD+PI double loop controller tuned by SCA, *2018 International Conference on Recent Innovations in Electrical, Electronics & Communication Engineering (ICRIEECE)*, pp. 337–342 (2018). https://doi.org/10.1109/ICRIEECE44171.2018.9009161
14. F. Babaei, A. Safari, SCA based fractional-order PID controller considering delayed EV aggregators. J. Oper. Autom. Power Eng. **8**(1), 75–85 (2020)
15. A. Prakash et al., HVDC tie-link modeling for restructured AGC using a novel fractional order cascade controller. Electric Power Syst. Res. **170**, 244–258 (2019)
16. R.K. Sahu, S. Panda, U.K. Rout, DE optimized parallel 2-DOF PID controller for load frequency control of power system with governor dead-band nonlinearity. Int. J. Electr. Power Energy Syst. **49**, 19–33 (2013)
17. E. Celik, N. Öztürk, Y. Arya, C. Ocak, (1+ PD)-PID cascade controller design for performance betterment of load frequency control in diverse electric power systems. Neural Comput. Appl. **33**(22), 15433–15456 (2021)
18. Na.R. Babu, L.C. Saikia, S.K. Bhagat, S.K. Ramoji, B. Dekaraja, M.K. Behera, Optimal Location of AC-HVDC Tie-line in a Multi-Area LFC system incorporated with renewable and ESD considering CA optimized PI-TID cascade controller, in *2020 IEEE 17th India Council International Conference (INDICON)*, pp. 1–6. IEEE (2020)
19. S. Mirjalili, SCA: a sine cosine algorithm for solving optimization problems. Knowl. Based Syst. **96**, 120–133 (2016)
20. T. Jena, M.K. Debnath, S.K. Sanyal, Optimal fuzzy-PID controller with derivative filter for load frequency control including UPFC and SMES. Int. J. Electr. Comput. Eng. **9**(4), 2813 (2019)
21. M.K. Debnath, R. Agrawal, S.R. Tripathy, S. Choudhury, Artificial neural network tuned PID controller for LFC investigation including distributed generation. Int. J. Numer. Model. Electron. Netw. Dev. Fields **33**(5), e2740 (2020)
22. G. Mohapatra, M.K. Debnath, K.K. Mohapatra, IMO-based novel adaptive dual-mode controller design for AGC investigation in different types of systems. Cogent Eng. **7**(1), 1711675 (2020)
23. M.K. Debnath, T. Jena, S.K. Sanyal, Frequency control analysis with PID-fuzzy-PID hybrid controller tuned by modified GWO technique. Int. Trans. Electr. Energy Syst. **29**(10), e12074 (2019)
24. N.C. Patel, M.K. Debnath, D.P. Bagarty, P. Das, Load frequency control of a non-linear power system with optimal PID controller with derivative filter, in *2017 IEEE International Conference on Power, Control, Signals and Instrumentation Engineering (ICPCSI)*, pp. 1515–1520. IEEE (2017)
25. N.C. Patel, M.K. Debnath, B.K. Sahu, S.S. Dash, R. Bayindir, Multi-staged PID controller tuned by invasive weed optimization algorithm for LFC issues, in *2018 7th International Conference on Renewable Energy Research and Applications (ICRERA)*, pp. 1358–1362. IEEE (2018)

Steady State Analysis of Three Phase Transmission System for Balanced and Unbalanced Case

Insha Jehangir, Ravi Bhushan, and Neeraj Gupta

Abstract With the various unbalances in the modern power system the steady state analysis needs to be conducted for three phase power system. This paper discusses the various reasons for unbalance in transmission systems along with the consequences that unbalance causes in our power system. A detailed discussion is done on the load flow method adopted i.e. the Newton-Raphson load flow method along with the mathematics involved and salient points. IEEE 5 and 118 bus systems are used to implement load flow analysis using Newton-Raphson load flow method.

Keywords Three-phase systems · Three phase load flow analysis · Newton Raphson algorithm · Transmission systems

1 Introduction

The system unbalance is neglected in steady state analysis for many studies and in such cases single phase analysis of such systems suffices. However in actual world it is practically impossible to attain that level of balance in our systems. For example the non-uniform distribution of single phase loads on a three-phase 4 wire system is a significant reason for unbalance as equal distribution of single-phase loads on a three-phase system is highly unlikely to achieve. Current can only be balanced in the system if load is equally distributed in all the three phases of the system. It is mainly the industrial loads that have the ability to cause such unbalance in our three phase systems. Domestic loads do not have the ability to cause major unbalances in our power system. Flow of unbalanced currents leads to unbalanced voltage supply and when unbalanced voltage is applied to our AC motors negative sequence current flows in our rotor which in-turn causes heating in our AC motors and to control this heating we have to resort to derating of our motors. Derating of motor leads to reduced efficiency [1]. Another cause of unbalance in three phase systems is single phasing [2]. In a three phase induction machine if one of the phases gets blown

I. Jehangir (✉) · R. Bhushan · N. Gupta
Department of Electrical Engineering, NIT Srinagar, Srinagar, India
e-mail: inshajehangir1117@gmail.com

J. Kumar et al. (eds.), *Control Applications in Modern Power Systems*, Lecture Notes in Electrical Engineering 974, https://doi.org/10.1007/978-981-19-7788-6_15

out, machine gets fed from only two phases as one phase goes out of service. This is called single phasing and leads to unbalance in the system. Another cause for unbalance is that for power factor improvement we connect shunt capacitor banks across our loads.It supplies reactive power demanded by the load and improves voltage profile of our system. These capacitor banks are connected via fuses [3]. If any fuse blows then capacitor of a phase will go out and voltage of that phase will dip as it wont receive reactive power support. Hence the phases receiving reactive power support will have a better voltage profile than the phase which didn't receive reactive power support rendering to an unbalanced system. Another example of cause of unbalance is that it is highly impractical to think that a transmission system will have perfectly balanced impedance when untransposed as the middle conductor will have maximum flux linking it which leads to maximum amount of power loss in the middle conductor. Hence the voltage of upper and lower conductors will be more than the middle conductor rendering to unbalance in the system.

In practice it is uneconomical to balance the load completely or to achieve perfectly balanced transmission system impedance. A few effects of power system unbalance are flow of negative sequence currents in the rotor of ac machine causing machine rotor overheating [4], zero sequence currents causing relay mal-operations [5] and if we have a three-phase rectifier bridge connected huge current will be drawn by it due to unbalanced voltage supplied to it which causes burning of power electronic devices [6]. Mechanical stresses in motors due to lower than normal torque output also causes unbalance. The use of long-distance transmission motivated the development of analytical techniques for the assessment of power system unbalance [7].

The paper is organised as: in Sect. 1 causes and consequences of unbalance have been discussed. In Sect. 2 three-phase load flow analysis has been discussed which includes the admittance matrix and the power flow equations. In Sect. 3 Newton-Raphson algorithm for three phase load flow has been discussed along with its mathematical formulation which includes the vector terms and formation of jacobian matrices. In Sect. 4 results have been discussed. In Sect. 5 conclusion has been discussed.

2 Three-Phase Load Flow Analysis

The various power flow equations for injected active and reactive power for buses y and z for Fig. 1 are given in this section [8].

For evaluation of unbalance in a practical [9], interconnected power system it is essential to have a robust and reliable three-phase load flow algorithm [8].

Three-phase load flow is conducted in a system to obtain information of the condition of the three-phase power system under the specified conditions of load, generation and system configuration [10].

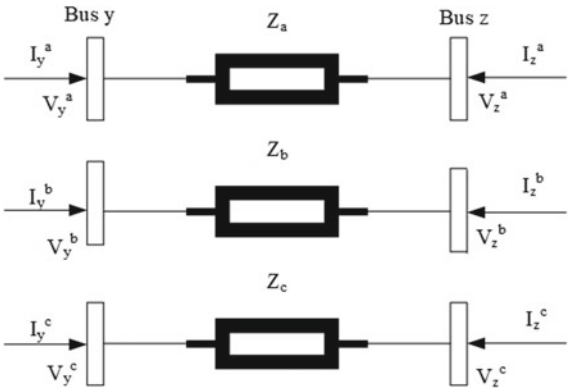

Fig. 1 Reference three-phase transmission system

Equation (1) gives relationship between three-phase currents and voltages which are related by transfer admittance matrix:

$$\begin{bmatrix} I_y^{abc} \\ I_z^{abc} \end{bmatrix} = \begin{bmatrix} Y_{yy}^{abc} & Y_{yz}^{abc} \\ Y_{zy}^{abc} & Y_{zz}^{abc} \end{bmatrix} \begin{bmatrix} V_y^{abc} \\ V_z^{abc} \end{bmatrix}. \tag{1}$$

2.1 Formation of Admittance Matrix

The Y-bus matrix is given as:

$$Y_{yy}^{abc} = \begin{bmatrix} R_{yz}^{aa-g} + j\omega L_{yz}^{aa-g} & R_{yz}^{ab-g} + j\omega L_{yz}^{ab-g} & R_{yz}^{ac-g} + j\omega L_{yz}^{ac-g} \\ R_{yz}^{ba-g} + j\omega L_{yz}^{ba-g} & R_{yz}^{bb-g} + j\omega L_{yz}^{bb-g} & R_{yz}^{bc-g} + j\omega L_{yz}^{bc-g} \\ R_{yz}^{ca-g} + j\omega L_{yz}^{ca-g} & R_{yz}^{cb-g} + j\omega L_{yz}^{cb-g} & R_{yz}^{cc-g} + j\omega L_{yz}^{cc-g} \end{bmatrix}^{-1}, \tag{2}$$

$$Y_{yy}^{abc} = Y_{zz}^{abc} = -Y_{yz}^{abc} = -Y_{zy}^{abc}, \tag{3}$$

$$V_y^{abc} = \begin{bmatrix} V_y^a & V_y^b & V_y^c \end{bmatrix}^T = \begin{bmatrix} V_y^a e^{\theta_y^a} & V_y^b e^{\theta_y^b} & V_y^c e^{\theta_y^c} \end{bmatrix}^T, \tag{4}$$

$$V_z^{abc} = \begin{bmatrix} V_z^a & V_z^b & V_z^c \end{bmatrix}^T = \begin{bmatrix} V_z^a e^{\theta_z^a} & V_z^b e^{\theta_z^b} & V_z^c e^{\theta_z^c} \end{bmatrix}^T, \tag{5}$$

$$I_y^{abc} = \begin{bmatrix} I_y^a & I_y^b & I_y^c \end{bmatrix}^T, \tag{6}$$

$$I_z^{abc} = \begin{bmatrix} I_z^a & I_z^b & I_z^c \end{bmatrix}^T, \tag{7}$$

Here 'T' refers to transpose of a matrix.

The complex power expression, Eq. (8) gives us the various expressions for the active and reactive power injected at bus y and z respectively in Fig. 1:

$$\begin{bmatrix} S_y^{abc} \\ S_z^{abc} \end{bmatrix} = \begin{bmatrix} P_y^{abc} + jQ_y^{abc} \\ P_z^{abc} + jQ_z^{abc} \end{bmatrix} \begin{bmatrix} V_y^{abc} I_y^{abc*} \\ V_z^{abc} I_z^{abc*} \end{bmatrix}. \tag{8}$$

2.2 Power Flow Equations

Expression for active and reactive power injected in bus y for all the three phases is given below in Eqs. (9) and (10) respectively [11]:

$$P_y^{\delta} = V_y^{\delta} \left\{ \sum_{i=y,z} \sum_{j=a,b,c} V_i^j [G_{yi}^{\delta j} \cos(\theta_y^{\delta} - \theta_i^j) + B_{yi}^{\delta j} \sin(\theta_y^{\delta} - \theta_i^j)] \right\}, \tag{9}$$

$$Q_y^{\delta} = V_y^{\delta} \left\{ \sum_{i=y,z} \sum_{j=a,b,c} V_i^j [G_{yi}^{\delta j} \sin(\theta_y^{\delta} - \theta_i^j) - B_{yi}^{\delta j} \cos(\theta_y^{\delta} - \theta_i^j)] \right\}, \tag{10}$$

Expression for active and reactive power injected in bus z for all the three phases is given below in Eqs. (11) and (12) respectively:

$$P_z^{\delta} = V_z^{\delta} \left\{ \sum_{i=z,y} \sum_{j=a,b,c} V_i^j [G_{zi}^{\delta j} \cos(\theta_z^{\delta} - \theta_i^j) + B_{zi}^{\delta j} \sin(\theta_z^{\delta} - \theta_i^j)] \right\}, \tag{11}$$

$$Q_z^{\delta} = V_z^{\delta} \left\{ \sum_{i=z,y} \sum_{j=a,b,c} V_i^j [G_{zi}^{\delta j} \sin(\theta_z^{\delta} - \theta_i^j) - B_{zi}^{\delta j} \cos(\theta_z^{\delta} - \theta_i^j)] \right\}. \tag{12}$$

3 Newton-Raphson Algorithm for Three-Phase Load Flow

We have various conventional methods to conduct the three-phase load flow analysis like the fast-decoupled load flow method, Newton-Raphson load flow method, Gauss Seidel method etc. Here the adopted method is the Newton-Raphson load flow method due to its two advantages [12]:

(I) Convergence Characteristic is Fast.
(II) Strong Reliability towards Convergence.

The equation for iterative solution is given below [13]:

$$\begin{bmatrix} \Delta P_d^{\delta} \\ \Delta Q_d^{\delta} \end{bmatrix}^i = \begin{bmatrix} \frac{\partial P_d^{\delta}}{\partial \theta_j^{\delta}} & \frac{\partial P_d^{\delta}}{\partial V_j^{\delta}}(V_j^{\delta}) \\ \frac{\partial Q_d^{\delta}}{\partial \theta_j^{\delta}} & \frac{\partial Q_d^{\delta}}{\partial V_j^{\delta}}(V_j^{\delta}) \end{bmatrix}^i \begin{bmatrix} \Delta \theta_j^{\delta} \\ \frac{\Delta V_j^{\delta}}{V_j^{\delta}} \end{bmatrix}^i, \tag{13}$$

Here $d = y, z$ and (i) refers to the iteration number.

3.1 Vector Terms

$$\Delta P_d^{\delta} = \left[\Delta P_y^a \ \Delta P_y^b \ \Delta P_y^c \ \Delta P_z^a \ \Delta P_z^b \ \Delta P_z^c \ \right]^T, \tag{14}$$

$$\Delta Q_d^{\delta} = \left[\Delta Q_y^a \ \Delta Q_y^b \ \Delta Q_y^c \ \Delta Q_z^a \ \Delta Q_z^b \ \Delta Q_z^c \ \right]^T, \tag{15}$$

$$\Delta \theta_j^{\delta} = \left[\Delta \theta_y^a \ \Delta \theta_y^b \ \Delta \theta_y^c \ \Delta \theta_z^a \ \Delta \theta_z^b \ \Delta \theta_z^c \ \right]^T, \tag{16}$$

$$\frac{\Delta V_j^{\delta}}{V_j^{\delta}} = \left[\frac{\Delta V_y^a}{V_y^a} \ \frac{\Delta V_y^b}{V_y^b} \ \frac{\Delta V_y^c}{V_y^c} \ \frac{\Delta V_z^a}{V_z^a} \ \frac{\Delta V_z^b}{V_z^b} \ \frac{\Delta V_z^c}{V_z^c} \ \right]^T. \tag{17}$$

3.2 Formation of Jacobian Matrices

The Jacobian terms are given as [14]:

$$\frac{\partial P_d^{\delta}}{\partial \theta_j^{\delta}} = \begin{bmatrix} \frac{\partial P_d^a}{\partial \theta_j^a} & \frac{\partial P_d^a}{\partial \theta_j^b} & \frac{\partial P_d^a}{\partial \theta_j^c} \\ \frac{\partial P_d^b}{\partial \theta_j^a} & \frac{\partial P_d^b}{\partial \theta_j^b} & \frac{\partial P_d^b}{\partial \theta_j^c} \\ \frac{\partial P_d^c}{\partial \theta_j^a} & \frac{\partial P_d^c}{\partial \theta_j^b} & \frac{\partial P_d^c}{\partial \theta_j^c} \end{bmatrix}, \tag{18}$$

$$\frac{\partial P_d^{\delta}}{\partial V_j^{\delta}}(V_j^{\delta}) = \begin{bmatrix} \frac{\partial P_d^a}{\partial V_j^a}(V_j^a) & \frac{\partial P_d^a}{\partial V_j^b}(V_j^b) & \frac{\partial P_d^a}{\partial V_j^c}(V_j^c) \\ \frac{\partial P_d^b}{\partial V_j^a}(V_j^a) & \frac{\partial P_d^b}{\partial V_j^b}(V_j^b) & \frac{\partial P_d^b}{\partial V_j^c}(V_j^c) \\ \frac{\partial P_d^c}{\partial V_j^a}(V_j^a) & \frac{\partial P_d^c}{\partial V_j^b}(V_j^b) & \frac{\partial P_d^c}{\partial V_j^c}(V_j^c) \end{bmatrix}, \tag{19}$$

$$\frac{\partial Q_d^{\delta}}{\partial \theta_j^{\delta}} = \begin{bmatrix} \frac{\partial Q_d^a}{\partial \theta_j^a} & \frac{\partial Q_d^a}{\partial \theta_j^b} & \frac{\partial Q_d^a}{\partial \theta_j^c} \\ \frac{\partial Q_d^b}{\partial \theta_j^a} & \frac{\partial Q_d^b}{\partial \theta_j^b} & \frac{\partial Q_d^b}{\partial \theta_j^c} \\ \frac{\partial Q_d^c}{\partial \theta_j^a} & \frac{\partial Q_d^c}{\partial \theta_j^b} & \frac{\partial Q_d^c}{\partial \theta_j^c} \end{bmatrix}, \tag{20}$$

$$\frac{\partial Q_d^{\delta}}{\partial V_j^{\delta}}(V_j^{\delta}) = \begin{bmatrix} \frac{\partial Q_d^a}{\partial V_j^a}(V_j^a) & \frac{\partial Q_d^a}{\partial V_j^b}(V_j^b) & \frac{\partial Q_d^a}{\partial V_j^c}(V_j^c) \\ \frac{\partial Q_d^b}{\partial V_j^a}(V_j^a) & \frac{\partial Q_d^b}{\partial V_j^b}(V_j^b) & \frac{\partial Q_d^b}{\partial V_j^c}(V_j^c) \\ \frac{\partial Q_d^c}{\partial V_j^a}(V_j^a) & \frac{\partial Q_d^c}{\partial V_j^b}(V_j^b) & \frac{\partial Q_d^c}{\partial V_j^c}(V_j^c) \end{bmatrix}. \tag{21}$$

For dth element connected between buses y and z, the self and mutual terms are given below [15]:

$y = z, \delta 1 = \delta 2$

$$\frac{\partial P_{y,d}^{\delta 1}}{\partial \theta_{y,d}^{\delta 1}} = -Q_y^{\delta 1 cal} - (V_y^{\delta 1})^2 B_{yy}^{\delta 1 \delta 1}, \tag{22}$$

$$\frac{\partial P_{y,d}^{\delta 1}}{\partial V_{y,d}^{\delta 1}}(V_{y,d}^{\delta 1}) = P_y^{\delta 1 cal} + (V_y^{\delta 1})^2 G_{yy}^{\delta 1 \delta 1}, \tag{23}$$

$$\frac{\partial Q_{y,d}^{\delta 1}}{\partial \theta_{y,d}^{\delta 1}} = P_y^{\delta 1 cal} - (V_y^{\delta 1})^2 G_{yy}^{\delta 1 \delta 1}, \tag{24}$$

$$\frac{\partial Q_{y,d}^{\delta 1}}{\partial V_{y,d}^{\delta 1}}(V_{y,d}^{\delta 1}) = Q_y^{\delta 1 cal} - (V_y^{\delta 1})^2 B_{yy}^{\delta 1 \delta 1}. \tag{25}$$

$y = z, \delta 1 \neq \delta 2$

$$\frac{\partial P_{y,d}^{\delta 1}}{\partial \theta_{y,d}^{\delta 2}} = V_y^{\delta 1} V_y^{\delta 2} [G_{yy}^{\delta 1 \delta 2} \sin(\theta_y^{\delta 1} - \theta_y^{\delta 2}) - B_{yy}^{\delta 1 \delta 2} \cos(\theta_y^{\delta 1} - \theta_y^{\delta 2})], \tag{26}$$

$$\frac{\partial P_{y,d}^{\delta 1}}{\partial V_{y,d}^{\delta 2}}(V_{y,d}^{\delta 2}) = V_y^{\delta 1} V_y^{\delta 2} [G_{yy}^{\delta 1 \delta 2} \cos(\theta_y^{\delta 1} - \theta_y^{\delta 2}) + B_{yy}^{\delta 1 \delta 2} \sin(\theta_y^{\delta 1} - \theta_y^{\delta 2})], \tag{27}$$

$$\frac{\partial Q_{y,d}^{\delta 1}}{\partial \theta_{y,d}^{\delta 2}} = -V_y^{\delta 1} V_y^{\delta 2} [G_{yy}^{\delta 1 \delta 2} \cos(\theta_y^{\delta 1} - \theta_y^{\delta 2}) + B_{yy}^{\delta 1 \delta 2} \sin(\theta_y^{\delta 1} - \theta_y^{\delta 2})], \tag{28}$$

$$\frac{\partial Q_{y,d}^{\delta 1}}{\partial V_{y,d}^{\delta 2}}(V_{y,d}^{\delta 2}) = V_y^{\delta 1} V_y^{\delta 2} [G_{yy}^{\delta 1 \delta 2} \sin(\theta_y^{\delta 1} - \theta_y^{\delta 2}) - B_{yy}^{\delta 1 \delta 2} \cos(\theta_y^{\delta 1} - \theta_y^{\delta 2})]. \tag{29}$$

$y \neq z$

$$\frac{\partial P_{y,d}^{\delta 1}}{\partial \theta_{z,d}^{\delta 2}} = V_y^{\delta 1} V_z^{\delta 2} [G_{yz}^{\delta 1 \delta 2} \sin(\theta_y^{\delta 1} - \theta_z^{\delta 2}) - B_{yz}^{\delta 1 \delta 2} \cos(\theta_y^{\delta 1} - \theta_z^{\delta 2})], \tag{30}$$

$$\frac{\partial P_{y,d}^{\delta 1}}{\partial V_{z,d}^{\delta 2}}(V_{z,d}^{\delta 2}) = V_y^{\delta 1} V_z^{\delta 2} [G_{yz}^{\delta 1 \delta 2} \cos(\theta_y^{\delta 1} - \theta_z^{\delta 2}) + B_{yz}^{\delta 1 \delta 2} \sin(\theta_y^{\delta 1} - \theta_z^{\delta 2})], \tag{31}$$

$$\frac{\partial Q_{y,d}^{\delta 1}}{\partial \theta_{z,d}^{\delta 2}} = -V_y^{\delta 1} V_z^{\delta 2} [G_{yz}^{\delta 1 \delta 2} \cos(\theta_y^{\delta 1} - \theta_z^{\delta 2}) + B_{yz}^{\delta 1 \delta 2} \sin(\theta_y^{\delta 1} - \theta_z^{\delta 2})], \quad (32)$$

$$\frac{\partial Q_{y,d}^{\delta 1}}{\partial V_{z,d}^{\delta 2}}(V_{z,d}^{\delta 2}) = V_y^{\delta 1} V_z^{\delta 2} [G_{yz}^{\delta 1 \delta 2} \sin(\theta_y^{\delta 1} - \theta_z^{\delta 2}) - B_{yz}^{\delta 1 \delta 2} \cos(\theta_y^{\delta 1} - \theta_z^{\delta 2})]. \quad (33)$$

The basic algorithm of Newton Raphson remains same for single phase systems and three-phase systems [16]. When assuming flat start the three phases are initialised at $0, -2\pi/3$ and $2\pi/3$ respectively for phase sequence a, b, c. The storage and computational requirements of a three-phase load flow program are higher than single phase program as the mismatch matrix and correction matrix will have each value of order 3×1 and individual jacobian term will be of order 3×3 [17]. Equation (13) applies to only one three-phase transmission line connected between buses y and z but the discussion can be further extended to a more practical case with n_d transmission lines connected between n_b generic buses d and j where $d = 1 \ldots n_b - 1$ and $j = 1 \ldots n_b - 1$. We take $n_b - 1$ buses as we are not showing contribution of slack bus in linearized system of equations [18].

4 Results and Discussion

Load flow analysis has been conducted for IEEE 5 bus and IEEE 118 bus systems both for balanced and unbalanced case. In case of balanced case the magnitudes of voltages of all the 3 phases come out as equal and the phases of voltages are 120° apart. In case of unbalanced system the magnitude of voltage of the 3 phases come out to be unequal and the phases of voltages are not 120° apart [19].

4.1 IEEE 5-Bus System

(a) Balanced System

First the analysis has been conducted for IEEE 5 bus system for balanced case and resulting voltage magnitudes for all the buses are shown in Table 1 [20].

Now the analysis has been conducted to obtain voltage angles for all the buses and are given in Table 2.

In Fig. 2 the graph depicts voltage magnitude of all the load buses and it can be seen that all the voltage magnitude values lie between the range of nominal values.

In Fig. 3 the graph depicts the voltage angles for all load buses and it can be seen that system is balanced as we have phase difference of 120° between the phase values.

Table 1 Voltage magnitude of 5 bus system for balanced case

Bus No.	a	b	c
1	1.0600	1.0600	1.0600
2	1.0000	1.0000	1.0000
3	0.9895	0.9895	0.9895
4	0.9864	0.9864	0.9864
5	0.9745	0.9745	0.9745

Table 2 Voltage angle of 5 bus system for unbalanced case

Bus No.	a	b	c
1	0	4.1888	2.0944
2	−0.0341	4.1581	2.0543
3	−0.0793	4.1077	2.0156
4	−0.0821	4.1026	2.0073
5	−0.1003	4.1078	1.9807

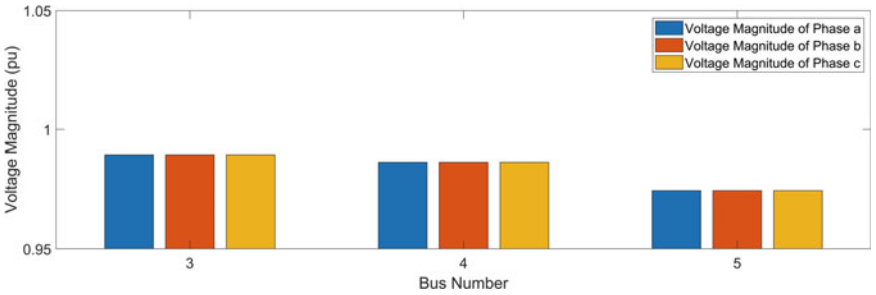

Fig. 2 Voltage magnitude of 5 bus system for balanced case

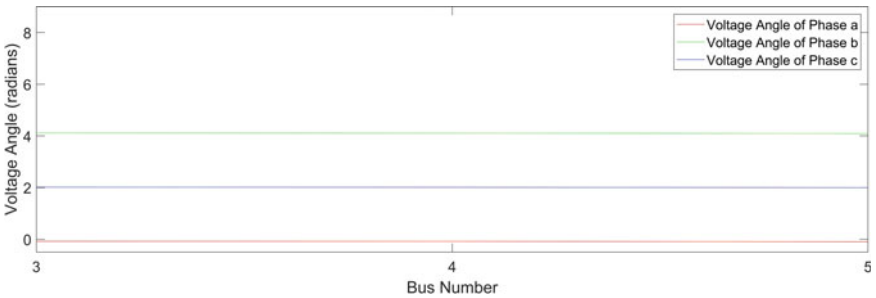

Fig. 3 Voltage angle of 5 bus system for balanced case

(b) Unbalanced System

Now the analysis has been conducted for IEEE 5 bus system for unbalanced case and resulting voltage magnitudes for all the buses are shown in Table 3.

Now the analysis has been conducted to obtain voltage angles for all the buses and are shown in Table 4.

In Fig. 4 the graph depicts that the voltage magnitude values of the load buses lies between the range of nominal values but are not equal for all the three phases as system is unbalanced.

In Fig. 5 the graph depicts the voltage angles of all the phases. The voltage angles are not 120° apart as system is unbalanced.

Table 3 Voltage magnitude of 5 bus system for unbalanced case

Bus No.	a	b	c
1	1.0600	1.0600	1.0600
2	1.0000	1.0000	1.0000
3	0.9843	0.9900	0.9935
4	0.9834	0.9850	0.9900
5	0.9813	0.9766	0.9649

Table 4 Voltage angle of 5 bus system for balanced case

Bus No.	a	b	c
1	0	4.1888	2.0944
2	−0.0345	4.1543	2.0599
3	−0.0790	4.1098	2.0154
4	−0.0844	4.1044	2.0100
5	−0.0975	4.0913	1.9969

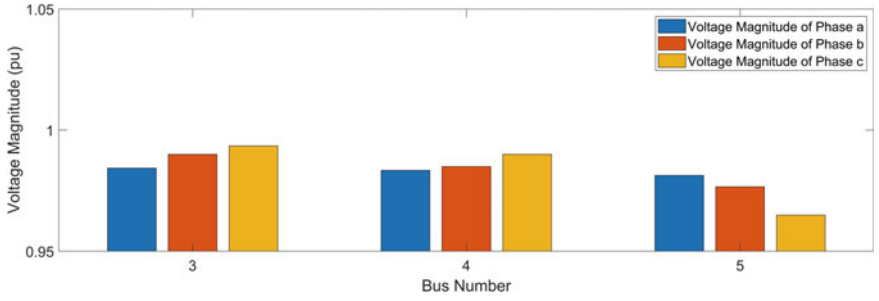

Fig. 4 Voltage magnitude of 5 bus system for unbalanced case

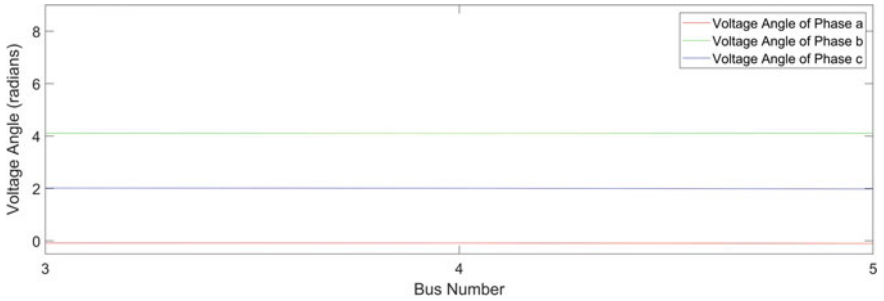

Fig. 5 Voltage angle of 5 bus system for unbalanced case

4.2 IEEE 118-Bus System

(a) Balanced System

In Fig. 6 the graph depicts the voltage magnitude of all the load buses and it can be seen that all the values lies between the range of nominal values.

In Fig. 7 the zoomed in view of Fig. 5 for voltage magnitude for balanced case is given.

In Fig. 8 the graph depicts the voltage angles for all load buses. Since the system is balanced each phase has a phase difference of 120°.

(b) Unbalanced System

In Fig. 9 the graph depicts that the voltage magnitude of the load buses lies between the range of nominal values but are not equal for all the three phases as system is unbalanced.

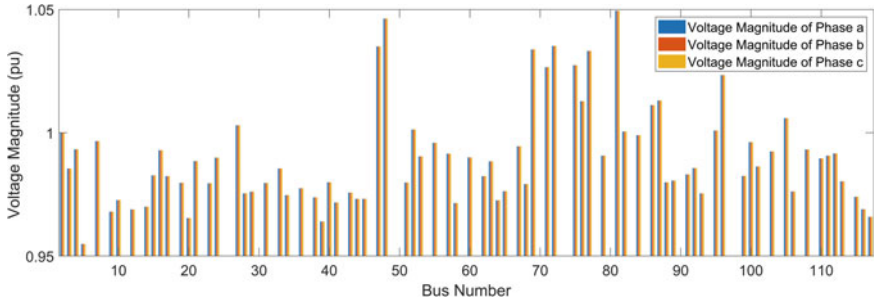

Fig. 6 Voltage magnitude of 118 bus system for balanced case

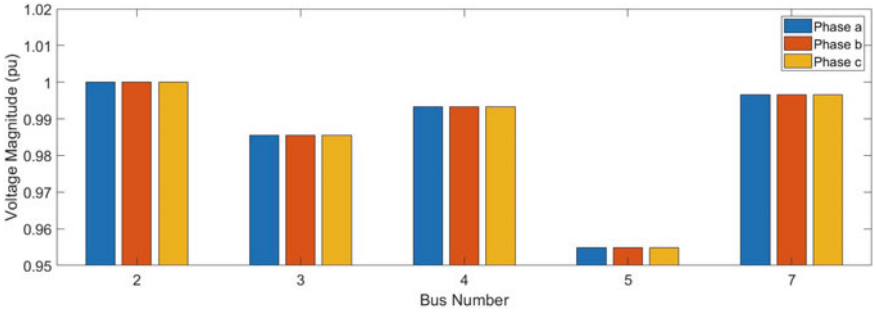

Fig. 7 Zoomed in view of Fig. 5 for voltage magnitude for balanced case

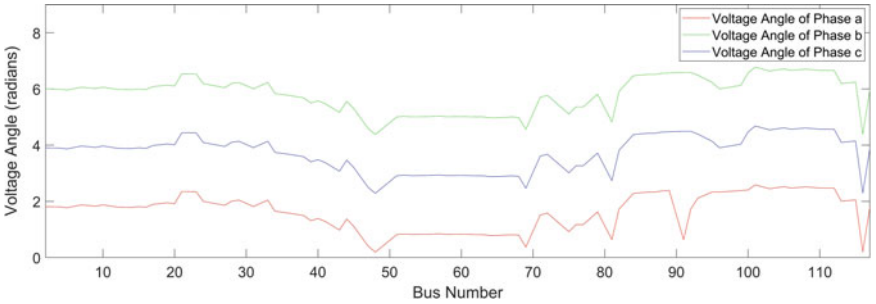

Fig. 8 Voltage angle of 118 bus system for balanced case

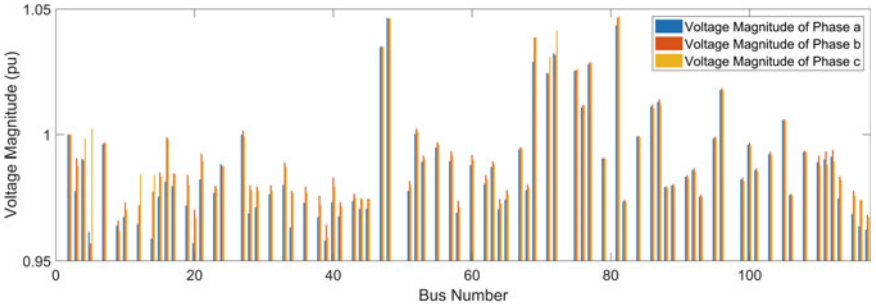

Fig. 9 Voltage magnitude of 118 bus system for unbalanced case

In Fig. 10 the zoomed in view of Fig. 8 for voltage magnitude for unbalanced case is given.

In Fig. 11 the graph depicts that voltage angles of all the phases. The voltage angles are not 120° apart the system is unbalanced.

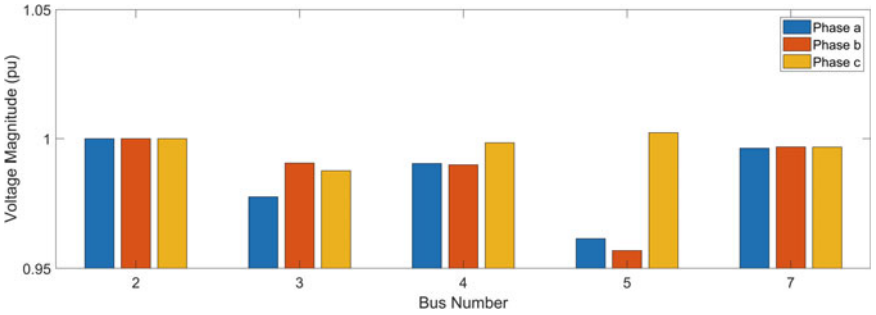

Fig. 10 Zoomed in view of Fig. 8 for voltage magnitude for unbalanced case

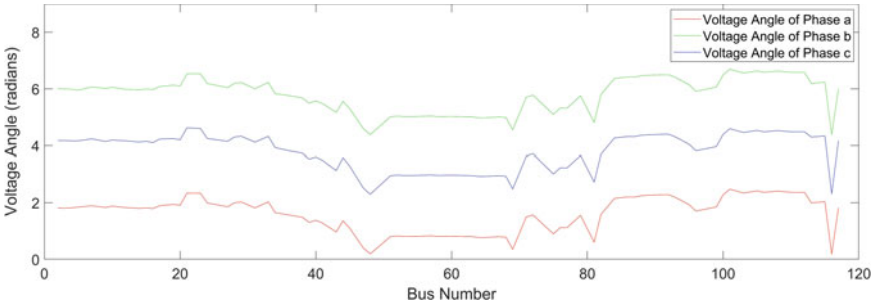

Fig. 11 Voltage angle of 118 bus system for unbalanced case

5 Conclusion

The proposed three phase Newton-Raphson load flow method has been successfully implemented on IEEE 5 and IEEE 118 bus systems under both balanced as well as unbalanced conditions. The obtained results validate the robustness and accuracy of the proposed method as the resulting magnitudes and angles of all the buses have been obtained well within the standard ranges of voltage magnitudes and voltage angles.

References

1. A. Kalyuzhny, G. Kushnir, Analysis of current unbalance in transmission systems with short lines. IEEE Trans. Power Deliv. **22**(2), 1040–1048 (2007)
2. W.H. Kersting, Causes and effects of single-phasing induction motors. IEEE Trans. Ind. Appl. **41**(6), 1499–1505 (2005)
3. J. Liang, K. Zhu, Capacitor health monitoring based on the disturbances of element breakdown faults. IEEE Trans. Power Deliv. (2022)
4. S.-H. Im, G. Bon-Gwan, Study of induction motor inter-turn fault part II: online model-based fault diagnosis method. Energies **15**(3), 977 (2022)

5. Y. Li, H. He, Z. Li, Z. Zhang, Predictive zero-sequence current control of multiple paralleled power converters. IEEE Trans. Ind. Electron. (2022)
6. S.P. Dubey, S.P. Makhija, Power quality problems and solutions in renewable energy, in *Handbook of Renewable Energy Technology & Systems* (2022), pp. 553–571
7. A. Thankgod, D. Idoniboyeobu, S. Braide, Analysis of effects of conductor transposition on the 132kv Alaoji-Port Harcourt transmission line (2022)
8. K.A. Birt, J.J. Graffy, J.D. McDonald, A.H. El-Abiad, Three phase load flow program. IEEE Trans. Power Appar. Syst. **95**(1), 59–65 (1976)
9. S.T. Hosseinabadi, Fast and scalable power system learning, analysis, and planning. Ph.D. dissertation, Virginia Tech (2022)
10. J. Arrillaga, B.J. Harker, Fast-decoupled three-phase load flow. Proc. Inst. Electr. Eng. **125**(8), 734–740 (1978). IET Digital Library
11. A.S. Nair, S. Abhyankar, S. Peles, P. Ranganathan, Computational and numerical analysis of AC optimal power flow formulations on large-scale power grids. Electr. Power Syst. Res. **202**, 107594 (2022)
12. M.C. Herrera, O.D. Montoya, A. Molina-Cabrera, L.F. Grisales-Noreña, A. Giral-Ramírez, Convergence analysis of the triangular-based power flow method for AC distribution grids. Int. J. Electr. & Comput. Eng. (2088-8708) **12**(1) (2022)
13. H. Le Nguyen, Newton-Raphson method in complex form [power system load flow analysis]. IEEE Trans. Power Syst. **12**(3), 1355–1359 (1997)
14. A.G. Bhutad, S.V. Kulkarni, S.A. Khaparde, Three-phase load flow methods for radial distribution networks, in *Tencon 2003. Conference on Convergent Technologies for Asia-Pacific Region*, vol. 2 (IEEE, 2003)
15. D. Rusinaru, L.G. Manescu, M. Ciontu, M. Alba, Three-phase load flow analysis of the unbalanced distribution networks, in *2016 International Conference on Applied and Theoretical Electricity (ICATE)*, October 2016 (IEEE, 2016), pp. 1–5
16. J. Arrillaga, C.P. Arnold, *Computer analysis of power systems* (Wiley, New York, 1990)
17. X.P. Zhang, Fast three phase load flow methods. IEEE Trans. Power Syst. **11**(3), 1547–1554 (1996)
18. E. Acha, C.R. Fuerte-Esquivel, H. Ambriz-Perez, C. Angeles-Camacho, *FACTS: Modelling and Simulation in Power Networks* (Wiley, 2004)
19. A.H. Lone, N. Gupta, Load flow analysis of islanded microgrids, in *2021 IEEE 4th International Conference on Computing, Power and Communication Technologies (Gucon)* (IEEE, 2021), pp. 1–6
20. N. Gupta, N. Daratha, Probabilistic three-phase load flow for unbalanced electrical systems with wind farms. Int. J. Electr. Power & Energy Syst. **87**, 154–165 (2017)

Some Approaches to Model Order Reduction of Linear Interval System and Its Application

Raj Anand and Amarnath Jha

Abstract This paper represents the mixed approach for model order minimization of a large-scale linear interval system. The desired order of numerator coefficient is determined by applying Cauer's second form, and the desired order of denominator coefficient is determined by using the extension of the differentiation method. Some typical numerical examples are considered for testing the accuracy and computational simplicity of the proposed approach in which various step output parameters of the original model and the minimized model along with integral square error have been compared. The calculation of PID parameters along with model order reduction by the proposed approach for an interval transfer function of oblique wing aircraft has also been done. Kharitonov's theorem verifies the system's stability.

Keywords Large scale linear interval models · Model order reduction · Cauer second form · Kharitonov's theorem · Extension of differentiation method · Modified Routh approximation · PID controller and Integral square error

1 Introduction

The implementation and controller design for a large-scale complex linear interval system is always a critical challenge because the presence of uncertain variables increases the system's complexity. The analysis and synthesis of such a large-scale real-time system become very tedious and costly. Therefore it is essential to use minimized modeling techniques for the basic insight of the characteristics for the original system and to make it easier for analysis. The model order reduction is a

R. Anand (✉)
Department of Electrical Engineering, Netaji Subhas University of Technology, New Delhi, India
e-mail: raja.ee20@nsut.ac.in

A. Jha
Department of Instrumentation and Control Engineering, Netaji Subhas University of Technology, New Delhi, India
e-mail: anjha@nsut.ac.in

J. Kumar et al. (eds.), *Control Applications in Modern Power Systems*, Lecture Notes in Electrical Engineering 974, https://doi.org/10.1007/978-981-19-7788-6_16

branch of control theory that efficiently reduces the complex system by preserving its output and input behavior. The main advantage of the reduced model is that it provides a greater understanding of the large-order system, trouble-free design, and quick solutions. The enhancement of model order reduction fundamentals was begins in the early 1980s, and the reduction approaches are available for both the time and frequency domains. Some recently obtained model reduction techniques like Model reduction of linear hybrid systems [1] which is based on the balanced truncation method, minimization of large-order continuous systems using sine cosine algorithm [2] and conventional method based on Pade [3] all are limited to reduce non-interval continuous system. So later, research on interval system got huge attention after initialization of work on Kharitonov's theorem for the study of the stability of interval system which generates four interval polynomials and the stability is tested by using Routh's criterion. Some popular model reduction techniques for linear interval systems are Routh-Pade approximation for interval systems and Gamma-delta Routh approximation [4–7] But, the limitation of the above methods was that obtained reduced models are unstable even if original systems are stable, so to improve the effectiveness of the reduced model, some soft computing methods [8, 8] and the number of mixed methods [10–15] but the drawback of some of these methods was that they were unable to generate full interval array [16–19] and inefficient to retain reduced model stability.

The proposed approach is efficient in retaining the stability and reliability of the minimized order model only if the original models are stable. In this paper, the order of the linear interval system is reduced by using a mixed approach. The extended differentiation approach is applied to obtain desired order denominator coefficients, and the numerator coefficients are obtained by applying Cauer's second form. The verification of the proposed approach is done by considering two typical examples along with the demonstration of comparative study and model reduction of oblique wing aircraft by proposed method along with PID tuning also have been presented. The entire paper is sub-divided as follows: the preliminaries are explained in Sect. 2, Sect. 3 defines the problem methodology for the proposed approach, in Sect. 4, typical numerical testing is done with a comparative study and Sect. 5 reports the conclusion.

2 Preliminaries

In interval arithmetic, numeric is lying in bounds. Let us consider that $R = \left[R^-, R^+\right] \equiv \left\{R|R \in \left[R^-, R^+\right]\right\}$, $T = \left[T^-, T^+\right]\left\{T|T \in \left[T^-, T^+\right]\right\}$ is the real intervals, A represents the Division, multiplication, addition, and subtraction of numbers in bounds, i.e. $A \in \{\div, \times, +, -\}$. The operations between intervals R and T i.e. $\left[R^-, R^+\right]$ A $\left[T^-, T^+\right]$ are defined as follows:

Addition:

$$\mathrm{R} + \mathrm{T} = \left[\mathrm{R}^{-} + \mathrm{T}^{-}, \mathrm{R}^{+} + \mathrm{T}^{+}\right]$$

Subtraction:

$$\mathrm{R} - \mathrm{T} = \left[\mathrm{R}^{-} + \mathrm{T}^{+}, \mathrm{R}^{+} + \mathrm{T}^{-}\right]$$

Multiplication:

$$\mathrm{R} \times \mathrm{T}\begin{bmatrix} \min\left(\mathrm{R}^{-}\mathrm{T}^{-}, \mathrm{R}^{-}\mathrm{T}^{+}, \mathrm{R}^{+}\mathrm{T}^{-}, \mathrm{R}^{+}\mathrm{T}^{+}\right), \\ \max\left(\mathrm{R}^{-}\mathrm{T}^{-}, \mathrm{R}^{-}\mathrm{T}^{+}, \mathrm{R}^{+}\mathrm{T}^{-}, \mathrm{R}^{+}\mathrm{T}^{+}\right) \end{bmatrix}$$

Division:

$$\frac{\mathrm{R}}{\mathrm{T}} = \mathrm{R} \cdot \left(\frac{1}{\mathrm{T}}\right), \text{ Where, } \frac{1}{\mathrm{T}} = \left\{\frac{1}{(\mathrm{T}|\mathrm{T})} \in \mathrm{T}\right\},$$

$$\text{Provided, } \mathrm{T} \neq 0.$$

It must be noted that the above arithmetic rules are limited for only four operations that are Division, multiplication, subtraction, and addition.

2.1 Kharitonov's Theorem

Suppose real interval polynomial family (s) of degree n in the form of $\beta(s) := \{\beta(s) = X_n s^n + \cdots + X_0 \colon X_i \in [X_i^-, X_i^+],\ i = 0, 1, 2, \ldots, n.$

The whole family's Hurwitz stability is set up by using Kharitonov's theorem which is astonishingly simple, required, and appropriate.

Kharitonov's theorem states that every polynomial in the family β(s) is Hurwitz if and only if the following four extreme polynomials are Hurwitz.

$$\beta^1(s) = x_0^- + x_1^- s + x_2^+ s^2 + x_3^+ s^3 + x_4^- s^4 + \cdots\cdots$$
$$\beta^2(s) = x_0^- + x_1^+ s + x_2^+ s^2 + x_3^- s^3 + x_4^- s^4 + \cdots\cdots$$
$$\beta^3(s) = x_0^+ + x_1^- s + x_2^- s^2 + x_3^+ s^3 + x_4^+ s^4 + \cdots\cdots$$
$$\beta^4(s) = x_0^+ + x_1^+ s + x_2^- s^2 + x_3^- s^3 + x_4^+ s^4 + \cdots\cdots$$

2.2 Integral Square Error

The significance of the integral square error (ISE) is that it verifies the preciseness of the proposed. The calculation of ISE is done from the transient part of the original and minimized model. It is defined as

$$\mathrm{ISE} = \int_0^{\infty} [\mathrm{F(t)} - \mathrm{C(t)}]^2 \mathrm{dt}$$

Here, F(t) represents the step output of the original model, and C(t) is the step output for the reduced model.

3 Problem Methodology

Consider a stable linear interval system of order n, denoted by

$$\mathrm{F_n(s)} = \frac{\left[y_{21}^-, y_{21}^+\right] + \left[y_{22}^-, y_{22}^+\right]\mathrm{s} + \cdots\cdots + \left[y_{2n,}^-, y_{2n}^+\right]\mathrm{s}^{n-1}}{\left[y_{11}^-, y_{11}^+\right] + \left[y_{12}^-, y_{12}^+\right]\mathrm{s} + \cdots\cdots + \left[y_{1,n+1}^-, y_{1,n+1}^+\right]\mathrm{s}^{n}} = \frac{\mathrm{N(s)}}{\mathrm{D(s)}} \qquad (1)$$

where, $[y_{2j}^-, y_{2j}^+]$ for $1 \le j \le n$ and $\left[y_{1j,}^-, y_{1j}^+\right]$ for $1 \le j \le n+1$ represents lower and upper bounds of N(s) and D(s) of the original model. Let, $\mathrm{C_r(s)}$ represents the minimized order model of the original interval system $\mathrm{F_n(s)}$.

$$\mathrm{C_r(s)} = \frac{\left[p_{21}^-, p_{21}^+\right] + \left[p_{22}^-, p_{22}^+\right]\mathrm{s} + \cdots\cdots + \left[p_{2r,}^-, p_{2r}^+\right]\mathrm{s}^{r-1}}{\left[p_{11}^-, p_{11}^+\right] + \left[p_{12}^-, p_{12}^+\right]\mathrm{s} + \cdots + \left[p_{1,r+1}^-, p_{1,r+1}^+\right]\mathrm{s}^{r}} = \frac{\mathrm{N_r(s)}}{\mathrm{D_r(s)}} \qquad (2)$$

where, $\left[p_{2j}^-, p_{2j}^+\right]$ for $i = 1, 2, 3 \ldots\ldots .r$ and $\left[p_{1j}^-, p_{1j}^+\right]$ for $j = 1, 2, 3 \ldots r+1$ and p_i and q_j are lower and upper bounds of $\mathrm{N_r(s)}$ and $\mathrm{D_r(s)}$, obtained order of the reduced model system is $r < n$.

4 Procedure to Get Desired Order Reduced Denominator Polynomials $\mathbf{D_r(s)}$ from the Denominator of Original Interval Transfer Function Model D(S) by Extension of Differentiation Method

(i) The denominator coefficients of $\mathrm{F_n(s)}$ are considered in first row of Table 1.
(ii) Differentiation of the first row gives the second row.

Table 1 Table of denominators for linear intervals

Row1	$[y_{11}^{-}, y_{11}^{+}] = [y_{n}^{-}, y_{n}^{+}]$	$[y_{12}^{-}, y_{12}^{+}] = [y_{n-1}^{-}, y_{n-1}^{+}]$	⋯
Row2	$[y_{21}^{-}, y_{21}^{+}] = (n)[y_{n}^{-}, y_{n}^{+}]$	$[y_{22}^{-}, y_{22}^{+}] = (n-1)[y_{n-1}^{-}, y_{n-1}^{+}]$	⋯
Row3	$[y_{31}^{-}, y_{31}^{+}] = [y_{n-1}^{-}, y_{n-1}^{+}]$	$[y_{32}^{-}, y_{32}^{+}] = [y_{n-2}^{-}, y_{n-2}^{+}]$	⋯
Row4	$[y_{41}^{-}, y_{41}^{+}] = (n-1)[y_{41}^{-}, y_{41}^{+}]$	$[y_{42}^{-}, y_{42}^{+}] = (n-2)[y_{42}^{-}, y_{42}^{+}]$	⋯
Row5	$\left[y_{51}^{-}, y_{51}^{+}\right]$	$[y_{52}^{-}, y_{52}^{+}]$	⋯

(iii) The third row has been found by modified Routh approximation, which provides minimized denominator order of $n-1$ by using following relation $\left[y_{ij}^{-}, y_{ij}^{+}\right] = \left[y_{i-2,j+1}^{-}, y_{i-2,j+1}^{+}\right] - \frac{y_{i-2,1}}{y_{i-1,1}}\left[y_{i-1,j+1}^{-}, y_{i-1,j+1}^{+}\right]$, here $i = 3,5,7\ldots.$ and $j = 1,2,3,\ldots.n-1$.
$y_{i-2,1} = \frac{y_{i-2,1}^{-}+y_{i-2,1}^{+}}{2}$; $y_{i-1,1} = \frac{y_{i-1,1}^{-}+y_{i-1,1}^{+}}{2}$, are the middle values of the coefficients.

(iv) Differentiation of 3rd-row results from row 4 and minimized denominator of $n-2$ order are derived by applying modified Routh approximation d rows.

(v) Minimized denominator order of D(s) given by

$$\left[y_{n-1}^{-}, y_{n-1}^{+}\right]s^{n-1} + \left[y_{n-2}^{-}, y_{n-2}^{+}\right]s^{n-2} + \cdots\cdots + \left[y_{0}^{-}, y_{0}^{+}\right] \tag{3}$$

4.1 Procedure to Obtain Reduced-Order of the Numerator Polynomial $\mathbf{N_r(s)}$ from Numerator of Original Model N(s)

The minimized order of numerator is derived by the Cauer's second form.

(i) The calculation of coefficient value from the Cauer's second form $[f_p^{-}, f_p^{+}]$ $p = 1, 2, 3\ldots n$ are obtained by making Routh array represented in step II.

$$
\begin{aligned}
&\left[f_1^-, f_1^+\right] = \frac{\left[y_{11}^-, y_{11}^+\right]}{\left[y_{21}^-, y_{21}^+\right]} \left\{ \begin{matrix} \left[y_{11}^-, y_{11}^+\right]\left[y_{12}^-, y_{12}^+\right] \cdots ... \\ \left[y_{21}^-, y_{21}^+\right]\left[y_{22}^-, y_{22}^+\right] \cdots \cdots \end{matrix} \right. \\
\text{(ii)} \quad &\left[f_2^-, f_2^+\right] = \frac{\left[y_{21}^-, y_{21}^+\right]}{\left[y_{31}^-, y_{31}^+\right]} \left\{ \begin{matrix} \left[y_{21}^-, y_{21}^+\right]\left[y_{22}^-, y_{22}^+\right] \cdots \cdots \\ \left[y_{31}^-, y_{31}^+\right]\left[y_{32}^-, y_{32}^+\right] \cdots \cdots \end{matrix} \right. \\
&\left[f_3^-, f_3^+\right] = \frac{\left[y_{31}^-, y_{31}^+\right]}{\left[y_{41}^-, y_{41}^+\right]} \left\{ \begin{matrix} \left[y_{31}^-, y_{31}^+\right]\left[y_{32}^-, y_{32}^+\right] \cdots \cdots \\ \left[y_{41}^-, y_{41}^+\right]\left[y_{42}^-, y_{42}^+\right] \cdots \cdots \end{matrix} \right. \\
&\quad \cdots\cdots \quad \cdots\cdots \quad \cdots\cdots \quad \cdots\cdots \quad \cdots\cdots
\end{aligned}
$$

(iii) Denominator and numerator of the original model are the first two rows of the Routh array and the Routh algorithm calculates the rest rows.

$$\left[y_{ij}^-, y_{ij}^+\right] = \left[y_{(i-2,j+1)}^-, y_{(i-2,j+1)}^+\right] - \left[f_{i-2}^-, f_{i-2}^+\right]\left[y_{(i-1,j+1)}^-, y_{(i-2,j+1)}^+\right]$$

where i = 3, 4 ….. and j = 1, 2 ….

$$\left[f_i^-, f_i^+\right] = \frac{\left[y_{(i,1)}^-, y_{(i,1)}^+\right]}{\left[y_{(i+1,1)}^-, y_{(i+1,1)}^+\right]} \text{for} i = 1, 2, 3, \ldots..r$$

To obtain numerator of $c_r(s)$

$$\left[p_{(i+1,1)}^-, p_{(i+1,1)}^+\right] = \frac{\left[p_{i,1}^-, p_{i,1}^+\right]}{\left[f_i^-, f_i^+\right]}, \text{ here, } i = 1, 2, 3 \ldots r \text{ and } r \leq n$$

$$\left[p_{(i+1,j+1)}^-, p_{(i+1,j+1)}^+\right] = \frac{\left[p_{(i,j+1)}^-, p_{(i,j+1)}^+\right] - \left[p_{(i+2,j)}^-, p_{(i+2,j)}^+\right]}{\left[f_i^-, f_i^+\right]}$$

where i = 1, 2……(r−j) and j = 1, 2…..(r−1).

The reduced-order numerator represented as

$$N_r(s) = \left[p_{21}^-, p_{21}^+\right] + \left[p_{22}^-, p_{22}^+\right]s + \cdots + \left[p_{2r}^-, p_{2r}^+\right]s^{r-1}. \tag{4}$$

5 Results and Discussion

Example 1 Suppose a third order interval system model [4] is reduced in second order by proposed method.

$$F(s) = \frac{[2,3]s^2 + [17.8, 18.5]s + [15, 16]}{[2,3]s^3 + [17, 18]s^2 + [35, 36]s + [20.5, 21.5]}$$

Step 1. Reduce the denominator by extension of the differentiation method by using Table 1.

Row1	higher order	[2,3]	[17,18]	[35,36] [20.5, 21.5]
Row 2	differentiation	[6,9]	[34,36]	[35,36]
Row3	second order	[5, 6.67]	[23,24.34]	[20.5,21.5]

So, obtained second order reduced denominator polynomial is

$$D_2(s) = [5, 6.67]s^2 + [23, 24.34]s + [20.5, 21.5]$$

Step 2. Minimized order of numerator is calculated by Cauer's second form.

$$\left[f_1^-, f_1^+\right] = [1.281, 1.433]$$

$$\left[f_2^-, f_2^+\right] = [1.262, 1.599]$$

$$\left[p_{21}^-, p_{21}^+\right] = [12.820, 17.03]$$

$$\left[p_{22}^-, p_{22}^+\right] = [10.458, 8.4660]$$

So, first order reduced numerator is represented as

$$N_2 = [10.458, 8.4660]s + [12.820, 17.03]$$

So, obtained second order reduced model is

$$R_2(s)|_{\substack{\text{proposed} \\ \text{method}}} = \frac{[10.458, 8.4660]s + [12.820, 17.03]}{[5, 6.67]s^2 + [23, 24.34]s + [20.5, 21.5]}$$

The reduced second order models by some other techniques (Gamma-delta approximation, Impulse-energy method, and Mihalov-Cauer) are given below for comparison purposes.

$$R_2(s)|_{\substack{\gamma-\delta \\ \text{method}}} = \frac{[1.0091, 1.2554]s + [0.8109, 1.1166]}{s^2 + [2.0181, 2.4429]s + [1.492, 1.5051]}$$

.

$$R_2(s)|_{\substack{\text{impulse} \\ \text{energy} \\ \text{method}}} = \frac{[1.172, 1.3682]s + [1.0269, 1.1097]}{s^2 + [2.344, 2.6234]s + [1.4033, 1.5164]}$$

$$R_2(s)|_{\substack{\text{mihalov-cauer} \\ \text{method}}} = \frac{[11.195, 20.370\text{s} + [14.168, 16.942]}{[17.001, 18]s^2 + [31.38, 33.61]s + [20.306, 21.706]}$$

Figures 1 and 2 represent the comparison of step output for upper and lower bounds of the original system with the minimized model by the proposed method and the minimized model derived by methods like Gamma-delta, Impulse-Energy, and Mihalov-Cauer for the same problem. The comparison of other performance parameters like Overshoot, Rise time, settling time, and ISE are presented in Tables 2 and 3.

Example 2 Consider an interval system transfer function model of sixth order F(s) whose numerator and denominator are N(s) and D(s) are to be reduced in second order by proposed method.

$$\begin{aligned} N(s) = {} & [3.1, 3.6]s^5 + [104.1, 104.7]s^4 + [310.1, 312.6]s^3 + [230, 240.6]s^2 \\ & + [28, 29.2]s + [9, 9.9] \end{aligned}$$

$$\begin{aligned} D(s) = {} & [2.1, 2.6]s^6 + [76.1, 76.7]s^5 + [119.1, 119.6]s^4 + [111, 111.6]s^3 + \\ & [71.8, 72.3]s^2 + [31, 31.7]s + [9, 9.9] \end{aligned}$$

Step 1. By using the Table 1, the obtained second order polynomial of the denominator is represented as

$D_2(s) = [3.920, 5.670]s^2 + [9.636, 11.264]s + [9, 9.9]$

Step 2. Reduction of numerator by Cauer second form (Fig. 3 and Tables 4, 5)

$$\begin{aligned} \left[f_1^-, f_1^+\right] &= [0.9090, 1.1] \\ \left[f_2^-, f_2^+\right] &= [3.2727, 3.6397] \\ \left[p_{21}^-, p_{21}^+\right] &= [2.4727, 10.8910] \\ \left[p_{31}^-, p_{31}^+\right] &= [0.6793, 3.3278] \end{aligned}$$

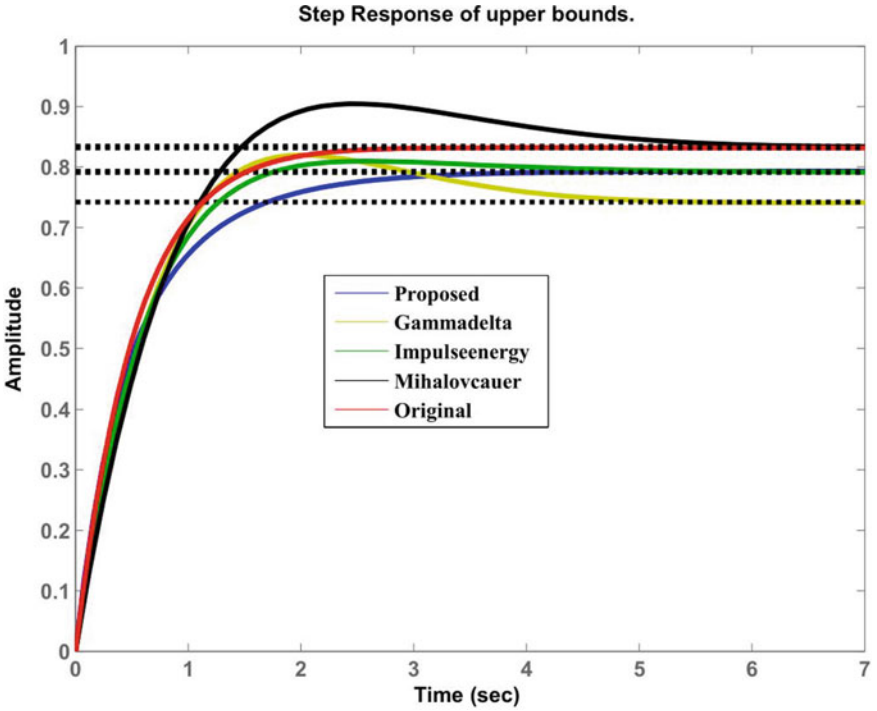

Fig. 1 Comparison of lower bound step outputs of original model reduced model (Proposed) and reduced model of other methods

$$\left[p_{22}^{-}, p_{22}^{+}\right] = [7.21325, 9.8529]$$

So obtained first order numerator given as

$$N_2 = [7.21325, 9.8529]\,s + [2.4727, 10.8910]$$

$$R_2(s)|_{\substack{\text{proposed}\\ \text{method.}}} = \frac{N_2(s)}{D_2(s)} = \frac{[7.21325, 9.8529]s + [2.4727, 10.8910]}{[3.920, 5.670]s^2 + [9.636, 11.264]s + [9, 9.9]}$$

Example 3 Consider an interval transfer function of oblique wing aircraft H(s). The objective of the problem is to derive the second order minimized model by the proposed method and calculate the PID controller's parameters, which stabilize H(s).

$$H(s) = \frac{[2, 3]s^2 + [17.8, 18.5]s + [15, 16]}{[1, 1]s^3 + [9.245, 10.749]s^2 + [5.8, 9]s + [4, 4]}$$

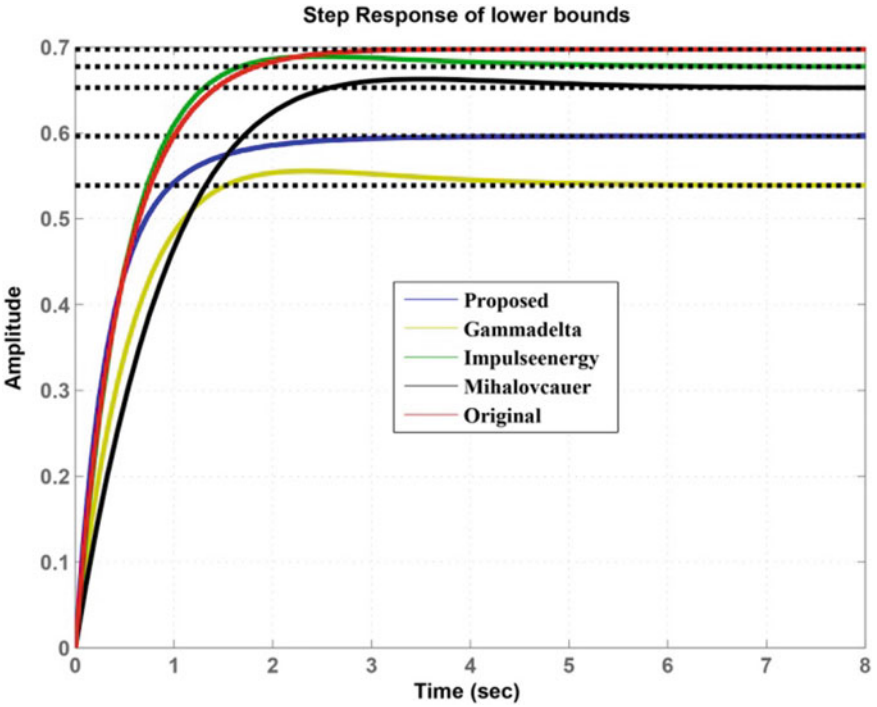

Fig. 2 Comparison of upper bound step outputs of original model reduced model (Proposed) and reduced model of other methods

Table 2 Upper bound parameters

Parameters	Original	Proposed	Gamma-delta	Impulse-energy	Mihalov-Cauer
Overshoot	0.0191	0	10.4950	2.3821	8.4053
Settling time	1.9052	2.5877	4.0884	3.1868	4.6888
Rise time	1.113	1.3332	0.8281	1.0482	1.0547
Peak time	4.0561	7.2268	1.9953	2.6220	2.4312
ISE	–	2.62790838 $\times e^{-7}$	1.93886305 $\times e^{-7}$	1.34488219 $\times e^{-7}$	3.7612084 $\times e^{-7}$

Table 3 Lower bound parameters

Parameters	Original	Proposed	Gamma-delta	Impulse-energy	Mihalov-Cauer
Overshoot	0.0150	0	3.1103	1.7475	1.5388
Settling time	2.0245	1.9232	3.3565	1.4351	2.2448
Rise time	1.1431	0.9116	0.9483	0.9461	1.5357
Peak time	4.6591	8.8507	2.3424	2.4651	3.5376
ISE	–	2.0747211 $\times e^{-7}$	0.816533143 $\times e^{-7}$	3.04124522 $\times e^{-7}$	5.02828226 $\times e^{-7}$

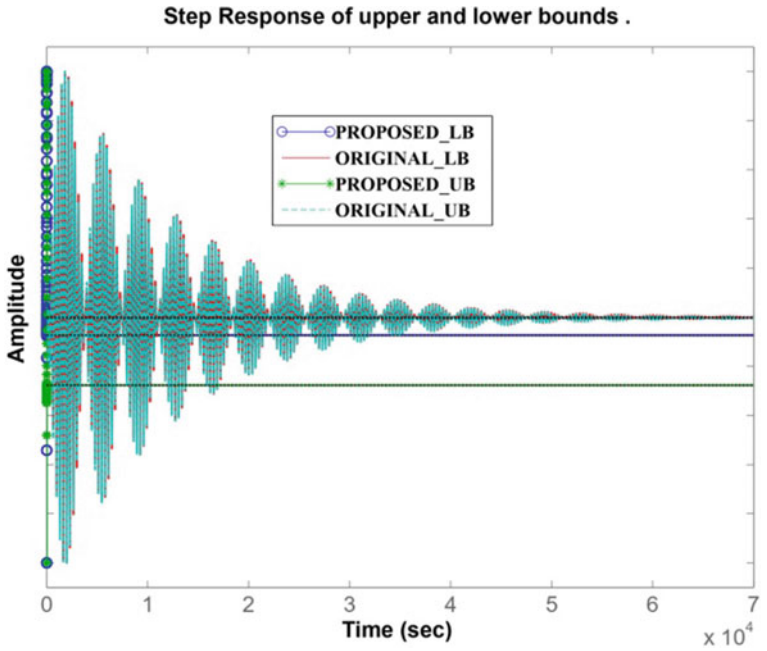

Fig. 3 Comparison of lower and upper bounds step responses for the original and minimized model

Table 4 Upper bound parameters

Parameters	Original model	Proposed model
Overshoot	656.9067	176.9834
Settling time	7.2439 e^4	6.1859
Rise time	0.1439	0.1439
Peak time	1.0839	1.0839
ISE	–	1.60742032 $\times e^{-6}$

Table 5 Lower bound parameters

Parameters	Original model	Proposed model
Overshoot	571.4491	115.9256
Settling time	7.0702 e^4	3.8035
Rise time	0.4347	0.1334
Peak time	32.2125	0.8334
ISE	–	0.837782488 $\times e^{-6}$

Obtained reduced model by proposed method represented as

$$R(s) = \frac{N_r(s)}{D_r(s)} = \frac{[10.458, 8.4660]s + [12.820, 17.03]}{[2.0647, 3.5687]s^2 + [-1.216, 2.153]s + [4, 4]}$$

Kharitonov's polynomials of R(s) are represented as

Numerator Kharitonov's polynomial $N_r(s)$

$$N_1(s) = 10.458s + 12.820$$
$$N_2(s) = 8.4660s + 12.820$$
$$N_3(s) = 10.458s + 17.03$$
$$N_4(s) = 8.4660s + 17.03$$

Denominator Kharitonov's polynomial $D_r(s)$

$$D_1(s) = 3.5687s^2 - 1.216s + 4$$
$$D_2(s) = 3.5687s^2 + 1.216s + 4$$
$$D_3(s) = 2.0647s^2 - 1.216s + 4$$
$$D_4(s) = 2.0647s^2 + 1.216s + 4$$

Therefore, 16 transfer functions ($k_1, k_2 \ldots$ K16) of $R_2(s)$ obtained from Kharitonov's polynomials of reduced model. The PID parameters and obtained PID tuned step response are represented in Table 6 and Fig. 5 for all transfer function models respectively and Fig. 4 represents the step response of $R_2(s)$ (Table 6).

6 Conclusion

The paper presents the model order reduction of the linear interval system based on two methods. For the minimization of numerator order, Cauer's second form is used, and the denominator of the model is reduced by using the extension of the differentiation method (i.e. differentiation method based on Routh array). The comparison of the reduced model's upper and lower bounds step responses with the actual model results most precise approximation as testing is done in the examples and real-time PID design application for the interval plant. The proposed method is highly efficient in providing minimum ISE, the most accurate approximated model, and guarantees the overall stability of the minimized model.

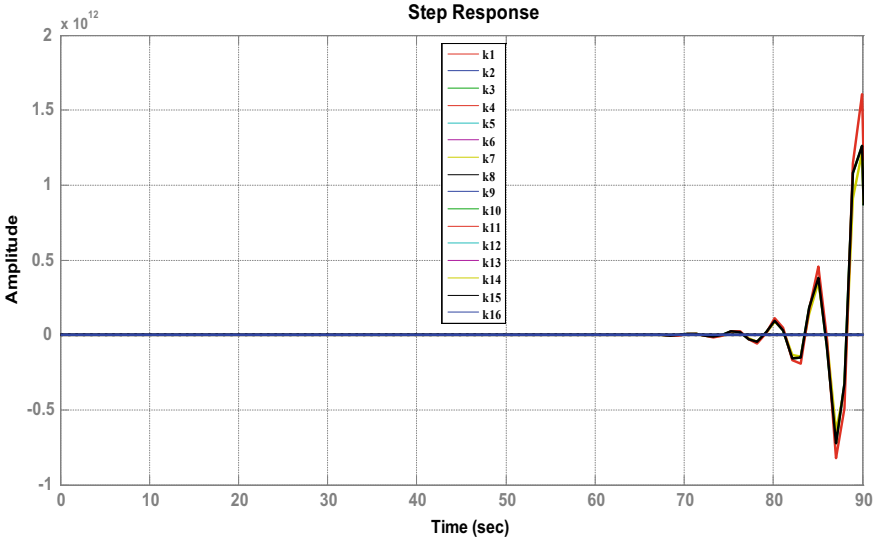

Fig. 4 Step responses of sixteen reduced model $R_2(s)$

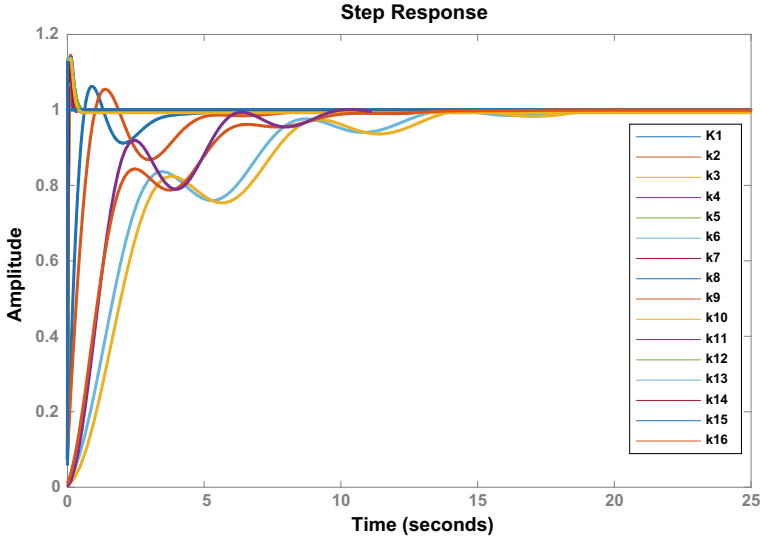

Fig. 5 PID tuned step responses

Table 6 Parameters of PID

Transfer function	Kp	Ki	Kd
k1	1.3063	71.9481	0.027113
k2	0.5139	0.4910	0.0354
k3	7.496	52.327	0.0158
k4	0.013812	0.17506	0.0002724
k5	15.8232	92.358	0.03457
k6	0.041449	0.11024	0.003896
k7	137.9063	1761.5214	0.0188123
k8	0.67947	0.90057	0.014974
k9	13.0696	97.4857	0.02705
k10	0.016601	0.073543	0.0009368
K11	13.5074	187.249	0.015553
K12	6.4336	35.0978	0.016015
K13	99.1335	5547.7752	0.032176
K14	15.7344	150.308	0.02677
K15	7453.2463	66,045,869.67	0.015115
K16	0.03499	0.16056	0.0019063

References

1. M. Petreczky, J. Leth, R. Wisniewski, A.C. Antoulas, I.V. Gosea, Model reduction of linear hybrid systems, in *2020 59th IEEE Conference on Decision and Control* (CDC, 2020), pp. 110–117
2. P. Tapan, S.P. Singh, V.P. Singh, Analytic hierarchy process-based model reduction of higher order continuous systems using sine cosine algorithm. Int. J. Syst. Control Commun. **11**(1), 52–67 (2020)
3. K. Jay, An order reduction of LTI systems using Pade and Routh-Pade approximations. J. Fut. Eng. Technol. **16**(1) (August 2020)
4. K.K. Deveerasetty, S.K. Nagar, Model order reduction of interval systems using an arithmetic operation. Int. J. Syst. Sci. **51**(5), 886–902 (April 2020)
5. A. Kumar, V.G. Rayudu, A. Sikander, R. Prasad, Prajapati, A new technique for the reduced-order modeling of linear dynamic systems and controller design. Circ. Syst. Signal Process. **39**, 4849–4867 (October 2020)
6. P.D. Dewangan, V.P. Singh, S.L. Sinha, Improved approximation for SISO and MIMO continuous interval systems ensuring stability. Circ. Syst. Signal Process. **39**(9), 4705–4716 (2020)
7. P.K. Juneja, A. Sharma, A. Sharma, R.R. Mishra, F.S. Gill, A review on model order reduction techniques for reducing order of industrial process transfer function model, in *2020 International Conference on Advances in Computing, Communication & Materials (ICACCM)* (2020), pp. 346–350
8. K. Jay, et al., A new soft computing approach for order diminution of interval system. Int. J. Syst. Assur. Eng. Manag. **2**, 366–373 (November 2020)
9. J.K. Bokam, V.P. Singh, R. Devarapalli, F.P. García Márquez, An improvement of Gamma approximation for reduction of continuous interval systems, in *Archives of Control Sciences* (2021)

10. A.P. Padhy, V. Singh, V.P. Singh, Stable approximation of discrete interval systems. Circ. Syst. Signal Process. **40**(10), 5204–5219 (October 2021)
11. S.R. Potturu, R. Prasad, Qualitative analysis of stable reduced order models for interval systems using mixed methods. IETE J. Res. **67**(1), 108–116 (January 2021)
12. M. Elsisi, M. Soliman, Optimal design of robust resilient automatic voltage regulators, in *ISA Transactions* (2021), pp. 257–258
13. S.K. Gautam, S. Nema, R.K. Nema, Model order reduction of interval systems using routh approximation with mid-point concept and stability equation method, in *2021 IEEE 2nd International Conference on Electrical Power and Energy Systems (ICEPES)* (IEEE, 2021), pp. 1–5
14. H. Mallesam Dora, Model order reduction of discrete uncertain system using modified δ-γ routh approximation and affine arithmetic method. J. Adv. Res. Electr. Eng. Technol. **3**(1), 22–25 (October 2021)
15. V.P. Meena, V.P. Singh, L. Barik, Kharitonov polynomial-based order reduction of continuous interval systems, in *Circuits, Systems and Signal Processing* (2021) , pp. 1–19
16. A. Kumar, R. Prasad, A novel order reduction method for linear dynamic systems and its application for designing of PID and lead/lag compensators. Trans. Inst. Measur. Control **43**(5), 1226–1238 (2021)
17. Nafees, A. Sikander, G.S. Ahamad, A novel reduction approach for linear system approximation, in *Circuits, Systems, and Signal Processing* (2021), pp. 1–25
18. S. Kumar, A.K. Suman, Investigation and implementation of model order reduction technique for large scale dynamical systems, in *Archives of Computational Methods in Engineering* (2022), pp. 1–22
19. S. Batool, M. Imran, M.I. Ahmad, Accuracy enhancing model reduction technique for weighted and limited interval systems with error bound. J. Control Autom. Electr. Syst. 1–13 (January 2022)

Stabilizing Voltage and Frequency of Multi-area Interconnected Power System with Time Delays

Ch. Naga Sai Kalyan and Chintalapudi V. Suresh

Abstract This paper focuses on regulating both terminal voltage and frequency of a multi-area interconnected power system (MAIPS) simultaneously under the regulation of the Three-Degree-of-Freedom (DOF)-PID (3DOFPID) controller. For this, combined load frequency control (LFC) and automatic voltage regulation (AVR) of MAIPS are investigated by subjugating area-1 with a 10% step load. However, 3DOFPID is fine-tuned optimally using a seagull optimization algorithm (SOA) and the supremacy of 3DOFPID is demonstrated with the performances of 2DOFPID/PID. Communication time delays (CTDs) are conceived in the loops of AVR and LFC to conduct research work close to a more realistic approach. The dynamical behaviour of MAIPS is compared under SOA optimized 3DOFPID without and with considering CTDs to reveal its impact on performance. Simulation results reveal the predominant effect of CTDs on performance regulation of both terminal voltage and system frequency.

Keywords MAIPS · 3DOFPID · SOA · CTDs · 10% step load

1 Introduction

Voltage and frequency are powerful indicators especially when it comes to the operation and control of modern power systems (MPS). MPS is becoming complex day by day with the integration of diverse source generation plants with a focus on meeting the load demand comfortably. Handling the complex interconnected system is a hustle and should be addressed conscientiously. Variation of demand in any control area leads to fluctuations in the frequency of other areas as the control areas are connected via tie-lines. Tie-line facilitates the power flow exchange among deficit and surplus generation areas. Hence, it is necessary to develop a robust controller to hold the deviations in frequency and power flow in the tie-line and not vary beyond

Ch. Naga Sai Kalyan (✉) · C. V. Suresh
EEE Department, Vasireddy Venkatadri Institute of Technology, Guntur 522508, India
e-mail: kalyanchallapalli@gmail.com

J. Kumar et al. (eds.), *Control Applications in Modern Power Systems*, Lecture Notes in Electrical Engineering 974, https://doi.org/10.1007/978-981-19-7788-6_17

the limits. Such kind of automatic regulator is exist and is termed a load frequency controller [1].

In addition to the above, holding voltage within specified limits is also one of the considerable parameters while assessing the stability of MAIPS. However, this can be addressed with AVR by varying field excitation of the alternator [2]. The literature review showcased that rigorous controller approaches are listed in LFC and AVR domains separately and researchers are hardly focused on proposing controllers for LFC-AVR combined study. Numerous control approaches like conventional PI/PID are fine-tuned using ant colony optimizer (ACO) [3], moth flame optimization (MFO), Multiverse optimization (MVO) [4], and harmony search algorithm (HSA) [5]. Fractional order (FO) type classical FOPI, FOPID optimized with volleyball algorithm (VBA) [6], Elephant herd optimizer (EHO), dragonfly algorithm (DFA), symbiotic-organism-search-algorithm (SOSA), Sine–cosine algorithm (SCA) [7], Bat algorithm (BA). Various fuzzy (F) FPI, FPID and FO based fuzzy regulators like FFOPID and cascade controllers optimized with water cycle algorithm (WCA), teaching–learning optimization (TLO), and Marine predator algorithm (MPA) [8], Constrained Population Extremal (CPE) [9], cuckoo search algorithm (CSA).

However, the above-mentioned controllers are proposed for the power system for the LFC study and the coupling of AVR is not deliberated. Few controlling techniques are reported in LFC-AVR combined study such as particle swarm optimization based PI [10], PID rendered optimally using differential evolution (DE) [11] and simulated annealing (SA) [12] strategy, PID plus double derivative (PIDD) [13] tuned using grey wolf optimizer (GWO), FOPID based on lightening search algorithm [14]. But none of them adopted the realistic non-linearity parameters of CTDs with the system. In [15, 16], considered the CTDs with MAIPS but limited the analysis to the classical controller. The literature survey discloses that the implementation of DOF controllers for the LFC-AVR study is not reported. This enlightens the authors in this paper to propose a 3DOFPID controller as a regulator for the LFC-AVR system and is a maiden attempt. DOF controllers fine-tuned with DFA, WCA [17], SOA and bacteria-foraging approach (BFA) techniques are reported in the literature. SOA is one of the finest searching strategies that researchers are currently focusing on as a solution to non-linear constraint problems. Thus, SOA is preferred in this paper to render 3DOFPID gains optimally in the LFC-AVR study.

Considering the above literature, contributions of this work:

(a) LFC-AVR of MAIPS is developed in MATLAB/SIMULINK.
(b) 3DOFPID optimized with SOA is proposed as a secondary regulator in the loops of LFC-AVR.
(c) Efficacy of 3DOFPID is revealed with PID/2DOFPID.
(d) Finally, the impact of CTDs on the LFC-AVR model of MAIPS performance is showcased and justified.

2 Power System Under Investigation

Nuclear-Hydro-Thermal units are considered as generation utilities in both the areas of MAIPS with equal generation capacity. Each area has a capacity of 2000 MW of which nuclear unit is having a rating of 1000 MW and thermal and hydro is 750 MW and 250 MW respectively. In both the areas, LFC with AVR link up is enacted via K_1, K_2, K_3 and K_4 coupling parameters. Figure 1 depicts the LFC-AVR system transfer function model and AVR is shown in Fig. 2. Researchers all around the world focused on only LFC and neglected the AVR coupling owing to its least impact on LFC performance. Besides that, the changes in the LFC loop hardly affect the AVR performance whereas the alterations in AVR loops greatly affect the LFC performance and are explained using Eq. (1).

$$P_e = \frac{|V||E|}{X_S} \mathrm{Sin}(\delta) \tag{1}$$

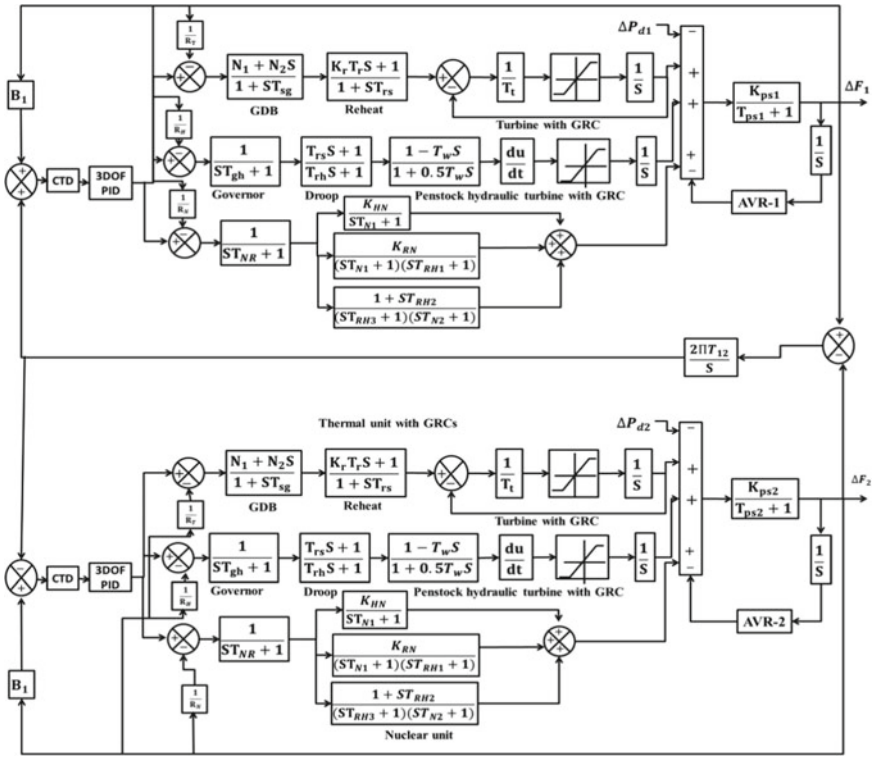

Fig. 1 LFC-AVR combined model of MAIPS with CTDs

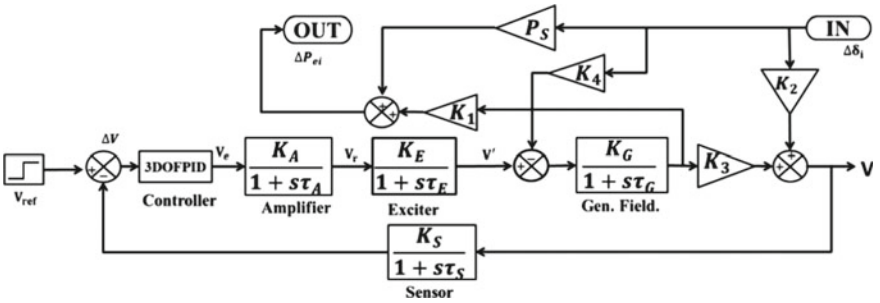

Fig. 2 AVR with coupling parameters

where P_e, V and E represent real power, terminal voltage and E.M.F. induced in alternator winding respectively. XS indicates the reactance and 'δ' is the load angle. The variations in V and δ alter the real power generation and thus AVR is having a significant impact on the LFC loop. The detailed mathematical modeling involved in the coupling of LFC-AVR is discussed in Kalyan and Sambasiva Rao [18].

3 Communication Time Delays

Communication between devices and sensors housing in different distant locations will only be possible through communication channels. Modern IPS are wide and complex and employ communication channels to get signals from remote terminal units (RTUs). Data from RTUs is transmitted to the command control room for generating an error signal. The error signal is transmitted to the regulator in the plant location and based on that error the regulator changes the operating point of the power system. Real power mismatch is a powerful indicator in LFC which greatly influences the deviations in system frequency. Transmitting and receiving signals via communication channels won't be done instantly, because the channels inherit the property of time delays. Transport type delay is considered in this paper and is modeled as given in Eq. (2).

$$e^{-s\tau_d} = \frac{1 - \frac{\tau_d}{2}s}{1 + \frac{\tau_d}{2}s}. \tag{2}$$

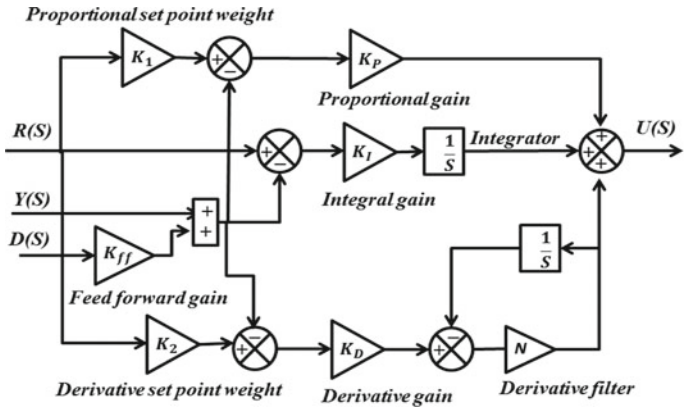

Fig. 3 Architecture of 3DOFPID

4 3DOFPID Controller

3DOFPID controller as a secondary regulator in the LFC-AVR model is a maiden attempt and achieved the control action using multiple control loops. DOF represents the number of independent control loops that regulate the system individually. Initially, analysis is carried out with PID and 2DOFPID and later extended to 3DOFPID.

Figure 3 represents the architecture of 3DOFPID implemented in this paper. The three individual loops in 3DOFPID account for stability improvement, disturbance elimination and response shaping. However, the efficacy of 3DOFPID depends on its parametric values that needed to be optimized using some optimization algorithms. In this paper, SOA is utilized to find 3DOFPID controller gains optimally subjected to the time-domain performance index of integral square error (ISE) given in Eq. (3).

$$J_{ISE} = \int_0^T (\Delta f_1^2 + \Delta P_{tie,12}^2 + \Delta f_2^2)dt \tag{3}$$

5 Seagull Optimization Algorithm

Seagulls technically termed Laridae are smart and intelligent birds that are usually found, especially on seashores. The intelligent behaviour of seagulls inspires the researchers Dhiman and Kumar [19] to propose an SOA algorithm in 2019. Seagulls feed on amphibians, earthworms, fish and other insects that comes into omnivores family. The species of seagulls are usually differentiated using length and weight.

They can drink both fresh and salt water. Seagulls are very intelligent, especially in search of prey; they can trap the fish by spraying bread crumbs into the water and can make a special sound like rain to attract earthworms that are hidden in the soil. SOA can handle the balance between exploitation and exploration phenomena.

A special parameter 'B' is introduced in the algorithm to avoid the chances of collision among the birds during the migration phase. These are very smart in finding new locations with abundant sources of food and water during migration. The position of the search agent $\vec{P}_S$ is initialized upon incorporating the special parameter 'B' as given in Eq. (4).

$$\vec{P}_S = B \chi \vec{K}_S(x) \tag{4}$$

'$\vec{K}_S(x)$' indicates the current position in the current iteration. The special parameter that dominates the other particle movement can be modelled as

$$B = F_c - (x*(F_c/\text{Max.Iter})) \tag{5}$$

The frequency of special parameter 'B' will be regulated by the parameter 'F_C' considered to be 2 in this paper and can be decayed from 2 to 0 linearly. Later, the particles move towards best $\vec{P}_{bs}(x)$ is given as

$$\vec{N}_S = A \chi (\vec{P}_{bs}(x) - \vec{K}_S(x)) \tag{6}$$

where, 'A' is the randomized parameter which can be calculated as

$$A = 2*B^2*\text{rand}() \tag{7}$$

At the time of migration also, seagulls attack the birds to feed above the sea water in three dimensional spaces and that spiral movement can be modeled as

$$T' = d*\text{Cos}(z) \tag{8}$$

$$D' = d*\text{Sin}(z) \tag{9}$$

$$P' = d*z \tag{10}$$

'z' represents the random number from [0–2Π] and 'd' is the radius of spiral movement. Finally, upon saving the best solution the other particle positions are updated as

$$\vec{K}_S(x) = (\vec{N}_S*T'*D'*P') + \vec{P}_{bs}(x) \tag{11}$$

6 Simulation Results

6.1 Case-1: Analysis of Combined LFC-AVR Model of MAIPS Without Considering CTDs

The Combined LFC-AVR model of MAIPS is analyzed in this subsection without considering CTDs. Carried out the analysis upon laying the perturbation of 10% step load (10%SLP) on area-1. Different controllers such as 3DOFPID/2DOFPID/PID are enacted as secondary regulators in LFC-AVR loops one by one and their parameters are rendered optimally using the SOA algorithm. Dynamical responses under various controllers under the same disturbing conditions are compared in Fig. 4, to reveal the best control strategy. Responses are analyzed in terms of the deviation of frequency in area-1 (Δf_1), area-2 (Δf_2), tie-line power (ΔP_{tie12}) and voltage at area-1 (V_1) and area-2 (V_2). Analyzing the responses shown in Fig. 4, concluded that 3DOFPID shows its superiority in regulating MAIPS dynamical behaviour. Further, the undershoot (Us) of responses are greatly enhanced with 3DOFPID ($\Delta f_1 = 0.2490$ Hz, $\Delta f_2 = 0.252$ Hz, $\Delta P_{tie12} = 0.0047$ Pu.MW) compared to that of ($\Delta f_1 = 0.5462$ Hz, $\Delta f_2 = 0.4908$ Hz, $\Delta P_{tie12} = 0.02108$ Pu.MW) 2DOFPID and ($\Delta f_1 = 0.5731$ Hz, $\Delta f_2 = 0.638$ Hz, $\Delta P_{tie12} = 0.02468$ Pu.MW) PID. Moreover, the 3DOFPID index is enhanced by 80.66%with PID and 66.05%with 2DOFPID. Responses to settling time along with optimal control gains are noted in Tables 1 and 2.

6.2 Case-2: Analysis of Combined LFC-AVR Model of MAIPS with Considering CTDs.

In this subsection, MAIPS of the LFC-AVR model is perceived with CTDs and carried the analysis for 10%SLP on area-1. Dynamical responses of the system with SOA optimized 3DOFPID/2DOFPID/PID controllers as secondary regulators in LFC-AVR loops are shown in Fig. 5. Noticing the dynamical behaviour shown in Fig. 5, concluded that 3DOFPID shows its superiority even though MAIPS is perceived with CTDs in controlling dynamical behaviour. Further, the undershoot (Us) of responses are greatly enhanced with 3DOFPID ($\Delta f_1 = 0.6076$ Hz, $\Delta f_2 = 0.5735$ Hz, $\Delta P_{tie12} = 0.01415$ Pu.MW) compared to that of ($\Delta f_1 = 0.690$ Hz, $\Delta f_2 = 0.6218$ Hz, $\Delta P_{tie12} = 0.01958$ Pu.MW) 2DOFPID and ($\Delta f_1 = 0.6334$ Hz, $\Delta f_2 = 0.6568$ Hz, $\Delta P_{tie12} = 0.06844$ Pu.MW) PID. Finally, the controller objective function values are evaluated for this case and concluded that the ISE of 3DOFPID is improved by 84.97%with PID and 75.39%with 2DOFPID.

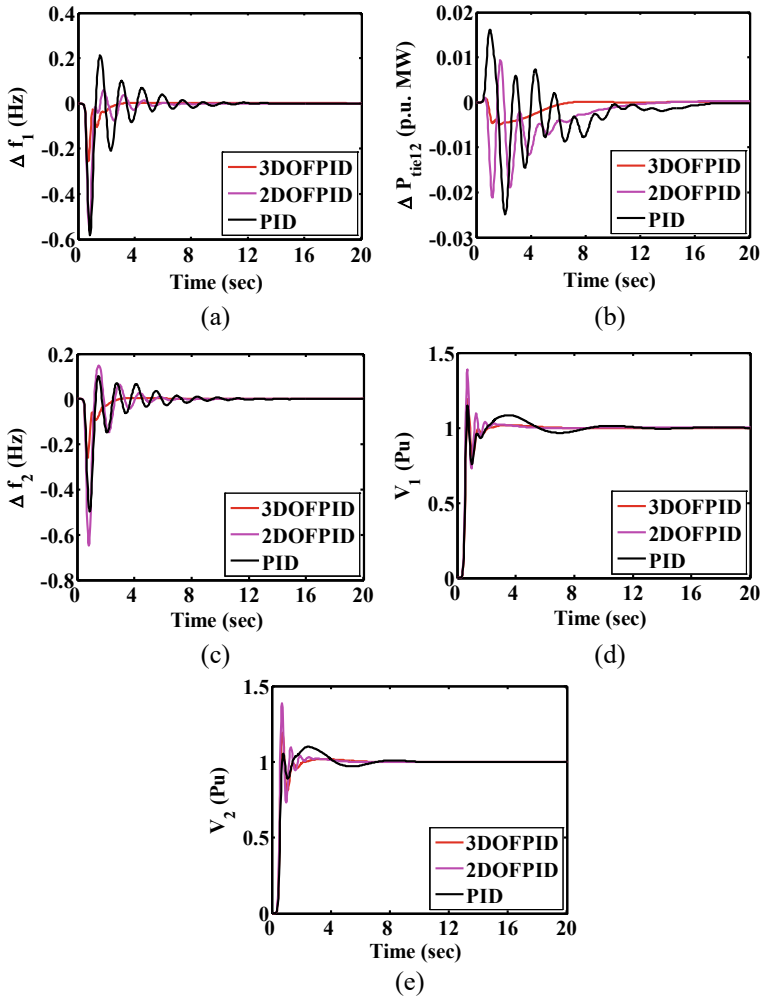

Fig. 4 Responses for case-1

Table 1 Responses settling time (in Sec)

Settling time	Case-1			Case-2		
	3DOFPID	2DOFPID	PID	3DOFPID	2DOFPID	PID
Δf_1	3.31	6.89	8.14	6.83	7.98	8.949
ΔP_{tie12}	8.76	13.89	17.77	12.89	15.13	19.78
Δf_2	4.28	7.54	11.25	6.98	8.46	11.64
V_1	5.46	6.38	12.61	5.89	6.06	9.861
V_2	5.74	7.25	9.68	6.66	7.53	9.98
ISE*10^{-4}	8.36	24.65	43.27	14.59	59.32	97.15

Table 2 Controller optimal gains

Parameters	LFC			AVR		
	3DOFPID	2DOFPID	PID	3DOFPID	2DOFPID	PID
K_P	0.6036	0.5710	0.6727	0.7801	0.8934	0.9876
K_I	0.1679	0.9012	0.8932	0.4897	0.1782	0.7645
K_D	0.8007	0.3212	0.7932	0.5510	0.5003	0.6932
K_1	0.0871	0.0671	–	0.0685	0.0268	–
K_2	0.0273	0.1091	–	0.0312	0.0672	–
K_{ff}	0.3277	–	–	0.4321	–	–

6.3 Case-3: Demonstrating the Predominance of CTDs on LFC-AVR System Performance

Responses of the LFC-AVR model of MAIPS under SOA based 3DOFPID regulation are compared in Fig. 6, to reveal the impact of CTDs on LFC-AVR performance. Noticing the responses in Fig. 6, it is clear that the responses are a little bit more deviated with considering CTDs. Considering CTDs, the peak undershoots/overshoots of the system are slightly high with CTDs compared to the situation of not deliberating CTDs with the MAIPS. This is due to the delay in control signal generation results in a variation of power system operating points leading to a mismatch in real power generation. If the controller is designed without taking CTDs with MAIPS, that may not be robust in handling system dynamical behaviour during large perturbation and parametric uncertainties. Further, the designed controller couldn't safeguard system stability in case of unpredictable delays emerges with the system. A realistic time delay of 0.12 s is taken and recommends considering CTDs with IPS while developing a secondary regulator.

7 Conclusion

3DOFPID rendered optimally using nature-inspired SOA is implemented as a regulator in both LFC and AVR loops successfully. Efficacy of 3DOFPID is showcased upon comparing with 2DOFPID/PID performances under the same load disturbing conditions. Earlier, the realistic non-linearity constraint of CTDs is considered with MAIPS to furnish work close to real nature. Comparative analysis reveals the significance of CTDs on both the performances of LFC and AVR in regulating frequency and terminal voltage. The delay in receiving the error signals received by the secondary regulators leads to the delay in altering the power system operating point thereby more fluctuations in system dynamical behaviour. This paper supports considering CTDs with MAIPS while furnishing a secondary regulator to avoid system instability in case of unintended time delays arise within the system.

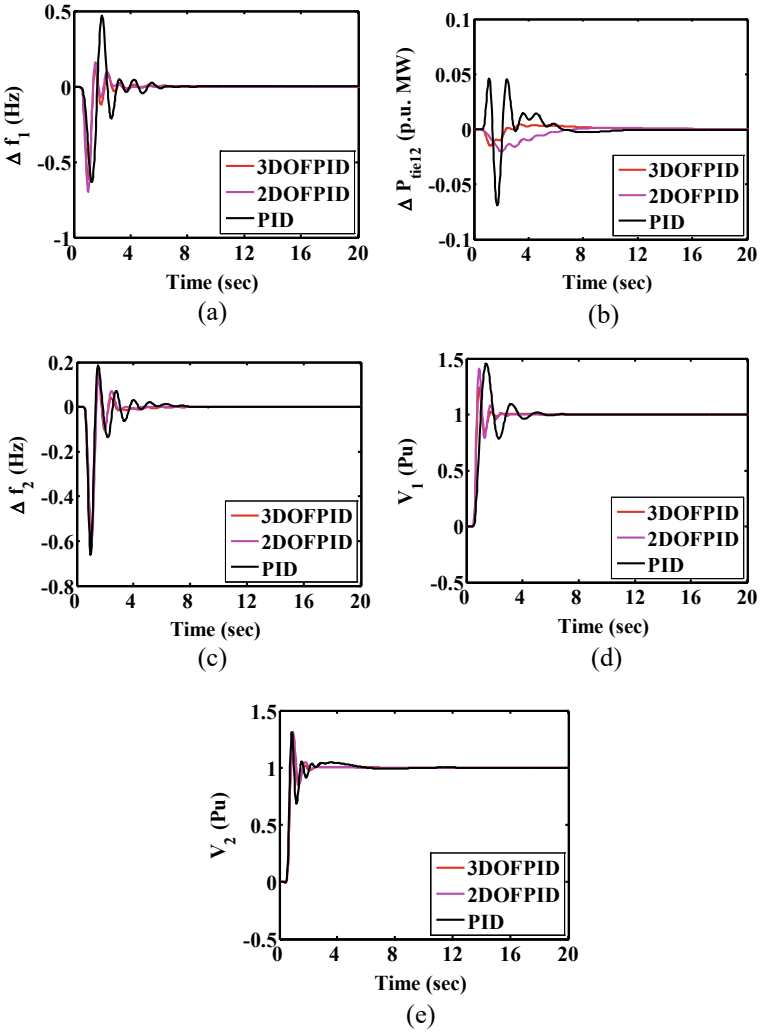

Fig. 5 Responses for case-2

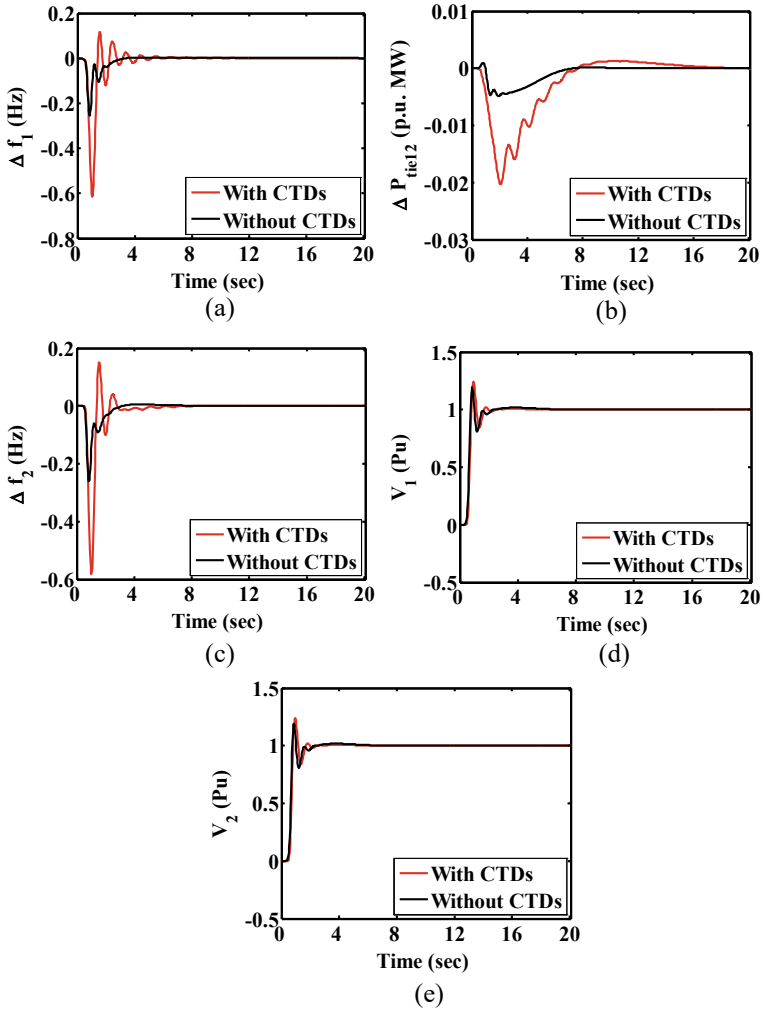

Fig. 6 Responses for case-3

References

1. D.H. Tungadio, Y. Sun, Load frequency controllers considering renewable energy integration in power system. Energy Rep. **5**, 436–454 (2019)
2. K. Challapalli, G. Sambasiva Rao, Frequency and voltage stabilization in combined load frequency control and automatic voltage regulation of multi area system with hybrid generation utilities by AC/DC links. Int. J. Sustain. Energy **39**(10), 1009–1029 (2020), https://doi.org/10.1080/14786451.2020.1797740
3. B. Dhanasekaran, S. Siddhan, J. Kaliannan, Ant colony optimization technique tuned controller for frequency regulation of single area nuclear power generating system. Microprocess. Microsyst. **73**, 102953 (2020)

4. P.K. Sahoo, S. Mohapatra, D.K. Gupta, S. Panda, Multi verse optimized fractional order PDPI controller for load frequency control. IETE J. Res. (2020). https://doi.org/10.1080/03772063.2020.1756933
5. M. Omar, M.A. Ebrahim, A. Abdelghany, F. Bendary, Tuning of PID controller for load frequency control problem via harmony search algorithm. Int. J. Elec. Eng. Com. Sci. **1** (2), 255–263 (2016)
6. A. Prakash, S. Murali, R. Shankar, R. Bhushan, HVDC tie-link modeling for restructured AGC using a novel fractional order cascade controller. Electr. Power Syst. Res. **170**, 244–258 (2019)
7. W. Tasnin, W., L.C. Saikia, Comparative performance of different energy storage devices in AGC of multi-source system including geothermal power plant. J. Renew. Sustain. Energy (2018). https://doi.org/10.1063/1.5016596
8. A.H. Yakout, M.A. Attia, H. Kotb, Marine predator algorithm based cascaded PIDA load frequency controller for electric power systems with wave energy conversion systems. Alexandria Eng. J. **60**, 4213–4222 (2021)
9. M.R. Chen, Z.G. Qiang, X.X. Qiang, Population extremal optimization-based extended distributed model predictive load frequency control of multi-area interconnected power systems. J. Franklin Inst. **355**(17), 8266–8295 (2018)
10. A. Gupta, A. Chauhan, R. Khanna, Design of AVR and ALFC for single area power system including damping control, in *Recent Advances in Engineering and Computational Sciences (RAECS)* (Chandigarh, 2014), pp. 1–5
11. C.H.N. Kalyan, G. Sambasiva Rao, Demonstrating the effect of excitation cross coupling and communication time delays on automatic generation control, in *2021 4th Biennial International Conference on Nascent Technologies in Engineering* (ICNTE) (2021), pp. 1–6. https://doi.org/10.1109/ICNTE51185.2021.9487779
12. K.R.M Vijaya Chandrakala, S. Balamurugan, Simulated annealing based optimal frequency and terminal voltage control of multi-source multi area system. Electr. Power Energy Syst. **78**, 823–829 (2016)
13. C.H.N. Kalyan, UPFC and SMES based coordinated control strategy for simultaneous frequency and voltage stability of an interconnected power system, in *2021 1st International Conference on Power Electronics and Energy (ICPEE)* (2021), pp. 1–6. https://doi.org/10.1109/ICPEE50452.2021.9358576
14. R. Rajbongshi, L.C. Saikia, Combined voltage and frequency control of a multi-area multi-source system incorporating dish-Stirling solar thermal and HVDC link. IET Renew. Power Gen. **12**(3), 323–334 (2018)
15. C.H.N. Kalyan, S., G. Sambasiva Rao, Combined frequency and voltage stabilization of multi-area multisource system by DE-AEFA optimized PID controller with coordinated performance of IPFC and RFBs. Int. J. Amb. Energy. https://doi.org/10.1080/01430750.2020.1860130
16. C.H.N. Kalyan, S., G. Sambasiva Rao, Impact of communication time delays on combined LFC and AVR of a multi-area hybrid system with IPFC-RFBs coordinated control strategy. Prot. Control Mod Power Syst. **6**, 7 (2021). https://doi.org/10.1186/s41601-021-00185-z
17. C.H.N. Kalyan, Water cycle algorithm based intelligent controller for frequency regulation of dual area hybrid system with time delays, in *2021 IEEE International Power and Renewable Energy Conference (IPRECON)* (2021), pp. 1–5, https://doi.org/10.1109/IPRECON52453.2021.9640646
18. C.H.N. Kalyan, S., G. Sambasiva Rao, Coordinated control strategy for simultaneous frequency and voltage stabilization of the multi-area interconnected system considering communication time delays. Int. J. Amb. Energy (2021). https://doi.org/10.1080/01430750.2021.1967192
19. G. Dhiman, V. Kumar, Seagull optimization algorithm: theory and its applications for large-scale industrial engineering problems. Knowledge- Based Systems **165**, 169–196 (2019)

Position Control of DC Servo System Using Fractional Order PID Controller Based on Particle Swarm Optimization

Rama Koteswara Rao Alla, Ganjerupalli Sai Sumanth, and Kandipati Rajani

Abstract Increasing demand of robotics in industrial sector results in usage of DC servo motors because of its high efficiency, high torque to weight ratio, accuracy and resolution. Due to these advantages, the DC servo motor has numerous applications like positioning of dish antennas, balancing the position of aircraft and being used at joints of robots etc. So, for positioning the DC servo motor at desired and accurate position a controller is needed to control it. Fractional-Order Proportional Integral-Derivative (FOPID) controller has been used in this work for the position control, which is advanced than Proportional Integral Derivative (PID) controller. The PID controller consists of only three control parameters but FOPID consists of five control parameters which results in more accurate positioning compared to PID controller. To tune the FOPID controller parameters, particle swarm optimization (PSO) has been used to achieve accurate and desired positioning. To make position control automatic the closed loop operation is performed, there by adjusting the position of DC servomotor to its desired position. This paper analyzes the position control of DC servo system performance with FOPID controller tuned by PSO optimization algorithm.

Keywords DC servo motor · FOPID and PSO

1 Introduction

The most common controller in industrial sector is PID controller because of its simple structure, safety and reliability [1]. Despite the PID controller's advantages,

R. K. R. Alla (✉) · G. S. Sumanth
RVR & JC College of Engineering, Guntur, Andhra Pradesh 522019, India
e-mail: ramnitkkr@gmail.com

G. S. Sumanth
e-mail: saisumanth1500@gmail.com

K. Rajani
Vignan's Lara Institute of Technology and Sciences, Guntur, Andhra Pradesh, India
e-mail: rajanikandipati@gmail.com

J. Kumar et al. (eds.), *Control Applications in Modern Power Systems*, Lecture Notes in Electrical Engineering 974, https://doi.org/10.1007/978-981-19-7788-6_18

it requires ongoing development to achieve high performance results. So, the FOPID controller is the alternative to achieve best results. The FOPID controller consists of total of five control parameters which are to be tuned to achieve best results. As a result, the system performance can be improved with the FOPID [2].

To get an optimal control, it must be found the optimal set of values of K_p, K_i, K_d, λ, μ [3]. There are many-methods to-find the optimal-values. One of the methods is PSO which is a computation technique. This method blends social psychology concepts in human agents' socio-cognition with evolutionary computations. It depends on behaviors of things-such as bird-flocking and fish-schooling. It has a basic-concept, is easy to appliance, has a computationally effective method, is a flexible and well-proportioned tool and is highly efficient compared to GA [4].

Finding the best values for K_p, K_i, K_d, λ, μ [5] and-to match-the user's requirement for a particular process-plant necessitates optimization of parameters in five-dimensional hyperspace [6]. This paper gives a brief framework about FOPID, PSO and control of DC servo motor and their results.

2 Fractional Order PID Controller

Igor Podlubny investigated-the fractional-order PID controller, abbreviated as FOPID, in 1997 [7]. The FOPID controller is an evolution for traditional PID controller, it consists of two more additional parameters compared to PID controller [8]. Those parameters are λ, μ which may be non-integer values. The block diagram of FOPID is depicted in Fig. 1.

The integro-differential equation for a FOPID controller's control action is specified by:

$$u(t) = K_p e(t) + K_i D^{-\lambda} e(t) + K_d D^{\mu} e(t) \tag{1}$$

and the resulting controller transfer function becomes

$$GFOID(S) = K_p + K_i / S^{\lambda} + K_d \cdot S^{\mu} \tag{2}$$

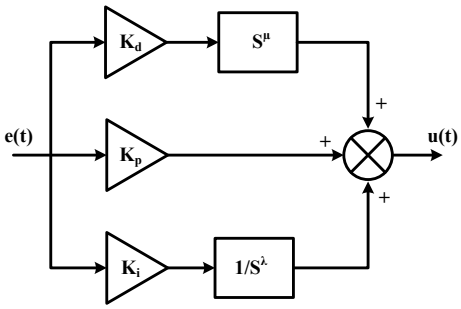

Fig. 1 Block diagram for FOPID

where, λ and μ are an arbitrary non-real values. A classic PID controller is obtained by taking $\lambda = 1$ and $\mu = 1$ [9].

However, the optimization challenge connected with the system becomes more complicated as the number of parameters to be tuned increases [10]. So, for achieving the required optimized performance the PSO optimization algorithm has been used [11]. The fractional PID has its fundamental basis embedded in the theory of fractional Calculus [12]. Order by fractions Calculus is a branch of mathematics that extends a function's derivative or integral to non-integer (fractional) order. (dny/dtn) n-fold integrals are evaluated in fractional calculus, where-n is complex,-irrational-or- fractional [13].

3 DC Servo Motor Modeling

By using the control systems, a mechanical equivalent of DC servo motor can be modeled, which is known as inertia model [14]. The inertia model has the same properties as that of real servo motor. To develop the inertia model of servo motor the electrical and mechanical components are to be considered [15]. The electrical components are resistance (R) and inductance (L), whereas the mechanical components are inertia constants (K_t, K_e, K_n) and load inertia (J) and damping (b) and angular position (θ). The saturation effect for output speed is another key non-linear feature in servomotors [16]. Backlash is also one of the types of nonlinearity that effects the servomotor gear system [17].

$$\frac{\theta(S)}{V(S)} = \frac{K_t}{S[(JS+b)(LS+R)+K_tK_e]+K_nK_t} \tag{3}$$

The above equation is the generalized DC servo-motor transfer function. The DC servo system transfer function after considering the required parameters in the generalized transfer function is given as

$$\frac{\theta(S)}{V(S)} = \frac{10}{5S^3+60S^2+100.1S+0.1}. \tag{4}$$

4 Particle Swarm Optimization

Evolutionary method, Particle Swarm-Optimization (PSO) approach-has been proposed by Kennedy-and Eberhart in 1995 [18]. A-population-of random-solutions are-used to start-the swarm. Each element in the swarm represents a fresh set of unknown parameters that must be improved, and each particle represents a sample in the search space that strives to adapt its path toward a prospective area based on

its own flying experience and trades social information with other particles [19]. To-accurately-identify the solution space, the-goal is-to flock the-particles toward-the optimal fitting-solution obtained in last-iterations [20]. The movement of bird from one place to another is equal to development of the solution in PSO [21]. The flow chart below illustrates in what way the PSO algorithm is used to optimize the FOPID controller parameters for the considered system [22] (Fig. 2).

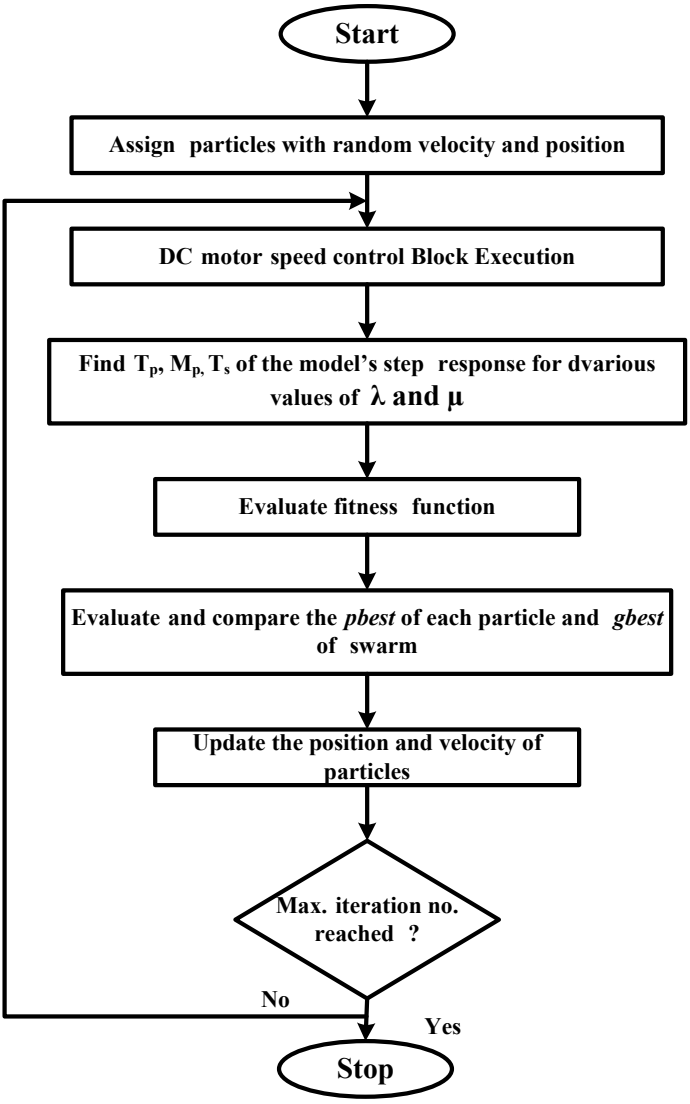

Fig. 2 PSO algorithm flow chart

5 Simulation Results and Discussions

MATLAB SIMULINK is used to do the simulation. The analysis shows the best results for the positioning of DC servo motor by FOPID controller tuned using particle swarm optimization. Here, the input given is step input there by obtaining the step response of DC servo motor. The optimal or best control parameters obtained are given below.

5.1 Without Using PSO

By considering some values of control parameters in FOPID controller using trial and error method: $K_P = 5.4115$, $K_i = 2.0841$, $K_d = 5.2487$, $\lambda = 0.15918$, $\mu = 0.67146$. The closed loop system transfer function including the POPID controller can be derived as below:

$$\frac{\theta(S)}{V(S)} = \frac{5.4115S^{0.15918} + 52.487S^{0.83064} + 20.841}{5S^{3.15918} + 60S^{2.15918} + 100.1S^{1.15918} + 0.1S^{0.15918}} \tag{5}$$

Figure 3 gives the step response of closed loop DC servo system. To show the performance of the system the time domain specifications are tabulated in Table 1.

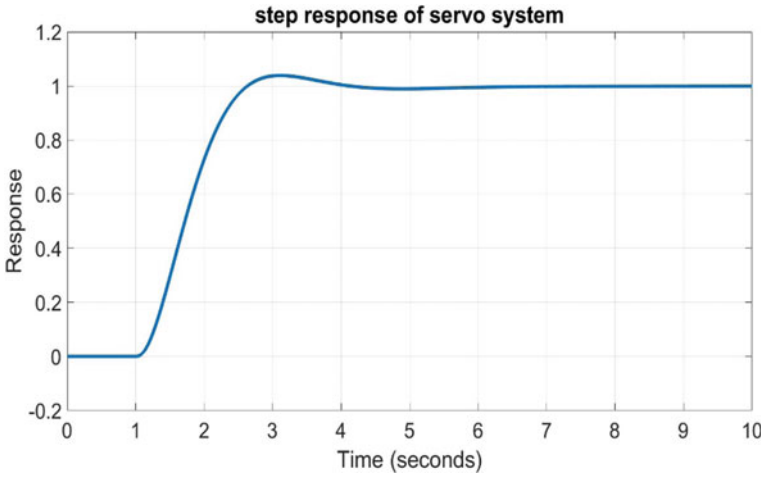

Fig. 3 Step response of DC servo system without using PSO

Table 1 Time domain specifications without PSO

S. no	Specification	Value
1	Delay time	1.908
2	Rise time	2.804
3	Peak time	3.481
4	Peak overshoot	9%
5	Settling time	4.460

5.2 With Using PSO

Case-1: For tuning FOPID parameters using PSO, iteration count and run count are taken as 10 and 5 respectively. After completion of iterations, the best values for K_p, K_i, K_d, λ, μ are $K_p = 1.0000$, $K_i = 19.6941$, $K_d = 9.6602$, $\lambda = 0.0100$, $\mu = 0.9501$. The closed loop system transfer function including the POPID controller can be derived as below:

$$\frac{\theta(S)}{V(S)} = \frac{10S^{0.01} + 196.94 + 96.6S^{0.96}}{5S^{3.01} + 60S^{2.01} + 100.1S^{1.01} + 0.1S^{0.01}} \tag{6}$$

The graph between parameters variation and number of iterations is shown in Fig. 4. The step response of closed loop DC servo system is shown in Fig. 5. To show the effectiveness of the system the time domain specifications are given in Table 2.

Case-2: For tuning FOPID parameters using PSO, iteration count and run count are 5 and 2 respectively. After completion of iterations, the best values for K_p, K_i, K_d, λ, μ are $K_p = 20.8829$ $K_i = 0.0100$ $K_d = 5.7627$ $\lambda = 0.0968$ $\mu = 0.9748$.

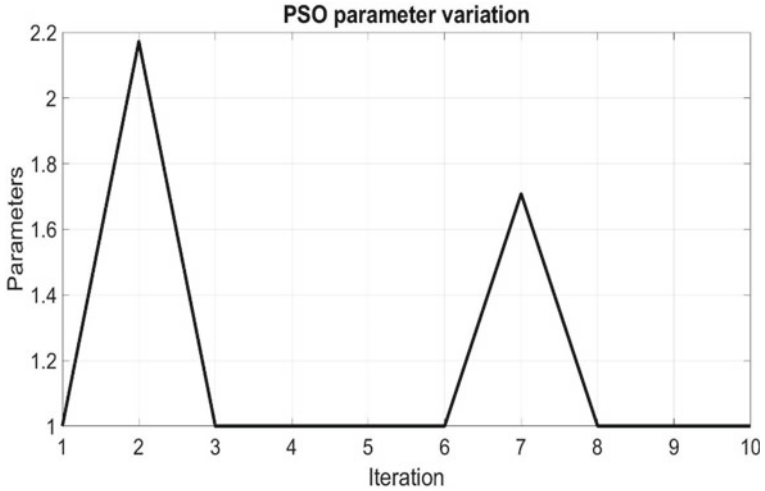

Fig. 4 Variation of parameters with respect to iterations

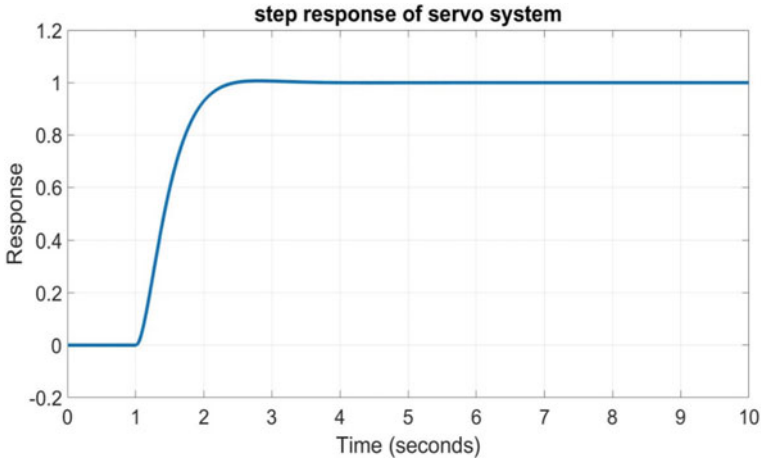

Fig. 5 Step response of DC servo system for 10 iterations

Table 2 Time domain specifications with FOPID tuned by PSO

S. no	Specification	With 10 iterations	With 5 iterations
1	Delay time	1.423 s	1.515 s
2	Rise time	2.405 s	2.215 s
3	Peak time	2.805 s	2.706 s
4	Peak overshoot	0.7%	6.6%
5	Settling time	2.805 s	3.8 s

The graph between parameters variation and number of iterations is shown in Fig. 6. The step response of closed loop DC servo system is shown in Fig. 7. To show the effectiveness of the system the time domain specifications are given in Table 2.

The iteration count does not make any large variation in the output step response but there is a slight variation. The variation is due to the reduced number of iterations producing less accurate best variables/parameters. The difference can be observed from Fig. 8.

6 Conclusion

The positioning of dish antennas, balancing the position of aircraft, and using DC servo motors at robot joints are some of the applications for DC servo motors. A controller is required to regulate the DC servo motor in order to position it at the desired and exact position. Fractional Order Proportional Integral Derivative (FOPID) controller has been used in this work for the position control, which is advanced than Proportional Integral Derivative (PID) controller. The PID controller

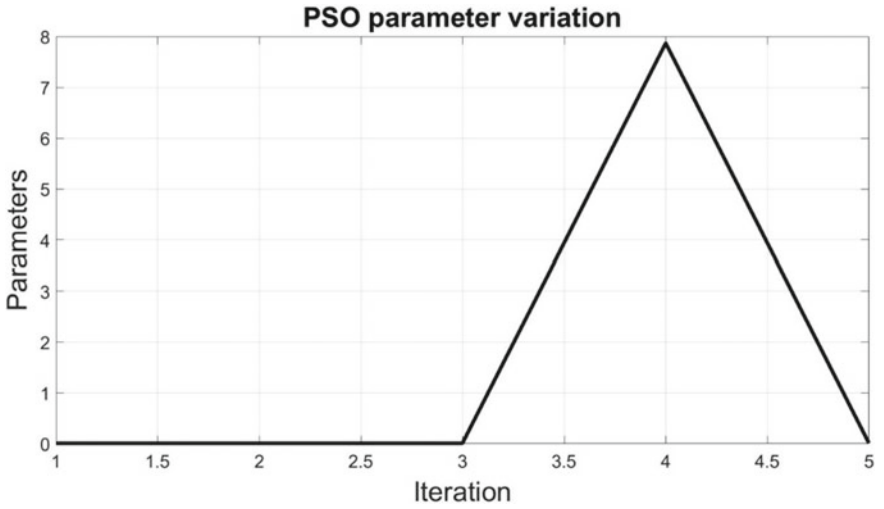

Fig. 6 Variation of parameters with respect to iterations

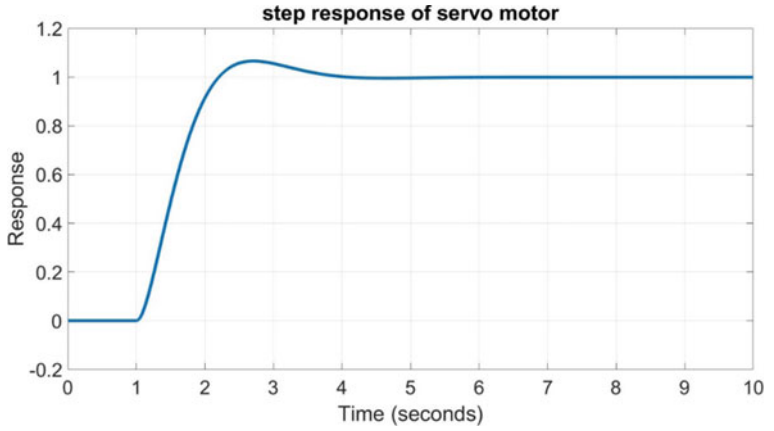

Fig.7 Step response of DC servo system for 5 iterations

consists of only three control parameters but FOPID consists of five control parameters which results in more accurate positioning compared to PID controller. DC servo system position control with fractional-order PID controller tuned by the PSO algorithm has been done in this paper. Based on the simulation results, it can be inferred that the required position of a DC servo system may be obtained smoothly utilizing a FOPID controller tuned by PSO. The time domain specifications of the system with and without PSO tuned FOPID are also tabulated. In terms of settling time, overshoot, peak time, rising time, and delay time, the FOPID tuned by PSO

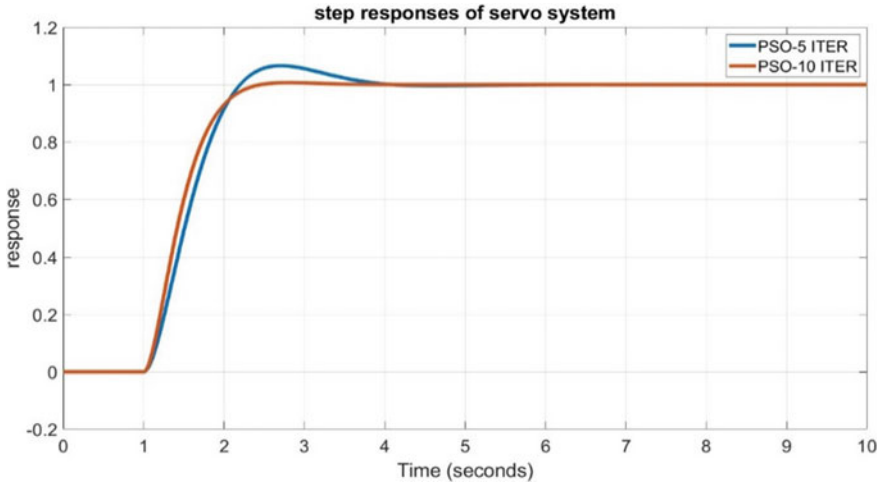

Fig. 8 Comparison of step response for different iteration counts

outperforms the FOPID without PSO, which can be observed from the time domain parameters in terms of overshoot, settling time, etc.

References

1. D. Xue, C. Zhao, Y. Chen, Fractional order PID control of a DC motor with elastic shaft: a case study, in *Proceedings of 2006 American Control Conference* (2006), pp. 3182–3187
2. M. Zamani, M.K. Ghartemani, N. Sadati, FOPID controller design for robust performance using particle swarm optimization. Fract. Calc. Appl. Anal. **10**(2) (2007)
3. V.K. Kadiyala, R.K. Jathoth, S. Pothalaiah, Design and implementation of fractional order PID controller for aerofin control system, in *Proceedings of 2009 World Congress NaBIC* (2009), pp. 696–701
4. D. Maiti, S. Biswas, A. Konar, Design of a fractional order PID controller using particle swarm optimization technique, in *Second National Conference on Recent Trends in Information Systems* (2008), p. 30
5. A.M. Concepcion, B.M. Vinagre, V. Feliu, Y. Chen, Tuning and auto-tuning of fractional order controllers for industry applications. Control Eng. Pract. **16**, 792–812 (2008)
6. A. Chatterjee, V. Mukherjee, S. Ghoshal, Velocity relaxed and craziness-based swarm optimized intelligent PID and PSS controlled AVR system. Int. J. Electr. Power Energy Syst. **31**(7–8), 323–333 (2009)
7. A. Dzielinski, D. Sierociuk, Simulation and experimental tools for fractional order control education, in *Proceedings of IFAC"08* (2008)
8. S. Ghosal, R.K. Darbar, B. Neogi, A. Das, D.N. Tibarewala, Application of swarm intelligence computation techniques in PID controller tuning: a review, in *Proceedings of the International Confernece INDIA 2012, AISC 132* (2012), pp. 195–208
9. R.K.R Alla, J.S. Lather, G.L. Pahuja, PI controller performance analysis using lambert W function approach for first order systems with time delay. Int. J. Adv. Sci. Technol. **86**, 1–8 (2016)

10. Z.-L. Gaing, A particle swarm optimization approach for optimum design of PID controller in AVR system. IEEE Trans. Energy Conv. **19**(2), (2004)
11. S. Padhee, A. Gautam, Y. Singh, G. Kaur, A novel evolutionary tuning method for fractional order PID controller. Int. J. Soft Comput. Eng. (IJSCE) **1**(3) (2011)
12. R. Matusu, Application of fractional order calculus to control theory. Int. J. Math. Models Methods Appl. Sci. **5**(7) (2011)
13. R. Matusu, Application of fractional order calculus to control theory. Int. J. Math. Models Methods Appl. Sci. **5**(7), 1162–1169 (2011)
14. K. Rajani, Modelling and control of switched reluctance motor. B.Sc Thesis, Vignan's Engineering College, Vadlamudi, Guntur, (2011)
15. K. Rajani, K. Rachananjali, K. Krishna, V.S.L. Tirumala, Speed control of 1-φ induction motor using 1-φ matrix converter. Int. J. Control Theory Appl. **9**, 267–271 (2016)
16. R. Singhal, S. Padhee, G. Kaur, Design of fractional order PID controller for speed control of DC motor. Int. J. Sci. Res. Publ. **2**(6) (2012)
17. R.K.R. Alla, N. Lekyasri, K. Rajani, PID control design for second order systems. I.J. Eng. Manuf. **4**, 45–56 (2019)
18. R.K.R. Alla, J.S. Lather, G.L. Pahuja, Comparison of PI controller performance for first order systems with time delay. J. Eng. Sci. Technol. **12**(4), 1081–1091 (2017)
19. M.R. Dastranj, M. Rouhani, A. Hajipoor, Design of optimal fractional order PID controller using PSO algorithm. Int. J. Comput. Theory Eng. **4**(3) (2012)
20. S.N.V. Akhila, K. Rajani, Control of SRM using 3-level Neutral point diode clamped converter with PI and Fuzzy controller. Int. Adv. Res. J. Sci. Eng. Technol. **3**(8), 211–217 (2016)
21. S. Vaneshani, H. Jazayeri-Rad, Optimized fuzzy control by particle swarm optimization technique for control of CSTR. World Acad. Sci. Eng. Technol. **59**, (2011)
22. K. Sundaravadivu, K. Saravanan, Design of fractional order PID controller for liquid level control of spherical tank. Eur. J. Sci. Res. **84**(3), 345–353 (2012)

Modular Dual Active Bridge Converter Phase Control to Charge EV

Reena Singh, Suresh Kumar Gawre, and Dyanamina Giribabu

Abstract This paper presents a control scheme for a bidirectional Dual Active Bridge converter to charge an electric vehicle battery. Providing constant power in a higher range with higher efficiency, the DAB DC-DC converter plays an important role in minimizing the number of passive components. The high-frequency transformer isolates eight semiconductor switches with a transformer of high frequency. The high Dc link capacitor has been minimized for stable output voltage using single-phase shifting (SPS). This control scheme has one control degree of freedom under this control scheme the converter can achieve low current stress, zero-voltage switching (ZVS), and high dynamics. Multiple DAB converter modules are connected parallelly to increase the charging current which results in lower charging time. A 600 W power converter is developed and simulated in MATLAB to charge the vehicle battery and its performance has been analyzed.

Keywords Electric vehicle · Dual Active Bridge · Battery charging

1 Introduction

Electric vehicles are becoming popular in the Indian market due to increasing fossil fuel prices and environmental pollution issues. Also, the Indian government is providing subsidies for buying personal and commercial electric vehicles. The development of EVs largely depends on the development of suitable chargers, capable of quickly charging the vehicle's battery that complies with grid standards.

The EV charger is broadly classified into the on-board charger (typically slow charger) and off-board charger (fast charger). The working scheme of an EV charging system with on-board and off-board charging with different power levels (levels 1, 2 & 3) is depicted in Fig. 1. In each type of charger, the converter topologies differ significantly in power ratings. Many converter topologies have been proposed, analyzed, and compared on charging time, power levels, and other factors [1]. These

R. Singh (✉) · S. K. Gawre · D. Giribabu
Department of Electrical Engineering, MANIT, Bhopal, India
e-mail: reenas630s@gmail.com

J. Kumar et al. (eds.), *Control Applications in Modern Power Systems*, Lecture Notes in Electrical Engineering 974, https://doi.org/10.1007/978-981-19-7788-6_19

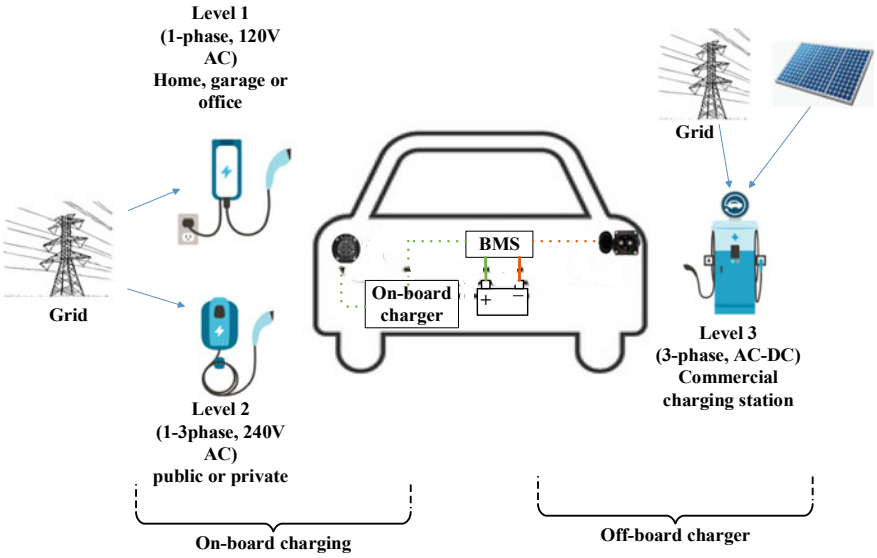

Fig. 1 Ev charging system

days, researchers are working on on-board charging to further reduce the charging time. For faster adoption of EVs fast charging is necessary. However, fast charging requires high-power density with a lower voltage range of battery which makes power electronics converter unique and unfeasible for on-board charger implementation. Off-board chargers with rated power greater than or equal to 50 kW are characterized as fast chargers [2].

Level 3 DC chargers usually accommodate a very high-power level of 120–240 kW. There are two power conversion stages in each DC charging station. AC to DC and DC to DC conversion stages are built into these standalone units. To increase power levels and enable fast charging, power conversion modules are stacked inside a charging station. A DC fast charging station delivers an electric vehicle's battery with a high-power DC current directly, without passing through an on-board AC/DC converter. Most electric vehicles on the road cannot handle more than 50 kW. In the coming years, new cars will be able to charge at higher rates of power. As EV batteries grow and have a greater range, DC charging stations that deliver up to 120 kW are being developed to assist long-range EV batteries [3].

The DC-link between the charger and the battery management system (BMS) is interconnected using one or more DC/DC power converters in various configurations of EV charging systems. Bidirectional Dual Active Bridge converters are among the most widely used DC/DC converters in charging stations because they offer an array of advantages, such as high-power density, bidirectional power transfer capability, zero-voltage switching (ZVS), and symmetrical structure [4].

As shown in Fig. 2 a charging station, the DC/DC converter must be capable of connecting to a rectified 3-phase Vienna rectifier bus voltage (700–800 V) at its

input and the battery of an electric vehicle at its output, ensuring that rated power is delivered. DC/DC converters find applications in a variety of equipment. and illustrates its use in electric vehicle charging stations, solar photovoltaics, and energy storage systems [5].

A DC/DC converter must be able to handle high levels of power. Furthermore, the converter must be able to parallel the output power throughput of a single power stage converter so that it can be scaled upwards as needed by DC charger station standards. As technology develops, charging stations are moving toward converters that can handle bidirectional power flow. V2G, for example, is a new practice that involves connecting the batteries of an electric vehicle to the AC grid. DC/DC converters with bidirectional capabilities allow for forward and reverse charging of batteries, allowing the grid to stabilize during peak load periods by supplying power from the batteries back to the grid.

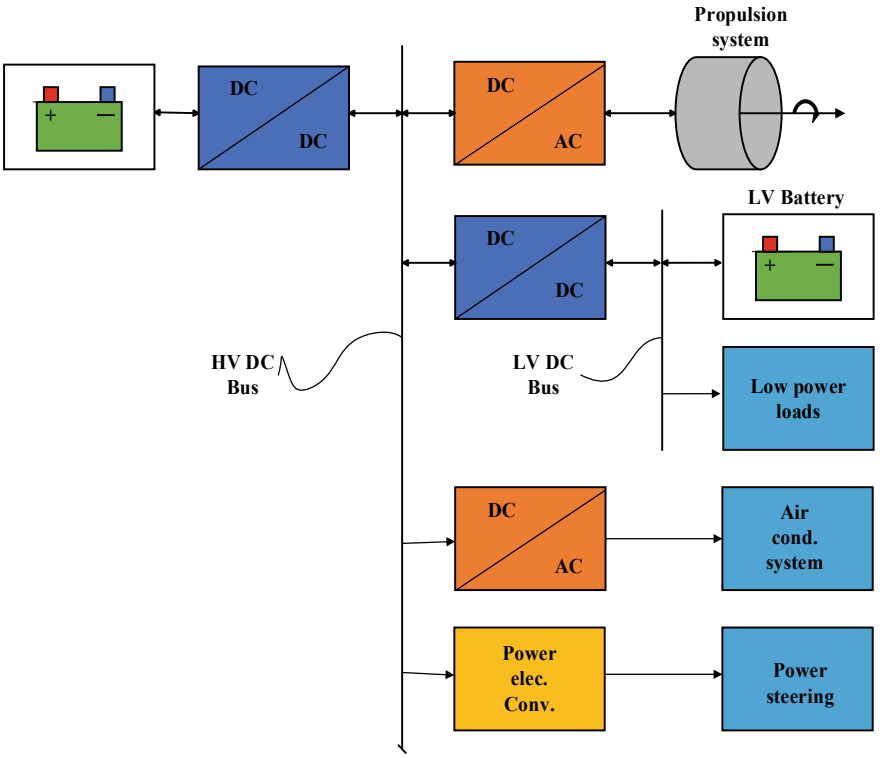

Fig. 2 Electric vehicle power system architecture

2 Dab Converter Working and Modelling

DAB is becoming the favoured topology among designers for applications that require bidirectional power flow and galvanic separation due to its many advantages, including its symmetric construction, zero-voltage switching (ZVS), bidirectional power transfer capability, and high-power density. The bridge can act as an inverter or rectifier depending on the direction of power flow. Inductor current I_L is to be found out to know how much power is transferred and its direction [6]. First, find out the V_L across leakage inductance and then by using it draw the current flowing through inductor and then figure out I_{in} and I_{out}.

Assuming that the primary bridge has no phase shift and 50% duty ratio, it will produce square wave. The second bridge also operates with 50% duty ratio with phase shift. This phase shift controls power flow.

$$I_{outavg} = \frac{\Delta Q}{T_s/2} = \frac{V_o}{R_L} \tag{1}$$

where,

I_{outavg} is average output current
T_s is time period
V_o is output voltage
R_L is load resistance

$$I_2 = t_1 \frac{(V_g + V_o/n)}{L} \tag{2}$$

where,

V_g is input voltage
V_o is output voltage

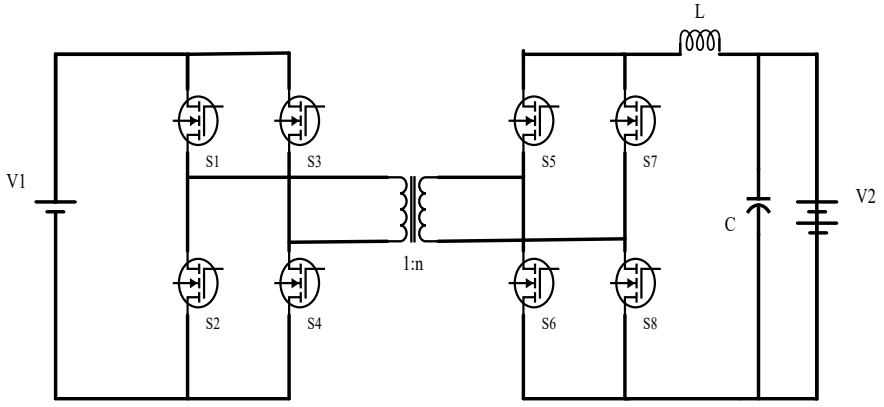

Fig. 3 Bidirectional isolated DAB converter

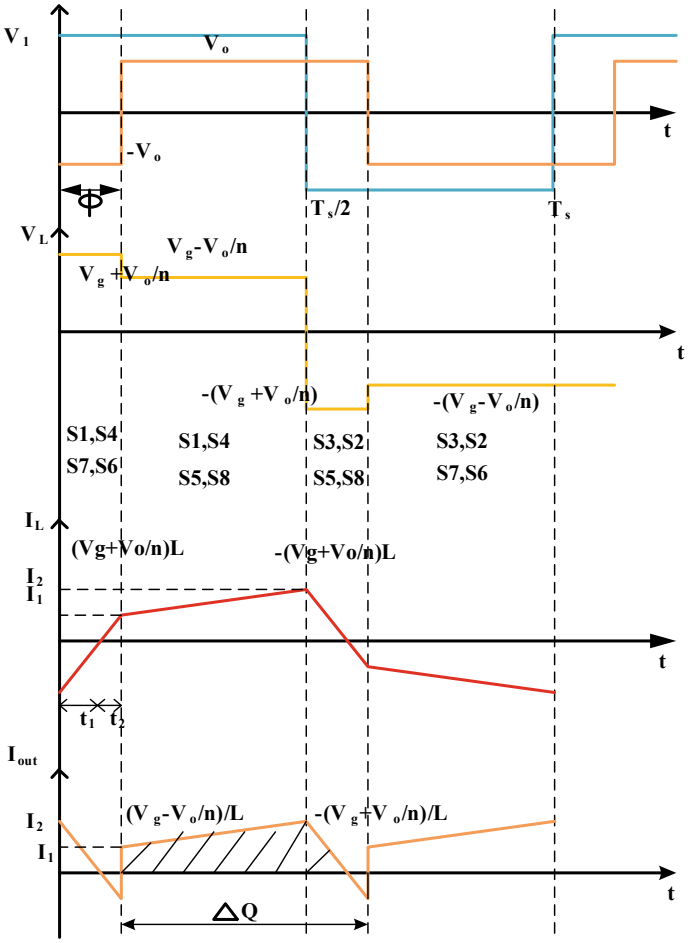

Fig. 4 Input–Output voltage waveform, Voltage across inductor waveform, Current across inductor and Output current [7]

n is number of turns
L is inductor

$$I_1 = t_2 \frac{(V_g + V/n)}{L} \tag{3}$$

$$I_1 + I_2 = \varphi \frac{(V_g + V_o/n)}{L} \tag{4}$$

$$I_2 - I_1 = (\frac{T_s}{2} - \varphi)(\frac{V_g - V_o/n}{L}) \tag{5}$$

$$\Delta Q = \frac{1}{2}(I_1 + I_2)\left(\frac{T_s}{2} - \varphi\right) + \frac{1}{2}t_1 I_2 - \frac{1}{2}t_2 I_1 \tag{6}$$

$$\Delta Q = \varphi\left(\frac{V_g + \frac{V_o}{n}}{L}\right)\left(\frac{T_s}{2} - \varphi\right) + \frac{1}{2}\frac{I_2^2}{\frac{(V_g + V_o/n)}{L}} - \frac{1}{2}\frac{I_1^2}{\frac{(V_g + V_o/n)}{L}} \tag{7}$$

$$\Delta Q = V_g Q \frac{(\frac{T_s}{2} - \varphi)}{L} \tag{8}$$

$$I_o = \frac{\Delta Q}{n\frac{T_s}{2}} \tag{9}$$

where,
I_o is output current

$$I_o = \frac{V_g \varphi\left(1 - \frac{\varphi}{T_s/2}\right)}{nL} \tag{10}$$

$$I_o = \frac{V_g \varphi\left(1 - \frac{\varphi}{T_s/2}\right)}{nL} \tag{11}$$

$$I_o = \frac{V_g D\frac{T_s}{2}(1 - D)}{nL} = \frac{V_g D(1 - D)}{2nLf_s} \tag{12}$$

where,
D is duty ratio
f_s is switching frequency

$$P_o = V_o I_o = \frac{V_o V_g D(1 - D)}{2nLf_s} \tag{13}$$

where,
P_o is output power.

3 Single-Phase Shift Controlling of DAB

In, an intensive study of the SPS control of DAB converters powered by voltage has been conducted. It is very easy to implement, as it only offers one control degree of freedom. The control is ideal for applications where the input and output voltages are fixed. Figure 5 illustrates the main working model of a DAB power converter. In the bridge, v_{AB} is the primary side voltage V_1, and v_{CD} is the secondary side voltage V_2. L_k is the leakage inductance, and n represents the ratio of turns from V_1 to V_2.

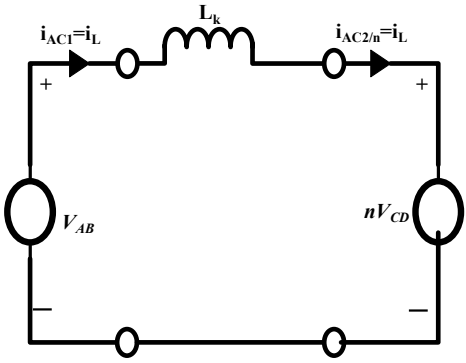

Fig. 5 Basic model of DAB

The transfer of power is associated with the shifting of phase angle between v_{AB} and v_{CD}, as well as the shape of v_{AB} and v_{CD}. Waveforms v_{AB} and v_{CD} can be multi-level or two-level, depending on the topology and the modulation method [8, 9].

Various types of dual active bridge power converters make use of phase shift control There is a relatively large leakage inductance in this type of converter in comparison to other types. The duty cycle of the two active bridges of the DAB converter is fixed at 50%, and when the phase of v_{AB} is leading v_{CD}, the power will be transferred from the V_1 side to the V_2 side while the reverse holds when v_{AB} is lagging v_{CD}. This approach is called conventional phase shift control (CPS). By modifying the duty cycle of the two active bridges as shown in Fig. 6 the converter performance can be improved [10, 11].

Under those circumstances, the converter is able to provide low current stress, wide ZVS range, and high dynamics. Because of the advantages offered by the SPS control, SST signal processing and high voltage direct current transmission are two situations where DAB converters are commonly employed (HVDC) [12]. The conversion efficiency of SPS can be limited due to considerable switching losses produced by constrained ZVS ranges and high non-active power if the voltage conversion ratio fluctuates [13].

In the proposed single-phase controller, the PI controller compares the dc voltage to the reference voltage to control the voltage. A reference current signal is generated using the sinusoidally extracted input voltage signal. The switching pulses for the converter are generated by comparing the battery current to the reference current [14, 15]. The suggested method is more capable than the typical DAB converter, owing to the old method's loss of ZVS (Table 1).

4 Simulation Analysis

Validation of the proposed control structure was done using MATLAB/Simulink to conduct the analysis. A fast charging test was performed on the converter. The actual

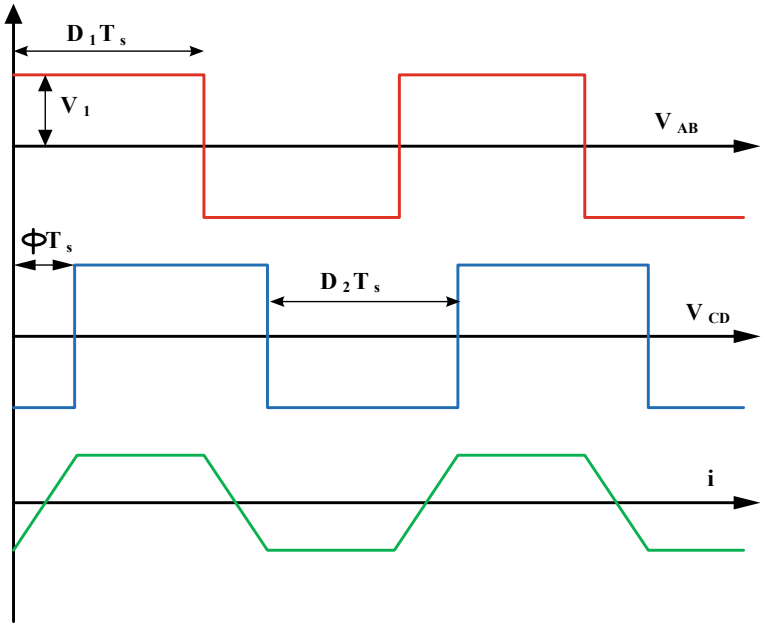

Fig. 6 PWM modulation strategy for Dual Active Bridge converter

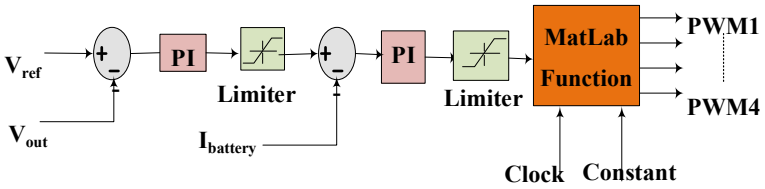

Fig. 7 Single-phase shift DAB controller

Table 1 Calculated values of converter parameters

Parameter	Value
V_{AB}	400 V
V_{CD}	12 V
P_O	600 W
I_O	50 A
F_{SW}	100 kHz
I_{ripple}	20%
V_{ripple}	1%

fast charging parameters vary from the simulated system as the system is analyzed for controlling and performance purposes. The DAB converter is simulated with a battery, the output waveforms are depicted as battery SoC% in Fig. 8a, output current waveform in Fig. 8b and voltage waveform in Fig. 8c. The output current and voltage waveforms are analyzed for ripple content.

The proposed control scheme has one control degree of freedom under this control scheme the converter has achieved low current stress, zero-voltage switching (ZVS), and high dynamics. For the converter to work and be reliable, it must have a stable output voltage and current. Rough voltage and current can also shorten the life of a battery.

As observed from Fig. 8a the battery is charging rapidly using the proposed single-phase shift control modular dual active bridge converter. The modular design of the converter allows high charging current to charge the battery faster and it is desirable, the converter also provides galvanic isolation which is desirable and this converter provides bidirectional power flow. Also, the ripple content in the current and voltage waveform as shown in Fig. 8b and c respectively are low which is good for battery life and performance. The proposed control strategy is simple and easy to implement to control the DAB converter.

In Table 2, the performance of the modular DAB converter with SPS control is compared with the simple DAB converter without SPS control [5].

5 Conclusion

In this paper, an averaged model of modular DAB converter-based battery charger has been proposed and converter parameters are analyzed. In the proposed model the DAB converters are connected parallelly to increase the power density and it is controlled by using single-phase shift control which allows a single degree of freedom. In this control scheme, the converter achieves low current stress, zero-voltage switching, and high dynamics. A 600 W DAB converter is designed and simulated in the Simulink and its performance has been analyzed and compared with a simple DAB converter.

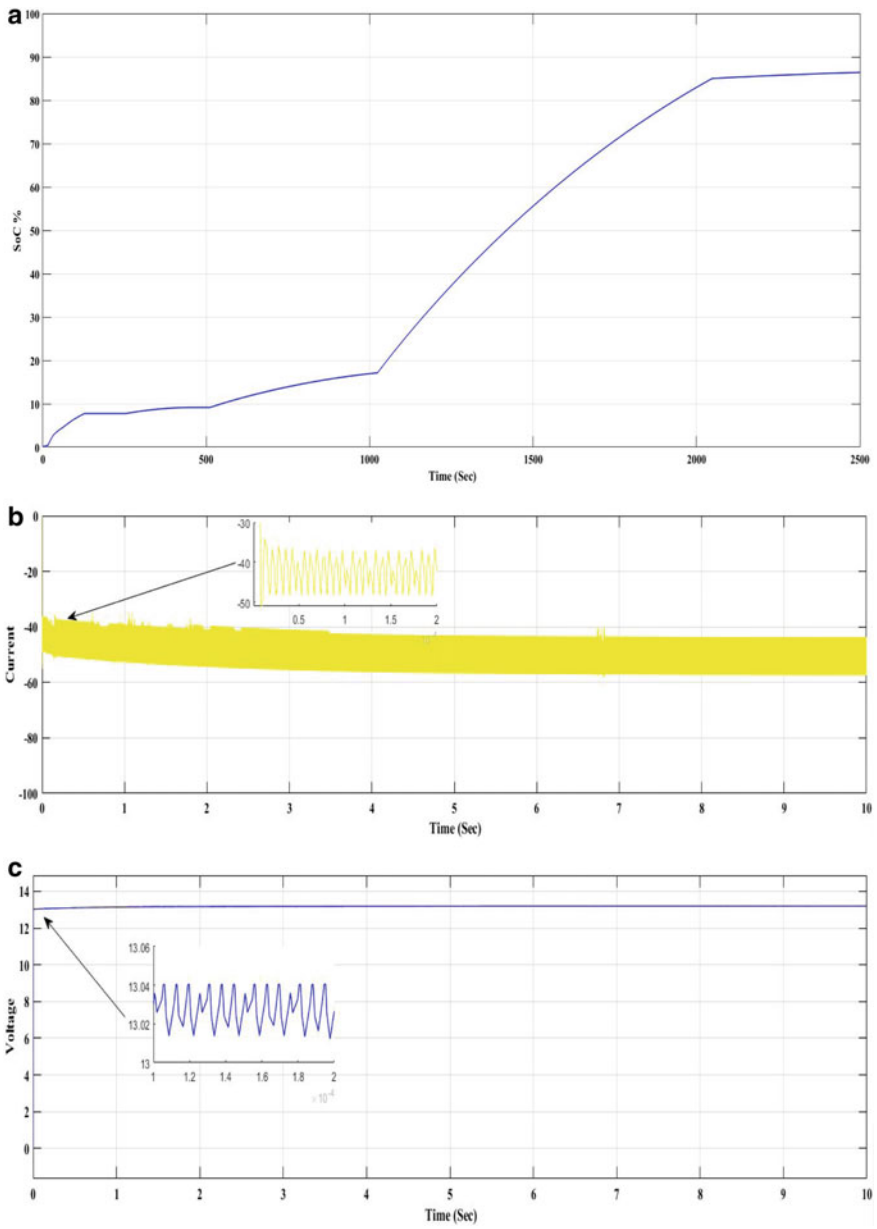

Fig. 8 **a** SoC% of battery. **b** Ripple current for modular DAB. **c** Ripple voltage for modular DAB

Table 2 Comparison of converter performance [5]

S. no	Parameter	DAB	Modular DAB with SPS control
1	SoC% (in 40 min)	0–21%	0–87%
2	Charging current	1 A	35 A
3	Voltage ripple	0.01	0.02
4	Efficiency	Moderate	High

References

1. K. Drobnič, G. Grandi, M. Hammami, R. Mandrioli, A. Viatkin, M. Vujacic, A ripple-free DC output current fast charger for electric vehicles based on grid-tied modular three-phase interleaved converters. Int. Symp. Indus. Electron. (INDEL) **2018**, 1–7 (2018). https://doi.org/10.1109/INDEL.2018.8637627
2. M. Hammami, A. Viatkin, M. Ricco, G. Grandi, A DC/DC fast charger for electric vehicles with minimum input/output ripple based on multiphase interleaved converters. Int. Conf. Clean Electr. Power (ICCEP) **2019**, 187–192 (2019). https://doi.org/10.1109/ICCEP.2019.8890200
3. H. Ramakrishnan, N.N. Kumar, M. Bhardwaj, L. Song, *Level 3 Electric Vehicle Charging Stations*, no. June 2019 Texas Instruments (2021), pp. 1–86
4. J. Zeng, Z. Yan, J. Liu, Z. Huang, A high voltage-gain bidirectional dc–dc converter with full-range ZVS using decoupling control strategy. IEEE J. Emerg. Sel. Top. Power Electron. **8**(3), 2775–2784 (2020). https://doi.org/10.1109/JESTPE.2019.2911331
5. R. Singh, S.K. Gawre, G. Dyanamina, Review and analysis of DC-DC power converter performance for fast charging of EVs, in *2021 IEEE 2nd International Conference on Electrical Power and Energy Systems (ICEPES)* (2021), pp. 1–5. https://doi.org/10.1109/ICEPES52894.2021.9699502
6. K. Meena, K. Jayaswal, D.K. Palwalia, Analysis of dual active bridge converter for solid state transformer application using single-phase shift control technique. Int. Conf. Invent. Comput. Technol. (ICICT) **2020**, 1–6 (2020). https://doi.org/10.1109/ICICT48043.2020.9112398
7. G. Xu, D. Sha, Y. Xu, X. Liao, Hybrid-bridge-based DAB converter with voltage match control for wide voltage conversion gain application. IEEE Trans. Power Electron. (2017)
8. S. Chaurasiya, N. Mishra, B. Singh, A 50 kW bidirectional fast EV Charger with G2V & V2G/V2V capability and wide voltage range, in *2020 IEEE 5th International Conference on Computing Communication and Automation (ICCCA)* (2020), pp. 652–657. https://doi.org/10.1109/ICCCA49541.2020.9250857
9. D. Sha, G. Xu, *High-Frequency Isolated Bidirectional Dual Active Bridge DC–DC Converters with Wide Voltage Gain* (Springer Science and Business Media LLC, 2019)
10. C. Kamalakannan, L. Padma Suresh, S. Sekhar Dash, B.K. Panigrahi, *Power Electronics and Renewable Energy Systems* (Springer Proceedings of ICPERES, 2014)
11. X. Chen, G. Xu, H. Han, D. Liu, Y. Sun, M. Su, Light-load efficiency enhancement of high-frequency dual-active-bridge converter under SPS control. IEEE Trans. Industr. Electron. **68**(12), 12941–12946 (2021). https://doi.org/10.1109/TIE.2020.3044803
12. G. Jean-Pierre, N. Altin, A.E. Shafei, A. Nasiri, A Control scheme based on Lyapunov function for cascaded H-bridge multilevel active rectifiers. IEEE Appl. Power Electron. Conf. Exposit. (APEC) **2020**, 2021–2026 (2020). https://doi.org/10.1109/APEC39645.2020.9124234
13. G.E. Sfakianakis, J. Everts, E.A. Lomonova, Overview of the requirements and implementations of bidirectional isolated AC–DC converters for automotive battery charging applications. Tenth Int. Conf. Ecol. Veh. Renew. Energ. (EVER) **2015**, 1–12 (2015). https://doi.org/10.1109/EVER.2015.7112939

14. Y. Sang, A. Junyent-Ferré, T.C. Green, Operational principles of three-phase single active bridge DC/DC converters under duty cycle control. IEEE Trans. Power Electron. **35**(8), 8737–8750 (2020). https://doi.org/10.1109/TPEL.2020.2964901
15. J. Yin, J. Lu, H. Jiang, Y. Liu, J. Peng, Modified phase-shift scheme for optimal transient response of dual-active-bridge DC/DC converters considering the resistive impact. IEEE Access **9**, 87706–87714 (2021). https://doi.org/10.1109/ACCESS.2021.3088839